UNIVERSITY OF SOUTHAMPTON

FACULTY OF ENGINEERING, SCIENCE AND MATHEMATICS
SCHOOL OF ELECTRONICS AND COMPUTER SCIENCE

Coherent Versus Non-Coherent Space-Time Shift Keying for Co-Located and Distributed MIMO Systems

by

Shinya Sugiura
B.Eng., M.Eng.

A thesis for the degree of
Doctor of Philosophy

August 2010

SUPERVISORS:
Professor Lajos Hanzo
and Professor Sheng Chen

𝔇edicated to my family

UNIVERSITY OF SOUTHAMPTON

ABSTRACT

FACULTY OF ENGINEERING, SCIENCE AND MATHEMATICS
SCHOOL OF ELECTRONICS AND COMPUTER SCIENCE

Doctor of Philosophy

COHERENT VERSUS NON-COHERENT SPACE-TIME SHIFT KEYING FOR CO-LOCATED AND DISTRIBUTED MIMO SYSTEMS

by Shinya Sugiura

In this thesis, we propose the novel Space-Time Coding (STC) concept of Space-Time Shift Keying (STSK) and explore its characteristics in the contexts of both co-located and cooperative Multiple-Input Multiple-Output (MIMO) systems using both coherent and non-coherent detection. Furthermore, we conceive new serially-concatenated turbo-coding assisted STSK arrangements for the sake of approaching the channel capacity limit, which are designed with the aid of EXtrinsic Information Transfer (EXIT) charts.

The basic STSK concept is first proposed for the family of co-located MIMO systems employing coherent detection. More specifically, in order to generate space-time codewords, these Coherent STSK (CSTSK) encoding schemes activate one out of Q dispersion matrices. The CSTSK scheme is capable of striking an attractive tradeoff between the achievable diversity gain and the transmission rate, hence having the potential of outperforming other classic MIMO arrangements. Since no inter-channel interference is imposed at the CSTSK receiver, the employment of single-stream-based Maximum Likelihood (ML) detection becomes realistic. Furthermore, for the sake of achieving an infinitesimally low Bit-Error Ratio (BER) at low SNRs, we conceive a three-stage concatenated turbo CSTSK scheme.

In order to mitigate the effects of potential Channel State Information (CSI) estimation errors as well as the high pilot overhead, the Differentially-encoded STSK (DSTSK) philosophy is conceived with the aid of the Cayley transform and differential unitary space-time modulation. The DSTSK receiver benefits from low-complexity non-coherent single-stream-based ML detection, while retaining the CSTSK scheme's fundamental benefits. In order to create further flexible STSK architecture, the above-mentioned co-located CSTSK scheme is generalized so that P out of Q dispersion matrices are activated during each space-time block interval. Owing to its highly flexible structure, this generalized STSK scheme subsumes diverse other MIMO arrangements.

Finally, the STSK concept is combined with cooperative MIMO techniques, which are capable of attaining the maximum achievable diversity gain by eliminating the undesired performance limitations imposed by uncorrelated fading. More specifically, considering the usual twin-phase cooperative transmission regime constituted by a broadcast phase and by a cooperative phase, the CSTSK and DSTSK schemes developed for co-located MIMO systems are employed during the cooperative transmission phase.

DECLARATION OF AUTHORSHIP

I, **Shinya Sugiura**, declare that the thesis entitled **Coherent Versus Non-Coherent Space-Time Shift Keying for Co-Located and Distributed MIMO Systems** and the work presented in the thesis are both my own, and have been generated by me as the result of my own original research. I confirm that:

- this work was done wholly or mainly while in candidature for a research degree at this University;
- where any part of this thesis has previously been submitted for a degree or any other qualification at this University or any other institution, this has been clearly stated;
- where I have consulted the published work of others, this is always clearly attributed;
- where I have quoted from the work of others, the source is always given. With the exception of such quotations, this thesis is entirely my own work;
- I have acknowledged all main sources of help;
- where the thesis is based on work done by myself jointly with others, I have made clear exactly what was done by others and what I have contributed myself;
- parts of this work have been published as: [1–10].

Signed: .....

Date: .....

Acknowledgements

I would like to express my sincere gratitude to Professor Lajos Hanzo and Professor Sheng Chen for their patience, insightful advice and continuous support of my research. Their instructive advice has always stimulated and guided me in the whole plan and execution of this study.

Many thanks also to my colleagues and the staff of the Communications Group for the useful discussions and comments throughout my research. Special thanks to my colleagues, Dr. Shuang Tan, Dr. Nan Wu, Mr. Wang Yao, Dr. Mohammed El-Hajjar, Dr. Raja Ali Riaz, Dr. Muhammad Fasih, Dr. Soon X. Ng, Dr. Rong Zhang, Professor Lie-Liang Yang and Dr. Robert Maunder for their technical support and collaborative work.

The financial support of Toyota Central Research & Development Laboratories, Inc. and of the EPSRC is gratefully acknowledged. Also, I would like to thank Dr. Kunitoshi Nishikawa, a director of Toyota Central Research & Development Laboratories, Inc. and Dr. Hideo Iizuka with Toyota Motor Engineering & Manufacturing North America, Inc., without whose help and encouragement I would never have started this study.

I would like to express my warmest gratitude to my father, Yoshihiko, and mother, Fumiko, and sister, Yumi, and brother, Koji, for the lifelong encouragement, understanding and faith. Finally, I would like to greatly thank my wife, Aya, for her enormous patience, emotional support and inspiration.

List of Publications

Journal Papers (7):

1. **S. Sugiura**, S. Chen and L. Hanzo, "Coherent and differential space-time shift keying: a dispersion matrix approach," *IEEE Transactions on Communications*, accepted for publication.

2. **S. Sugiura**, S. Chen and L. Hanzo, "Coherent versus non-coherent decode-and-forward relaying aided cooperative space-time shift keying," *IEEE Transactions on Wireless Communications*, submitted.

3. **S. Sugiura**, S. X. Ng, L. Kong, S. Chen and L. Hanzo, "Multiple-relay aided differential distributed turbo coding for asynchronous cooperative networks," *IEEE Transactions on Vehicular Technology*, submitted.

4. **S. Sugiura**, S. Chen and L. Hanzo, "Generalized space-time shift keying designed for flexible diversity-, multiplexing- and complexity-tradeoffs," *IEEE Transactions on Wireless Communications*, submitted.

5. S. Chen, **S. Sugiura** and L. Hanzo, "Semi-blind joint channel estimation and data detection for space-time shift keying systems," *IEEE Signal Processing Letters*, submitted.

6. **S. Sugiura**, S. Chen and L. Hanzo, "Cooperative differential space-time spreading for the asynchronous relay aided CDMA uplink using interference rejection spreading code," *IEEE Signal Processing Letters*, vol. 17, no. 2, pp. 117–120, February 2010.

7. **S. Sugiura**, S. Chen and L. Hanzo, "Reduced-complexity iterative Markov chain MBER detection for MIMO systems," *IEEE Signal Processing Letters*, vol. 16, no. 3, pp. 160–163, March 2009.

Conference Papers (9):

1. **S. Sugiura**, S. Chen and L. Hanzo, "Space-time shift keying: A unified MIMO architecture," in *Proceedings of the IEEE Global Telecommunications Conference (GLOBECOM 2010)*, Miami, Florida, USA, 6–10 December 2010, 5 pages, accepted for publication. (http://eprints.ecs.soton.ac.uk/21311/)

2. **S. Sugiura**, S. Chen and L. Hanzo, "Packet-reliability based decode-and-forward relaying aided distributed space-time shift keying," in *Proceedings of the IEEE Global Telecommunications Conference (GLOBECOM 2010)*, Miami, Florida, USA, 6–10 December 2010, 5 pages, accepted for publication. (http://eprints.ecs.soton.ac.uk/21312/)

3. **S. Sugiura**, S. Chen and L. Hanzo, "A unified MIMO architecture subsuming space shift keying, OSTBC, BLAST and LDC," in *Proceedings of the IEEE 72nd Vehicular Technology Conference (VTC2010-Fall)*, Ottawa, Canada, 6–9 September 2010, 5 pages, accepted for publication. (http://eprints.ecs.soton.ac.uk/21275/)

4. **S. Sugiura**, S. Chen and L. Hanzo, "Distributed differential space-time spreading for the asynchronous relay aided interference-free cooperative CDMA uplink," in *Proceedings of the IEEE International Conference on Communications (ICC)*, Cape Town, South Africa, 23–27 May 2010, 5 pages.

5. **S. Sugiura**, S. X. Ng, L. Kong, S. Chen and L. Hanzo, "Multiple-relay aided distributed turbo coding assisted unitary differential space-time spreading for asynchronous cooperative networks," in *Proceedings of the IEEE 71st Vehicular Technology Conference (VTC2010-Spring)*, Taipei, Taiwan, 16–19 May 2010, 5 pages.

6. **S. Sugiura**, D. Yang, S. Chen, L.-L. Yang and L. Hanzo, "Effect of array geometry on the capacity of the turbo-coded beamforming uplink," in *Proceedings of the IEEE 70th Vehicular Technology Conference (VTC2009-Fall)*, Anchorage, Alaska, 20–23 September 2009, 4 pages.

7. **S. Sugiura** and L. Hanzo, "Iterative detection assisted cooperative vehicular ad hoc networking using differential linear dispersion coding," in *Proceedings of the IEEE 70th Vehicular Technology Conference (VTC2009-Fall)*, Anchorage, Alaska, 20–23 September 2009, 5 pages.

8. **S. Sugiura**, S. Chen and L. Hanzo, "Markov chain minimum bit error rate detection for multi-functional MIMO systems," in *Proceedings of the IEEE International Conference on Communications (ICC)*, Dresden, Germany, 14–18 June 2009, 5 pages.

9. **S. Sugiura**, N. Wu and L. Hanzo, "Improved Markov chain MBER detection for steered linear dispersion coded MIMO systems," in *Proceedings of the IEEE 69th Vehicular Technology Conference (VTC2009-Spring)*, Barcelona, Spain, 26–29 April 2009, 5 pages.

Contents

List of Symbols

General notation

- The superscript * is used to indicate complex conjugation. Therefore, a^* represents the complex conjugate of the variable a.
- The superscript $^{\mathrm{T}}$ is used to indicate matrix transpose operation. Therefore, $\mathbf{a}^{\mathrm{T}}$ represents the transpose of the matrix $\mathbf{a}$.
- The superscript $^{\mathrm{H}}$ is used to indicate complex conjugate transpose operation. Therefore, $\mathbf{a}^{\mathrm{H}}$ represents the complex conjugate transpose of the matrix $\mathbf{a}$.
- The notation $\hat{x}$ represents the estimate of x.

Special symbols

$\boldsymbol{A}_q$: The qth $(M \times T)$-element dispersion matrix.

C: The channel capacity.

$\boldsymbol{\chi}$: The Dispersion Character Matrix (DCM)

$\det[\,\cdot\,]$: The determinant operation.

$E[\,\cdot\,]$: The expected value of $\cdot$.

$\exp[\,\cdot\,]$: The exponential operation.

$||\cdot||$: The Frobenius norm.

G_r: The feedback generator polynomial.

G: The feedforward generator polynomial.

$\boldsymbol{I}$: The identity matrix.

I_{A}: The *a priori* information input.

I_{E}: The extrinsic information output.

$\Im[\,\cdot\,]$: The imaginary part of a complex value.

$\boldsymbol{H}$: The Channel State Information (CSI) matrix.

$\mathcal{K}$: The constraint length.

$\log[\,\cdot\,]$: The logarithm operation.

$\mathcal{L}$: The constellation size.

L_{tap}: The number of resolvable paths in wideband channels.

M: The number of transmit antennas.

$\max[\,\cdot\,]$: The maximum value of a matrix/vector.

$\min[\,\cdot\,]$: The minimum value of a matrix/vector.

N: The number of receiver antennas.

$\boldsymbol{V}$: The complex-valued AWGN signal matrix.

$\boldsymbol{V}'$: The equivalent complex-valued AWGN signal vector.

N_0: Single-sided power spectral density of white noise.

N_{b}: The number of legitimate sequences.

N'_{b}: The number of sequences generated by the Gibbs-Sampler.

N_{LS}: The length of the complementary code pair.

N_{MC}: The number of successive Markov chain samplings.

N_{P}: The number of parallel Markov chains.

ν: The number of RAKE fingers.

$\otimes$: The Kronecker product.

$p(\,\cdot\,)$: The probability density function.

$P_{\mathrm{e}}(\,\cdot\,)$: The error probability function.

P_{S}: The transmission power of the source node.

P_{R}: The total transmission power of the relay nodes.

P_{LS}: The dimension of Walsh-Hadamard matrix.

Π: The interleaver.

Π^{-1}: The deinterleaver.

π: The circular constant.

Q: The number of dispersion matrices.

R: The transmission rate.

$\Re[\,\cdot\,]$: The real part of a complex value.

ρ_{s}: The spatial correlation factor between two channel components.

$\boldsymbol{S}$: The signal matrix/vector.

σ^2_{H}: The variance of the Gaussian channel estimation error.

$\sum$: The sum operation.

T: The symbol durations per space-time block.

T_{c}: The chip duration.

$T_{\mathrm{s}}^{\mathrm{S}}$: The symbol duration of the broadcast phase.

$\tau_{\max}$: The maximum synchronization delay.

τ_n: The synchronization delay of the nth source.

τ_{nk}: The synchronization delay of the kth relay node associated with the nth source.

$\mathrm{tr}[\,\cdot\,]$: The trace operation of a matrix

$vec[\,\cdot\,]$: The vertical stacking of the columns of a matrix

$\boldsymbol{W}$: The complex-valued weight matrix.

W_0: The width of the Interference-Free Window (IFW).

$\boldsymbol{w}_m$: The complex-valued weight vector for the mth substream.

$\boldsymbol{Y}$: The received signal matrix.

$\boldsymbol{Y}'$: The equivalent received signal vector.

Chapter 1

Introduction

Against the recent background of rapidly-increasing demand for high-speed multimedia wireless tranceivers communicating over dispersive fading channels, a bandwidth efficient and reliable transmission technology is desired. Multiple-Input Multiple-Output (MIMO) techniques constitute promising solutions, where multiple Antenna Elements (AEs) are employed at a transmitter and/or a receiver in conjunction with appropriate space-time coding and modulation. The exploitation of the spatial dimension provides a wireless system with an additional degree of freedom, hence facilitating the attainment of additional diversity gains, multiplexing gains and beamforming gains. As a result of two decades of intensive investigations the field of MIMO theory and practice has substantially matured.

More explicitly, the pioneering studies by Foschini [17, 18] and by Telatar [19] revealed that MIMO systems have the potential of attaining a high rate without requiring additional bandwidth, where there is a linear relationship between the channel capacity and the number of AEs employed. This property becomes especially beneficial when considering that classic Shannon theory predicted that the channel capacity is a logarithmic function of the associated Signal-to-Noise Ratio (SNR) value. By contrast, several years prior to the invention of this high-rate MIMO architecture, the philosophy of Space-Time Codes (STCs), including Space-Time Block Codes (STBCs) [20, 21] and Space-Time Trellis Codes (STTCs) [22], were proposed, which form another core concept of MIMO systems. This transmit diversity concept is capable of combating the detrimental effects of fading channels, by exploiting the maximum achievable diversity order. Importantly, regardless of the type of MIMO gains, we exploit both the space- and time-dimensions for space-time processing.

1.1 MIMO Channels and System Model

One of the most challenging problems that wireless applications face is multipath propagation, resulting in fading channels, where multiple signal replicas arrive simultaneously at the receive antenna element, due to the effects of scattering, reflection and diffraction. These random-phase signal replicas cancel or strengthen the received signals during the movement of the terminal or the surrounding environments and hence the resultant channel gain suffers from time-varying fluctuations. Hence the Bit Error Ratio (BER) performance of the system may be severely degraded. In order to combat this limitation imposed by small-scale fading, the concept of diversity was widely investigated, including the spatial diversity gain of MIMO systems.

Let us now consider a MIMO wireless communication system having M transmit AEs and N receive AEs. Then, the classic block-based MIMO system model of non-dispersive Rayleigh fading channels may be characterized as the complex-valued baseband representation, which may be formulated as

$$\boldsymbol{Y}(i) \;=\; \boldsymbol{H}(i)\boldsymbol{S}(i) + \boldsymbol{V}(i), \tag{1.1}$$

$$\begin{bmatrix} y_{11}(i) & \cdots & y_{1T}(i) \\ \vdots & \ddots & \vdots \\ y_{N1}(i) & \cdots & y_{NT}(i) \end{bmatrix} = \begin{bmatrix} h_{11}(i) & \cdots & h_{1M}(i) \\ \vdots & \ddots & \vdots \\ h_{N1}(i) & \cdots & h_{NM}(i) \end{bmatrix} \times \begin{bmatrix} s_{11}(i) & \cdots & s_{1T}(i) \\ \vdots & \ddots & \vdots \\ s_{M1}(i) & \cdots & s_{MT}(i) \end{bmatrix} + \begin{bmatrix} v_{11}(i) & \cdots & v_{1T}(i) \\ \vdots & \ddots & \vdots \\ v_{N1}(i) & \cdots & v_{NT}(i) \end{bmatrix},$$

where $s_{mt}(i)$ in $\boldsymbol{S}(i) = \{s_{mt}(i) : 1 \leq m \leq M, 1 \leq t \leq T\} \in \mathcal{C}^{M\times T}$ represents the signals transmitted from the mth antenna element during the tth symbol interval, while $y_{nt}(i)$ in $\boldsymbol{Y}(i) = \{y_{nt}(i) : 1 \leq n \leq N, 1 \leq t \leq T\} \in \mathcal{C}^{N\times T}$ represents the signals received by the nth antenna element during the tth symbol interval. Each element of both the complex-valued Channel Impulse Response (CIR) $\boldsymbol{H}(i) = \{h_{nm}(i) : 1 \leq n \leq N, 1 \leq m \leq M\} \in \mathcal{C}^{N\times M}$ and of the Additive White Gaussian Noise (AWGN) $\boldsymbol{V}(i) = \{v_{nt}(i) : 1 \leq n \leq N, 1 \leq t \leq T\} \in \mathcal{C}^{N\times T}$ obeys the complex-valued independent and identical Gaussian distributions of $\mathcal{CN}(0, 1)$ and $\mathcal{CN}(0, N_0)$, respectively, where N_0 represents the thermal-noise power. Furthermore, the integer i denotes the block index, while T represents symbol durations per space-time block. According to the monograph [23], many of the diverse MIMO arrangements developed may be characterized as Eq. (1.1) and therefore we employ this block-based system model throughout the thesis.

The above-mentioned system model employed is simplified in this thesis, while still retaining the key ideas. For instance, multipath propagation environments give rise to several delayed replicas of the transmitted signals, whose effect is referred to as delay spread. When

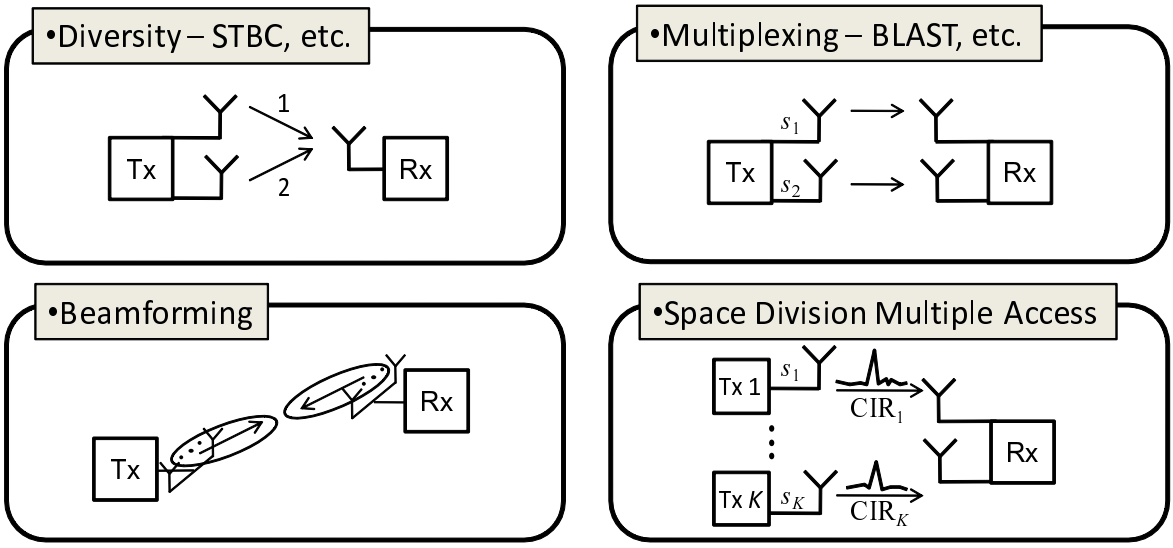

Figure 1.1: Classification of four MIMO functions.

the delay spread is comparable to or larger than the symbol duration, the resultant channels become dispersive, hence imposing a performance degradation owing to Inter-Symbol Interference (ISI). In order to solve this problem, multi-carrier transmission schemes extends the symbol duration, while in single-antenna direct-sequence spread-spectrum systems equalization technique have been employed in wireless systems, such as the Third Generation (3G) [24], Worldwide interoperability for Microwave Access (WiMAX) [25] and Long-Term Evolution (LTE) systems [26]. Finally, large-scale fading induced by the shadowing effects of buildings or large vehicles introduces an additional log-normal distributed variation, which results in correlation between the received signals of the MIMO elements.

1.2 Co-Located Multiple Antenna Elements

Depending on the desirable MIMO gain, MIMO techniques may be classified into four different categories, such as diversity, multiplexing, multiple access and beamforming techniques, as shown in Fig. 1.1. In order to provide further insights, these four MIMO types are briefly summarized below.

1.2.1 Spatial Diversity

Spatial diversity [27] techniques rely on multiple AEs in order to improve the attainable system performance in fading channels. More specifically, spatial diversity is based on the concept of efficiently combining the received signals associated with the different pairs of transmit and receive AEs, which experience independent fading paths imposed by the random fluctuations of the received signal levels, as shown in Fig. 1.2. The AEs have to

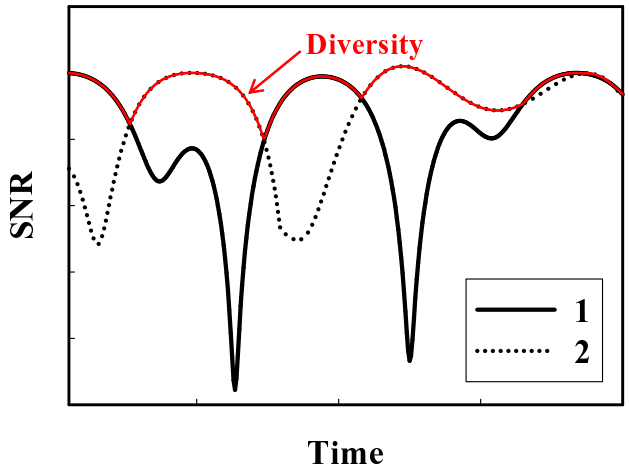

Figure 1.2: Diversity concept.

be spaced sufficiently far apart for the sake of attaining a diversity gain from the gleaned independently-faded received signal replicas. Since the minimum antenna separation required for experiencing independent fading is approximately 0.38 λ [28], the desirable antenna separation is on the order of tens times the wavelengths. A further attractive feature of spatial diversity is that it does not sacrifice additional time slots neither does it reduce the spectrum efficiency in comparison to classic time- and frequency-diversity schemes. To be specific, the maximum attainable diversity order is equal to the product of the number of transmit and receive AEs given by $(M \cdot N)$, assuming that the channel between each transmit-receive antenna pair is faded independently.

Furthermore, spatial diversity techniques may be divided into two classes, namely receive diversity and transmit diversity. Receive diversity is the classic technique, where the independently fading multiple paths are combined at the receiver side. The Base Station (BS) has significant space to allow the installation of multiple AEs spaced sufficiently far apart, in order to achieve receive diversity in uplink scenarios. More specifically, the diverse techniques of coherent signal combining were developed depending on the specific treatment of the combined signals' phase and amplitude, which are Selection Combining (SC), threshold combining, Equal-Gain Combining (EGC) and Maximum-Ratio Combining (MRC), as summarized in [29]. Furthermore, the theoretical capacity bound of received signal combining employed in conjunction with adaptive transmission was derived in [30]. Although receive diversity is capable of achieving the maximum attainable diversity order, which is proportional to the number of receive AEs, it is often impractical to employ multiple antennas at the mobile handset's receiver.

By contrast, transmit diversity relies on multiple AEs at the transmitter, where the precoded signals are appropriately allocated to the transmit AEs and to the time slots in advance of the transmission. Hence, the employment of transmit diversity is desirable for downlink

scenarios, where more antenna-installation space and processing capability are affordable at the BS. Historically, the first transmit diversity scheme was based on delay-diversity considered in the context of employing simulcasting at the BS [31] for a single-BS aided downlink [32]. In 1998 Alamouti [20] proposed a sophisticated transmit diversity scheme designed for the scenario of two transmit antennas, which enables a simple transmit diversity implementation and single-symbol-based low-complexity Maximum Likelihood (ML) detection at the receiver, while dispensing with the necessity of channel knowledge at the transmitter, but requires pilot-based DL channel estimation. Since then, Alamouti's scheme has been followed by the development of diverse STBCs, such as those portrayed in [33–36]. By contrast, STTCs [37] were developed as the extension of conventional trellis codes [38] embedded into multi-antenna systems, which may be designed for the sake of achieving both spatial diversity as well as a space-time coding gain. Furthermore, motivated by the concept of STCs, Space-Time Spreading (STS) [39] was proposed, in order to achieve a transmit diversity gain with the aid of spreading the transmitted signals across multiple antennas in the context of Direct-Sequence Code Division Multiple Access (DS-CDMA) systems, while supporting multiple users.

Although the above-mentioned spatial diversity schemes [20, 33–39] assumed that perfect Channel State Information (CSI) was available at the receiver, it is often quite challenging to acquire accurate CSI amongst all the MIMO channel elements, especially for rapidly moving vehicles, since doubling the vehicular speed requires doubling the pilot density. The resultant CSI estimation errors may cause a severe degradation of the achievable performance. Since each of the MIMO subchannels has to be sampled at multiples of the Doppler frequency, at high speeds an increased pilot overhead has to be tolerated for the sake of accurately estimating each MIMO channel component, which also gives rise to a substantial increase of the CSI-estimation complexity. To this end, the class of Differential STCs (DSTCs) [40–45] has been proposed and developed, allowing us to dispense with any CSI estimation and hence to avoid the performance deterioration associated with imperfect CSI estimation. In [40], Tarokh *et al.* introduced a differentially-encoded counterpart of Alamouti scheme, assuming the employment of Phase Shift Keying (PSK). Additionally, the DSTCs based on Unitary Space-Time Modulation (USTM) and on group codes were proposed in [41] and [42], respectively. Furthermore, Multiple-Symbol Differential Detection (MSDD) was also developed for the sake of combating time-selective fading [43], even when the Doppler-frequency was high [44].

1.2.2 Multiplexing/Space-Shift Keying

In contrast to the above-mentioned spatial diversity technique, which employs multiple transmit and/or receive antennas for achieving a high diversity gain, Spatial Division Multiplexing (SDM), which is represented for example by the family of Bell Labs Layered Space-Time (BLAST) schemes [17, 52], exploits the MIMO channels for the sake of increasing the at-

Table 1.1: Contributions to spatial diversity techniques (Part I)

Year	Authors	Contribution
1959	Brennan [29]	Introduced the three receive diversity schemes, namely SC, EGC and MRC.
1991	Wittneben [31]	Proposed a delay-diversity scheme for base station simulcasting.
1993	Seshadri and Winters [32]	Proposed a single-BS aided transmit diversity scheme, motivated by [31].
1998	Alamouti [20]	Invented the STBC transmit diversity concept designed for two transmit AEs, which enables unity-rate full diversity transmission as well as a simple linear detection.
	Tarokh *et al.* [37]	Derived performance criteria for achieving the maximum diversity and coding gains, in addition to the design of STTCs.
1999	Alouini and Goldsmith [30]	Derived the Shannon capacity of adaptive transmission techniques in conjunction with diversity combining.
	Tarokh *et al.* [33]	Extended Alamouti's scheme [20] so that more than two transmit antennas are supported.
2000	Tarokh and Jafarkhani [40]	Proposed differential encoding and non-coherent detection for the Alamouti scheme of [20] using PSK.
	Hochwald and Marzetta [41]	Proposed a differentially-encoded transmit diversity scheme based on Unitary Space-Time Modulation (USTM).
	Hughes [42]	Proposed a differential space-time modulation scheme, which was based on group codes.
2001	Jafarkhani [34]	Proposed the family of Quasi-Orthogonal STBCs (QOSTBCs) for the sake of achieving high-rate transmission.
	Hochwald *et al.* [39]	Developed STS-based transmit diversity, which was standardized for W-CDMA systems.
	Liu *et al.* [43]	Introduced the double-differential STC concept, in order to combat time-selective fading.
2002	Schober and Lampe [44]	Proposed an Multiple-Symbol Differential Detection (MSDD) receiver designed for Differential Space-Time Modulation (DSTM), in order to combat rapid fading as well as to mitigate the typical 3-dB degradation imposed by differential decoding.
2003	Xin *et al.* [35]	Proposed a unified approach to designing STBCs using linear constellation precoding.

Table 1.2: Contributions to spatial diversity techniques (Part II)

Year	Authors	Contribution
2003	Gamal and Damen [36]	Proposed Threaded Algebraic STBCs (TASTBCs) that is capable of achieving both a high rate and full diversity, in order to support up to M adaptively reconfigurable layers.
2004	Jongren and Skoglund [46]	Considered how the presence of quantized channel information obtained from a feedback link may be utilized for determining a transmit weighting matrix in OSTBCs.
2005	Zhu and Jafarkhani [45]	Proposed a differential modulation scheme based on QOSTBCs.
2006	Vu an Paulraj [47]	Proposed linear precoder designs exploiting statistical channel knowledge at the transmitter in STBCs.
2007	Zhang *et al.* [48]	Proposed a systematic design of high-rate full-diversity Space-Time-Frequency (STF) codes for MIMO frequency-selective block-fading channels.
2008	Shin and Win [49]	Considered a general family of MIMO channels known as double-scattering channels by embracing both rank-deficient and spatial correlation effects.
2009	Kim and Caire [50]	Studied a multiple antenna channel with partial CSI at the transmitter.
2010	Wang *et al.* [51]	Investigated the capacity enhancement of secondary users through spatial diversity in spectrum-sharing environments, which is based on a geographical relationship.

tainable transmission rate. This performance gain is referred to as multiplexing gain. More specifically, M independent signal substreams are transmitted from different transmit AEs at the same frequency and within the same time slot, therefore the corresponding transmission rate is multiplied by the number of transmit antennas, assuming the employment of the same modulation scheme for each of the substreams.

By contrast, the SDM receiver differentiates each of the M co-channel substreams based on the knowledge of the $(M \times N)$-element MIMO channels. Since the M substreams are multiplexed and hence interfere with each other, we have to decompose the substreams with the aid of a MIMO detection algorithm. For instance, an efficient ordered successive detection scheme was designed for V-BLAST in [53], and since then diverse SDM detection algorithms have been developed [54, 55]. Alternatively, the co-channel interferences associated with the MIMO channels may be reduced by employing pre-processing at the transmitter side, which requires the knowledge of the channel to be encountered. This technique is referred to as transmitter pre-processing or Multi-User Transmission (MUT) [56]. This makes the receiver's operation less complex and hence is imminently suitable for downlink scenarios.

However, the potential CSI errors encountered at the transmitter may result in a substantial performance deterioration, suggesting that both an accurate DL CSI-estimates and a robust feedback channel is required for MUT.

In 1998, Foschini [57] formulated the theoretical capacity analysis of MIMO channels as the evolution of Shannon's capacity [58] presented in 1948. This study showed that the idealized MIMO capacity increases linearly upon increasing the number of transmit AEs. This capacity limit is referred to as the Continuous-input Continuous-output Memoryless Channel (CCMC) capacity, since it is defined under the assumption of continuous-amplitude discrete-time Gaussian-distributed transmitted signals, where only the transmit power and the bandwidth are restricted. The discovery of this MIMO capacity introduced a new extended limit and demonstrated the MIMO's potential of achieving a high transmission rate as well as high power and bandwidth efficiency. Moreover, in [59] the Discrete-input Continuous-output Memoryless Channel (DCMC) capacity was defined for MIMO channels in combination with the specific multi-dimensional signaling set employed.

Recently, Mesleh *et al.* [60, 61] proposed the sophisticated concept of Spatial Modulation (SM), which serves as a novel MIMO encoding principle, which is fundamentally different from that of the SDM scheme.[1] In the SM scheme, the transmitter activates one out of M transmit AEs, whose antenna-activation process acts as an additional means of conveying information bits, and then only the activated antenna transmits a signal modulated with the aid of the classic $\mathcal{L}$-point constellation, such as PSK and Quadrature Amplitude Modulation (QAM). Unlike BLAST, SM schemes do not transmit simultaneously via M AEs, hence single-antenna based low-complexity ML detection can be employed at the receiver, while dispensing with symbol-level Inter-Antenna Synchronization (IAS) at the transmitter. A special case of SM is constituted by the scenario, where we deactivate the classic PSK/QAM signaling and simply use the presence or absence of energy assigned to a specific antenna, which is also referred to as Space Shift Keying (SSK) [63]. The SM/SSK philosophy was investigated in both uncoded [60, 61, 63, 64] and channel-encoded scenarios [65–67], while the optimal ML detector designed for the uncoded SM/SSK scheme was presented in [63]. Although SM/SSK has the potential of outperforming other MIMO arrangements [60, 61, 63, 66], SM/SSK was not designed for achieving any transmit diversity gain and hence has to rely on the provision of receive diversity in order to combat the effects of fading channels. Furthermore, in [68] the generalized SSK scheme was proposed, which extends the SSK scheme so that multiple AEs are activated simultaneously. This leads to an increase in the transmission rate, at the cost of increasing the computational complexity owing to an increased ICI.

[1] In order to expound a little further, the original concept of SM dates back to [62], where multiple AEs are simultaneously activated according to index table.

Table 1.3: Contributions to multiplexing techniques

Year	Authors	Contribution
1996	Foschini *et al.* [17]	Conceived the concept of spatial multiplexing.
1998	Wolniansky *et al.* [52]	Introduced the Vertical-Bell Labs Layered Space-Time (V-BLAST) architecture in order to realize a practical SDM implementation.
1999	Golden *et al.* [53]	Presented the ordered successive detection concept designed for V-BLAST.
	Telatar [69]	Characterized the CCMC capacity of MIMO channels under the assumption of continuous-amplitude discrete-time Gaussian-distributed transmitted signals.
	Viterbo and Boutros [54]	Introduced a SD-assisted receiver, in order to provide an efficient approximation of the exhaustive ML search.
2000	Ariyavisitakul [70]	Presented the embodiment of BLAST designed for a turbo-coded system operating at a low average SNR and in the presence of ISI.
2001	Sampath *et al.* [56]	Proposed eigenbeam spatial division multiplexing, assuming that perfect CSI is available at the transmitter.
2002	Bolcskei *et al.* [71]	Dealt with the capacity behavior of OFDM-based spatial multiplexing systems in broad-band fading environments.
2003	Gorokhov *et al.* [72]	Discussed the problem of receive antenna subset selection in spatial multiplexing systems, which was developed for maximizing the channel capacity.
2004	Vikalo *et al.* [73]	Proposed a modified Sphere Decoding (SD) algorithm to estimate the maximum a posteriori probability for soft iterative decoding.
2005	Sharif and Hassibi [74]	Proposed a spatial multiplexing scheme which constructs M random beams and transmits information, with the aid of limited feedback.
2006	Ng and Hanzo [59]	Characterized the DCMC capacity of MIMO channels in combination with specific multi-dimensional signaling sets.
2007	Andrews *et al.* [75]	Overviewed several approaches to handling interference in multicell MIMO systems in cellular networks.
2008	Studer *et al.* [76]	Provide VLSI implementation results to show that soft-output SD is capable of striking flexible trade-offs between complexity and BER performance.
2009	Zhang *et al.* [77]	Proposed a clustered base transceiver station (BTS) coordination strategy for a large cellular MIMO network.
2010	Xu *et al.* [78]	Proposed a framework for analyzing three facets of MIMO video broadcast, namely video distortion, transmit power, and delay.

Table 1.4: Contributions to spatial modulation/space-shift keying techniques

Year	Authors	Contribution
2001	Chau and Yu [62]	Proposed the SSK scheme, which allocates source bits directly to the transmit AEs, where simultaneous signal transmissions are required at the transmitter.
2006	Mesleh *et al.* [60, 61]	Proposed a practical SM scheme, where the previous SSK scheme [62] was modified for the sake of dispensing with symbol-level IAS between the transmit AEs.
2008	Jeganathan *et al.* [63]	Optimal ML detection was derived for the uncoded SSK and SM schemes.
2009	Jeganathan *et al.* [66]	Two-stage turbo-coded SSK was presented as the extension of [63].
	Handte *et al.* [79]	Transmitter preprocessing was combined with the SM/SSK scheme, in order to combat the effects of spatial correlations.
2010	Renzo and Haas [80]	Achievable BER performance of uncoded SSK over correlated Nakagami-m fading channels was investigated.

1.2.3 Space Division Multiple Access

Space Division Multiple Access (SDMA) [81], also known as Multi-User MIMO (MU-MIMO) [82], utilizes user-specific Channel Impulse Responses (CIRs) for differentiating the supported users in uplink scenarios, and hence the achievable performance of SDMA is not affected by the supported users' locations. In SDMA system the users communicate with a BS by using the same bandwidth and time slots. Accordingly, it can be argued that SDMA is a close relative of SDM in a sense that both schemes exhibit a capacity gain by decomposing multiplexed MIMO channels into parallel channels. More specifically, SDMA utilizes this multiplexing gain in order to increase the number of supported users, while SDM exploits it for the sake of increasing the throughput of peer-to-peer communication links. Since SDMA arrangements do not require additional time- or frequency-slots, their spectrum efficiency is directly enhanced by this scheme.

1.2.4 Beamforming

In a beamforming scheme [24, 83–85], half-wavelength spaced antenna elements are used to create an angularly selective filtering pattern, potentially at both the receivers and/or transmitters. The beamforming pattern based on *a priori* knowledge of the Directions-of-Departure (DODs) or Directions-of-Arrival (DOAs) results in achieving the beamforming gain, directly increasing the corresponding SNR. This also indicates an increase in the maximum communication range as well as a reduction of the ISI and flat fading. Furthermore, when a beamforming antenna array is employed at the receiver, multiple signals originating

from different sources can be separated by the angular filtering, i.e. co-channel interference nulling, based on the user-specific DOAs. However, when the users' DODs or DOAs are close, this angular filtering capability is severely deteriorated, since its filtering resolution is determined by the antenna beamwidth of the array pattern, which is determined by the number of array elements.

1.3 Diversity and Multiplexing Tradeoffs

In contrast to V-BLAST which is capable of achieving a high multiplexing gain, the class of STBCs is used to combat fading channels based on the concept of spatial diversity. However, it is not necessary to use the AEs purely either for multiplexing or for diversity. To be more specific, some of the space-time dimensions can be used for achieving a diversity gain, while the remaining dimensions may be used for attaining a multiplexing gain. According to the tutorial paper by Zheng and Tse [86], given a certain number of AEs, there is fundamental limitation regarding the achievable diversity-multiplexing gain tradeoff. This indicates that the degree of freedom in a MIMO system is determined by the number of AEs, which should be appropriately dedicated to each of the gains in MIMO systems so as to make the best use of the MIMO's capability. More explicitly, a system is capable of achieving an r-fold spatial multiplexing, when the data rate $R(\mathrm{SNR})$ at a certain SNR value satisfies

$$\lim_{\mathrm{SNR}\to\infty} \frac{R(\mathrm{SNR})}{\log_2 \mathrm{SNR}} = r, \tag{1.2}$$

while the diversity gain may be defined in terms of the achievable BER improvement as

$$\lim_{\mathrm{SNR}\to\infty} \frac{\log P_\mathrm{e}(\mathrm{SNR})}{\log \mathrm{SNR}} = -d, \tag{1.3}$$

where $P_\mathrm{e}(\mathrm{SNR})$ represents the average error probability. It was shown in [86] that if the fading block length satisfies the relationship of $T \geq M + N - 1$, then we have [86]

$$d(r) = (M - r)(N - r), \quad 0 \leq r \leq \min(M, N). \tag{1.4}$$

The recent MIMO studies revealed that some combinations of the four MIMO techniques allow us to simultaneously exploit several MIMO functions [87–92]. To elaborate a little further, the degree of freedom provided by multiple antennas can be allocated to achieve diversity, multiplexing and beamforming gains for the sake of enhancing robustness against fading, for increasing the data rates and/or for reducing the interference, respectively. Furthermore, Hassibi *et al.* [88] developed a sophisticated MIMO space-time processing architecture referred to as Linear Dispersion Codes (LDCs), which amalgamate the benefits of STC and SDM. The LDC was designed for striking a flexible diversity-multiplexing gain tradeoff for an arbitrary number of transmit and receive antennas, when using diverse modulation constellation sizes [88, 93]. Additionally, motivated by the LDCs, a differentially-encoded

LDC (DLDC), which was also referred to as the Cayley unitary differential space-time modulation, was developed in [89], where non-coherent detection may be used at the receiver, which is also capable of achieving flexible diversity versus multiplexing tradeoffs.

1.4 Cooperative MIMO Arrangements

In Sections 1.2 and 1.3, we have seen that the family of co-located MIMO techniques has the potential of substantially enhancing the attainable performance of wireless systems through spatial diversity, multiplexing and beamforming gains as well as by expecting their combinations. These advantages are attained under the assumption that each terminal is equipped with multiple AEs and the corresponding Radio Frequency (RF) branches, including amplifiers, Digital-to-Analog (D/A) converters, analog filters and so on. Furthermore, considering the implementation of transmit diversity techniques, the antenna spacing has to be on the order of ten wavelengths, in order for each antenna element to experience an independent fading. However, it is unrealistic for a Mobile Station (MS) to satisfy these assumptions, owing to its cost- and size-constraints.

In comparison to the above-mentioned co-located MIMO arrangements, recently a new distributed MIMO concept has been developed, where a collection of mobile nodes, each having a single AE, acts as a Virtual Antenna Array (VAA), in order to combat the above-mentioned limitations of the collocated MIMOs. More specifically, the large separation of the distributed AEs enables us to achieve the best attainable diversity gain of uncorrelated elements, even in the face of large-scale fading induced by shadowing effects. This distributed AE arrangement benefits from uncorrelated fading channels, which can be exploited for cooperative space-time diversity, hence creating additional design degrees of freedom while imposing new challenges in the design of the cooperative transmission protocol.

To provide a historical perspective, the original concept of cooperative communications dates back to the early work of Cover and Gamal in 1979 [99], where the achievable capacity of a relay channel was characterized from a viewpoint of information theory. Recently, the cooperative philosophy was rejuvenated with the aid of distributed signal processing and antenna array theory [100–117]. Sendonaris *et al.* [100, 103, 104] introduced a Decode-and-Forward (DF)-based user cooperation technique in the context of CDMA, while Laneman and Wornell [101, 105] exploited the spatial diversity created by coordinated transmission and processing implemented by distributed radios. In [102] Dohler *et al.* introduced a VAA philosophy, which is based on the distributed counterpart of Alamouti's scheme [20]. Furthermore, a number of cooperative space-time diversity protocols were developed in [107], comparing several scenarios, such as DF and Amplify-and-Forward (AF), as well as selection and incremental relaying. In [112], Jing and Hassibi presented the uncoordinated cooperative STC operating with the aid of LDCs. To avoid the problems associated with CSI estimation, the concept of differential STCs [118] developed for co-located MIMO systems was extended

Table 1.5: Contributions to diversity versus multiplexing tradeoffs and related techniques

Year	Authors	Contribution
1999	Tarokh *et al.* [87]	STBC and V-BLAST were combined in order to exploit both space-time diversity as well as multiplexing gains.
2002	Hassibi and Hochwald [88]	Proposed the achievable LDCs which are capable of striking a flexible tradeoff between diversity and multiplexing gain.
	Hassibi and Hochwald [89]	Proposed a differentially-encoded LDC architecture combined with PAM, which is based on the Cayley unitary transform technique.
	Jongren *et al.* [90]	Combined the benefits of conventional transmit beamforming and of orthogonal STBCs, assuming that the transmitter has partial knowledge of the channels.
2003	Zheng and Tse [86]	Characterized the MIMO's fundamental tradeoff between diversity and multiplexing gains.
2004	Tao and Cheng [91]	Proposed a generalized layered space-time code as an extension of [87], where the optimal serial decoding order was derived in order to improve the performance.
2005	Heath and Paulraj [94]	Proposed switching between spatial multiplexing and transmit diversity as a simple way to improve the diversity performance of spatial multiplexing.
2006	El Gamal *et al.* [95]	Explored the fundamental performance tradeoff of the delay-limited multi-input-multi-output (MIMO) automatic retransmission request (ARQ) channel.
2007	El-Hajjar and Hanzo [96]	Presented the capacity analysis of a multi-functional MIMO system that combines the benefits of V-BLAST, STBC and beamforming.
2008	Sezgin *et al.* [97]	Studied an LDC system combined with transmitter preprocessing and a linear MMSE detector operating in a Ricean flat-fading environment.
2009	Wu and Hanzo [98]	Proposed irregular-precoded LDCs, while deriving the DCMC capacity of LDCs.
2010	Sugiura *et al.* [11]	Proposed a Space-Time Shift Keying (STSK) philospohy, which is capable of striking a flexible rate-diversity tradeoff, while imposing no ICI at the receiver.

Table 1.6: Contributions to distributed MIMO techniques (Part I)

Year	Authors	Contribution
1979	Cover and El Gamal [99]	Characterized the channel capacity of relay networks.
1983	Willems [121]	Introduced multiple-access channels with generalized feedback, which allows the sources to act as the relays for one another.
1998	Sendonaris *et al.* [100]	Introduced a cooperative diversity gain achieved via user cooperation.
2000	Laneman and Wornell [101]	Exploited the spatial diversity created by antenna sharing as well as coordinated transmission and/or processing by distributed radios.
2002	Dohler *et al.* [102]	Proposed the VAA philosophy based on Alamouti's scheme [20].
2003	Sendonaris *et al.* [103, 104]	Proposed a simple user cooperation technique based on DF signaling in the context of CDMA systems.
	Laneman and Wornell [105]	Presented space-time coded cooperation, which attains a higher cooperative diversity than repetition-based cooperation.
	Zhao and Valenti [106]	Proposed a distributed turbo-coding technique for quasi-static fading relay channels.
2004	Laneman *et al.* [107]	Analyzed and compared a number of cooperative diversity protocols, such as DF, AF, selection-aided cooperation and incremental cooperation.
	Janani *et al.* [108]	Introduced the concept of coded cooperation, where the codewords are encoded across the cooperating nodes.
	Nabar *et al.* [109]	Analyzed cooperative STCs from an information theoretical point of view.
2005	Tarasak *et al.* [110]	Introduced a differential modulation scheme for a two-user cooperative diversity DF and selection relaying protocols.

to cooperative MIMO systems [110, 116, 119, 120]. Furthermore, the concept of coded cooperation was proposed in [108], exploiting a beneficial combination of classic channel coding and cooperative space-time coding, which was further extended in order to support a specific form of Distributed Turbo Coding (DTC) [106, 113] that is capable of maintaining an excellent BER performance of low SNRs.

1.5 Outline and Novel Contributions

1.5.1 Outline of the Thesis

Having briefly reviewed the literature of MIMO techniques, let us now highlight the outline of this thesis, which is organized as shown in Fig. 1.3.

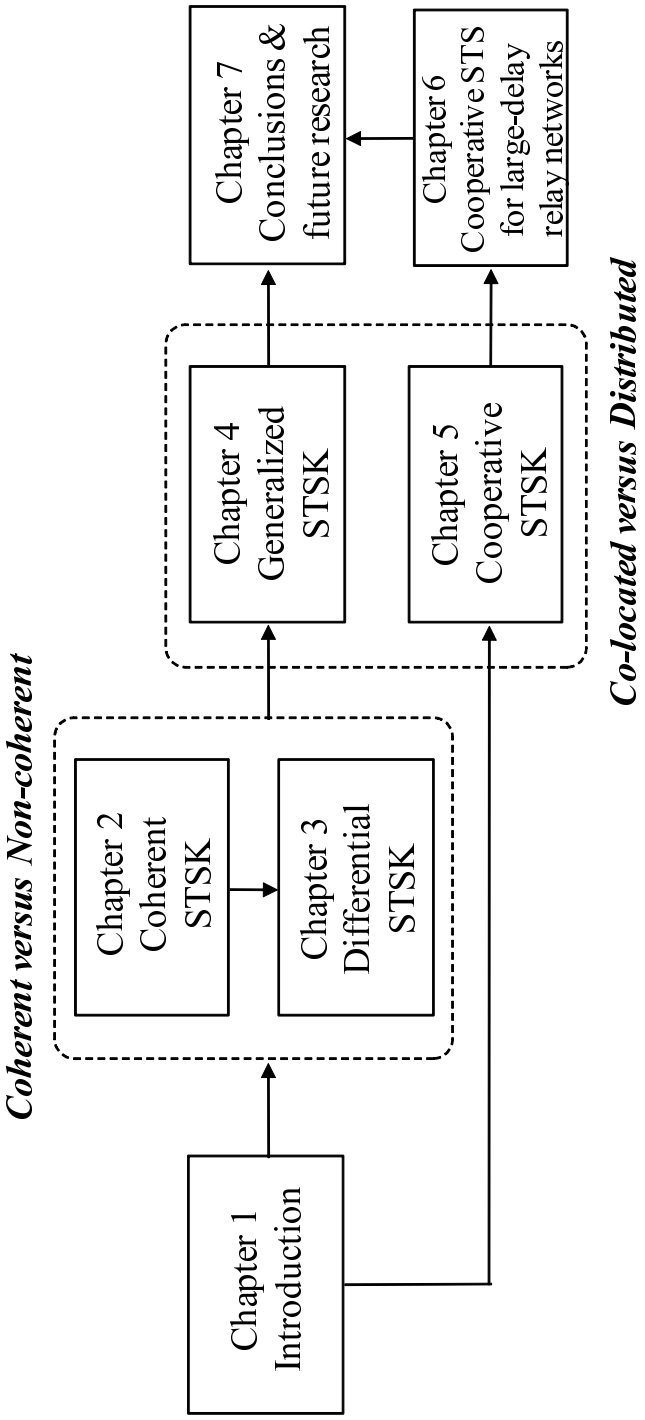

Figure 1.3: Organization of the thesis.

Table 1.7: Contributions to distributed MIMO techniques (Part II)

Year	Authors	Contribution
2006	Bletsas *et al.* [111]	Proposed a distributed a method to select the best relay that requires no topology information and is based on the instantaneous channel conditions.
	Jing and Hassibi [112]	Proposed cooperative STC based on LDCs, where each relay node encodes its signals in a distributed manner.
	Li *et al.* [113]	Proposed soft-information relaying, based on DTCs [106].
	Wei *et al.* [122]	Proposed a MMSE receiver designed to combine disparate inputs in the asynchronous multiple-relay channels.
2007	Xiao *et al.* [114]	Introduced a network coding technique to cooperative diversity, featuring the algebraic superposition of channel codes over a finite field.
	Bletsas *et al.* [115]	Presented simple DF and AF opportunistic relaying schemes, in conjunction with distributed relay selection algorithms.
2008	Jing and Jafarkhani [116]	Proposed a differential distributed STC scheme, based on the coherent distributed STCs of [112].
2009	Sirkeci-Mergen and Scaglione *et al.* [117]	Proposed the concept of randomized cooperative STCs, which facilitates the totally uncoordinated cooperation.
2010	Kim [123]	Presented a randomized cooperative broadcasting technique that is flexible to topology changes and robust to transmission errors in large-scale wireless networks.

▷ Chapter 2: Coherent Space-Time Shift Keying for Co-Located MIMO Systems
In Chapter 2, motivated by the recent concept of SM/SSK, we propose a novel Coherent Space-Time Shift Keying (CSTSK) modulation scheme for co-located MIMO communication systems, where the concept of SM is extended to include both the space and time dimensions, in order to provide a general shift-keying framework. Here, we provide the theory and fundamental design of the STSK scheme. Section 2.2 presents the review of the classic MIMO arrangements, such as Orthogonal Space-Time Block Codes (OSTBCs), SDM, LDCs and SM/SSK schemes. In Section 2.3, the novel CSTSK concept is proposed, which activates one out of Q dispersion matrices during each transmitted block and allows us to strike a flexible diversity versus rate tradeoff. We will show that our CSTSK scheme is capable of utilizing a realistic single-stream-based ML detector due to the absence of any Inter-Channel Interference (ICI). Additionally, we propose a modified version of the STSK scheme, namely the Asynchronous CSTSK (ACSTSK) scheme, which dispenses with the requirement of perfect Inter-Antenna Synchronization (IAS). Furthermore, Section 2.4 presents the three-stage serially-concatenated STSK scheme, which is capable of achieving a near-capacity performance. The capacity of our STSK scheme is characterized in Section 2.5, while the dispersion matrix design

criterion used for the STSK scheme advocated is provided in Section 2.6.

▷ Chapter 3: Differential Space-Time Shift Keying for Co-Located MIMO Systems
In Chapter 3, we propose a differentially-encoded counterpart of the CSTSK scheme introduced in Chapter 2, which does not require CSI at the receiver, while achieving the fundamental benefits of the CSTSK scheme. This is achieved with the aid of the Cayley transform technique. Section 3.2 reviews the classic differentially-encoded MIMO schemes, such as Differential OSTBC (DOSTBC) and DLDC. In Section 3.3, we detail the encoding principle of our DSTSK scheme and characterize its computational complexity. Furthermore, the Asynchronous DSTSK (ADSTSK) concept is proposed, in order to dispense with perfect-IAS between the transmit AEs, similarly to the ACSTSK scheme of Chapter 2. In Section 3.4, the uncoded DSTSK scheme is extended to a three-stage serially-concatenated DSTSK scheme.

▷ Chapter 4: Generalized Space-Time Shift Keying for Co-Located MIMO Systems
In Chapter 4, we further generalize the CSTSK scheme proposed in Chapter 2 for the sake of striking flexible tradeoffs between the throughput, the diversity gain and the computational complexity. This is achieved by the Generalized STSK (GSTSK) concept, which simultaneously activates P out of Q dispersion matrices during each block interval. Section 4.2 propose the modulation principle of our GSTSK scheme, where we assure that our GSTSK scheme subsumes diverse MIMO schemes, such as the OSTBCs, the BLAST scheme, the LDCs, the SM/SSK scheme and the CSTSK scheme. Then in Section 4.3, we introduce the optimal ML detector as well as the SISO demapper for the GSTSK scheme. While in Section 4.4 we derive the unified capacity upper bound of GSTSK scheme, in Section 4.5 the theoretical BER upper bound and the maximum achievable diversity order are characterized with the aid of the Moment-Generating Functions (MGFs). We note that these bounds serves as the unified ones, since the GSTSK scheme subsumes diverse MIMO arrangements.

▷ Chapter 5: Cooperative Space-Time Shift Keying for Distributed MIMO Systems
In Chapters 2, 3 and 4, the STSK family are developed for co-located MIMO systems. In contrast, in this chapter we propose their distributed-MIMO counterparts, in order to exploit uncorrelated MIMO channels, which may be achieved by the recent cooperative MIMO technique. Section 5.2 reviews the background and the problems of the cooperative transmissions. In Section 5.3, the system model as well as the Inter-Element Interference (IEI)-free detection algorithm of the cooperative CSTSK and ACSTSK schemes are provided. Furthermore, Section 5.4 proposes the cooperative DSTSK and ADSTSK schemes, which dispenses with the CSI estimation at any nodes.

▷ Chapter 6: Cooperative Differential Space-Time Spreading for Large-Delay Relay Networks
Although the cooperative ACSTSK and ADSTSK schemes proposed in Chapter 5 exhibits a beneficial robustness against Inter-Relay Synchronization (IRS) errors, these

schemes still suffer from the effects of IRS error when its value exceeds the single symbol duration. To this end, in Chapter 6 we propose a Cooperative Differential STS (CD-STS) system employing Loosely-Synchronized (LS) spreading codes, which is capable of achieving a beneficial cooperative diversity gain even in large-delay relay networks. In Section 6.2 we introduce the mathematical model of the uncoded CDSTS system, while in Section 6.3 the fundamental properties of the LS codes are provided. Furthermore, in Section 6.5 the recent concept of DTCs is incorporated into our uncoded CDSTS system of Section 6.2 for the sake of gleaning a multiple-relay-assisted asynchronous DTC. In Section 6.7, the DTC-CDSTS scheme is designed with the aid of EXIT chart analysis.

▷ Chapter 7: Conclusions and Future Research
Chapter 7 summarizes the main findings of the thesis and also outlines a range of suggestions for future research.

1.5.2 Novel Contributions of the Thesis

The thesis is based on 12 publications and 4 submitted papers, which [1–16] cover the following novel aspects.

- The STSK concept employing the dispersion-matrix activation philosophy is proposed, where the recent concept of SM is extended to include both the space- and time-dimensions, hence it is capable of striking flexible diversity and multiplexing tradeoffs. The STSK scheme enables us to carry out single-stream-based ML detection, which is unaffected by ICI.

- In order to dispense with symbol-level IAS, we introduce the concept of Asynchronous CSTSK (ACSTSK) as the extension of the above-mentioned STSK scheme, where the design space of the set of dispersion matrices preassigned to the transmitter is appropriately restricted.

- A three-stage serially concatenated RSC- and URC-coded STSK scheme is proposed for the sake of achieving infinitesimally low BER values. The convergence behaviour of the three-stage system is analyzed and designed with the aid of EXIT charts, leading to near-capacity performance.

- A Differential STSK (DSTSK) scheme assisted by the Cayley unitary transform is proposed, where no CSI is required at the receiver. The resultant DSTSK arrangements exhibits similar characteristics to those of its coherently-detected STSK counterparts. Additionally, we present the Asynchronous DSTSK (ADSTSK) concept, which dispenses with the requirement of perfect IAS, similarly to the above-mentioned ACSTSK scheme.

- We propose a novel Generalized STSK (GSTSK) architecture as the extension of the STSK scheme, which acts as a unified MIMO framework, and demonstrate that due to its substantial flexibility, our G-STSK framework includes diverse MIMO arrangements, such as the SM/SSK, STSK, LDCs, STBCs and BLAST scheme.

- Moreover, we also derive the Discrete-input Continuous-output Memoryless Channel (DCMC) capacity for our G-STSK scheme, which serves as the unified capacity limit, hence quantifying the capacity of diverse MIMO arrangements.

- Based on the above-mentioned STSK philosophy, a Cooperative STSK family, such as cooperative CSTSK, ACSTSK, DSTSK and ADSTSK schemes, are developed, where each Relay Node (RN) activates Decode-and-Forward (DF) STSK transmissions, depending on the success or failure of Cyclic Redundancy Checking (CRC). As an explicit benefit of its design flexibility, our CSTSK arrangement enables us to adapt the number of the RNs, the transmission rate as well as the achievable diversity order.

- For the sake of achieving a useful cooperative diversity gain in a large-delay relay network, we conceive the Loosely-Synchronized (LS)-code aided Cooperative Differential STS (CDSTS) scheme. Furthermore, we incorporate the concept of DTC into the CDSTS scheme for the sake of achieving a near-capacity performance, where the related system parameters are designed with the aid of EXIT charts.

Chapter 2

Coherent Space-Time Shift Keying for Co-Located MIMO Systems

2.1 Introduction

Multiple-antenna-assisted wireless communication systems have attracted substantial attention due to their potential of supporting reliable high-rate transmissions, as exemplified by V-BLAST [52] and diverse STBCs [20, 22]. In contrast to these classic MIMO arrangements, the sophisticated concepts of Spatial Modulation (SM) [60, 61, 63, 124] and Space-Shift Keying (SSK) [66, 80] have been recently proposed for MIMO-aided communication systems having low-complexity encoding/decoding implementations, while achieving a high BER performance.

In this chapter, inspired by the philosophy of SM/SSK schemes, we propose the novel concept of Space-Time Shift Keying (STSK) modulation, which constitutes a generalized shift-keying architecture exploiting both the space- as well as time-dimensions, hence including the SM and SSK schemes as special cases. The remainder of this chapter is organized as follows. In Section 2.2 we first review several conventional MIMO arrangements, namely the OSTBC, BLAST, LDC and SM/SSK schemes. Section 2.3 outlines the proposed concept of STSK modulation, which is then extended to include the turbo-coding principle in Section 2.4. The capacity of our STSK scheme is derived in Section 2.5 and the optimization criterion used for the design of the dispersion matrices is provided in Section 2.6. In Section 2.7 we provide our performance results. Finally, we conclude this chapter in Section 2.8.

2.2 Review of the classic MIMO arrangements

In this section different MIMO arrangements, such as the OSTBC, the BLAST, the LDC and SM/SSK schemes, will be reviewed. All the systems presented in this section are derived on

the basis of the block-based signal model of Eq. (1.1), which is repeated here for convenience:

$$\boldsymbol{Y} = \boldsymbol{H}\boldsymbol{S} + \boldsymbol{V}, \tag{2.1}$$

where the block index i is omitted for the sake of simplicity.

2.2.1 Orthogonal Space-Time Block Codes

As discussed in Section 1.2.1, the class of Space-Time Block Codes (STBCs) [20, 22] was developed to achieve the maximum attainable diversity order of $M \cdot N$. For example, the system model of the well-known (2×1)-element unity-rate orthogonal STBC scheme, namely Alamouti's scheme [20], may be expressed as

$$\begin{bmatrix} y_1 & y_2 \end{bmatrix} = \begin{bmatrix} h_{11} & h_{12} \end{bmatrix} \times \begin{bmatrix} s_1/\sqrt{2} & s_2/\sqrt{2} \\ -s_2^*/\sqrt{2} & s_1^*/\sqrt{2} \end{bmatrix} + \begin{bmatrix} v_1 & v_2 \end{bmatrix}, \tag{2.2}$$

where s_1 and s_2 are the two successive PSK-modulated symbols, while the parameters M, N and T are given by $M = 2$, $N = 1$ and $T = 2$. Note that the OSTBC transmitter does not require any *prior* knowledge of the CSI, which enables a substantially more simple implementation in comparison to closed-loop systems.

At the receiver, the PSK symbols s_1 and s_2 can be estimated by calculating $(h_{11}^* y_1 + h_{12} y_2^*)$ and $(-h_{12} y_1^* + h_{11}^* y_2)$, respectively, which are as follows:

$$\hat{s_1} = h_{11}^* y_1 + h_{12} y_2^* = \frac{(|h_{11}|^2 + |h_{12}|^2)}{\sqrt{2}} s_1 + h_{11}^* v_1 + h_{12} v_2^* \tag{2.3}$$

$$\hat{s_2} = -h_{12} y_1^* + h_{11}^* y_2 = \frac{(|h_{11}|^2 + |h_{12}|^2)}{\sqrt{2}} s_2 - h_{12} v_2^* + h_{11}^* v_1. \tag{2.4}$$

It may be observed from Eqs. (2.3) and (2.4) that a full transmit-diversity order of two can be attained due to the coefficient of $(|h_{11}|^2 + |h_{12}|^2)$, while dispensing with the employment of a high-complexity detector. Although Alamouti's above-mentioned scheme is limited to the case of $M = 2$ transmit antennas and PSK modulation, this principle was generalized for higher number of transmit antennas as well as for the classic QAM scheme, as detailed in [33]. Again, we note that since no multiplexing gain is achieved by OSTBCs, the normalized transmission rate R_{OSTBC} of full-rate OSTBCs is limited to $R_{\text{OSTBC}} = \log_2 \mathcal{L}$ bits/symbol, where $\mathcal{L}$ represents the number of constellation points employed.

2.2.2 Spatial Division Multiplexing

In contrast to the above-mentioned OSTBCs, the SDM concept, including the family of BLAST, was developed for the sake of achieving a high throughput, as described in Section 1.2.2. Here, the system model of the $(M \times N)$-element SDM scheme may be expressed as

$$\begin{bmatrix} y_1 \\ \vdots \\ y_N \end{bmatrix} = \sqrt{\frac{1}{M}} \begin{bmatrix} h_{11} & \cdots & h_{1M} \\ \vdots & \ddots & \vdots \\ h_{N1} & \cdots & h_{NM} \end{bmatrix} \times \begin{bmatrix} s_1 \\ \vdots \\ s_M \end{bmatrix} + \begin{bmatrix} v_1 \\ \vdots \\ v_N \end{bmatrix}, \tag{2.5}$$

where we have $T = 1$ and M independent substreams $\boldsymbol{S} = [s_1, s_2 \cdots, s_M]^{\mathrm{T}}$ per block. We note that although inter-substream coding is not required at the SDM receiver, the multiple substreams $[s_1, s_2 \cdots, s_M]^{\mathrm{T}}$ have to be decomposed at the receiver. Therefore, the attainable performance and the processing complexity imposed largely depend on the detection algorithm employed, similarly to the MUDs used in CDMA systems [125]. Here, we may employ the optimal ML criterion for SDM detection, at the expense of potentially encountering a prohibitively high complexity, which increases exponentially with the number of multiplexed substreams. More specifically, the computational complexity imposed by the ML detector to decode a single bit, which is evaluated in terms of the number of real-valued multiplications, is given by

$$\frac{(4MN + 2N)\mathcal{L}^M}{M \log_2 \mathcal{L}}. \tag{2.6}$$

It may be more practical to utilize the family of classic linear MUDs [126], such as the Zero Forcing (ZF), the Minimum Mean Square Error (MMSE) and the Minimum BER (MBER) detectors. Furthermore, the employment of near-ML detectors, such as the SD [54], the MCMC [127] and the Ant-Colony Optimization (ACO) [128] schemes, may enable us to attain near-optimal performance at a moderate complexity. Assuming that each substream employs the same $\mathcal{L}$-point PSK/QAM constellation, the normalized transmission rate R_{SDM} is given by $R_{\mathrm{SDM}} = M \cdot \log_2 \mathcal{L}$ bits/symbol.

2.2.3 Linear Dispersion Codes

Hassibi and Hochwald [88] proposed the unified space-time transmission architecture of LDCs, which subsumes both the SDM and OSTBC schemes in its ultimate form and it is capable of striking a flexible tradeoff between the achievable diversity and multiplexing gains.

At the transmitter, Q independently modulated symbols $\boldsymbol{K} = [s_1, s_2 \cdots, s_Q]^{\mathrm{T}} \in \mathcal{C}^{Q \times 1}$ are mapped to the space-time block $\boldsymbol{S}$ as follows:

$$\underbrace{\begin{bmatrix} t_{11} & \cdots & t_{1T} \\ \vdots & \ddots & \vdots \\ t_{M1} & \cdots & t_{MT} \end{bmatrix}}_{\boldsymbol{S}} = s_1 \underbrace{\begin{bmatrix} a_{11}^{(1)} & \cdots & a_{1T}^{(1)} \\ \vdots & \ddots & \vdots \\ a_{M1}^{(1)} & \cdots & a_{MT}^{(1)} \end{bmatrix}}_{\boldsymbol{A}_1} + \cdots + s_Q \underbrace{\begin{bmatrix} a_{11}^{(Q)} & \cdots & a_{1T}^{(Q)} \\ \vdots & \ddots & \vdots \\ a_{M1}^{(Q)} & \cdots & a_{MT}^{(Q)} \end{bmatrix}}_{\boldsymbol{A}_Q}, \tag{2.7}$$

with the aid of a set of dispersion matrices $\boldsymbol{A}_q \in \mathcal{C}^{M \times Q}$ $(q = 1, \cdots Q)$, which are prepared prior to the commencement of transmissions. Here, the dispersion matrices $\boldsymbol{A}_q$ are constructed using a certain criterion, such as the maximization of either the achievable diversity order [88] or of the channel capacity [98], while maintaining the power constraints of

$$\mathrm{tr}[\boldsymbol{A}_q \boldsymbol{A}_q^{\mathrm{H}}] = \frac{T}{Q} \quad (q = 1, \cdots Q), \tag{2.8}$$

leading to a unity transmission power per symbol duration. It can be seen from Eq. (2.7)

that Q symbols $\boldsymbol{K} = [s_1, s_2 \cdots, s_Q]^{\mathrm{T}}$ are dispersed into both the M-spatial and T-time dimensions, generating $(M \times T)$ space-time codewords $\boldsymbol{S}$.[1]

According to [93], by applying the vertical stacking operation $vec(\cdot)$ to both sides of Eq. (2.1), the block-based signal model can be rewritten in a more tractable vectorial form as

$$\bar{\boldsymbol{Y}} = \bar{\boldsymbol{H}}\boldsymbol{\chi}\boldsymbol{K} + \bar{\boldsymbol{V}}, \tag{2.9}$$

with the relations of

$$\bar{\boldsymbol{H}} = \boldsymbol{I} \otimes \boldsymbol{H} \tag{2.10}$$

$$\boldsymbol{\chi} = [vec(\boldsymbol{A}_1), vec(\boldsymbol{A}_2), \cdots, vec(\boldsymbol{A}_Q)], \tag{2.11}$$

where $\bar{\boldsymbol{Y}} \in \mathcal{C}^{NT\times 1}$ represents the equivalent received signals and $\bar{\boldsymbol{N}} \in \mathcal{C}^{NT\times 1}$ denotes the equivalent noise components obeying the complex-valued Gaussian distribution having a zero mean and a variance of N_0. Furthermore, $\otimes$ denotes the Kronecker product. To elaborate a little further, the assumption of having a block fading channel requires selectively short transmission blocks of Q symbols and/or a low Doppler frequency. Having arrived at the linearized system model of Eq. (2.9), which has a structure similar to that of SDM in Eq. (2.5), we can utilize the set of diverse MIMO detectors developed for the family of SDM schemes, rather than the exhaustive ML detector.

The normalized transmission rate R_{LDC} of the $\mathcal{L}$-PSK/QAM modulated LDC scheme employing the parameters M, N, T and Q is given by

$$R_{\mathrm{LDC}} = \frac{Q}{T} \cdot \log_2 \mathcal{L} \text{ (bits/symbol)}. \tag{2.12}$$

It should be emphasized that the LDC schemes are capable of striking a flexible balance between diversity and multiplexing by optimizing a set of the LDC parameters.

2.2.4 Spatial Modulation/Space-Shift Keying

In the above-mentioned conventional MIMO schemes, the source information is first modulated onto complex-valued symbols with the aid of classic modulation schemes, such as PSK and QAM, and then the modulated symbols are allocated to or dispersed to a space-time matrix $\boldsymbol{S}$.

By contrast, the so-called SM/SSK scheme [60, 61, 63, 66] is based on a new modulation criterion, namely the activation of one out of a total of M antenna elements during each symbol interval. This leads to an additional means of conveying source information, while removing the effects of ICI.[2] More specifically, let us assume having $B = \log_2(\mathcal{L} \cdot M) =$

[1] By appropriately designing a set of dispersion matrices, the LDC scheme is capable of operating in an arbitrary transmit- and receive-antenna configuration, given the desirable transmission rate and achievable diversity order. Hence, the system parameters are fully characterized by the dispersion-matrix set employed.

[2] Since our STSK scheme, which will be proposed in this chapter, is inspired by and partly based on the SM/SSK concept, it is useful to revisit the encoding and decoding principle of the SM/SSK scheme.

Table 2.1: Example of SM Scheme Employing $M = 4$ Transmit Antennas, Mapping 3 Bits Per Block, with the Aid of BPSK Constellation

Input bits m, l		Antenna index $\sharp m$	BPSK symbol s_l
00	0	$\sharp 1$	$+1$
00	1	$\sharp 1$	-1
01	0	$\sharp 2$	$+1$
01	1	$\sharp 2$	-1
10	0	$\sharp 3$	$+1$
10	1	$\sharp 3$	-1
11	0	$\sharp 4$	$+1$
11	1	$\sharp 4$	-1

$\log_2 \mathcal{L}+\log_2 M$ input bits per block. Then the modulated signals $\boldsymbol{S}_{m,l} \in \mathcal{C}^{M\times 1}$ are represented by[3]

$$\boldsymbol{S}_{m,l} = [\underbrace{0, \cdots, 0}_{m-1}, s_l, \underbrace{0, \cdots, 0}_{M-m}]^{\mathrm{T}}, \tag{2.13}$$

where s_l $(1 \leq l \leq \mathcal{L})$ represents the PSK/QAM symbol modulated according to the $\log_2 \mathcal{L}$ input bits, while the integer m $(1 \leq m \leq M)$ corresponds to the rest of the input bits, i.e. the $\log_2 M$ bits. According to [60, 61, 63, 66], it is normally assumed that the number of transmit antennas M is set to 2^ι, where ι is an integer value. Note that this restriction may make it challenging to implement SM/SSK schemes for an arbitrary number of transmit antennas M. Considering that the number of symbol durations T per block is set to $T = 1$, the normalized transmission rate $R_{\mathrm{SM/SSK}}$ of the SM/SSK scheme is written as $R_{\mathrm{SM/SSK}} = \log_2(\mathcal{L} \cdot M)$ bits/symbol. It can be seen from Eq. (2.13) that since only one out of M antenna elements is activated during each symbol interval, symbol-level synchronization between the antenna elements is no longer needed. This allows us to avoid the elaborate calibration of the antenna-array.

To expound a little further, we exemplify the BPSK-modulated ($\mathcal{L} = 2$) SM/SSK modulation employing $M = 4$ transmit antennas in Table 2.1 and Fig. 2.1. As seen in Table 2.1, $B = 3$ input bits are divided into two bits and one bit, and then the first two bits determine the activated antenna element ($\sharp 1, \sharp 2, \sharp 3, \sharp 4$), while the last single bit generates the BPSK symbol s_l $(l = 1, 2)$. When binary symbols of "011" are input as shown in Fig. 2.1,

[3]As noted in [66], the SSK scheme can be viewed as the special case of the SM, where only the presence and absence of the energy assigned to each antenna element differentiates the transmitted information. More specifically, in the SSK scheme the activated antenna element only transmits a symbol of $s_1 = +1$, which may be considered to be $\mathcal{L} = 1$-case of the SM scheme.

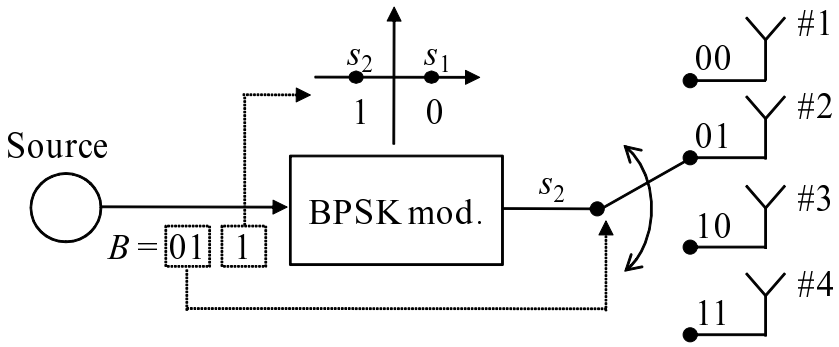

Figure 2.1: SM mapping example, where binary bits of 011 are input to the BPSK-modulated SM employing $M = 4$ transmit antenna elements.

the second antenna ♯2 is activated, while the second constellation point s_2 is selected as the transmitted symbol, according to the mapping rule seen in Table 2.1.

Furthermore, this SM/SSK arrangement allows the employment of low-complexity single-antenna-based ML detection at the receiver, while the BLAST scheme requires the potentially excessive-complexity joint detection of multiple antennas' signals. To be specific, since the conditional probability of $P(\boldsymbol{Y}|\boldsymbol{S}_{m,l}, \boldsymbol{H})$ is given by

$$P(\boldsymbol{Y}|\boldsymbol{S}_{m,l}, \boldsymbol{H}) = \frac{1}{(\pi N_0)^N} \exp\left(-\frac{||\boldsymbol{Y} - \boldsymbol{H}\boldsymbol{S}_{m,l}||^2}{N_0}\right), \tag{2.14}$$

the optimal ML detector is derived as [63]

$$\begin{aligned}(\hat{m}, \hat{l}) &= \arg\max_{m,l} P(\boldsymbol{Y}|\boldsymbol{S}_{m,l}, \boldsymbol{H}) &(2.15)\\ &= \arg\min_{m,l} ||\boldsymbol{Y} - \boldsymbol{H}\boldsymbol{S}_{m,l}||^2 &(2.16)\\ &= \arg\min_{m,l} ||\boldsymbol{Y} - s_l \boldsymbol{h}_m||^2, &(2.17)\end{aligned}$$

where $\boldsymbol{h}_m = [h_{1m}, \cdots, h_{Nm}]^{\mathrm{T}}$ denotes the mth column of the channel matrix $\boldsymbol{H}$. It is worth mentioning that upon increasing the number of transmit antennas M, the computational complexity required for this single-antenna-based ML detection increases linearly, while that of BLAST increases exponentially, as expressed in Eq. (2.6). To be specific, the computational complexity per bit, evaluated in terms of the number of real-valued multiplications, is given by

$$\frac{6MN\mathcal{L}}{\log_2(M \cdot \mathcal{L})}. \tag{2.18}$$

This advantage becomes even more dominant in a rank-deficient scenario, where the number of transmit antennas is higher than that of the receive antennas and hence either an excessive complexity or a substantial performance degradation is imposed on SDM. As a result, it was demonstrated in [60, 61, 63, 66] that SM has the potential of outperforming other MIMO arrangements, such as BLAST and Alamouti's STBC schemes in some scenarios.

On the other hand, since SM adopted V-BLAST's high-rate architecture, which was designed for achieving a multiplexing gain, rather than diversity gain, it has to rely on the

Table 2.2: System parameters

Number of transmit antennas	M
Number of receive antennas	N
Modulation	$\mathcal{L}-$PSK or $\mathcal{L}-$QAM
Channels	Frequency-flat Rayleigh fading
Detector	ML detector

Table 2.3: Bandwidth efficiency of QPSK-modulated SM systems for different number of transmit antennas M.

Modulation	M	Bandwidth efficiency (bit per channel use)
QPSK	1	2
	2	3
	4	4
	8	5
	16	6
	32	7
	64	8

employment of multiple DL receive AEs for the sake of combating the effects of fading channels. However, accommodating multiple DL elements imposes challenges, when transmitting to mobiles in DL scenarios. Additionally, when aiming for a linear increase in the transmission rate, the number of transmit antennas employed in the context of [60, 61, 63, 66] has to be increased exponentially.

Figs. 2.2(a) and 2.2(b) show the achievable BER performance of the QPSK-modulated SM scheme employing the optimal single-stream ML detector, where the number of transmit and receive antennas is varied. Observe in Fig. 2.2(a) that upon increasing the number of transmit antennas M, the achievable BER performance was improved, while in all the scenarios considered the diversity order was maintained to be four, which was achieved by the four receiver antennas. It was also seen in Fig. 2.2(b) that the SM system's diversity order was increased in accordance with the increase in the number of receiver antennas N from one to four.

Furthermore, Fig. 2.3 shows the computational complexity imposed by the ML receivers of the QPSK-modulated BLAST and SM schemes, which are quantified by Eqs. (2.6) and (2.18), respectively. Here, the number of receiver antennas was fixed to $N = 4$ and the

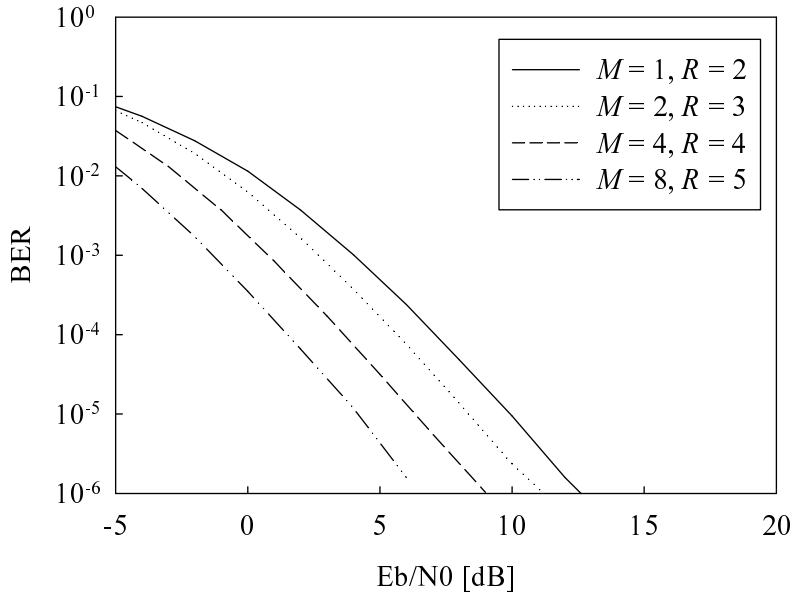

(a) $N = 4$

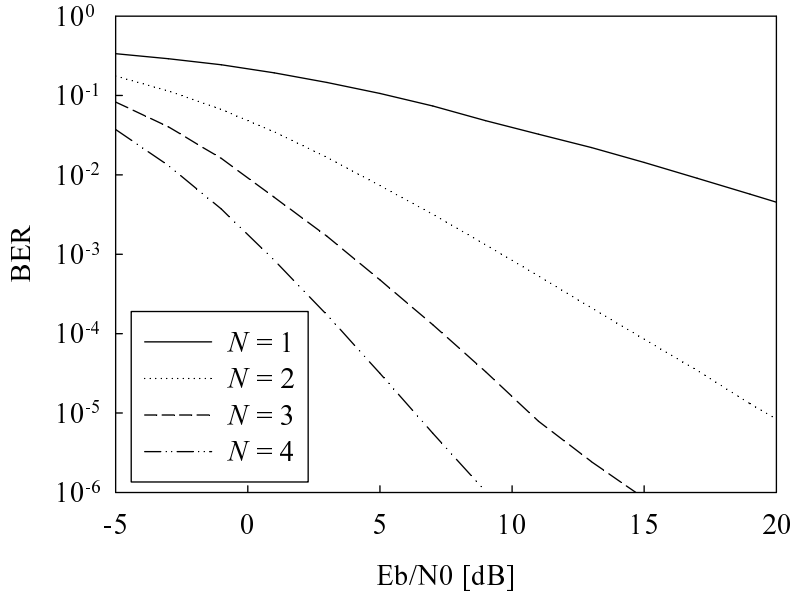

(b) $M = 4$

Figure 2.2: Achievable BER performance of the QPSK-modulated SM scheme of Fig. 2.1 employing the optimal ML detector, where the number of transmit antennas M and of receive antennas N is varied, such as (a) $M = 1, 2, 4, 8$ as well as $N = 4$ and (b) $M = 4$ as well as $N = 1, 2, 3, 4$. All other system parameters were summarized in Tables 2.2 and 2.3.

number of transmit antennas was varied. It can be seen from Fig. 2.3 that upon increasing the transmission rate R, the complexity advantage of the SM scheme over the BLAST scheme increased, while acknowledging that in the SM scheme the number of transmit antennas M has to be increased exponentially in order to achieve a linear increase of R_{SM}. Furthermore,

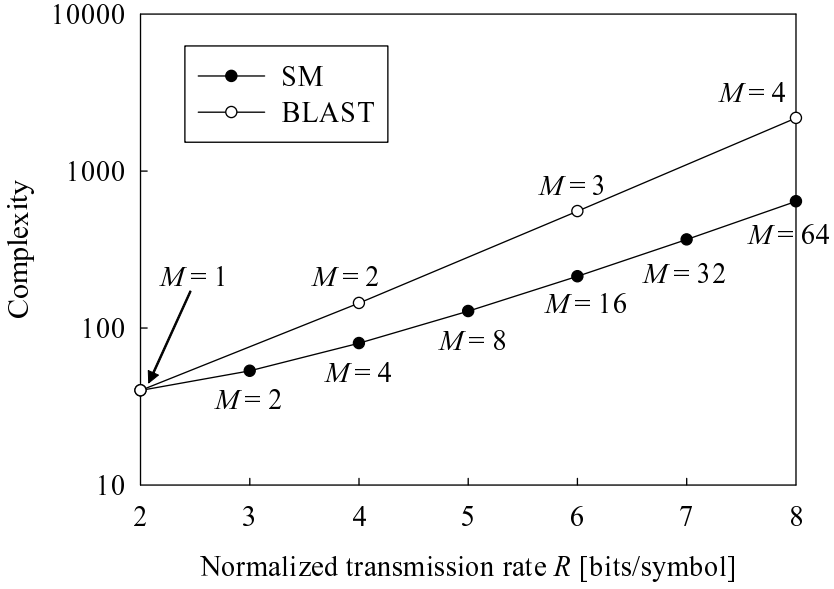

Figure 2.3: Computational complexity of ML detection, which is required to decode one bit, comparing the SM scheme of Fig. 2.1 and the BLAST schemes, both employing $N = 4$ receive antennas and the QPSK modulation, while the number of transmit antennas M is varied. All other system parameters were summarized in Tables 2.2 and 2.3.

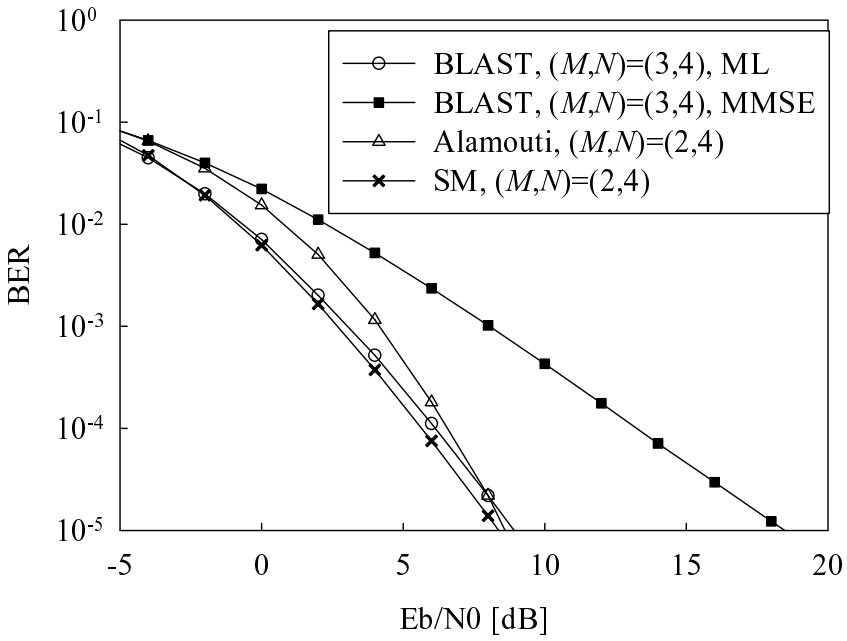

Figure 2.4: Achievable BER performance, comparing different MIMO arrangements attaining a transmission rate of 8 bits/symbol, i.e. the BPSK-modulated $(M \times N) = (3 \times 4)$-element BLAST scheme, the 8-PSK modulated $(M \times N) = (2 \times 4)$-element Alamouti scheme and the QPSK-modulated $(M \times N) = (2 \times 4)$-element SM scheme of Fig. 2.1. Here, the ML and MMSE detectors were compared for the BLAST scheme, while the ML detector was employed for the Alamouti and the SM schemes. All other system parameters were summarized in Table 2.2.

Fig. 2.4 shows the achievable BER performance, comparing different $(M \times N)$-element MIMO arrangements, which attain a transmission rate of 8 bits/symbol, i.e. the BPSK-modulated (3×4)-element BLAST scheme, the 8-PSK modulated (2×4)-element Alamouti code and the QPSK-modulated (2×4)-element SM schemes. Here, the ML and MMSE detectors were compared in the context of the BLAST scheme, while the ML detector was employed for the Alamouti and the SM schemes. Observe in Fig. 2.4 that the SM scheme slightly outperformed the BLAST scheme employing the ML detector, while the complexity of the SM scheme was less than half that of the BLAST scheme. Additionally, when the BLAST employed the MMSE scheme for the sake of reducing the complexity, the BER performance substantially deteriorated due to the reduced receive diversity gain. Moreover, although the Alamouti scheme achieved the full-diversity order of eight, the corresponding BER performance was better for the SM scheme in the range of BER $\geq 10^{-5}$. Again, it should be noted that only the SM scheme is capable of operating without symbol-level synchronization between the antenna elements and hence its BER performance is not degraded by the potential inter-antenna synchronization errors, unlike the other MIMO schemes.

2.3 Space-Time Shift Keying

As described in Section 2.2.4, the recently-proposed SM/SSK scheme of Fig. 2.1 is based on the concept that source information is assigned to the spatial indices, i.e. to the transmit antennas, where only the spatial dimension is utilized for the classic modulation scheme and hence no transmit diversity gain is achieved. Considering the fact that the LDC scheme is capable of striking a flexible tradeoff between diversity and multiplexing gains by making the best use of both the spatial and time dimensions, it might be useful to extend the SM/SSK scheme so that both these two dimensions can be utilized. To this end, in this section we propose the so-called STSK modulation scheme, whose merits are listed as follows:

- The STSK scheme is capable of striking an attractive tradeoff between the achievable diversity gain and multiplexing gain, by invoking the SM/SSK scheme of Fig. 2.1. Hence, our STSK scheme is capable of achieving both transmit as well as receive diversity gains, unlike the conventional SM and SSK schemes of Section 2.2.4, which can only attain receive diversity gain.

- Since no ICI is imposed by the resultant equivalent system model of the STSK scheme, the employment of single-stream-based ML detection becomes realistic.

- The STSK scheme can be configured to support asynchronous MIMO transmissions, which does not necessitates symbol-level IAS, similarly to the SM/SSK scheme of Section 2.2.4.

- The STSK is capable of supporting an arbitrary transmit- and receive-antenna configuration, without any substantial information loss.

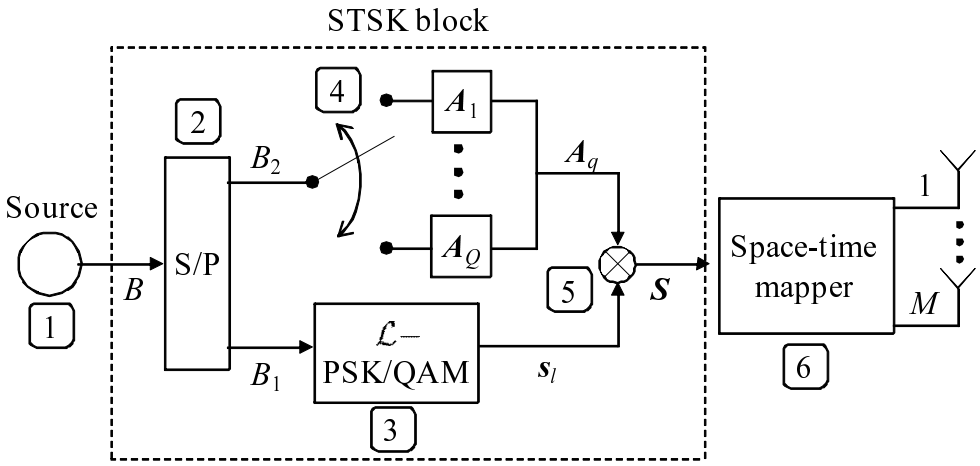

Figure 2.5: Transmitter structure of our coherent STSK scheme.

More specifically, the STSK scheme is based on the activation of Q number of appropriately indexed space-time dispersion matrices within each STSK block duration, rather than that of the indexed antennas at each symbol duration, as in the SM scheme of [60, 61, 63, 66].

In the rest of this section, we introduce two novel schemes, namely the Coherent STSK (CSTSK) and Asynchronous CSTSK (ACSTSK) modulation arrangements, which does not require any IAS between the RF antenna circuits at the transmitter. We also derive the optimal ML detector for our STSK scheme. Furthermore, the decoding complexity as well as the maximum achievable diversity order of our STSK scheme are also derived.

2.3.1 STSK Modulation Concept

Fig. 2.5 depicts the transmitter structure of our coherent STSK scheme, where Q dispersion matrices $\boldsymbol{A}_{q'} \in \mathcal{C}^{M\times T}$ $(q' = 1, \cdots, Q)$ are pre-assigned in advance of any transmission. A total of $B = \log_2(Q \cdot \mathcal{L})$ source bits are mapped to each space-time block $\boldsymbol{S} \in \mathcal{C}^{M\times T}$ by the

STSK scheme of Fig. 2.5, yielding

$$\boldsymbol{S} = s_l \boldsymbol{A}_q \tag{2.19}$$

$$\begin{aligned} &= 0 \underbrace{\begin{bmatrix} a_{11}^{(1)} & \cdots & a_{1T}^{(1)} \\ \vdots & \ddots & \vdots \\ a_{M1}^{(1)} & \cdots & a_{MT}^{(1)} \end{bmatrix}}_{\boldsymbol{A}_1} + \cdots + 0 \underbrace{\begin{bmatrix} a_{11}^{(q-1)} & \cdots & a_{1T}^{(q-1)} \\ \vdots & \ddots & \vdots \\ a_{M1}^{(q-1)} & \cdots & a_{MT}^{(q-1)} \end{bmatrix}}_{\boldsymbol{A}_{q-1}} \leftarrow \begin{pmatrix} \text{deactivated} \\ \text{matrices} \end{pmatrix} \\ &\quad + s_l \underbrace{\begin{bmatrix} a_{11}^{(q)} & \cdots & a_{1T}^{(q)} \\ \vdots & \ddots & \vdots \\ a_{M1}^{(q)} & \cdots & a_{MT}^{(q)} \end{bmatrix}}_{\boldsymbol{A}_q} \leftarrow \begin{pmatrix} \text{activated} \\ \text{matrix} \end{pmatrix} \\ &\quad + 0 \underbrace{\begin{bmatrix} a_{11}^{(q+1)} & \cdots & a_{1T}^{(q+1)} \\ \vdots & \ddots & \vdots \\ a_{M1}^{(q+1)} & \cdots & a_{MT}^{(q+1)} \end{bmatrix}}_{\boldsymbol{A}_{q+1}} + \cdots + 0 \underbrace{\begin{bmatrix} a_{11}^{(Q)} & \cdots & a_{1T}^{(Q)} \\ \vdots & \ddots & \vdots \\ a_{M1}^{(Q)} & \cdots & a_{MT}^{(Q)} \end{bmatrix}}_{\boldsymbol{A}_Q}, \leftarrow \begin{pmatrix} \text{deactivated} \\ \text{matrices} \end{pmatrix} \end{aligned} \tag{2.20}$$

where s_l is the complex-valued symbol of the conventional modulation scheme employed, such as $\mathcal{L}$-PSK or $\mathcal{L}$-QAM, which is associated with $B_1 = \log_2 \mathcal{L}$ number of input bits. By contrast, the specific matrix $\boldsymbol{A}_q$ is selected from the Q dispersion matrices $\boldsymbol{A}_{q'}$ $(q' = 1, \cdots, Q)$ according to $B_2 = \log_2 Q$ number of input bits. Additionally, in order to maintain a unity average transmission power for each STSK symbol duration, each of the Q dispersion matrices has to obey the power constraint of

$$\text{tr}[\boldsymbol{A}_{q'}^{\text{H}} \boldsymbol{A}_{q'}] = T \ (q' = 1, \cdots, Q), \tag{2.21}$$

where $\text{tr}[\cdot]$ indicates the trace operation. Our design rule used for generating the dispersion matrices $\boldsymbol{A}_q$ will be described in Section 2.6. Note that this power constraint of Eq. (2.21) is Q times higher than that of LDC in Eq. (2.8), since the LDC scheme linearly combines the Q dispersion matrices, while our STSK activates only one out of them.

In this way, an additional means of transmitting further information bits was created. To be specific, we exemplify in Table 2.4 the mapping rule of our STSK modulation scheme, where a fixed number of $B = \log_2(Q \cdot \mathcal{L}) = 3$ bits per space-time block $\boldsymbol{S}$ are transmitted by employing $\mathcal{L}$–PSK, for the specific cases of $(Q, \mathcal{L})$ =$(1, 8; 2, 4; 4, 2; 8, 1)$. As seen from Table 2.4, there are several possible combinations of the number of dispersion matrices Q and of the constellation size $\mathcal{L}$, given a total throughput of 3 source bits per space-time block. For example, assume that the information bits "101" are input to our STSK scheme employing QPSK modulation ($\mathcal{L} = 4$) and $Q = 2$. Then, according to Table 2.4 we arrive at the modulated space-time block of $\boldsymbol{S} = s_2 \boldsymbol{A}_2 = e^{j\frac{\pi}{2}} \boldsymbol{A}_2$.

Moreover, the normalized throughput per time-slot (or per symbol) R of our STSK scheme

Table 2.4: Example of STSK Modulation Scheme, Mapping 3 Bits Per Space-Time Block, with the Aid of $\mathcal{L}$–PSK Constellation

Input bits	$Q=1$ $\mathcal{L}=8$		$Q=2$ $\mathcal{L}=4$		$Q=4$ $\mathcal{L}=2$		$Q=8$ $\mathcal{L}=1$	
	$\boldsymbol{A}_q$	s_l	$\boldsymbol{A}_q$	s_l	$\boldsymbol{A}_q$	s_l	$\boldsymbol{A}_q$	s_l
000	$\boldsymbol{A}_1$	$s_1=1$	$\boldsymbol{A}_1$	$s_1=1$	$\boldsymbol{A}_1$	$s_1=1$	$\boldsymbol{A}_1$	$s_1=1$
001	$\boldsymbol{A}_1$	$s_2=e^{j\frac{\pi}{4}}$	$\boldsymbol{A}_1$	$s_2=e^{j\frac{\pi}{2}}$	$\boldsymbol{A}_1$	$s_2=e^{j\pi}$	$\boldsymbol{A}_2$	$s_1=1$
010	$\boldsymbol{A}_1$	$s_3=e^{j\frac{2\pi}{4}}$	$\boldsymbol{A}_1$	$s_3=e^{j\frac{2\pi}{2}}$	$\boldsymbol{A}_2$	$s_1=1$	$\boldsymbol{A}_3$	$s_1=1$
011	$\boldsymbol{A}_1$	$s_4=e^{j\frac{3\pi}{4}}$	$\boldsymbol{A}_1$	$s_4=e^{j\frac{3\pi}{2}}$	$\boldsymbol{A}_2$	$s_2=e^{j\pi}$	$\boldsymbol{A}_4$	$s_1=1$
100	$\boldsymbol{A}_1$	$s_5=e^{j\frac{4\pi}{4}}$	$\boldsymbol{A}_2$	$s_1=1$	$\boldsymbol{A}_3$	$s_1=1$	$\boldsymbol{A}_5$	$s_1=1$
101	$\boldsymbol{A}_1$	$s_6=e^{j\frac{5\pi}{4}}$	$\boldsymbol{A}_2$	$s_2=e^{j\frac{\pi}{2}}$	$\boldsymbol{A}_3$	$s_2=e^{j\pi}$	$\boldsymbol{A}_6$	$s_1=1$
110	$\boldsymbol{A}_1$	$s_7=e^{j\frac{6\pi}{4}}$	$\boldsymbol{A}_2$	$s_3=e^{j\frac{2\pi}{2}}$	$\boldsymbol{A}_4$	$s_1=1$	$\boldsymbol{A}_7$	$s_1=1$
111	$\boldsymbol{A}_1$	$s_8=e^{j\frac{7\pi}{4}}$	$\boldsymbol{A}_2$	$s_4=e^{j\frac{3\pi}{2}}$	$\boldsymbol{A}_4$	$s_2=e^{j\pi}$	$\boldsymbol{A}_8$	$s_1=1$

may be expressed as

$$R=\frac{\log_2(Q\cdot\mathcal{L})}{T}\quad[\text{bits/symbol}]. \tag{2.22}$$

In the rest of this chapter, we employ the parameter-based notation of our STSK scheme formulated as STSK(M,N,T,Q) for ease of treatment.

To elaborate a little further, our STSK scheme includes the SM arrangement as its special case. For example, it is readily seen that STSK$(2,N,1,2)$ employing $\boldsymbol{A}_1=[1\ 0]^{\mathrm{T}}$ and $\boldsymbol{A}_2=[0\ 1]^{\mathrm{T}}$ is equivalent to the SM scheme assisted by $M=2$ transmit antennas [61]. More generally, the STSK$(M,N,1,Q=M)$ scheme having the dispersion matrices of

$$\boldsymbol{A}_1=\begin{bmatrix}1\\0\\\vdots\\0\end{bmatrix},\boldsymbol{A}_2=\begin{bmatrix}0\\1\\\vdots\\0\end{bmatrix},\cdots,\boldsymbol{A}_Q=\begin{bmatrix}0\\0\\\vdots\\1\end{bmatrix} \tag{2.23}$$

exhibits a system structure, which is identical to that of the SM scheme employing (M,N) transmit and receive antennas. Again, since in our STSK scheme the source bits are mapped to both the space and time-domain, rather than only to the spatial domain of the SM scheme [60, 61, 63, 66], the SM arrangement is included in our STSK scheme associated with $T=1$, where mapping to the time dimension was deactivated. It should also be noted that while SM has to exponentially increase the number of transmit AEs for the sake of linearly increasing the number of transmitted input bits, our STSK scheme may circumvent this problem by increasing the number of dispersion matrices Q. Therefore, given an affordable tradeoff in terms of number of transmit antennas M, our STSK scheme is capable of optimizing the

derived transmission rate and diversity order in a more flexible and efficient manner by appropriately choosing T and Q.[4]

Following the above-mentioned introductory elaborations on the STSK transmitter's encoding operation obeying the architecture of Fig. 2.5, each of the steps numbered in the figure may be summarized as follows:

Algorithm 2.1: Encoding principle of the STSK's transmitter of Fig. 2.5

1. Given the $\mathcal{L}$-PSK/QAM CSTSK(M, N, T, Q) scheme, $B = \log_2(Q \cdot \mathcal{L})$ information bits are input to the STSK block in each of the Space-Time (ST) block durations T.

2. The $B = \log_2(Q \cdot \mathcal{L})$ information bits are Serial-to-Parallel (S/P) converted to $B_1 = \log_2 \mathcal{L}$ bits and $B_2 = \log_2 Q$ bits.

3. The $B_1 = \log_2 \mathcal{L}$ bits at the lower output of the S/P converter of Fig. 2.5 are then modulated to a complex-valued $\mathcal{L}$-PSK/QAM symbol $\{s_l;\ l = 1, \cdots \mathcal{L}\}$.

4. According to the $B_2 = \log_2 Q$ bits at the lower output of the S/P converter of Fig. 2.5, one out of the Q dispersion matrices $\boldsymbol{A}_1, \cdots, \boldsymbol{A}_Q \in \mathcal{C}^{M \times T}$ is chosen, which we refer to as the activated matrix $\{\boldsymbol{A}_q\ ; q = 1, \cdots Q\}$.

5. According to the modulated symbol s_l generated in *Step* 3 as well as the dispersion matrix $\boldsymbol{A}_q$ activated in *Step* 4, a ST matrix $\boldsymbol{S} \in \mathcal{C}^{M \times T}$ is calculated as follows: $\boldsymbol{S} = s_l \cdot \boldsymbol{A}_q$.

6. The space-time matrix $\boldsymbol{S}$ generated in *Step* 5 is then mapped to the space- and time-dimensions, where the specific component in the mth row and tth column of the matrix $\boldsymbol{S}$ is assigned to the mth antenna element in the tth symbol duration.

Having formalized our CSTSK scheme's encoding algorithm, we then propose a modified CSTSK structure in the following section.

[4]Furthermore, the generalized SSK scheme was presented in [68] as the extension of the SSK scheme, where multiple AEs are activated at each symbol interval, rather than a single one. This contributes to the enhancement of the transmission rate, which is achieved by simultaneous symbol transmissions from the different transmit AEs. This however imposes ICI, which may only be mitigated at the cost of an increased receiver complexity. We note that since the generalized SSK scheme does not exploit the time dimension similarly to the SM/SSK scheme, no transmit diversity gain can be achieved. In contrast to the generalized SSK scheme, our CSTSK arrangement remains unaffected by ICI and it is also capable of achieving a transmit diversity gain. Again, we note that in our CSTSK the equivalent receiver model of Eq. (2.25) does not exhibit any ICI, despite the fact that multiple antennas simultaneously transmit their signals. This is because only a single dispersion matrix $\boldsymbol{A}_q$ is activated in each block interval, which disperses a single symbol s_l across both the time- and space-dimensions.

2.3.2 Asynchronous STSK Modulation

Additionally, we introduce an improved STSK structure, which enables us to dispense with any symbol-level time-synchronization between the RF chains associated with the transmit AEs, similarly to the SM/SSK scheme. As mentioned in [60, 61, 63, 66], the SM and SSK schemes do not require any symbol-level time synchronization between the transmit antenna circuits, because a single antenna is activated at each symbol instant in these schemes. By contrast, our STSK scheme introduced in the previous section, potentially requires IAS for the STSK's dispersion matrix activation, which replaces the antenna activation. However, by carefully designing the dispersion matrices $\boldsymbol{A}_{q'}$ $(q' = 1, \cdots, Q)$ of our STSK, we will contrive an ASTSK arrangement dispensing with any IAS. More specifically, the structure of each dispersion matrix $\boldsymbol{A}_{q'}$ is constructed so that there is a single non-zero element for each column of the dispersion matrix $\boldsymbol{A}_{q'}$. This constraint enables us to avoid any simultaneous transmission by multiple antennas, similarly to the conventional SM and SSK schemes, while retaining all the benefits of our STSK scheme.

For example, let us consider the ASTSK$(3, N, 3, 4)$ system. Then a set of dispersion matrices $\boldsymbol{A}_{q'}$ $(q' = 1, 2, 3, 4)$ may be given by

$$\begin{aligned} \boldsymbol{A}_1 &= \begin{bmatrix} a_1^{(1)} & 0 & 0 \\ 0 & a_2^{(1)} & 0 \\ 0 & 0 & a_3^{(1)} \end{bmatrix}, \ \boldsymbol{A}_2 = \begin{bmatrix} 0 & 0 & a_3^{(2)} \\ a_1^{(2)} & 0 & 0 \\ 0 & a_2^{(2)} & 0 \end{bmatrix}, \\ \boldsymbol{A}_3 &= \begin{bmatrix} 0 & a_2^{(3)} & 0 \\ 0 & 0 & a_3^{(3)} \\ a_1^{(3)} & 0 & 0 \end{bmatrix}, \ \boldsymbol{A}_4 = \begin{bmatrix} 0 & a_2^{(4)} & 0 \\ a_1^{(4)} & 0 & 0 \\ 0 & 0 & a_3^{(4)} \end{bmatrix}, \end{aligned} \tag{2.24}$$

where in each column of the four dispersion matrices $\boldsymbol{A}_1, \boldsymbol{A}_2, \boldsymbol{A}_3, \boldsymbol{A}_4$, there is only a single non-zero element, while the other two elements are set to 0s. Hence, this ASTSK arrangement indicates that regardless of the specific dispersion matrix activated in the STSK modulation process of Fig. 2.5, only one antenna element transmits a signal at any symbol instance. It should be noted that since the introduction of the ASTSK concept reduces the search space of the set of dispersion matrices, the achievable performance may be degraded in comparison to that of the STSK scheme, while the ASTSK's dispersion-matrix design also becomes less complex.

2.3.3 Optimal ML Detector for the Proposed STSK Scheme

Having generated the space-time block $\boldsymbol{S}$ to be transmitted, we then introduce the ML detection algorithm of our STSK scheme. By applying the vectorial stacking operation $vec()$ to the received signal block $\boldsymbol{Y}$ in Eq. (2.1), we arrive at the linearized equivalent system model formulated as follows: [93]

$$\bar{\boldsymbol{Y}} = \bar{\boldsymbol{H}} \chi \boldsymbol{K}_{q,l} + \bar{\boldsymbol{V}}, \tag{2.25}$$

with the relations of

$$\bar{\boldsymbol{Y}} = vec(\boldsymbol{Y}) \in \mathcal{C}^{NT\times 1}, \tag{2.26}$$

$$\bar{\boldsymbol{H}} = \boldsymbol{I} \otimes \boldsymbol{H}(i) \in \mathcal{C}^{NT\times MT}, \tag{2.27}$$

$$\bar{\boldsymbol{V}} = vec(\boldsymbol{V}) \in \mathcal{C}^{NT\times 1}, \tag{2.28}$$

$$\chi = [vec(\boldsymbol{A}_1)\cdots vec(\boldsymbol{A}_Q)] \in \mathcal{C}^{MT\times Q}, \tag{2.29}$$

where $\boldsymbol{I}$ is the identity matrix and $\otimes$ is the Kronecker product. Furthermore, the equivalent transmitted signal vector $\boldsymbol{K}_{q,l} \in \mathcal{C}^{Q\times 1}$ is written as

$$\boldsymbol{K}_{q,l} = [\underbrace{0,\cdots,0}_{q-1}, s_l, \underbrace{0,\cdots,0}_{Q-q}]^{\mathrm{T}}, \tag{2.30}$$

where the modulated symbol s_l is situated in the qth element, noting that the index q corresponds to the index of the dispersion matrix $\boldsymbol{A}_q$ activated during the corresponding STSK block. Therefore, the number of legitimate transmit signal vectors $\boldsymbol{K}_{q,l}$ is given by $Q \cdot \mathcal{L}$.

Since the equivalent system model of Eq. (2.25) is free from the effects of ICI, we can employ the single-antenna-based ML detector of [63], which imposes a low complexity. Let us consider that (q, l) correspond to the specific input bits of a STSK block, which are mapped to the lth ($l = 1,\cdots,\mathcal{L}$) PSK/QAM symbol and qth ($q = 1,\cdots,Q$) dispersion matrix. Then the estimates $(\hat{q}, \hat{l})$ are given by

$$(\hat{q}, \hat{l}) = \arg\min_{q,l} ||\bar{\boldsymbol{Y}} - \bar{\boldsymbol{H}}\chi\boldsymbol{K}_{q,l}||^2 \tag{2.31}$$

$$= \arg\min_{q,l} ||\bar{\boldsymbol{Y}} - s_l \left(\bar{\boldsymbol{H}}\chi\right)_q ||^2, \tag{2.32}$$

where s_l represents the lth symbol in the $\mathcal{L}$-point constellation. Furthermore, $\left(\bar{\boldsymbol{H}}\chi\right)_q$ is the qth column vector of the matrix $\bar{\boldsymbol{H}}\chi$. As mentioned in [63], this low-complexity ML detector exhibits the optimal detection performance in the uncoded scenario, where no *a priori* information is provided and the source bits are equi-probable.

2.3.4 Computational Complexity

Let us now characterize the computational complexity imposed by the ML detection of our STSK scheme, which is given by

$$\frac{NTQ(4MT + 6\mathcal{L})}{\log_2(Q \cdot \mathcal{L})}, \tag{2.33}$$

for fast-block fading scenarios. Furthermore, for slow fading scenarios this can be reduced to

$$\frac{NTQ[(4MT + 4\mathcal{L})/\tau + 2\mathcal{L}]}{\log_2(Q \cdot \mathcal{L})}, \tag{2.34}$$

where τ represents an integer, quantifying the coherence time in slow fading environments as $\tau \cdot T$. Here, their complexity is evaluated in terms of the number of real-valued multiplications,

noting that a single complex-valued multiplication was considered equivalent to four real-valued multiplications. To be more specific, for the case of fast fading environments, the ML detector of our STSK scheme is required to calculate $\bar{\boldsymbol{H}}\chi\boldsymbol{K}_{q,l}$ $(1 \leq q \leq Q, 1 \leq l \leq \mathcal{L})$ for each STSK block, corresponding to the complexity of $NTQ(4MT+4\mathcal{L})/\log_2(Q\cdot\mathcal{L})$. On the other hand, in slow fading environments, this complexity is reduced to $NTQ(4MT+4\mathcal{L})/[\tau\log_2(Q\cdot\mathcal{L})]$, since the associated calculation can be reused during the channels' coherence time.

Moreover, the computational complexity of the ASTSK receiver is further simplified from the expressions seen in Eqs. (2.33) and (2.34) into

$$\frac{NTQ(4T+6\mathcal{L})}{\log_2(Q\cdot\mathcal{L})} \tag{2.35}$$

and

$$\frac{NTQ[(4T+4\mathcal{L})/\tau+2\mathcal{L}]}{\log_2(Q\cdot\mathcal{L})}, \tag{2.36}$$

respectively, because each dispersion matrix of the ASTSK scheme is sparse and hence the complexity imposed by calculating $\bar{\boldsymbol{H}}\chi$ becomes lower than that of the STSK scheme by a factor of M.

For reference, the complexity of the SM scheme is also given by

$$\begin{cases} 6MN\mathcal{L}/\log_2(M\cdot\mathcal{L}) & \text{(fast fading)} \\ (4/\tau+2)MN\mathcal{L}/\log_2(M\cdot\mathcal{L}) & \text{(slow fading)} \end{cases}. \tag{2.37}$$

Although the SM scheme typically imposes a lower complexity than those of our STSK scheme, both the proposed schemes have a substantially lower complexity ML receiver in comparison to classic MIMO schemes, such as V-BLAST, LDCs and DLDCs, which is an explicit benefit of our ICI-free system model. Furthermore, the ratio of the STSK's complexity in Eq. (2.33) over that of the SM/SSK scheme in Eq. (2.37) is given by $TQ(4MT+6\mathcal{L})/6M\mathcal{L}$. Observe in this formula that an increase in the value of T gives rise to the quadratic increase of the above-mentioned complexity ratio. As a benefit, it may also potentially increase the attainable transmit diversity gain, as will be noted in Section 2.3.5.

Fig. 2.6 shows the computational complexity per block required to implement the ML detection for the QPSK-modulated STSK$(2,2,2,Q)$ and ASTSK$(2,2,2,Q)$ schemes, expressed in Eqs. (2.34) and (2.36). Here Q was varied from $Q=1$ to $Q=64$, while channel's coherence factor was changed from $\tau=1$ to $\tau=\infty$. It can be seen for both the STSK and ASTSK cases that upon increasing the transmission rate, the corresponding complexity is increased. Additionally, upon increasing the channel's coherence time, the complexity was found to decrease, and the scenario of $\tau=1000$ approached the lower bound corresponding to the static channel's case of $\tau=\infty$. Furthermore, it was found that the ASTSK's complexity advantage over the STSK scheme is high, when the coherence time is low. As predicted from Eqs. (2.34) and (2.36), the lower bound of the STSK and ASTSK schemes' complexity coincided in the static channel's case of $\tau=\infty$.

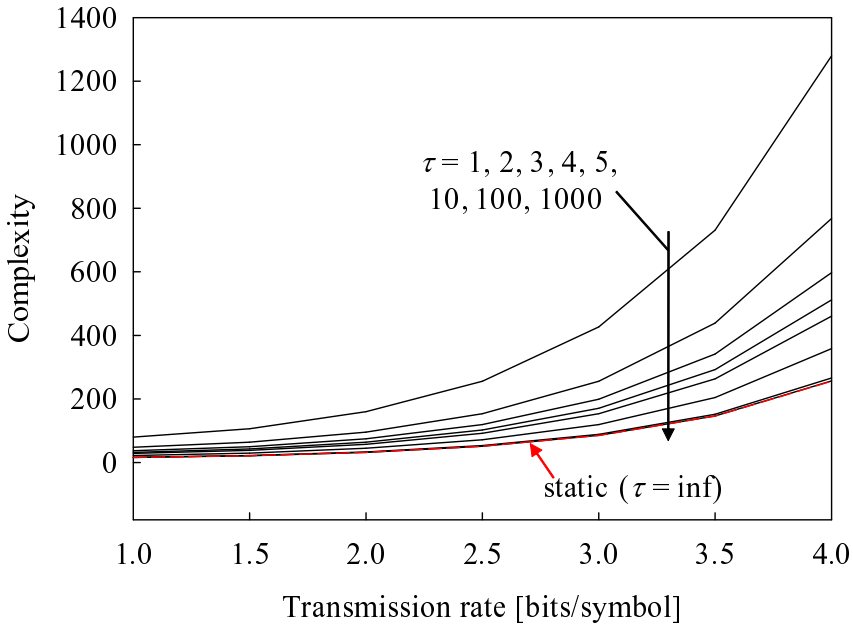

(a) STSK

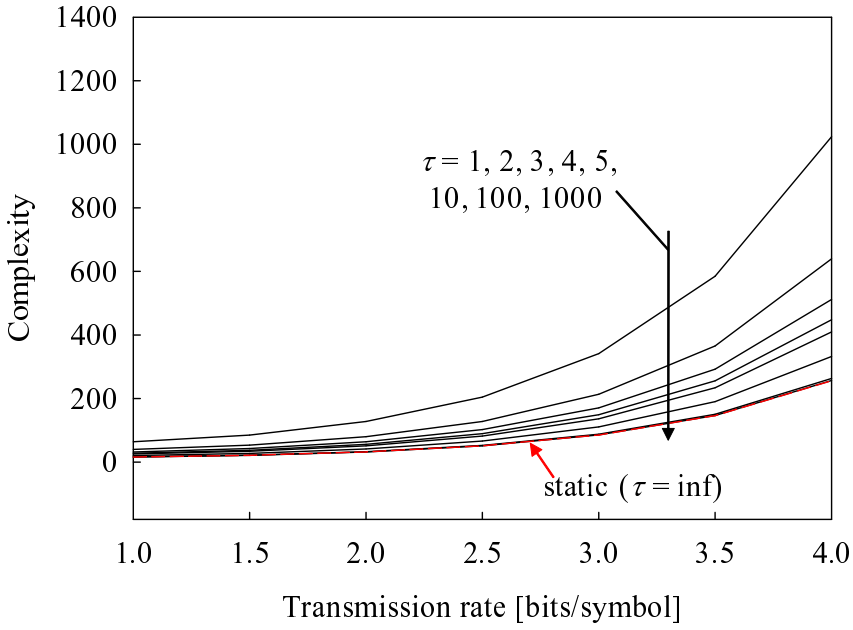

(b) ASTSK

Figure 2.6: Computational complexity per block required to implement the ML detection for the QPSK-modulated STSK$(2, 2, 2, Q)$ and ASTSK$(2, 2, 2, Q)$ schemes of Fig. 2.5, as expressed in Eqs. (2.34) and (2.36). Here Q was varied from $Q = 1$ to $Q = 64$, while the channel's coherence-time was changed from $\tau = 1$ to $\tau = \infty$. All other system parameters were summarized in Table 2.5.

Table 2.5: System parameters of the uncoded STSK scheme of Fig. 2.5

Number of transmit antennas	M
Number of receive antennas	N
Symbol durations per block	T
Number of dispersion matrices	Q
Modulation	$\mathcal{L}-$PSK or $\mathcal{L}-$QAM
Channels	Frequency-flat Rayleigh fading
Channel's coherence-time	τ block durations
Detector	ML detector of Eq. (2.32)

2.3.5 Maximum Achievable Diversity Order

For the general STSK block-based system model of Eq. (2.1), an upper bound of the average probability misinterpreting the transmitted space-time matrix $\boldsymbol{S}$ as $\boldsymbol{S}'$ is given by the Chernoff upper bound as follows: [37]

$$P(\boldsymbol{S} \to \boldsymbol{S}') \leq \frac{1}{\left| \boldsymbol{I}_{M \cdot N} + \frac{1}{4N_0} \boldsymbol{R} \otimes \boldsymbol{I}_N \right|}, \tag{2.38}$$

where we have

$$\boldsymbol{R} = (\boldsymbol{S} - \boldsymbol{S}')(\boldsymbol{S} - \boldsymbol{S}')^{\mathrm{H}}. \tag{2.39}$$

Furthermore, for high SNRs, Eq. (2.39) may be simplified to [93]

$$P(\boldsymbol{S} \to \boldsymbol{S}') \leq \underbrace{\left(\frac{1}{4N_0} \right)^{-m'N}}_{\text{diversity gain}} \cdot \underbrace{\prod_{m=1}^{m'} \frac{1}{\mu_m^N}}_{\text{coding gain}}, \tag{2.40}$$

where m' and μ_m are the rank and the nth eigenvalue of $\boldsymbol{R}$, respectively. Let us now define the STC's diversity order as the exponent of its erroneous decision probability curve in Eq. (2.40). Then the resultant diversity order is determined by the smallest value of the product $m'N$ in Eq. (2.40). Therefore, we may surmise that the maximum achievable diversity order of our STSK scheme is given by $N \cdot \min(M, T)$, where $\min(M, T)$ corresponds to the achievable transmit diversity gain. This implies that upon increasing the STSK block duration T, the associated transmit diversity order increases, provided that the number of transmit antennas M satisfies $M \geq T$. In other words, increasing T beyond M does not result in any further transmit diversity improvement. By contrast, a lower T value may have the double-merits of a low computational complexity as well as of a high transmission rate, according to Eqs. (2.33) and (2.22), although this is achieved at the cost of a reduced transmit diversity order.[5]

[5]The extreme example is the SM/SSK scheme, which may be considered as the CSTSK$(M, N, 1, Q = M)$ scheme having the specific dispersion-matrix structure expressed as Eq. (2.23), where a high transmission rate as well as low complexity is achieved, at the expense of having no transmit diversity gain.

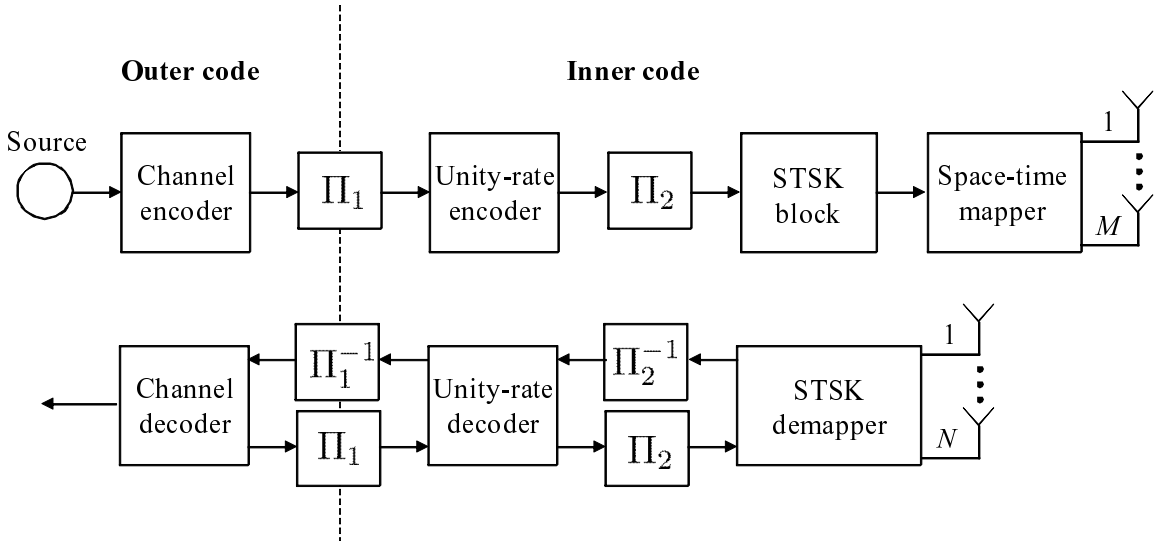

Figure 2.7: Schematic of a three-stage RSC- and URC-coded coherent STSK scheme using iterative detection.

2.4 Three-stage Concatenated Turbo STSK Scheme

Having presented the STSK modulation and detection principle in Section 2.3 in the context of uncoded scenarios, let us then invoke the turbo principle [27] to incorporate the proposed STSK scheme in a multiple-stage serially concatenated arrangement, for the sake of achieving a near-capacity performance. Furthermore, the iterative soft demapping principle is contrived for our STSK scheme.

2.4.1 System Overview

Fig 2.7 shows the schematic of the proposed three-stage channel- and Unity Rate-Coded (URC) STSK scheme using iterative detection. Here, the input source bits are channel-encoded by a half-rate Recursive Systematic Convolutional (RSC) code and are interleaved by a random bit interleaver Π_1. Then, the interleaved bits are further encoded by a recursive URC encoder [129][6], and then the coded bits are interleaved by the second random interleaver Π_2 of Fig. 2.7. Finally, the interleaved bits are input to the STSK block of Fig. 2.5, followed by the transmission of the space-time block $\boldsymbol{S}$.

As illustrated in Fig. 2.7, a three-stage iterative decoding algorithm is employed at the receiver. To be specific, the Soft-Input Soft-Output (SISO) decoders of the receiver iteratively exchange soft extrinsic information in the form of Log Likelihood Ratios (LLRs). The STSK demapper block of Fig. 2.7 receives its input signals from the MIMO channels, which are combined with the extrinsic information provided by the URC decoder. Simultaneously, the

[6]The role of the URC is to impose an Infinite Impulse Response (IIR), which improves the achievable iterative decoding performance by efficiently spreading the extrinsic information, as detailed in [23].

URC decoder block of Fig. 2.7 receives extrinsic information both from the RSC channel decoder as well as from the STSK demapper and generates extrinsic information for both of its surrounding blocks seen in Fig. 2.7. The RSC channel decoder of Fig. 2.7 exchanges extrinsic information with the URC decoder and outputs the estimated bits after the I_{out} iterations. Here, the iterations between the STSK and URC decoder blocks are referred to as the inner iterations, while those between the URC and RSC decoders as outer iterations. The corresponding number of iterations are denoted by I_{in} and I_{out}, respectively. To be more specific, I_{in} inner iterations are implemented per each outer iteration, indicating that the total number of iterations becomes $I_{\text{in}} \cdot I_{\text{out}}$.

2.4.2 Soft STSK Demapper

Let us now detail the soft demapper of our STSK scheme. According to the equivalent system model of Eq. (2.25) derived for our STSK scheme, the conditional probability $p(\boldsymbol{Y}|\boldsymbol{K}_{q,l})$ is given by

$$p(\bar{\boldsymbol{Y}}|\boldsymbol{K}_{q,l}) = \frac{1}{(\pi N_0)^{NT}} \exp\left(-\frac{||\bar{\boldsymbol{Y}} - \bar{\boldsymbol{H}}\chi\boldsymbol{K}_{q,l}||^2}{N_0}\right). \tag{2.41}$$

Bearing in mind that the equivalent received signals $\bar{\boldsymbol{Y}}$ carry B channel-coded binary bits $\boldsymbol{b} = [b_1, b_2, \cdots, b_B]$, the resultant extrinsic LLR value of bit b_k for $k = 1, \cdots, B$ may be expressed as [130]

$$\begin{aligned} L_{\text{e}}(b_k) &= \ln \frac{\sum_{\boldsymbol{K}_{q,l} \in K_1^k} p(\bar{\boldsymbol{Y}}|\boldsymbol{K}_{q,l}) \cdot \exp\left[\sum_{j \neq k} b_j L_a(b_j)\right]}{\sum_{\boldsymbol{K}_{q,l} \in K_0^k} p(\bar{\boldsymbol{Y}}|\boldsymbol{K}_{q,l}) \cdot \exp\left[\sum_{j \neq k} b_j L_a(b_j)\right]} \\ &= \ln \frac{\sum_{\boldsymbol{K}_{q,l} \in K_1^k} \exp\left[-||\bar{\boldsymbol{Y}} - \bar{\boldsymbol{H}}\chi\boldsymbol{K}_{q,l}||^2/N_0 + \sum_{j \neq k} b_j L_a(b_j)\right]}{\sum_{\boldsymbol{K}_{q,l} \in K_0^k} \exp\left[-||\bar{\boldsymbol{Y}} - \bar{\boldsymbol{H}}\chi\boldsymbol{K}_{q,l}||^2/N_0 + \sum_{j \neq k} b_j L_a(b_j)\right]}, \end{aligned} \tag{2.42}$$

where K_1^k and K_0^k represent the sub-space of the legitimate equivalent signals K, satisfying $K_1^k \equiv \{\boldsymbol{K}_{q,l} \in K : b_k = 1\}$ and $K_0^k \equiv \{\boldsymbol{K}_{q,l} \in K : b_k = 0\}$, respectively. Furthermore, Eq. (2.42) is readily simplified by the max-log approximation [27], yielding:

$$\begin{aligned} L_{\text{e}}(b_k) &= \max_{\boldsymbol{K}_{q,l} \in K_1^k} \left[-\frac{||\bar{\boldsymbol{Y}} - \bar{\boldsymbol{H}}\chi\boldsymbol{K}_{q,l}||^2}{N_0} + \sum_{j \neq k} b_j L_a(b_j)\right] \\ &- \max_{\boldsymbol{K}_{q,l} \in K_0^k} \left[-\frac{||\bar{\boldsymbol{Y}} - \bar{\boldsymbol{H}}\chi\boldsymbol{K}_{q,l}||^2}{N_0} + \sum_{j \neq k} b_j L_a(b_j)\right]. \end{aligned} \tag{2.43}$$

2.5 Capacity of the STSK Scheme

In this section, we characterize the Discrete-input Continuous-output Memoryless Channel (DCMC) capacity [59] of the STSK scheme, which is defined for MIMO channels in combination with the specific multi-dimensional signaling set employed. Note that in contrast to the

DCMC capacity, Shannon's channel capacity was defined for Continuous-input Continuous-output Memoryless Channels (CCMC) [131], assuming continuous-amplitude discrete-time Gaussian-distributed transmitted signals, where only the transmit power and the bandwidth are restricted.

According to [59], the DCMC capacity of our STSK scheme using $\mathcal{L}-$PSK or $\mathcal{L}-$QAM signaling may be expressed as

$$\begin{aligned} C &= \frac{1}{T} \max_{p(\boldsymbol{K}_{1,1}),\cdots,p(\boldsymbol{K}_{Q,\mathcal{L}})} \sum_{q,l} \int_{-\infty}^{\infty} \cdots \int_{-\infty}^{\infty} p(\bar{\boldsymbol{Y}}|\boldsymbol{K}_{q,l}) p(\boldsymbol{K}_{q,l}) \\ &\cdot \log_2 \left[\frac{p(\bar{\boldsymbol{Y}}|\boldsymbol{K}_{q,l})}{\sum_{q',l'} p(\bar{\boldsymbol{Y}}|\boldsymbol{K}_{q',l'}) p(\boldsymbol{K}_{q',l'})} \right] d\bar{\boldsymbol{Y}} \quad \text{(bits/symbol)}. \end{aligned} \tag{2.44}$$

Since Eq. (2.44) is maximized under the assumption that all the signals $\boldsymbol{K}_{q,l}$ are equiprobable, when we have $p(\boldsymbol{K}_{1,1}) = \cdots = p(\boldsymbol{K}_{Q,\mathcal{L}}) = 1/(Q \cdot \mathcal{L})$, Eq. (2.44) is simplified to [59]

$$C = \frac{1}{T} \left(\log_2(Q \cdot \mathcal{L}) - \frac{1}{Q \cdot \mathcal{L}} \sum_{q,l} E \left[\log_2 \left\{ \sum_{q',l'} \exp(\Psi_{q,l}^{q',l'}) \middle| \boldsymbol{K}_{q',l'} \right\} \right] \right), \tag{2.45}$$

where we have

$$\Psi_{q,l}^{q',l'} = -||\bar{\boldsymbol{H}} \chi(\boldsymbol{K}_{q,l} - \boldsymbol{K}_{q',l'}) + \bar{\boldsymbol{V}}||^2 + ||\bar{\boldsymbol{V}}||^2. \tag{2.46}$$

It is worth mentioning that as seen in Eq. (2.45), the DCMC capacity of our STSK scheme is dependent on the specific set of dispersion matrices employed. The design criteria employed are provided in the following section.

2.6 Dispersion Matrix Design Criterion

In our STSK scheme the specific design of the dispersion matrices $\boldsymbol{A}_{q'}$ ($q' = 1, \cdots, Q$) significantly affects the achievable performance, similarly to those of LDC and DLDC schemes. More specifically, the dispersion matrices optimized for the LDC and DLDC schemes in [23] for example do not provide our STSK scheme with a high performance owing to their different system models.

For our STSK scheme, the maximization of the DCMC capacity presented in Section 2.5 may be adopted as the design criterion of the dispersion matrices $\boldsymbol{A}_{q'}$, for the sake of maximizing the achievable capacity, given the constellation size $\mathcal{L}$ as well as the STSK parameters of (M, N, T, Q). Since this criterion optimizes the dispersion-matrix set so as to directly maximize the DCMC capacity, it is suitable for the near-capacity turbo-coded STSK scheme. By contrast, we can also employ the well-known rank- and determinant-criterion [23] in order to design the dispersion-matrix set, where the rank-criterion assures

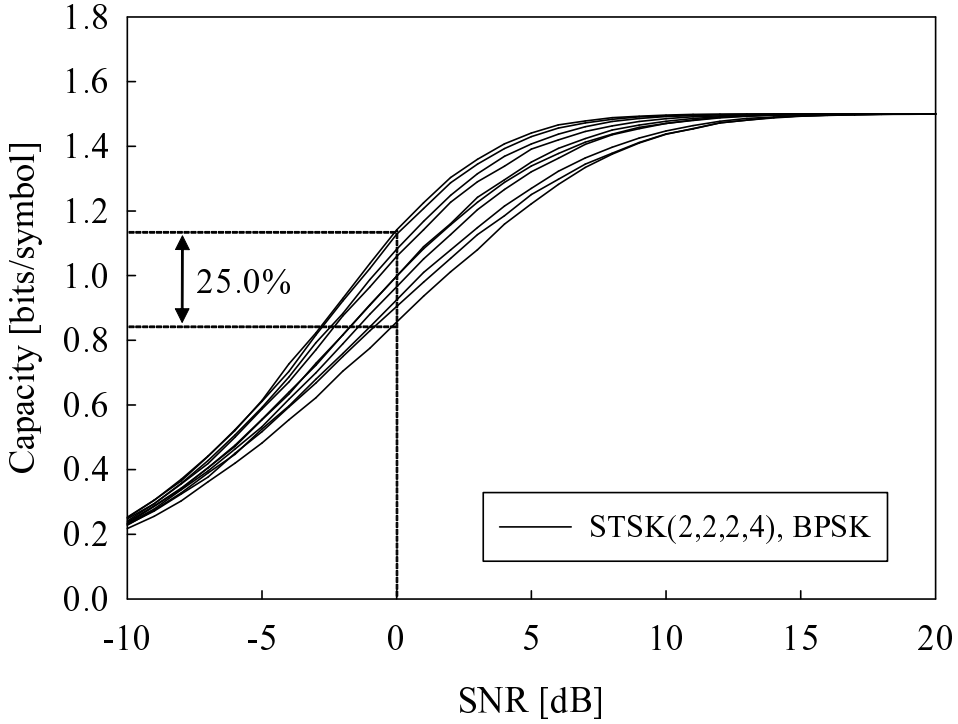

Figure 2.8: A group of DCMC capacity curves for our BPSK-modulated STSK$(2, 2, 2, 4)$ scheme of Fig. 2.5, achieving the transmission rate R of $R = 1.5$ bits/s/Hz, where each dispersion matrix set $\boldsymbol{A}_q$ $(q = 1, \cdots, Q)$ is generated randomly.

achieving maximum attainable diversity order, while the determinant-criterion provides a high space-time coding gain in the context of uncoded scenarios. Here, we show in Fig. 2.8 a group of DCMC capacity curves recorded for our BPSK-modulated STSK$(2, 2, 2, 4)$ scheme designed for achieving a transmission rate of $R = 1.5$ bits/symbol, where each dispersion matrix set $\boldsymbol{A}_{q'}$ $(q' = 1, \cdots, Q)$ was generated randomly. It can be seen in Fig. 2.8 that as expected, the achievable capacity substantially depends on the specific choice of the dispersion matrix set generated. More specifically, the capacity difference between the maximum and minimum capacity curves at the SNR point of 0 dB was as high as 25.0%. Furthermore, observe in Fig. 2.8 that the DCMC capacity curves corresponding to different dispersion matrix sets typically did not exhibit a cross-over point and they converged to the same maximum achievable transmission rate of R at high SNRs, implying that we can set a certain operational SNR point for the implementation of the exhaustive search.

In order to provide further insights, Fig. 2.9 plots the random search results of 10 000 dispersion-matrix generations, comparing the determinant and the DCMC criteria. Here, in order to guarantee achieving the maximum attainable diversity order based on the rank criterion, we omitted the results which did not exhibit full rank for any $\boldsymbol{R}$ of Eq. (2.39). Observe in Fig. 2.9 that the resultant distribution exhibited a low correlation between the determinant value and the DCMC capacity. This implies that maximizing the determinant

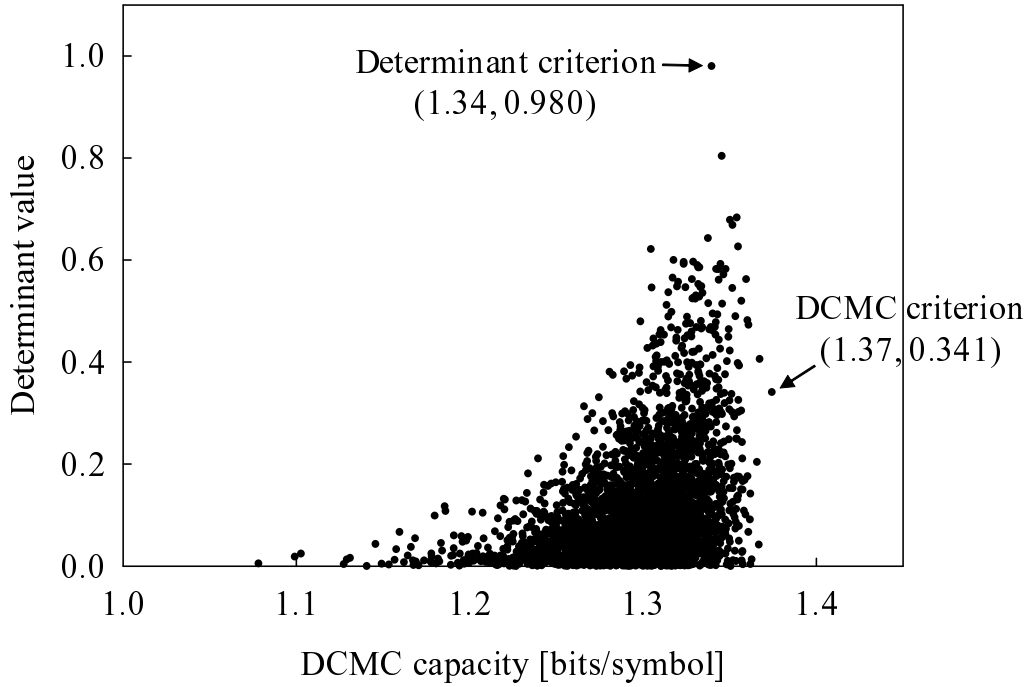

Figure 2.9: Exhaustive search results over 10 000 dispersion-matrix generations, comparing the relationships between the determinant values and the DCMC capacity for the BPSK-modulated STSK$(2, 2, 2, 4)$ scheme operated at SNR = 3 dB.

value does not maximize of the DCMC capacity.

Furthermore, in Fig. 2.10 we compared the exhaustive search based results recorded for the BPSK-modulated STSK$(2, 2, 2, Q)$ and ASTSK$(2, 2, 2, Q)$ schemes, where the parameter Q is given by $Q = 1, 2, 4, 8$ and 16. Here, we employed the determinant criterion. As seen in Fig. 2.10, there was no performance difference between the STSK and ASTSK schemes, when the number of dispersion matrices Q is low, namely $Q = 1, 2$ and 4. On the other hand, for the high-Q scenarios of $Q = 8$ and $Q = 16$, the determinant values of the ASTSK scheme were 16.3% and 81.8% lower than those of the STSK scheme, respectively. This is due to the fact that the restriction in Section 2.3.2 is imposed by the limited search space of the ASTSK's dispersion matrices and hence it becomes challenging to maintain a sufficiently high distances between the space-time codewords $\boldsymbol{S} = s_l \boldsymbol{A}_q$ $(1 \leq l \leq \mathcal{L}, 1 \leq q \leq Q)$, when the number of dispersion matrices Q is high. Finally, Fig. 2.11 shows the convergence characteristics of the exhaustive search implemented in Fig. 2.10 for the BSPK-modulated STSK$(2, 2, 2, 8)$ and ASTSK$(2, 2, 2, 8)$ schemes. Additionally, the ASTSK arrangement's exhaustive search tended to converge faster than that of the STSK scheme, owing to the ASTSK scheme's limited search space, which was confirmed by a range of other diverse simulation results.

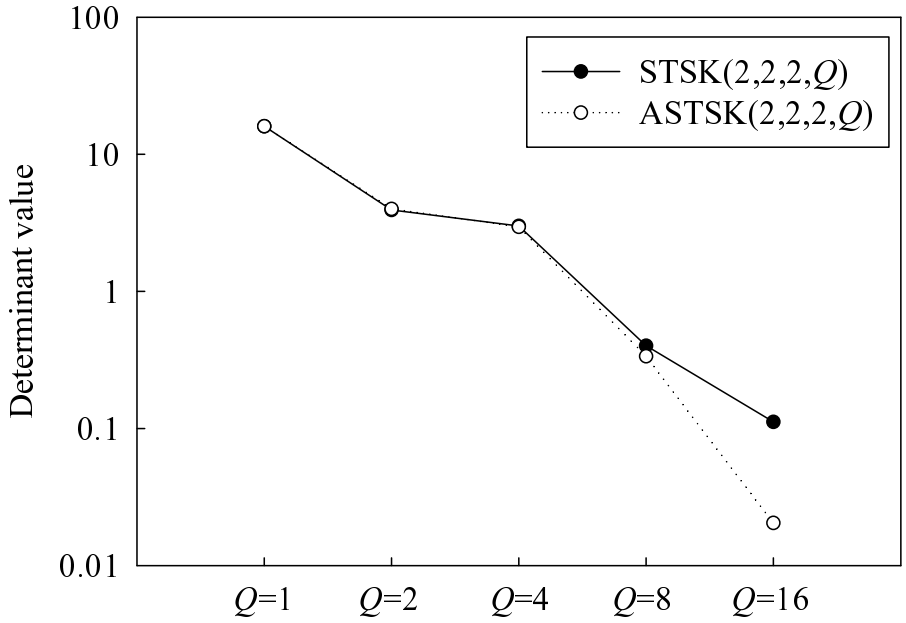

Figure 2.10: Determinant-criterion assisted exhaustive-search results over 10 000 000 dispersion-matrix generations of the BPSK-modulated STSK$(2, 2, 2, Q)$ and ASTSK$(2, 2, 2, Q)$ schemes of Fig. 2.5 for $Q = 1, 2, 4, 8$ and 16.

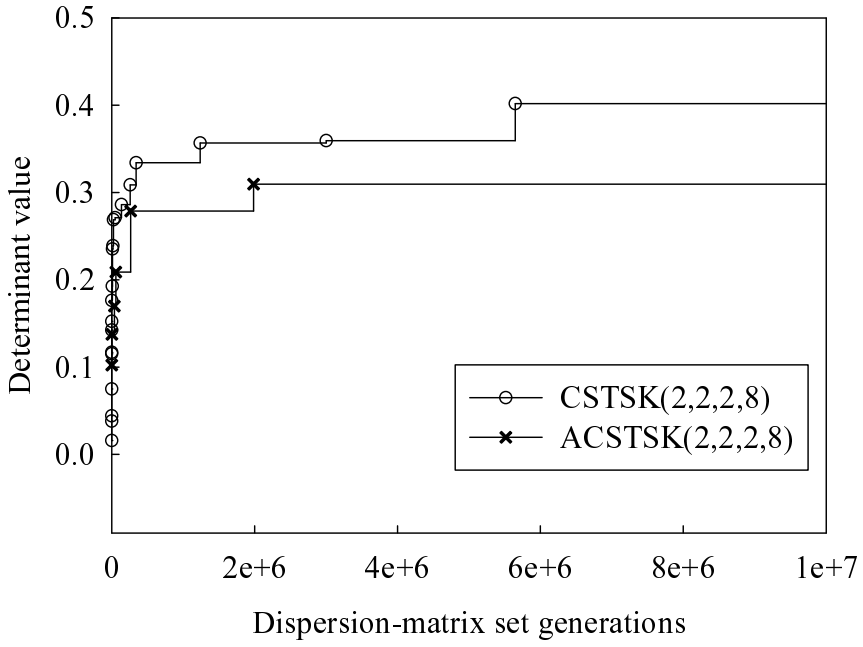

Figure 2.11: Convergence behavior of exhaustive-search results based on the determinant criterion over 10 000 000 dispersion-matrix generations of the BPSK-modulated STSK$(2, 2, 2, Q)$ and ASTSK$(2, 2, 2, Q)$ schemes of Fig. 2.5 for $Q = 1, 2, 4, 8$ and 16.

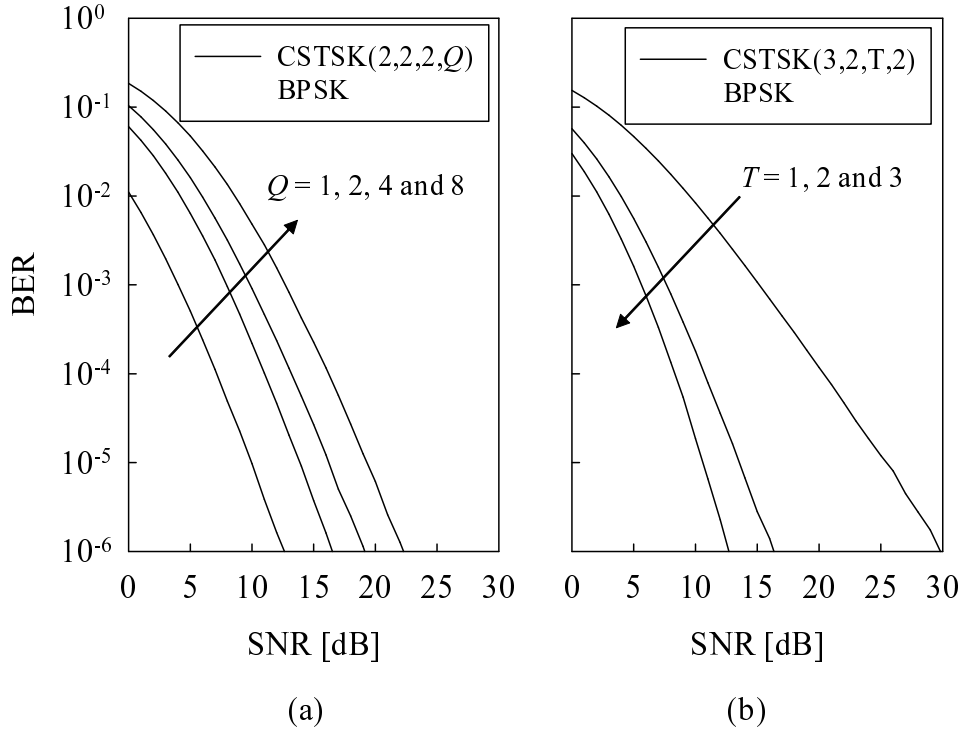

Figure 2.12: Achievable BER curves of our STSK system seen in Fig. 2.5, comparing the effects of (a) the number of dispersion matrices Q and (b) the space-time block duration T. All other system parameters were summarized in Table 2.5.

2.7 Performance Results

In this section we provide our performance results for characterizing both the uncoded and three-stage concatenated STSK schemes. Here, we assumed transmissions over Rayleigh block fading channels having a coherence time of T for our STSK scheme, which had a constant envelope over a STSK symbol, but faded independently between consecutive STSK blocks.

2.7.1 Uncoded Scenario

Figs. 2.12(a) and 2.12(b) characterize the achievable BER performance of our STSK system, comparing the effects of the number of dispersion matrices Q and of the space-time block duration T, respectively. Observe in Fig. 2.12(a) that upon increasing the value Q in our BPSK-modulated STSK$(2, 2, 2, Q)$ scheme from $Q = 1$ to $Q = 4$, the corresponding throughput increased from $R = 0.5$ bits/symbol to $R = 2.0$ bits/symbol, at the expense of a degraded BER performance, while maintaining a diversity order of four. Furthermore, it can be seen in Fig. 2.12(b) that the diversity order of our BPSK-modulated STSK$(3, 2, T, 2)$ arrangement increases upon increasing the space-time block duration T, at the cost of a throughput reduction from $R = 2.0$ bits/symbol to $R = 0.67$ bits/symbol.

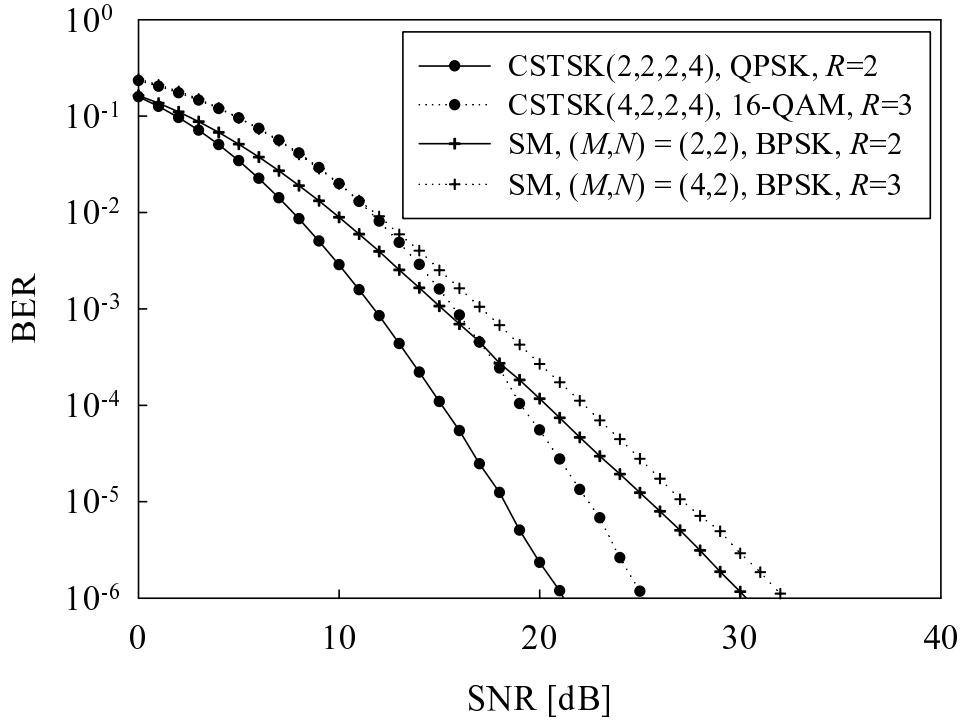

Figure 2.13: Achievable BER curves of our CSTSK scheme of Fig. 2.5 and the SM scheme of Fig. 2.1, for the cases of the employment of (M, N)=$(2, 2)$ antennas and of (M, N)=$(4, 2)$ antennas. All other system parameters were summarized in Table 2.5.

Fig. 2.13 compares the achievable BER performance of our STSK$(M, 2, 2, 4)$ scheme and that of the corresponding SM scheme, where the employment of the optimum ML detector of [63] was assumed for the SM scheme. Here, we simulated two scenarios, where the first one considered the normalized throughput of $R = 2.0$ bits/symbol and $(M, N) = (2, 2)$ AEs, while the second one assumed $R = 3.0$ bits/symbol and $(M, N) = (4, 2)$. It was found that our STSK scheme outperformed the SM scheme in both the scenarios, although the advantage of our STSK scheme over the SM scheme was reduced upon increasing the number of dispersion matrices Q. More specifically, our STSK scheme achieved a diversity order of four, as a benefit of exploiting both the achievable transmit and receive diversity gains, while the SM scheme attained only a receive diversity order of two.

Furthermore, in Fig. 2.14 we compared the diverse STSK schemes with orthogonal STBCs, having the corresponding transmission rate R as well as the same number of transmit and receive antennas (M, N), such as $(M, N) = (3, 2)$ and $(M, N) = (4, 3)$. More specifically, we considered four different STSK arrangements, which are given by the QPSK-modulated CSTSK$(3, 2, 2, 4)$, the 8-PSK modulated STSK$(3, 2, 2, 8)$, the 8-PSK modulated STSK$(4, 3, 2, 8)$ and the 16-QAM STSK$(4, 3, 2, 16)$. Here, the classic G_3 and G_4 codes [132] were employed as benchmarkers. Observe in Fig. 2.14 that each of the STSK schemes outperformed the corresponding STBC benchmarker, due to the CSTSK's capability of striking a flexible rate-diversity tradeoff. We note that each CSTSK arrangement was designed for

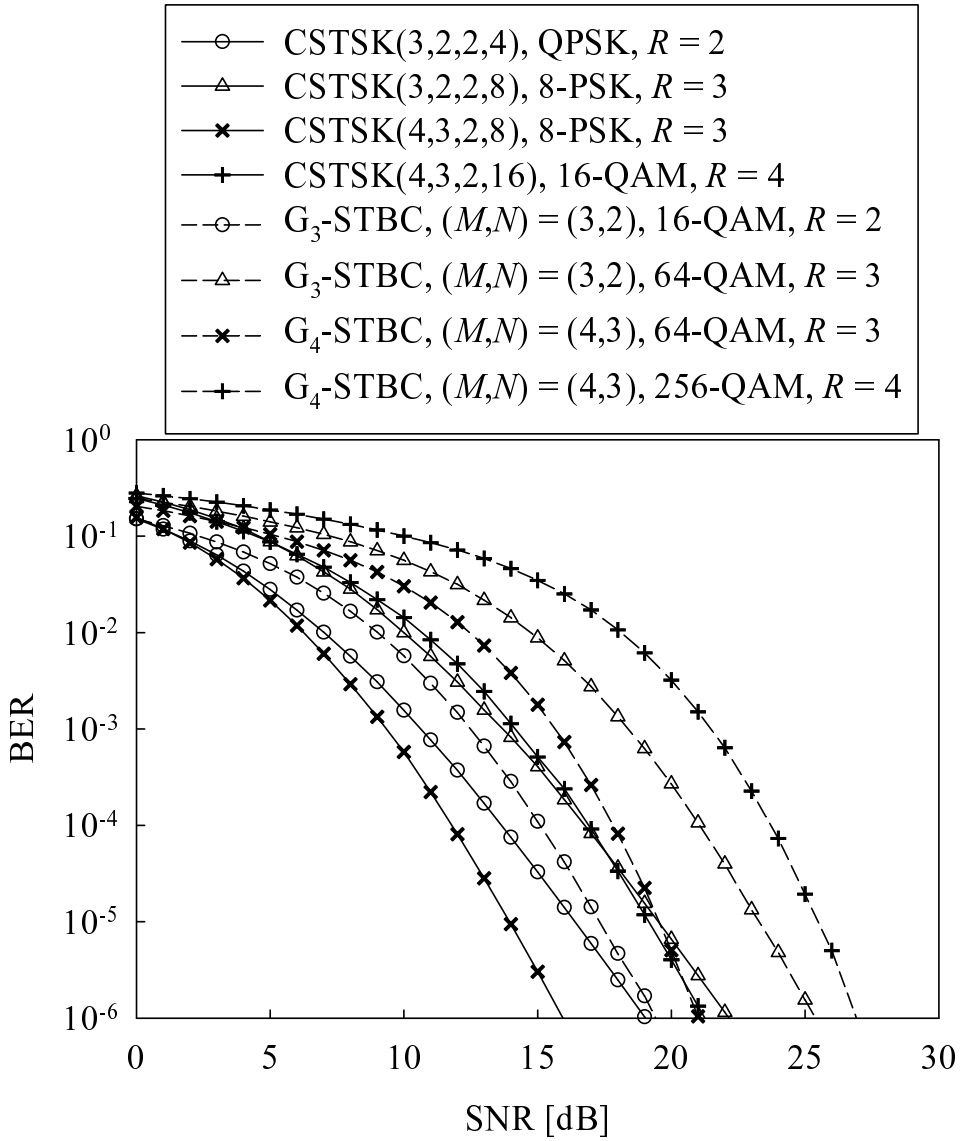

Figure 2.14: Achievable BER curves of the diverse CSTSK schemes of Fig. 2.5, compared with the orthogonal STBC schemes, having the identical transmission rate R as well as the number of transmit and the receive antennas (M, N), such as $(M, N) = (3, 2)$ and $(M, N) = (4, 3)$. Here, the classic G_3 and G_4 codes [132] were employed as the benchmarkers. All other system parameters were summarized in Table 2.5.

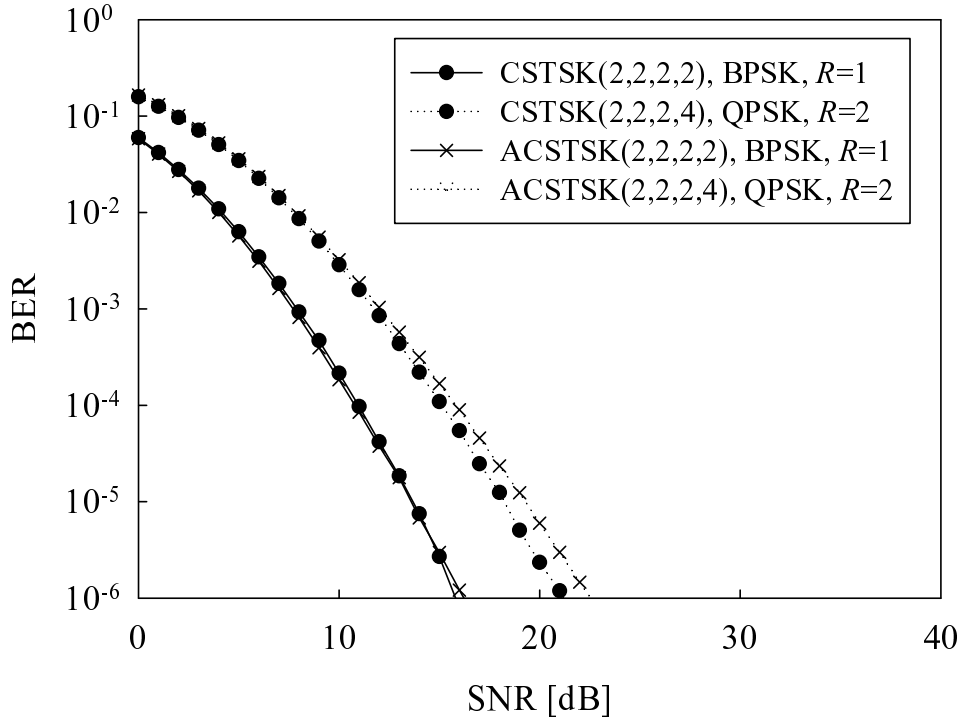

Figure 2.15: Achievable BER curves of our CSTSK$(2, 2, 2, Q)$ scheme and of our ASTSK$(2, 2, 2, Q)$ scheme seen in Fig. 2.5, while considering two scenarios, where one corresponds to $Q = 2$ dispersion matrices and BPSK modulation and the other employs $Q = 4$ dispersion matrices and QPSK modulation. All other system parameters were summarized in Table 2.5.

the relation of $M > T$, rather than for $M = T$, where we aimed for an enhanced transmission rate, at the cost of sacrificing the full diversity order.

Fig. 2.15 compares the achievable BER performance of our STSK scheme outlined in Section 2.3.1 and that of the A-STSK scheme of Section 2.3.2, while considering both the BPSK-modulated STSK$(2, 2, 2, 2)$ and QPSK-modulated STSK$(2, 2, 2, 4)$ scenarios. Observe in Fig. 2.15 that upon increasing the number of dispersion matrices Q, the BER performance of the A-STSK scheme became slightly worse than that of the STSK scheme, owing to the restricted search space of the A-STSK's dispersion matrix set. However, our exhaustive simulation results not included here owing to space limitations demonstrated that the A-STSK scheme did not exhibit any significant performance degradation over the unconstrained STSK scheme.

2.7.2 Coded Scenario

Let us now continue by characterizing the performance of the iteratively detected STSK scheme, while investigating the effects of diverse parameters on the system with the aid of EXIT charts [130, 133]. Again, the transmitter employed a half-rate RSC code having a

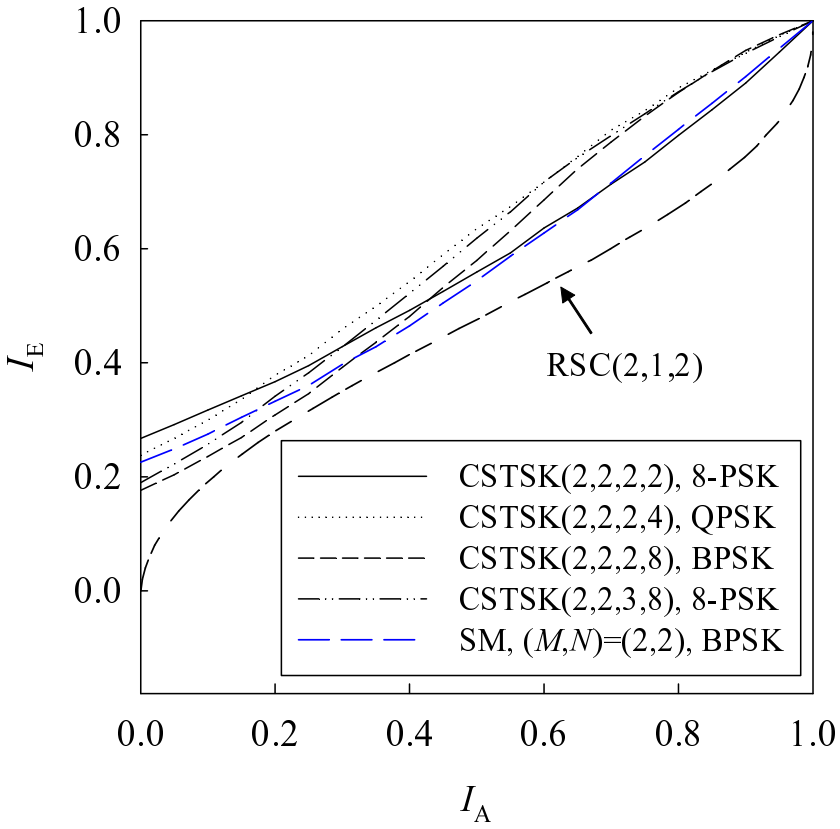

Figure 2.16: EXIT chart of our STSK$(2, 2, T, Q)$ systems obeying the architecture of Fig. 2.7, exhibiting the inner code rate of $R = 2.0$ bits/s/Hz, comparing different system parameters at SNR = -0.5 dB. The outer EXIT curve of the half-rate RSC$(2, 1, 2)$ code was also plotted. All other system parameters were summarized in Table 2.6.

constraint length of $\mathcal{K} = 2$ and octally represented generator polynomials of $(3, 2)_8$ as well as two random interleavers having lengths of $\Pi_1 = \Pi_2 = 200\,000$ bits. We also assumed that the number of inner and outer iterations was set to $I_{\text{in}} = 2$ and $I_{\text{out}} = 7$, respectively.

Fig. 2.16 shows the EXIT curves of four different PSK-modulated STSK$(2, 2, T, Q)$ systems having an uncoded throughput of 2.0 bits/symbol and an RSC-coded throughput of 1.0 bits/symbol, when considering SNR $= -5$ dB. Diverse system parameters, such as the constellation size $\mathcal{L}$, the number of dispersion matrices Q and the space-time block duration T were varied. Additionally, the EXIT curve of the identical-throughput SM scheme was also shown in Fig. 2.16. Furthermore, the EXIT curve of the RSC code employed in this paper was also plotted for reference. As seen in Fig. 2.16, all the inner-code EXIT curves reach the point of perfect convergence at $(I_A, I_E) = (1.0, 1.0)$, as a benefit of the URC code's employment. It is clear that the EXIT curve shape of our STSK scheme varied, depending on the parameters chosen. The EXIT curve of the QPSK-modulated STSK$(2, 2, 2, 4)$ system exhibited the widest open tunnel among all the curves, including that of the SM scheme.

Furthermore, Fig. 2.17 shows the EXIT chart of our QPSK-modulated STSK$(2, 2, 2, 4)$

Table 2.6: Basic system parameters of the coded STSK scheme of Fig. 2.7.

Number of transmit antennas	$M = 2$
Number of receive antennas	$N = 2$
Symbol durations per block	$T = 2$
Number of dispersion matrices	Q
Modulation	$\mathcal{L}-$PSK or $\mathcal{L}-$QAM
Channels	Frequency-flat Rayleigh fading
Channel's coherence-time	$\tau = 1$ block duration
Detector	Max-log MAP detector of Eq. (2.43)
Interleaver blocklength	200 000 bits
Outer channel code	RSC$(2, 1, 2)$
Generator polynomials	$(G_\mathrm{r}, G) = (3,2)_8$
Precoder	URC
Number of inner iterations	$I_\mathrm{in} = 1$
Number of outer iterations	$I_\mathrm{in} = 10$
System bandwidth efficiency	1 bit per channel use

system, where the SNR was gradually increased from -2 dB to 3 dB in steps of 0.5 dB. Here, we also plotted the Monte-Carlo simulation based EXIT trajectory for the case of SNR $= -0.5$ dB. It was found in Fig. 2.17 that provided the SNR was higher than -1 dB, an open EXIT tunnel was exhibited and $I_\mathrm{out} = 7$ outer iterations were necessary to converge to the $(I_\mathrm{A}, I_\mathrm{E}) = (1.0, 1.0)$ point at SNR $= -0.5$ dB. Next, the corresponding CCMC and DCMC capacity curves of our STSK scheme and the DCMC capacity curve of the SM scheme are shown in Fig. 2.18. We also plotted the maximum achievable rates for our STSK scheme, which were calculated based on our EXIT chart results. More explicitly, it was shown in [134] and detailed in [23] that the maximum achievable rate C_m may be expressed as

$$C_\mathrm{m}(\mathrm{SNR}) = R \cdot \mathcal{A}(\mathrm{SNR}), \tag{2.47}$$

where $\mathcal{A}(\mathrm{SNR})$ is the area under the inner decoder's EXIT curve corresponding to a certain SNR value. When employing a half-rate RSC code, the CCMC and DCMC capacity limits of our QPSK-modulated STSK$(2, 2, 2, 4)$ system were found to be SNR $= -3$ dB and -2.7 dB, while the maximum achievable rate was attainable at SNR $= -2.1$ dB.

Fig. 2.19 illustrates the achievable BER performance of our RSC-coded and URC-coded STSK$(2, 2, 2, 4)$ arrangement with the aid of QPSK modulation. As predicted from

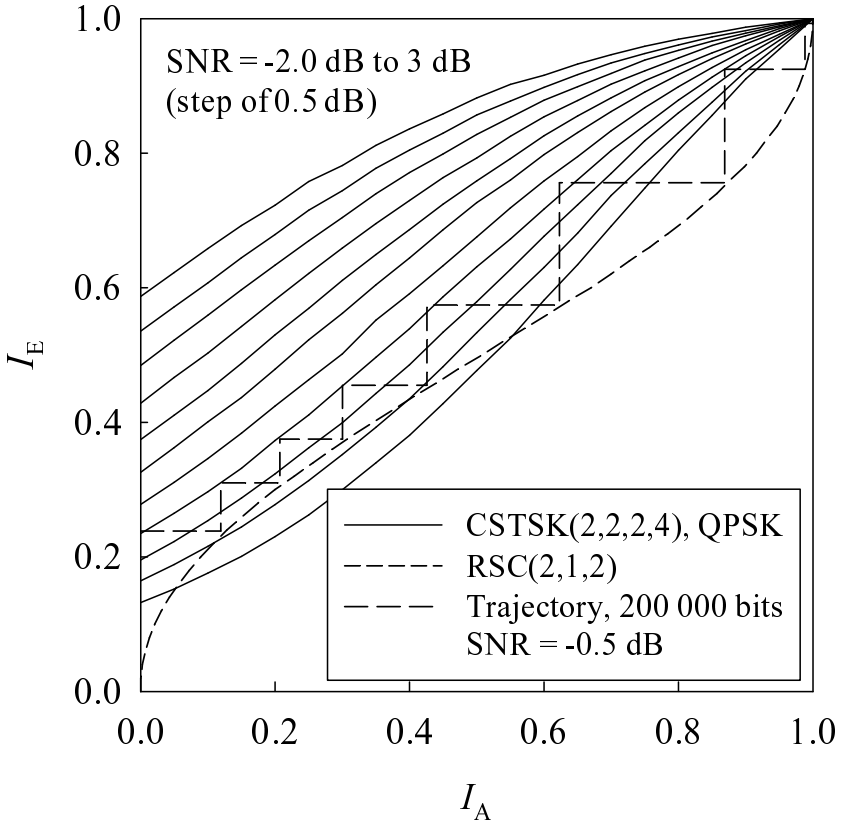

Figure 2.17: EXIT chart of our QPSK-modulated STSK$(2, 2, 2, 4)$ system obeying the architecture of Fig. 2.7. The outer EXIT curve of the half-rate RSC$(2, 1, 2)$ code was also plotted. All other system parameters were summarized in Table 2.6.

the corresponding EXIT chart of Fig 2.17, our STSK system exhibited an infinitesimally-low BER at SNR $= -0.8$ dB with the aid of $I_{\text{out}} = 10$ outer iterations, which was 1.6 dB away from the maximum achievable rate and 2.2 dB away from the DCMC capacity.

Finally, Fig. 2.20 shows the achievable BER performance of our RSC- and URC-coded CSTSK$(2, 2, 2, 4)$ and ACSTSK$(2, 2, 2, 4)$ schemes obeying the architecture of Fig. 2.7 and using QPSK modulation in conjunction with interleaver lengths of $\Pi_1 = \Pi_2 = 200\,000$ bits. We also plotted the corresponding BER curves of the RSC- and URC-coded SM scheme as well as those of the BLAST scheme as benchmarkers. The effective bandwidth efficiency of these systems was $R = 1.0$ bits/symbol. Observe in Fig. 2.20 that the CSTSK scheme exhibited the best performance, albeit this was only 0.1 dB better than that of the ACSTSK scheme. More specifically, the CSTSK and ACSTSK schemes outperformed the conventional SM and BLAST arrangements, which was an explicit benefit of their higher diversity gain. It is worth mentioning again that the ACSTSK and the SM schemes do not require symbol-level IAS, unlike the CSTSK and BLAST schemes.

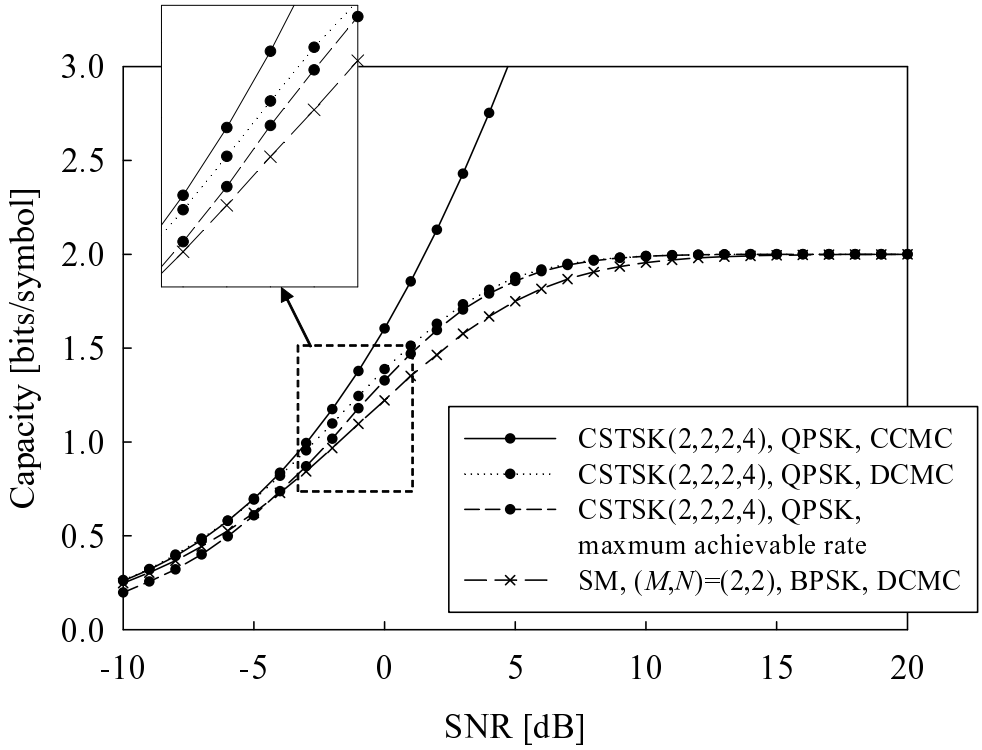

Figure 2.18: Bandwidth efficiency of our STSK$(2, 2, 2, 4)$ system obeying the architecture of Fig. 2.7 employing QPSK modulation, comparing the CCMC capacity, the DCMC capacity and the maximum achievable rate. The DCMC capacity of the BPSK-modulated SM employing $(M.N)$=$(2, 2)$ antenna elements was plotted as the benchmarker. All other system parameters were summarized in Table 2.6.

2.7.3 Interference-Limited Scenario

Although we have investigated both uncoded and coded STSK schemes in the above simulations, while focusing our attention on noise-limited scenarios, practical communication systems cannot avoid the interferences imposed by undesired MSs or BSs. For example, in a TDMA UL there may be inter-cell interference, imposed by the surrounding BSs and MSs situated in the interfering cells. A MS having a synchronization error may impose interference on the MSs and the BS in the same cell. Therefore, in this section we investigate interference-limited scenarios, where we consider an UL transmission and K interfering users, in addition to a single desired user. For the sake of simplicity, we assumed that the average Signal-to-Interference Ratio (SIR) ζ corresponding to each of the K interfering users was identical. Based on the system model of Eq. (2.1) having no interferences, the signal model corresponding to the interference-limited scenarios may be expressed as

$$\boldsymbol{Y} = \underbrace{\boldsymbol{HS}}_{\text{desired signals}} + \underbrace{\sqrt{\frac{1}{\zeta}} \sum_{k=1}^{K} \boldsymbol{H}_k \boldsymbol{S}_k}_{\text{interferences}} + \boldsymbol{V}, \tag{2.48}$$

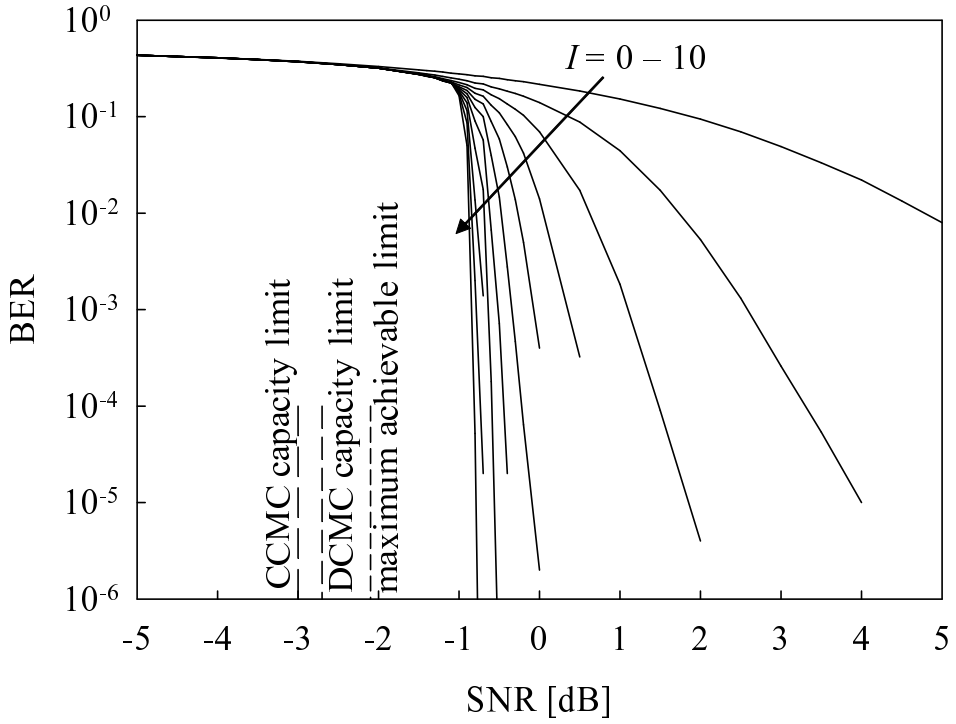

Figure 2.19: Achievable BER performance of our RSC-coded and URC-coded CSTSK$(2, 2, 2, 4)$ scheme obeying the architecture of Fig. 2.7 with the aid of QPSK modulation, using interleaver lengths of $\Pi_1 = \Pi_2 = 200\,000$ bits. All other system parameters were summarized in Table 2.6. The dashed-lines indicate the lowest possible SNRs, at which an infinitesimally low BER may be attained at the effective throughput of 1.0 bits/symbol, calculated from CCMC capacity, DCMC capacity and the maximum achievable rate.

where the first term represents the desired signal block, while the second term denotes the interference imposed by the K undesired users. Furthermore, $\boldsymbol{H}_k$ represents the MIMO channel envelopes between the kth user and the BS, obeying the same distributions as those of $\boldsymbol{H}$, while $\boldsymbol{S}_k$ represents the kth interfering user's STSK-modulated signals, similarly to that of the desired user $\boldsymbol{S}$.

Firstly, Fig. 2.21 shows the EXIT chart of the QPSK-modulated STSK$(2, 2, 2, 4)$ system at SNR = 2 dB, where the number of interfering users K was varied from $K = 0$ to $K = 7$, while maintaining an SIR per user of $\zeta = 5$ dB. Note that in this simulated scenario, the total interference power increased with the number of interfering users K. It can be seen from Fig. 2.21 that upon increasing the number of interfering users K, the inner EXIT curve was shifted further down and finally the EXIT tunnel became closed for the case of $K = 6$. In order to provide further insights, Fig. 2.22 shows the effects of the SIR ζ on the inner decoder's EXIT curves, where the number of interfering users K was set to $K = 5$, while the SIR per user was given by $\zeta = 20, 10, 7, 5, 4$ and 3 dB. As expected, the reduction of the SIR value ζ was found to severely degrade the achievable performance.

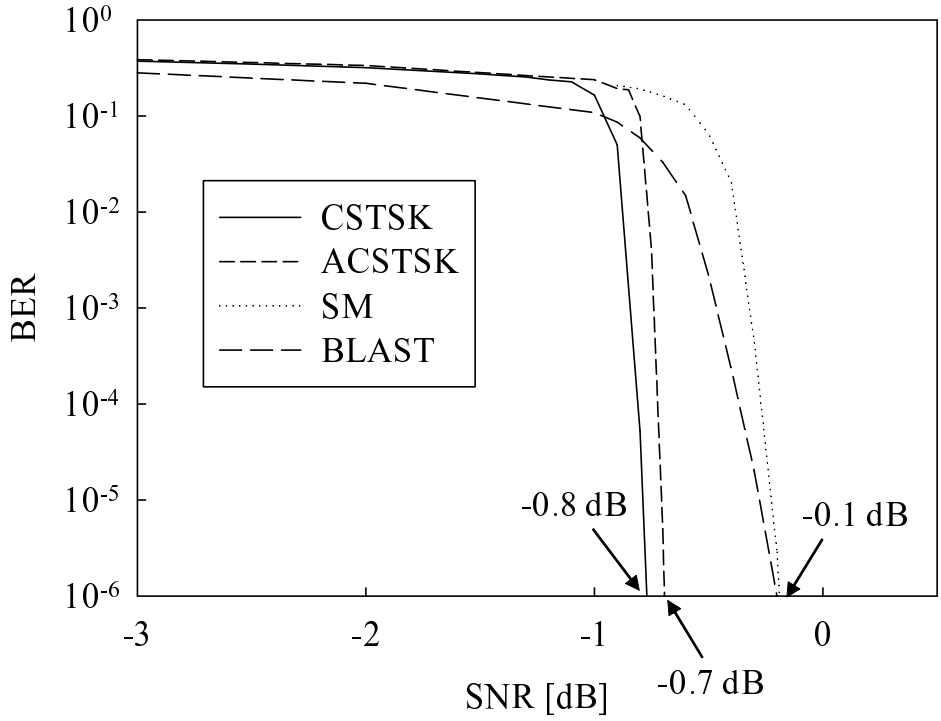

Figure 2.20: Achievable BER performance of our RSC-coded and URC-coded CSTSK$(2, 2, 2, 4)$ and ACSTSK$(2, 2, 2, 4)$ schemes obeying the architecture of Fig. 2.7 with the aid of QPSK modulation, using interleaver lengths of $\Pi_1 = \Pi_2 = 200\,000$ bits. All other system parameters were summarized in Table 2.6. We also plotted the corresponding BER curves of the RSC-coded and URC-coded SM scheme and BLAST scheme as benchmarkers. The effective bandwidth efficiency of these systems was given by $R = 1.0$ bits/symbol.

Lastly, in Figs. 2.23 and 2.24 we demonstrated the achievable BER performance in the interference-limited scenarios, which correspond to the EXIT charts of Figs. 2.21 and 2.22, respectively. Here, we assumed that the number of inner and outer iterations $(I_{\text{in}}, I_{\text{out}})$ was set to $(10, 2)$. As predicted from the EXIT chart analysis of Fig. 2.21, it was found in Fig. 2.23 that the BER cliff shifted towards higher SNRs, upon increasing the number of interfering users K. Nevertheless, our STSK system was capable of benefiting from the iterative gains, regardless of the value K. Moreover, it was also confirmed in Fig. 2.24 that the reduction of the SIR value ζ degraded the achievable BER performance and hence a BER floor was exhibited at $\zeta = 3$ dB.

2.8 Chapter Summary and Conclusions

In Section 2.2, we first reviewed the conventional coherently-detected MIMO arrangements, such as the OSTBC, the BLAST and the LDC schemes, while introducing the recently-proposed SM/SSK schemes. In Section 2.3, we have proposed a novel modulation principle,

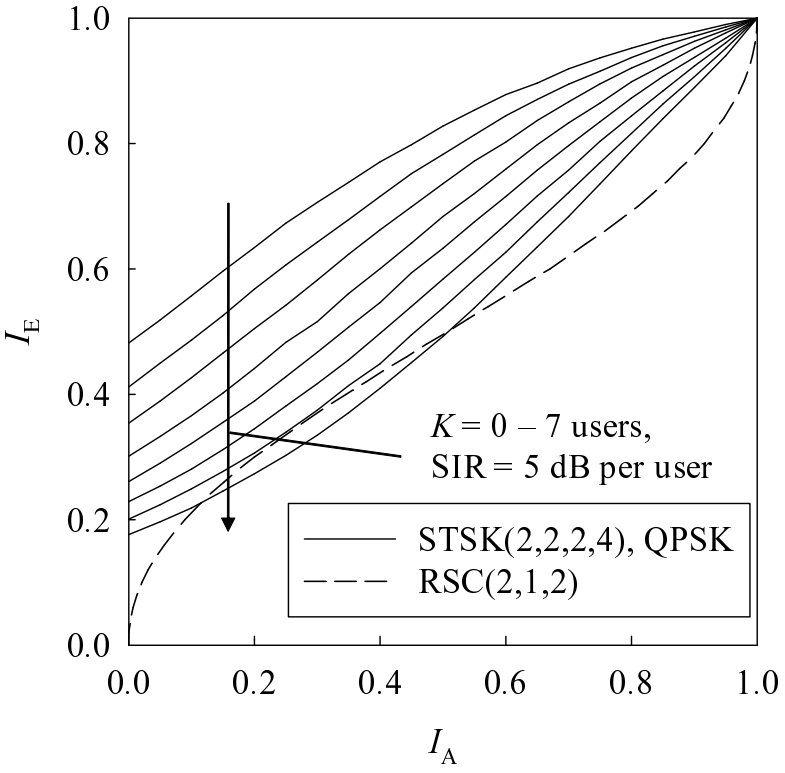

Figure 2.21: EXIT chart of our QPSK-modulated STSK$(2, 2, 2, 4)$ system obeying the architecture of Fig. 2.7 at SNR = 2 dB, where the number of interfering users K was varied from $K = 0$ to $K = 7$, while maintaining an SIR per user of $\zeta = 5$ dB. The outer EXIT curve of the half-rate RSC$(2, 1, 2)$ code was also plotted. All other system parameters were summarized in Table 2.6.

namely the CSTSK scheme, which is based on the concept of dispersion-matrix activation. The idea enables us to strike the required tradeoff between the MIMO's diversity and multiplexing gains, while maintaining a low decoding complexity owing to the resultant ICI-free system model obtained. It was also demonstrated in Section 2.3.1 that the proposed CSTSK schemes may be viewed as the family of unified shift keying arrangements, including the recently-proposed SM and SSK schemes as their special cases. Additionally, in Section 2.3.2 we presented the modified CSTSK scheme, i.e. the ACSTSK scheme, which enables us to avoid the symbol-level IAS conventionally required between the RF branches associated with the transmit AEs. Then, the optimal ML detector designed for the uncoded CSTSK scheme was derived in Section 2.3.3, followed by the characterization of the associated computational complexity imposed by the CSTSK detector in Section 2.3.4. The maximum achievable diversity order of our CSTSK scheme was derived in Section 2.3.5.

Moreover, in Section 2.4 the proposed CSTSK scheme was incorporated in a three-stage serially concatenated arrangement for the sake of achieving a near-capacity performance, where we also derived the soft CSTSK demapper in Section 2.4.2. In Section 2.5, we quantified the capacity of the proposed CSTSK scheme, which was also utilized to optimize dispersion-

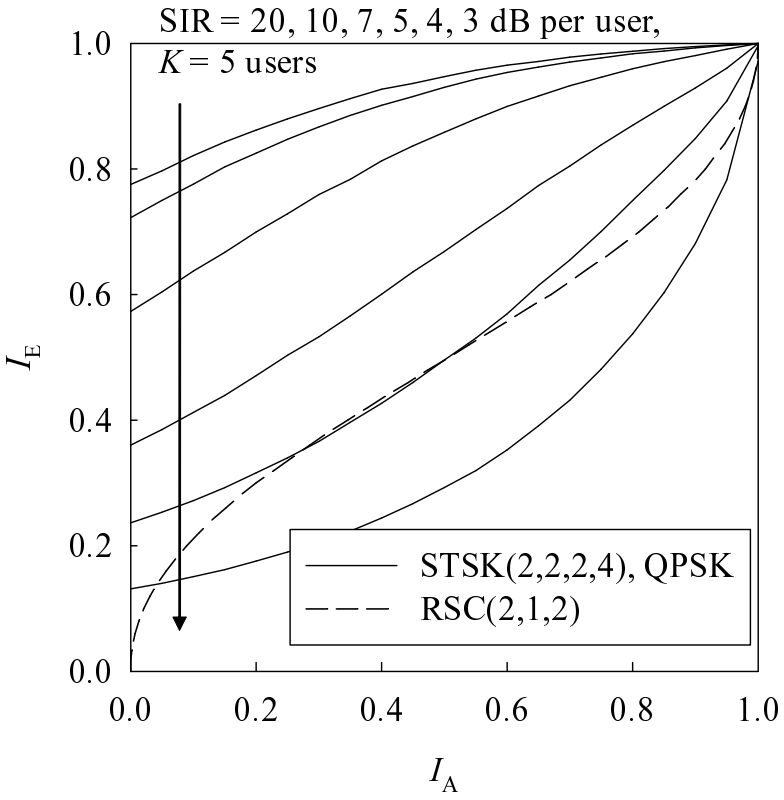

Figure 2.22: EXIT chart of our QPSK-modulated STSK$(2, 2, 2, 4)$ system obeying the architecture of Fig. 2.7 at SNR = 5 dB, where the number of interfering users K was set to $K = 5$, while the SIR per user was given by $\zeta = 20, 10, 7, 5, 4$ and 3 dB. The outer EXIT curve of the half-rate RSC$(2, 1, 2)$ code was also plotted. All other system parameters were summarized in Table 2.6.

matrix set. Furthermore, the design criteria used for generating our dispersion-matrix set employed for our CSTSK scheme were presented and their characteristics were compared in Section 2.6.

The performance of our CSTSK scheme was characterized in Section 2.7, where the uncoded CSTSK and ACSTSK schemes were considered in Section 2.7.1. The coded CSTSK scheme was characterized with the aid of EXIT chart analysis in Section 2.7.2. Then, we quantified the achievable performance of our CSTSK scheme in simplified interference-limited scenarios, while taking into account the effects of interferences imposed by the undesired users.

This chapter focused on the family of coherently-detected co-located MIMO arrangements, assuming that perfect CSI is available at the receiver. However, it is challenging to acquire accurate CSI for high-speed vehicles, without imposing an excessive complexity or substantial pilot overhead. As an attractive design alternative, in the following chapter, we consider the design of differentially-encoded MIMO arrangements, which facilitates non-coherent detection at the receiver.

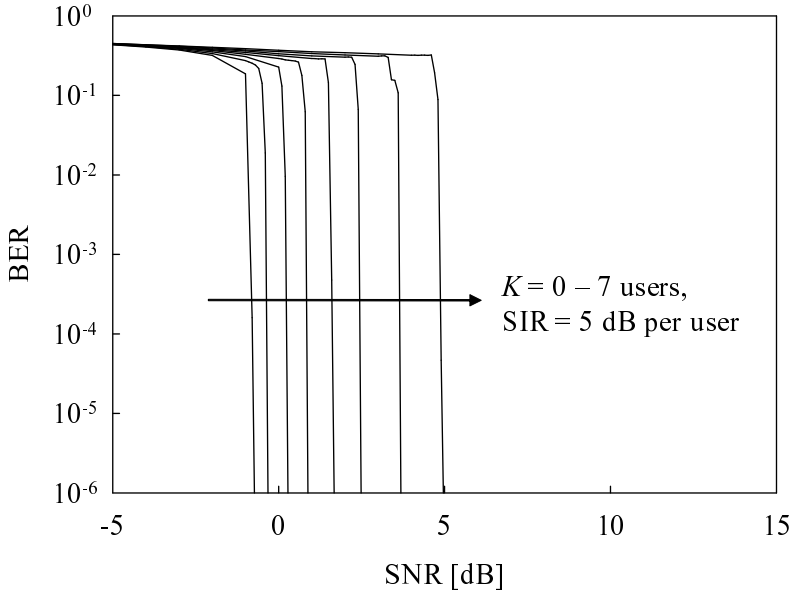

Figure 2.23: Achievable BER performance of our QPSK-modulated STSK$(2, 2, 2, 4)$ system obeying the architecture of Fig. 2.7 employing the number of inner and outer iterations (I_{in}, I_{out}) of $(10, 2)$, where the number of interfering users K was varied from $K = 0$ to $K = 10$, while maintaining the SIR per user at $\zeta = 5$ dB. All other system parameters were summarized in Table 2.6.

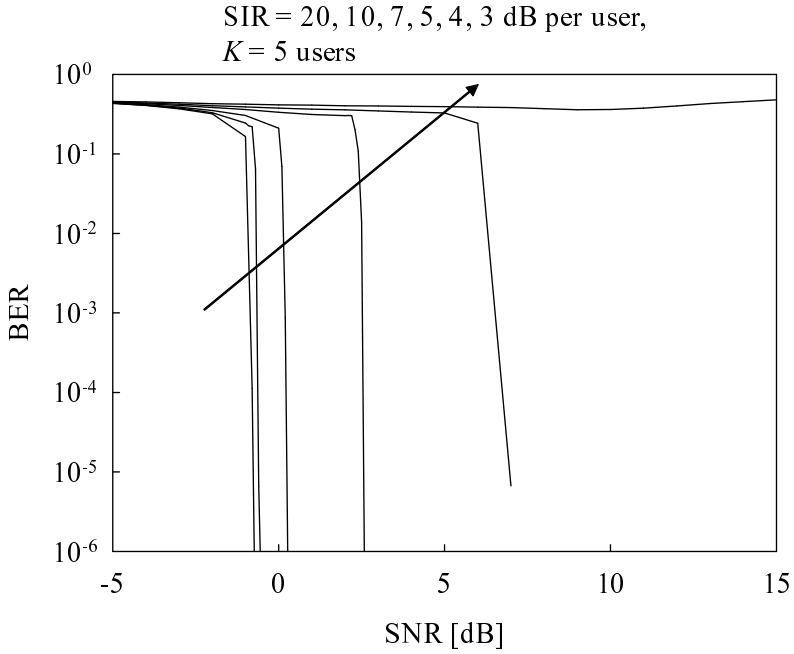

Figure 2.24: Achievable BER performance of our QPSK-modulated STSK$(2, 2, 2, 4)$ system obeying the architecture of Fig. 2.7 employing the number of inner and outer iterations (I_{in}, I_{out}) of $(10, 2)$, where the number of interfering users K was set to $K = 5$, while the SIR per user was given by $\zeta = 20, 10, 7, 5, 4$ and 3 dB. All other system parameters were summarized in Table 2.6.

Chapter 3

Differential Space-Time Shift Keying for Co-Located MIMO Systems

3.1 Introduction

In Chapter 2, we investigated coherently-detected digital transmissions designed for co-located MIMO systems, assuming that perfect CSI is available at the receiver. In this context, we proposed the novel STSK concept, which facilitates a flexible and efficient MIMO implementation, while subsuming diverse classic MIMO arrangements. In reality, when the channel changes slowly in comparison to the symbol duration employed, the receiver can accurately estimate the CSI, based on the pilot symbols inserted in the transmitted signals. On the other hand, it is a challenging task to acquire accurate CSI for each MIMO-link for high-speed vehicles, which may require a high pilot overhead and imposes a substantial complexity. Furthermore, the resultant CSI estimation error is expected to erode the achievable performance. Hence, it is beneficial to employ a MIMO arrangements, which do not require channel estimates either at the transmitter or at the receiver.

Differential encoding schemes designed for the single-antenna-aided systems, such as $\mathcal{L}$-point Differential Phase Shift Keying ($\mathcal{L}$-DPSK), have been widely adopted in order to dispense with potentially complex channel estimation at the receiver. The key concept of differential encoding is to utilize the previous symbol as a phase reference for the current symbol, hence requiring no coherent phase reference at the receiver. To be more specific, the $\mathcal{L}$-DPSK transmitter generates the symbols $s(i)$ by differentially encoding $\mathcal{L}$-PSK symbols $x(i) = \{e^{2\pi jl/\mathcal{L}}; l = 0, 1, \cdots, \mathcal{L}-1\}$ as follows:

$$s(i) = s(i-1)x(i), \tag{3.1}$$

where the initial symbol $s(0)$ is used as a reference for the next one and hence it does not include any information. Here, let us assume that the received signal obeys the form of $y(i) = hs(i) + v(i)$, where h represents the complex-valued channel envelope that does not change for at least two symbol durations and $v(i)$ denotes the corresponding noise component. Since the two successive received symbols are related as

$$\begin{aligned} y(i) &= hs(i) + v(i) && (3.2)\\ &= hs(i-1)x(i) + v(i) && (3.3)\\ &= y(i-1)x(i) \underbrace{-v(i-1)x(i) + v(i)}_{v'(i)}, && (3.4) \end{aligned}$$

the Maximum Likelihood (ML) detector may be formulated as

$$\hat{x}(i) = \arg \max_{x_l \in \mathcal{L}-\text{PSK}} |y(i) - y(i-1)x_l|^2, \quad (3.5)$$

which does not require any CSI for the detection and does not depend on the earlier detection results. Here, we note that since the variance of the equivalent noise component $v'(i)$ is twice that of the actual noise component $v(i)$, DPSK suffers from a 3 dB performance loss compared to the coherently-detected PSK scheme.

Motivated by the single-antenna-based differential-encoding concept, diverse Differential STCs (DSTCs) [40, 42, 135, 136] have been developed, in order to create non-coherent MIMO systems capable of achieving a high diversity gain. In this chapter, as the extension of the coherently-detected STSK scheme proposed in Chapter 2, we introduce a novel Differentially-encoded STSK (DSTSK) arrangement, which does not require any CSI estimation at the receiver. More specifically, the proposed DSTSK scheme employs the Cayley unitary transform based technique of [89], in order to generate unitary space-time codewords, which enables us to implement differential encoding. Hence the DSTSK scheme retains the fundamental benefits of the coherent STSK scheme, although naturally, the corresponding non-coherent receiver suffers from the usual performance loss compared to its coherent counterpart.

Against this background, the novelty and rationale of this chapter can be summarized as follows.

- Inspired by the coherent STSK scheme of Chapter 2, the new concept of DSTSK is proposed as a unified differential MIMO scheme, which is capable of striking a flexible diversity-versus-multiplexing gains tradeoff. Similarly to coherent STSK, we have an ICI-free system model, hence our DSTSK receiver is capable of using low-complexity the single-stream-based optimal ML detection in uncoded scenarios.

- The proposed DSTSK scheme is then further developed to ensure that no symbol-level IAS is required between the transmit antenna elements, hence substantially reducing the implementational complexity in comparison to the family of classic DSTC schemes.

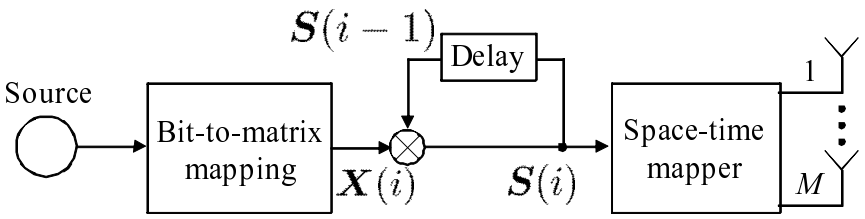

Figure 3.1: A differential unitary space-time encoder.

- Additionally, the DSTSK scheme is incorporated in a serially-concatenated three-stage turbo-coding arrangement, in order to achieve a near-capacity BER performance, while qualifying the maximum achievable rate of our turbo-coded DSTSK scheme.

The rest of this chapter is organized as follows. In Section 3.2, we review the diverse family of classic differentially-encoded MIMO schemes and in Section 3.3 outline our DSTSK concept in the context of uncoded scenarios, while characterizing the computational complexity imposed. Section 3.4 considers our DSTSK scheme employing the three-stage serially-concatenated turbo-coding principle. Our performance results are discussed in Section 3.5, and finally this chapter is concluded in Section 3.6.

3.2 Review of the Classic Differential MIMO Systems

This section will review the family of classic DSTCs, which were developed as the extensions of the coherently-detected STCs reviewed in Section 2.2. The typical encoding principle of the DSTCs is depicted in Fig. 3.1, where the information bits are first mapped to the $(M \times T)$-element unitary matrix $\boldsymbol{X}(i)$. Then, motivated by the above-mentioned DPSK scheme, the differential encoding operation of the $(M \times T)$-element space-time codewords $\boldsymbol{S}(i)$ is given by

$$\boldsymbol{S}(i) = \boldsymbol{S}(i-1)\boldsymbol{X}(i), \tag{3.6}$$

where the initial matrix $\boldsymbol{S}(0)$ is typically represented by the $(M \times M)$-element identity matrix $\boldsymbol{I}$. Furthermore, the number of symbol durations T has to be equal to the number of transmit antennas M, in order to implement the differential space-time encoding operation of Eq. (3.6). We also note that Eq. (3.6) requires the matrix $\boldsymbol{X}(i)$ to be a unitary matrix and, additionally, to satisfy the relation of $||\boldsymbol{X}(i)||^2 = T$. Otherwise, when the space-time block index i increases, the total power of the transmitted signals per block $||\boldsymbol{S}(i)||^2 = ||\boldsymbol{X}(i) \cdot \boldsymbol{X}(i-1) \cdots \boldsymbol{X}(1) \cdot \boldsymbol{S}(0)||^2$ tends to zero or to infinity.

According to the block-based system model of Eq. (1.1), the received signals $\boldsymbol{Y}(i)$ may

be expressed as

$$\begin{aligned} \boldsymbol{Y}(i) &= \boldsymbol{H}\boldsymbol{S}(i) + \boldsymbol{V}(i) && (3.7)\\ &= \boldsymbol{H}\boldsymbol{S}(i-1)\boldsymbol{X}(i) + \boldsymbol{V}(i) && (3.8)\\ &= \boldsymbol{Y}(i-1)\boldsymbol{X}(i) \underbrace{-\boldsymbol{V}(i-1)\boldsymbol{X}(i) + \boldsymbol{V}(i)}_{\boldsymbol{V}'(i)}, && (3.9) \end{aligned}$$

assuming that the elements of the channel matrix $\boldsymbol{H}$ remain constant over the two consecutive space-time block durations, that is to say, $2T$ symbol durations. Furthermore, recalling that the matrix $\boldsymbol{X}(i)$ is unitary, the equivalent noise components $\boldsymbol{V}'(i) = -\boldsymbol{V}(i-1)\boldsymbol{X}(i) + \boldsymbol{V}(i)$ in Eq. (3.9) obey the complex-valued Gaussian distributions of $\mathcal{CN}(0, 2N_0\boldsymbol{I})$ and hence the associated ML detector may be represented by

$$\hat{\boldsymbol{X}}(i) = \arg \max_{\boldsymbol{X} \in F} ||\boldsymbol{Y}(i) - \boldsymbol{Y}(i-1)\boldsymbol{X}||^2, \tag{3.10}$$

where F represents the legitimate signal space of the codewords$\boldsymbol{X}$ employed. Since the equivalent noise variance is doubled, the DSTCs also suffer from a 3 dB performance penalty in comparison to their coherently-detected counterpart, similarly to the classic DPSK scheme.

In what follows, depending on the specific design criterion of the signal space, DSTCs are classified into several categories, such as Differential OSTBCs (DOSTBCs) and DLDCs.

3.2.1 Differential Orthogonal Space-Time Block Code

Here, we review the class of DOSTBC schemes, which were developed as the differentially encoded counterparts of the coherently detected OSTBCs [20, 33]. As described in Section 2.2.1, the space-time block of the coherent Alamouti scheme, which may also be viewed as the $M = 2$ OSTBC scheme, is given by [20]

$$\begin{bmatrix} s_1/\sqrt{2} & s_2/\sqrt{2} \\ -s_2^*/\sqrt{2} & s_1^*/\sqrt{2} \end{bmatrix}, \tag{3.11}$$

where s_1 and s_2 are the independent $\mathcal{L}$-PSK symbols. In the DOSTBC scheme of Fig. 3.1 employing $M = 2$ transmit antennas, the matrix of Eq. (3.11) is directly applied to $\boldsymbol{X}(i)$ in Eq. (3.6), noting that the matrix $\boldsymbol{X}(i)$ herein satisfies the unitary condition. Therefore, according to the differential encoding rule of Eq. (3.6), the signals transmitted at symbol intervals $(2i + 2)$ and $(2i + 1)$ are represented as the linear combination of those at symbol intervals $2i$ and $(2i - 1)$.

At the receiver, the exhaustive ML search obeying the objective function of Eq. (3.10) may be employed, in order to detect the differentially-encoded space-time signals. Alternatively, the DOSTBC's receiver is also capable of implementing the low-complexity single-stream-based ML detection algorithm, while achieving the same optimal performance as that

of the exhaustive ML detector of Eq. (3.10). More specifically, let us consider the single-receive-antenna case of $N = 1$. Then the received signals $\boldsymbol{Y}(i) = [y_1(i)\ y_2(i)]$ of Eq. (3.9) may be rearranged as

$$\boldsymbol{Y}'(i) = \begin{bmatrix} y_1(i) \\ y_2^*(i) \end{bmatrix} \tag{3.12}$$

$$= \begin{bmatrix} y_1(i-1) & -y_2(i-1) \\ y_2^*(i-1) & y_1^*(i-1) \end{bmatrix} \begin{bmatrix} s_1(i) \\ s_2^*(i) \end{bmatrix} + \begin{bmatrix} v_1'(i) \\ v_2'^*(i) \end{bmatrix}. \tag{3.13}$$

Then, we arrive at the estimates $[\hat{s}_1(i)\ \hat{s}_2^*(i)]^{\mathrm{T}}$ as follows:

$$\begin{bmatrix} \hat{s}_1(i) \\ \hat{s}_2^*(i) \end{bmatrix} = \begin{bmatrix} y_1^*(i-1) & y_2(i-1) \\ -y_2^*(i-1) & y_1(i-1) \end{bmatrix} \begin{bmatrix} y_1(i) \\ y_2^*(i) \end{bmatrix} \tag{3.14}$$

$$= \underbrace{\begin{bmatrix} y_1^*(i-1) & y_2(i-1) \\ -y_2^*(i-1) & y_1(i-1) \end{bmatrix} \begin{bmatrix} y_1(i-1) & -y_2(i-1) \\ y_2^*(i-1) & y_1^*(i-1) \end{bmatrix}}_{||\boldsymbol{Y}(i-1)||^2 \boldsymbol{I}} \begin{bmatrix} s_1(i) \\ s_2^*(i) \end{bmatrix}$$

$$+ \begin{bmatrix} y_1^*(i-1) & y_2(i-1) \\ -y_2^*(i-1) & y_1(i-1) \end{bmatrix} \begin{bmatrix} v_1'(i) \\ v_2'^*(i) \end{bmatrix}, \tag{3.15}$$

where we have the relation of

$$\begin{aligned} ||\boldsymbol{Y}(i-1)||^2 &= [\boldsymbol{H}\boldsymbol{S}(i-1) + \boldsymbol{V}(i-1)]^{\mathrm{T}} [\boldsymbol{H}\boldsymbol{S}(i-1) + \boldsymbol{V}(i-1)]^* \\ &= \underbrace{\boldsymbol{S}^{\mathrm{T}}(i-1)\boldsymbol{H}^{\mathrm{T}}\boldsymbol{H}^*\boldsymbol{S}^*(i-1)}_{=|h_1|^2+|h_2|^2} \\ &+ \underbrace{\boldsymbol{V}^{\mathrm{T}}(i-1)\boldsymbol{H}^*\boldsymbol{S}^*(i-1) + \boldsymbol{S}^{\mathrm{T}}(i-1)\boldsymbol{H}^{\mathrm{T}}\boldsymbol{V}^*(i-1) + \boldsymbol{V}^{\mathrm{T}}(i-1)\boldsymbol{V}^*(i-1)}_{\text{noise components}}. \end{aligned}$$

Therefore, it can be seen from Eq. (3.15) that since the detected symbols are multiplied by the coefficients $(|h_1|^2 + |h_2|^2)$, even when one of the channel components is severely faded, the other component contributes to the reliable detection and hence we can exploit the full-diversity order of two. Furthermore, when multiple antenna elements are employed at the receiver ($N \geq 2$), the MRC can be used jointly for all $M \cdot N$ diversity components, without any loss of optimality [40]. Hence a diversity order of $M \cdot N$ may be achieved. Additionally, while the above-mentioned example considered $M = 2$ transmit antennas and PSK modulation, this scheme was extended to more transmit antennas, such as $M = 3$ and $M = 4$ [135] as well as to QAM constellations [137].

3.2.2 Differential Linear Dispersion Code

In [89], Hassibi and Hochwald proposed the differentially-encoded counterpart of the coherent LDC scheme of [88], namely the Differential LDC (DLDC) scheme, where the Cayley transform is employed in order to construct a set of unitary matrices $\boldsymbol{X}$, while achieving the basic benefits of LDCs mentioned in Section 2.2.3. More specifically, in coherent LDCs

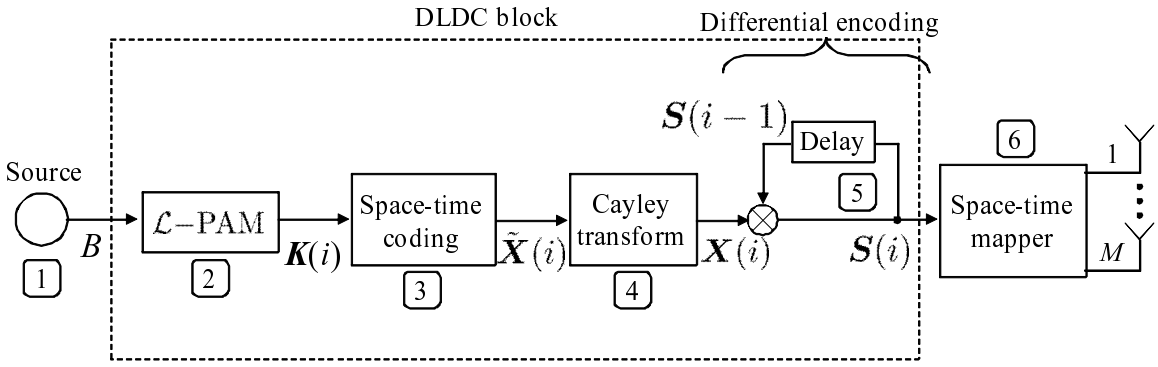

Figure 3.2: Schematic of a DLDC transmitter employing M transmit antennas and the Cayley transform, which was developed from the LDC scheme by taking into account the general DSTC architecture of Fig. 3.1.

$\mathcal{L}$-PSK/QAM symbols are dispersed into the spatial and temporal dimensions with the aid of the linear combination of Q dispersion matrices, which is represented by Eq. (2.7). Moreover, the linear combination of the Q dispersion matrices does not necessarily exhibit a unitary structure, hence it cannot be directly applied to the differential space-time encoding procedure described by Eq. (3.9) Instead, in the DLDC scheme's dispersion matrix is firstly decomposed into two dimensions as detailed below and then it is further processed, in order to generate a unitary space-time matrix with the aid of the Cayley unitary transform [89].

To elaborate a little further, the DLDC's encoding principle is summarized as follows. Similarly to LDCs, the information bits are firstly mapped to Q number of $(\log_2 \mathcal{L})$-bit real-valued symbols $\boldsymbol{K}(i) = [s_1(i), s_2(i), \cdots, s_Q(i)]^{\mathrm{T}}$ of an $\mathcal{L}$-point modulated constellation. Then the real-valued symbols $\boldsymbol{K}(i)$ are mapped to the space-time matrix $\tilde{\boldsymbol{X}}(i) \in \mathcal{C}^{M \times T}$ with the aid of Q dispersion matrices $\boldsymbol{A}_q$ $(q = 1, \cdots, Q)$ as follows:

$$\underbrace{\begin{bmatrix} t_{11} & \cdots & t_{1T} \\ \vdots & \ddots & \vdots \\ t_{M1} & \cdots & t_{MT} \end{bmatrix}}_{\tilde{\boldsymbol{X}}(i)} = s_1(i) \underbrace{\begin{bmatrix} a_{11}^{(1)} & \cdots & a_{1T}^{(1)} \\ \vdots & \ddots & \vdots \\ a_{M1}^{(1)} & \cdots & a_{MT}^{(1)} \end{bmatrix}}_{\boldsymbol{A}_1} + \cdots + s_Q(i) \underbrace{\begin{bmatrix} a_{11}^{(Q)} & \cdots & a_{1T}^{(Q)} \\ \vdots & \ddots & \vdots \\ a_{M1}^{(Q)} & \cdots & a_{MT}^{(Q)} \end{bmatrix}}_{\boldsymbol{A}_Q}, \quad (3.16)$$

where each of the dispersion matrices is designed as a Hermitian matrix and hence $\tilde{\boldsymbol{X}}(i)$ also exhibits a Hermitian structure. Since $\tilde{\boldsymbol{X}}(i)$ does not satisfy the unitary constraint, it cannot be directly applied to replace $\boldsymbol{X}(i)$ in the differential space-time modulation scheme formulated in Eq. (3.9). To this end, the Cayley transform [89] may be invoked, in order to uniquely map the Hermitian matrix $\tilde{\boldsymbol{X}}(i)$ to the unitary matrix $\boldsymbol{X}(i)$, which is given by

$$\boldsymbol{X}(i) = [\boldsymbol{I} - j\tilde{\boldsymbol{X}}(i)][\boldsymbol{I} + j\tilde{\boldsymbol{X}}(i)]^{-1}. \quad (3.17)$$

Note that the matrix $\boldsymbol{X}(i)$ is guaranteed to be unitary, according to

$$\begin{aligned}\boldsymbol{X}(i)\boldsymbol{X}^{\mathrm{H}}(i) &= [\boldsymbol{I} - j\tilde{\boldsymbol{X}}(i)][\boldsymbol{I} + j\tilde{\boldsymbol{X}}(i)]^{-1}\{[\boldsymbol{I} - j\tilde{\boldsymbol{X}}(i)][\boldsymbol{I} + j\tilde{\boldsymbol{X}}(i)]^{-1}\}^{\mathrm{H}} \\ &= [\boldsymbol{I} - j\tilde{\boldsymbol{X}}(i)][\boldsymbol{I} + j\tilde{\boldsymbol{X}}(i)]^{-1}[\boldsymbol{I} - j\tilde{\boldsymbol{X}}(i)]^{-1}[\boldsymbol{I} + j\tilde{\boldsymbol{X}}(i)] \\ &= \boldsymbol{I}, \end{aligned} \tag{3.18}$$

bearing in mind that the matrix $\tilde{\boldsymbol{X}}(i)$ is Hermitian. Therefore, the unitary space-time codewords $\boldsymbol{X}(i)$ generated according to Eq. (3.17) may now be applied according to the differential space-time encoding rule of Eq. (3.9). Furthermore, the transmission rate of the DLDC scheme is given by $R_{\mathrm{DLDC}} = Q \log_2 \mathcal{L}/T$. Accordingly, the DLDC scheme is also capable of achieving a multiplexing gain, which is linearly increased with the value Q, while DOSTBCs can only be designed for achieving a diversity gain.

It is worth mentioning that while the DLDC arrangement of Fig. 3.2 is capable of flexibly mapping Q real-valued symbols to the unitary matrix for an arbitrary number of transmit and receive antennas, the symbol duration per block T has to be equal to M due to the unitary constraint imposed by $\boldsymbol{X}(i)$ [23][1]. Hence, while the LDC coherent scheme is characterized by the four parameters of (M, N, T, Q), the DLDC scheme of Fig. 3.2 is uniquely identified by the following three parameters of (M, N, Q).

In order to summarize the DLDC transmitter's encoding operation, each step numbered in Fig. 3.2 is listed below.

Algorithm 3.1: Encoding principle of the DLDC's transmitter in Fig. 3.2

1. Given the system parameters of the $\mathcal{L}$-PAM DLDC scheme, i.e. (M, N, Q) as well as Q Hermitian dispersion matrices $\boldsymbol{A}_1, \cdots, \boldsymbol{A}_Q \in \mathcal{C}^{M \times M}$, $B = Q \cdot \log_2(\mathcal{L})$ information bits are input to the DLDC block in each of the space-time block durations $T = M$.

2. The $B = Q \cdot \log_2 \mathcal{L}$ input bits are mapped to $\mathcal{L}$-PAM symbols $\boldsymbol{K}(i) = [s_1(i), \cdots, s_Q(i)]^{\mathrm{T}} \in \mathcal{R}^{Q \times 1}$.

3. The Q PAM symbols $\boldsymbol{K}(i)$ generated in *Step* 2 are dispersed into the space- and time-dimensions with the aid of the Q dispersion matrices $\boldsymbol{A}_1, \cdots, \boldsymbol{A}_Q$ using the following operation: $\tilde{\boldsymbol{X}}(i) = \sum_{q=1}^{Q} s_q(i)\boldsymbol{A}_q$.

4. A unitary matrix $\boldsymbol{X}(i)$ is computed from the matrix $\tilde{\boldsymbol{X}}(i)$ obtained in *Step* 3 using the Cayley transform of $\boldsymbol{X}(i) = [\boldsymbol{I} - j\tilde{\boldsymbol{X}}(i)][\boldsymbol{I} + j\tilde{\boldsymbol{X}}(i)]^{-1}$.

[1] To expound a little further, a train of differential encoding operations of Eq. (3.6) requires the modulated unitary space-time codeword $\boldsymbol{X}(i)$ to be an $(M \times M)$-element square matrix, in order to maintain the matrix size of $\boldsymbol{S}(i)$. For this reason, the number of transmit antennas M is set equal to the number of symbol durations per block T. Due to this constraint, the maximum attainable diversity order of $N \cdot \min(M, T)$ is further simplified to $(N \cdot M)$.

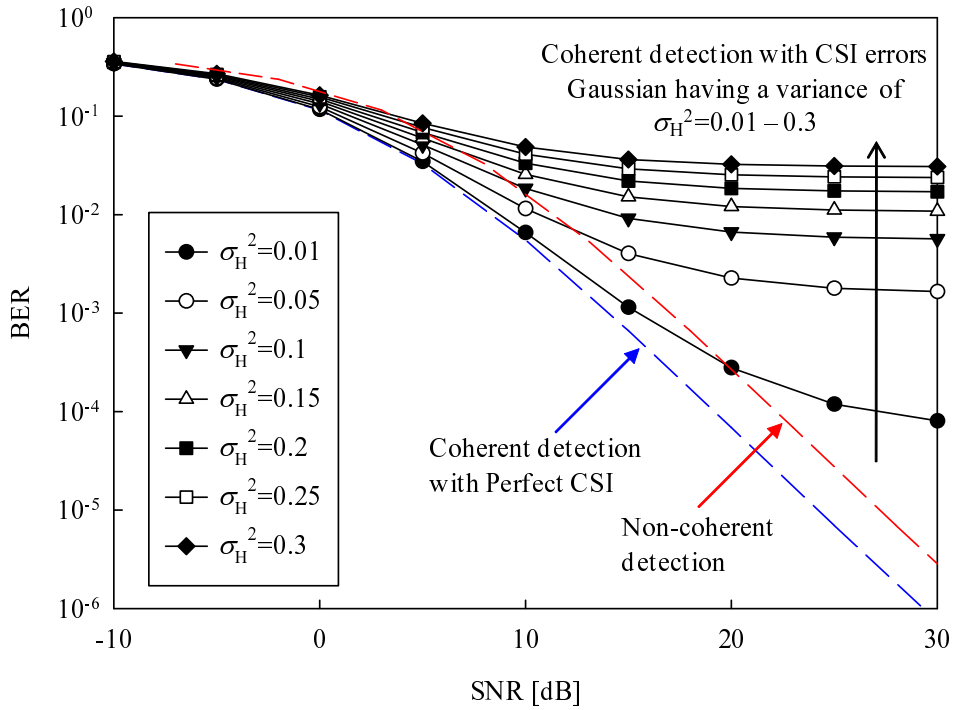

Figure 3.3: Achievable BER performance of coherent and non-coherent STC, characterizing the effects of channel estimation errors, where the (2×1)-element BPSK-modulated Alamouti scheme [20] and the (2×1)-element BPSK modulated DOSTBC schemes of Fig. 3.1 [40] were compared. All other system parameters were summarized in Table 3.1.

5. In order to generate a Space-Time (ST) codeword $\boldsymbol{S}(i)$ in the current ST block, the unitary matrix $\boldsymbol{X}(i)$ created in *Step* 4 is differentially encoded as follows: $\boldsymbol{S}(i) = \boldsymbol{S}(i-1)\boldsymbol{X}(i)$.

6. The ST matrix $\boldsymbol{S}(i)$ generated in *Step* 5 is mapped to the space- and time-dimensions, where the mth-row and tth column component of the matrix $\boldsymbol{S}(i)$ is assigned to the mth antenna element and in tth symbol duration.

3.2.3 Performance Results

In this section, we present our performance results for the family of DOSTBC schemes communicating over frequency-flat Rayleigh fading channels having the coherence time of $2T$.

Firstly, we demonstrate the effects of CSI estimation errors on the achievable performance of the coherent STC scheme. Fig 3.3 shows the achievable BER performance of the two space-time diversity schemes employing both coherent and non-coherent receivers, where the (2×1)-element Alamouti code [20] was employed for the coherent scheme, while the (2×1)-element DOSTBC scheme proposed by Tarokh and Jafarkhani [40] was used for the non-coherent scheme. In order to characterize the effects of the CSI estimation errors associated with coherent detection, we introduced the superposition of Gaussian noise having a variance

Table 3.1: Basic system parameters for the DOSTBC scheme of Fig. 3.1.

Number of transmit antennas	$M = 2$–4
Number of receive antennas	$N = 1$–4
Channels	Frequency-flat Rayleigh fading
Channel's coherence time	$\tau = 2$ block durations
	($2T$ symbol durations)
Modulation	$\mathcal{L}-$PSK or $\mathcal{L}-$QAM
Detector	ML detector

of σ_{H}^2 to each channel component h_i $(i = 1, 2)$, changing the variance σ_{H}^2 from $\sigma_{\mathrm{H}}^2 = 0.01$ to $\sigma_{\mathrm{H}}^2 = 0.3$. Firstly, observe in Fig 3.3 that the BER curve of the differentially-encoded scheme exhibited the well-known 3 dB performance loss compared to that of Alamouti's code assuming perfect CSI. However, upon considering the effects of CSI errors, the BER curves of the coherent detection aided scheme exhibited an error floor and its performance was severely degraded upon increasing the variance σ_{H}^2. Therefore, despite its 3 dB SNR disadvantage arising from the differential encoding, non-coherent detection was found to outperform its coherent counterpart suffering from CSI estimation errors.

To provide further insights, Fig. 3.4 shows the achievable BER performance of the BPSK-modulated DOSTBC schemes, where the number of transmit antennas M as well as that of the receive antennas N was varied. Specifically, Fig. 3.4(a) considered the scenarios of $(M, N) = (1, 1), (2, 1), (3, 1), (4, 1)$, while Fig. 3.4(b) considered $(M, N) = (2, 1), (2, 2), (2, 3), (2, 4)$. Here, all the curves corresponded to a transmission rate of $R = 1.0$ bits/symbol. It can be seen from Fig. 3.4(a) that the DOSTBC scheme is capable of achieving the maximum attainable transmit-diversity order, where the corresponding diversity order ranged from one to four and increased in accordance with the number of transmit antennas M. Moreover, observe in Fig. 3.4(b) that the maximum attainable diversity order represented by the product $(M \cdot N)$ was indeed achieved, when multiple antennas were employed both at the transmitter and at the receiver.

3.3 Differential Space-Time Shift Keying Scheme

Motivated by the beneficial properties of the coherent STSK scheme introduced in Chapter 2, the family of DSTSK schemes will be proposed in this section, in order to retain the main benefits of the coherent STSK scheme, while dispensing with CSI estimation at the receiver. More specifically, the detector of the above-mentioned coherent STSK scheme relies on the *prior* knowledge of CSI and hence the performance degradation imposed by CSI estimation errors is unavoidable. To circumvent this limitation, we conceived the corresponding DSTSK

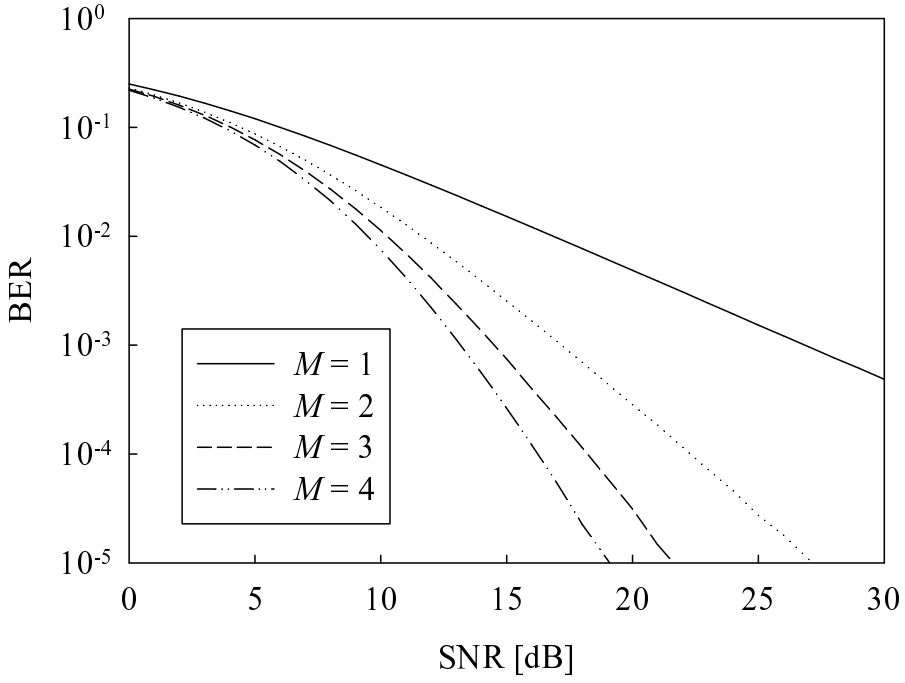

(a)

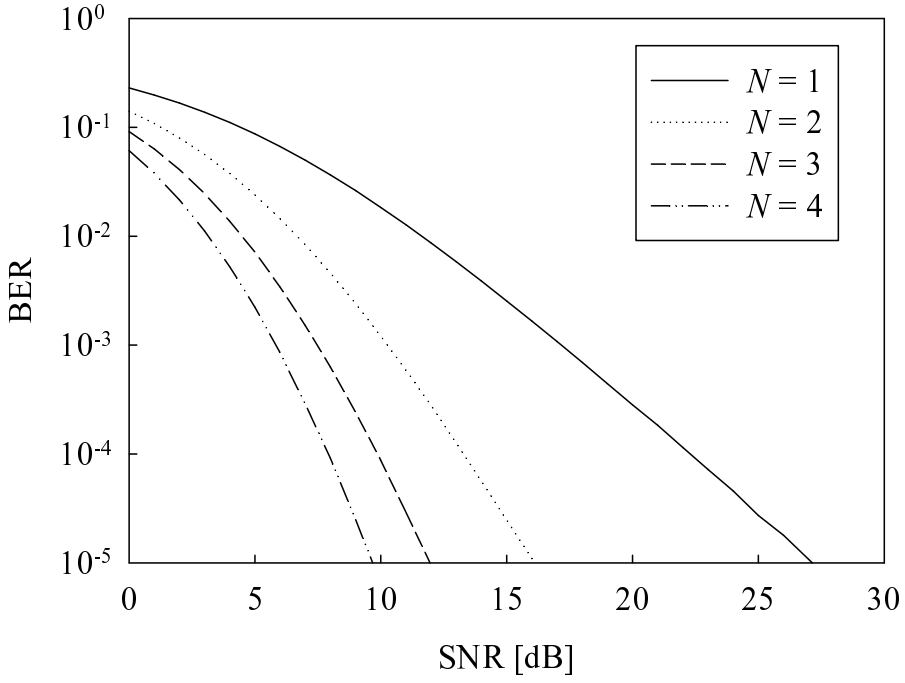

(b)

Figure 3.4: Achievable BER performance of the BPSK-modulated DOSTBC schemes, where the number of transmit antennas M as well as of receive antennas N was varied, where Fig. 3.4(a) considered the cases of $(M, N) = (1, 1), (2, 1), (3, 1), (4, 1)$ while Fig. 3.4(b) considered the cases of $(M, N) = (2, 1), (2, 2), (2, 3), (2, 4)$. Note that all the cases exhibited the transmission rate of $R = 1.0$ bits/symbol. All other system parameters were summarized in Table 3.1.

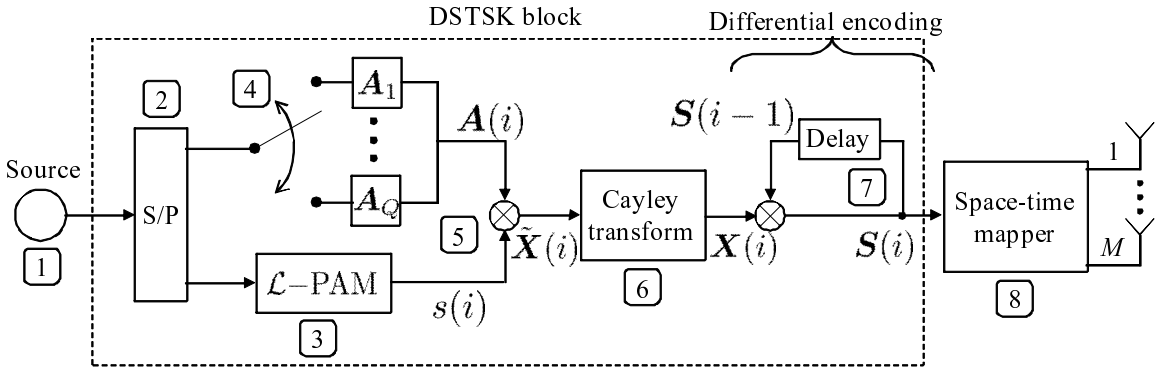

Figure 3.5: Transmitter structure of our DSTSK scheme, which was developed from the STSK architecture of Fig. 2.5 and the DSTC scheme of Fig. 3.1.

scheme as the extension of the coherent STSK scheme of Section 2.3 with the aid of the Cayley unitary transform proposed in [89] and detailed in Section 8.4 of [23].

Fig. 3.5 shows the transmitter structure of our DSTSK scheme, where Q Hermitian matrices $\boldsymbol{A}_q$ $(q = 1, 2, \cdots, Q)$ are pre-assigned as the dispersion matrices prior to transmissions and $\mathcal{L}$-level Pulse Amplitude Modulation (PAM) is employed. Similarly to the coherent STSK scheme of Fig. 2.5 and detailed in Section 2.3.1, each space-time block contains $\log_2(Q \cdot \mathcal{L})$ source bits, where $\log_2 Q$ bits are mapped to $\boldsymbol{A}(i)$ using the previously outlined process of dispersion-matrix activation, while $\log_2 \mathcal{L}$ bits are mapped to the $\mathcal{L}$-PAM symbols $s(i)$. Thus, analogously to Eq. (2.19), the Hermitian matrix $\boldsymbol{X}(i) \in \mathcal{C}^{M \times T}$ is calculated as

$$\tilde{\boldsymbol{X}}(i) = s(i)\boldsymbol{A}(i), \tag{3.19}$$

where we impose the relation of $M = T$.[2] Furthermore, based on the Cayley unitary transform technique of [89], the Hermitian matrix $\tilde{\boldsymbol{X}}(i)$ is transformed to the unitary matrix $\boldsymbol{X}(i)$ as follows

$$\boldsymbol{X}(i) = [\boldsymbol{I} - j\tilde{\boldsymbol{X}}(i)][\boldsymbol{I} + j\tilde{\boldsymbol{X}}(i)]^{-1}, \tag{3.20}$$

where $\boldsymbol{I}$ is the identity matrix. Finally, the space-time matrix $\boldsymbol{S}(i)$ is differentially-encoded as follows:

$$\boldsymbol{S}(i) = \boldsymbol{S}(i-1) \cdot \boldsymbol{X}(i), \tag{3.21}$$

where the symbols in the mth row of $\boldsymbol{S}(i)$ are transmitted from the mth transmit AE over T symbol durations. We note that the matrix $\tilde{\boldsymbol{X}}(i)$ of Eq. (3.19) mapped with the aid of dispersion-matrix activation as well as the classic PAM modulation is equivalent to that of the coherent STSK scheme, expressed as Eq. (2.19). Hence, the mapping example shown in Table 2.4 also corresponds to the DSTSK case. The only difference between the two is

[2] In order to enable the differential unitary space-time modulation of Eq. (3.6), our DSTSK scheme is imposed by this constraint, similarly to other classic DSTCs, such as OSTBCs and LDCs.

that the dispersion matrices employed for the coherent STSK scheme have to obey the power constraint of Eq. (2.21), while those of the DSTSK scheme do not.

Assuming that the fading channel envelope remains constant over the two DSTSK block durations $2T$, the corresponding received signal block $\boldsymbol{Y}(i)$ of Eq. (3.7) is modified to

$$\begin{aligned}\boldsymbol{Y}(i) &= \boldsymbol{H}(i)\boldsymbol{S}(i) + \boldsymbol{V}(i) \\ &= \boldsymbol{Y}(i-1)\boldsymbol{X}(i) + \boldsymbol{V}(i) - \boldsymbol{V}(i-1)\boldsymbol{X}(i),\end{aligned} \tag{3.22}$$

which does not include any channel components. We note that the Cayley unitary transform of Eq. (3.20) uniquely connects the unitary matrix $\boldsymbol{X}(i)$ with the Hermitian matrix $\tilde{\boldsymbol{X}}(i)$, therefore enabling the differential unitary encoding of Eq. (3.21) and leading to the linearized equivalent system model of Eq. (3.25). Furthermore, in order to ensure $\tilde{\boldsymbol{X}}(i)$ remains a Hermitian matrix, the modulated symbol $s(i)$ of Eq. (3.19) has to be a real-valued, rather than a complex-valued symbol, such as PSK and QAM. For this reason, we adopt a PAM constellation in our DSTSK scheme.

Instead of directly applying optimum ML detection to the received signal of Eq. (3.22), we introduce the linearization technique of [89] for the sake of facilitating the employment of the single-stream-based ML detector of Eq. (2.32). More specifically, upon multiplying both sides of Eq. (3.22) by $[\boldsymbol{I} + j\tilde{\boldsymbol{X}}(i)]$, we arrive at

$$\begin{aligned}\underbrace{\boldsymbol{Y}(i) - \boldsymbol{Y}(i-1)}_{\hat{\boldsymbol{Y}}(i)} &= \underbrace{-j[\boldsymbol{Y}(i) + \boldsymbol{Y}(i-1)]}_{\hat{\boldsymbol{H}}(i)}\tilde{\boldsymbol{X}}(i) \\ &\quad + \underbrace{\{-\boldsymbol{V}(i)[\boldsymbol{I} + j\tilde{\boldsymbol{X}}(i)] - \boldsymbol{V}(i-1)[\boldsymbol{I} - j\tilde{\boldsymbol{X}}(i)]\}}_{\hat{\boldsymbol{V}}(i)},\end{aligned} \tag{3.23}$$

where $\hat{\boldsymbol{Y}}(i)$ and $\hat{\boldsymbol{H}}(i)$ represent the equivalent received signals and the equivalent channel matrix, while the equivalent noise matrix $\hat{\boldsymbol{V}}(i)$ has independent columns with a covariance of

$$\hat{N}_0 = N_0(\boldsymbol{I} + \tilde{\boldsymbol{X}}^2(i)). \tag{3.24}$$

Finally, by applying the $vec(\ )$ operation to Eq. (3.23), we arrive at [89]

$$\bar{\boldsymbol{Y}}(i) = \bar{\boldsymbol{H}}(i)\chi\boldsymbol{K}(i) + \bar{\boldsymbol{V}}(i), \tag{3.25}$$

where we have

$$\bar{\boldsymbol{Y}}(i) = vec[\hat{\boldsymbol{Y}}(i)] \in \mathcal{C}^{NT\times 1} \tag{3.26}$$

$$\bar{\boldsymbol{H}}(i) = \boldsymbol{I} \otimes \hat{\boldsymbol{H}}(i) \in \mathcal{C}^{NT\times MT} \tag{3.27}$$

$$\bar{\boldsymbol{V}}(i) = vec[\hat{\boldsymbol{V}}(i)] \in \mathcal{C}^{NT\times 1}, \tag{3.28}$$

while χ and $\boldsymbol{K}(i)$ are given by Eqs. (2.29) and (2.30), respectively, in the same manner as the coherent STSK scheme of Section 2.3.1. In the rest of this chapter, the system notation

of our DSTSK scheme is expressed as 'DSTSK(M, N, T, Q)', similarly to the coherent STSK scheme in Chapter 2.

Clearly, since the linearized system model of our DSTSK scheme (Eq. (3.25)) exhibits the same structure as for that of its coherent STSK counterpart (Eq. (2.25)), we can readily invoke the single-antenna-based ML detector according to the criterion of Eq. (2.32), acknowledging that the resultant DSTSK's performance would inevitably suffer from the usual differential encoding induced SNR loss owing to the enhanced noise variance of Eq. (3.24).

Following the above-mentioned introductory elaborations, the encoding principle of our DSTSK scheme obeying the architecture of Fig. 3.5 may be contrasted to the DLDC architecture of Fig. 3.2 and formally summarized as follows:

Algorithm 3.2: Encoding principle of the DSTSK's transmitter in Fig. 3.5

1. Given the $\mathcal{L}$-PAM aided DSTSK$(M, N, T = M, Q)$ scheme employing Q Hermitian dispersion matrices $\boldsymbol{A}_1, \cdots, \boldsymbol{A}_Q \in \mathcal{C}^{M \times M}$, $B = \log_2(Q \cdot \mathcal{L})$ information bits are input to the DSTSK block in each of the ST block durations $T = M$.

2. The $B = \log_2(Q \cdot \mathcal{L})$ information bits, input in *Step* 1, are Serial-to-Parallel (S/P) converted to $B_1 = \log_2 \mathcal{L}$ bits and $B_2 = \log_2 Q$ bits.

3. The $B_1 = \log_2 \mathcal{L}$ bits at the lower output of the S/P converter of Fig. 3.5, are then modulated to a real-valued $\mathcal{L}$-PAM symbol $\{s_l(i);\ l = 1, \cdots \mathcal{L}\}$.

4. According to the $B_2 = \log_2 Q$ bits at the upper output of the S/P converter of Fig. 3.5 are mapped to one out of the Q dispersion matrices $\boldsymbol{A}_1, \cdots, \boldsymbol{A}_Q \in \mathcal{C}^{M \times T}$, which we refer to as the activated matrix $\{\boldsymbol{A}_q\ ; q = 1, \cdots Q\}$.

5. According to the modulated symbol $s_l(i)$ generated in *Step* 3 as well as to the dispersion matrix $\boldsymbol{A}_q$ activated in *Step* 4, a matrix $\tilde{\boldsymbol{X}}(i) \in \mathcal{C}^{M \times T}$ is computed as follows: $\tilde{\boldsymbol{X}}(i) = s_l(i) \cdot \boldsymbol{A}_q$.

6. Then a unitary matrix $\boldsymbol{X}(i)$ is computed from the matrix $\tilde{\boldsymbol{X}}(i)$ obtained in *Step* 5, using the Cayley transform of $\boldsymbol{X}(i) = [\boldsymbol{I} - j\tilde{\boldsymbol{X}}(i)][\boldsymbol{I} + j\tilde{\boldsymbol{X}}(i)]^{-1}$.

7. In order to generate a ST codeword $\boldsymbol{S}(i)$ for the current ST block, the unitary matrix $\boldsymbol{X}(i)$ generated in *Step* 6 is differentially encoded as follows: $\boldsymbol{S}(i) = \boldsymbol{S}(i-1)\boldsymbol{X}(i)$.

8. The ST matrix $\boldsymbol{S}(i)$ generated in *Step* 7 is then mapped to the space- and time-dimensions, where the components in the mth-row and tth column of the matrix $\boldsymbol{S}(i)$ is assigned to the mth antenna element in the tth symbol duration.

Let us now briefly compare Algorithm 3.2 of our DSTSK scheme seen in Fig. 3.5 to Algorithm 3.1 of the DLDC scheme portrayed in Fig. 3.2. In our DSTSK scheme, *Steps* 1–5 of Algorithm 3.2, which are invoked to generate the unitary matrix $\tilde{\boldsymbol{X}}(i)$, represent a different procedure

in comparison to that of the DSTSK scheme, namely to *Steps* 1–3 of Algorithm 3.1. This is because our DSTSK scheme of Fig. 3.5 employs the new concept of dispersion-matrix activation, while the DLDC scheme of Fig. 3.2 is based on the linear combination of multiple dispersion matrices. On the other hand, the latter part of Algorithms 3.1 and 3.2 is identical. This is represented by *Steps* 6–8 of Algorithm 3.2 and *Steps* 4–6 of Algorithm 3.1, since they both rely on the Cayley transform and on differential modulation.

Furthermore, when we compare Algorithm 2.1 of the CSTSK scheme obeying the architecture of Fig. 2.5 and Algorithm 3.2 of the DSTSK scheme shown in Fig. 3.5, we observe that *Steps* 2–5 of Algorithm 2.1 and those of Algorithm 3.2 are identical. This is because both the CSTSK and DSTSK schemes are based on the concept of dispersion-matrix activation.

Example 3.1: BPSK-modulated DSTSK$(2, 2, 2, 4)$'s transmitter

Let us consider an $(M \times N) = (2 \times 2)$ DSTSK system employing BPSK modulation and $Q = 4$ dispersion matrices formulated as

$$\begin{aligned}
\boldsymbol{A}_1 &= \begin{bmatrix} -0.7258 + j0.0000 & 0.0830 + j1.1336 \\ 0.0830 - j1.1336 & 0.5019 + j0.0000 \end{bmatrix}, \\
\boldsymbol{A}_2 &= \begin{bmatrix} 0.5610 + j0.0000 & 1.1171 - j0.1855 \\ 1.1171 + j0.1855 & -0.2025 + j0.0000 \end{bmatrix}, \\
\boldsymbol{A}_3 &= \begin{bmatrix} -0.0281 + j0.0000 & 0.2061 + j0.3085 \\ 0.2061 - j0.3085 & -0.1648 + j0.0000 \end{bmatrix}, \\
\boldsymbol{A}_4 &= \begin{bmatrix} 0.6732 + j0.0000 & -0.4042 + j0.3062 \\ -0.4042 - j0.3062 & -0.6678 + j0.0000 \end{bmatrix},
\end{aligned}$$

where the transmission rate R is given by $R = \log_2(\mathcal{L} \cdot Q)/M = \log_2(2 \cdot 4)/2 = 1.5$ bits/symbol and $\log_2(\mathcal{L} \cdot Q) = 3$ bits are input every block interval. For example, let us assume that source bits of "101" are input to the corresponding block of interest i. Then, according to Table 2.4, $\boldsymbol{A}(i) = \boldsymbol{A}_3$ and $s(i) = -1$ are selected, resulting in the Hermitian-matrix generation of

$$\begin{aligned}
\tilde{\boldsymbol{X}}(i) &= s(i)\boldsymbol{A}(i) = -\boldsymbol{A}_3 \\
&= \begin{bmatrix} 0.0281 + j0.0000 & -0.2061 - j0.3085 \\ -0.2061 + j0.3085 & 0.1648 + j0.0000 \end{bmatrix}.
\end{aligned}$$

Next, based on the Cayley unitary transform of Eq. (3.20), we arrive at

$$\begin{aligned}
\boldsymbol{X}(i) &= [\boldsymbol{I} - j\tilde{\boldsymbol{X}}(i)][\boldsymbol{I} + j\tilde{\boldsymbol{X}}(i)]^{-1} \\
&= \left\{ \begin{bmatrix} 1 & 0 \\ 0 & 1 \end{bmatrix} - \begin{bmatrix} 0.0000 + j0.0281 & 0.3085 - j0.2061 \\ -0.3085 - j0.2061 & 0.0000 + j0.1648 \end{bmatrix} \right\} \\
&\times \left\{ \begin{bmatrix} 1 & 0 \\ 0 & 1 \end{bmatrix} + \begin{bmatrix} 0.0000 + j0.0281 & 0.3085 - j0.2061 \\ -0.3085 - j0.2061 & 0.0000 + j0.1648 \end{bmatrix} \right\}^{-1} \\
&= \begin{bmatrix} 0.7636 - j0.0094 & -0.4691 + j0.4437 \\ 0.5895 + j0.2634 & 0.7236 - j0.2439 \end{bmatrix},
\end{aligned}$$

noting that the matrix $\boldsymbol{X}(i)$ has a unitary structure. Finally, $\boldsymbol{X}(i)$ is differentially encoded, according to Eq. (3.21). Then, the ith space-time block $\boldsymbol{S}(i) = \boldsymbol{S}(i-1)\boldsymbol{X}(i) = \boldsymbol{X}(i)$ will be transmitted from the $M = 2$ transmit antennas over the $T = M = 2$ symbol durations.

3.3.1 Asynchronous Differential Space-Time Shift Keying Scheme

While we assumed in Section 3.5 that each transmit antenna element is synchronized at the symbol level, we herein relax this limitation by imposing a constraint on the dispersion-matrix design. As proposed in Section 2.3.2 for the coherent STSK scheme, we can design a space-time block structure, which dispenses with IAS. This is achieved by appropriately restricting the search space of the dispersion matrix set $\boldsymbol{A}_{q'}$ $(q' = 1, \cdots, Q)$. Unfortunately, our asynchronous technique developed for the coherent STSK scheme of Fig. 2.5 cannot be directly applied to the DSTSK scheme of Fig. 3.5, because in the DSTSK arrangement the matrix $\tilde{\boldsymbol{X}}(i)$ generated with the aid of dispersion matrix activation is further processed by the Cayley unitary transform of Eq. (3.20), unlike in the coherent STSK scheme. Here, we impose another constraint on the set of dispersion matrices employed for the DSTSK scheme, in order to dispense with the symbol-level IAS. More specifically, each dispersion matrix $\boldsymbol{A}_{q'}$ $(q' = 1, \cdots, Q)$ is chosen from the matrix space constituted by the family of real-valued diagonal matrices.

For example, a set of dispersion matrices found for our Asynchronous DSTSK (ADSTSK) arrangements are represented by

$$\boldsymbol{A}_1 = \text{diag}\left\{\eta_1^{(1)}, \cdots, \eta_1^{(M)}\right\}, \cdots, \ \boldsymbol{A}_Q = \text{diag}\left\{\eta_Q^{(1)}, \cdots, \eta_Q^{(M)}\right\}, \tag{3.29}$$

where we have real-valued non-zero components $\eta_{q'}^{(m)}$ $(1 \leq m \leq M, 1 \leq q' \leq Q)$. This dispersion-matrix structure assists us in arriving at a diagonal space-time matrix $\boldsymbol{X}(i)$ after the Cayley unitary transform. Therefore, under the assumption that the initial signals $\boldsymbol{S}(0)$ are given by the identity matrix $\boldsymbol{S}(0) = \boldsymbol{I}$, the differentially encoded matrix retains its diagonal form, which dispenses with the requirement of simultaneous transmissions by the different transmit antennas, indicating that only a single antenna transmits a signal during each symbol interval.

Apparently, this real-valued and diagonal constraint imposed by our ADSTSK scheme substantially reduces the degrees of freedom in the dispersion-matrix design, in comparison to that of the unconstrained DSTSK scheme. Their relationship is similar to that between the coherent STSK and the coherent ASTSK arrangements of Section 2.3. On the other hand, it is also expected that retaining the above-mentioned diagonal constraint may lead to a rapid convergence for the dispersion-matrix optimization, because of lower search space of dispersion-matrix set than that of the unconstrained DSTSK scheme. These characteristics will be investigated in Section 3.5.

To elaborate a little further, we compare the search space of both the ASTSK and of the ADSTSK schemes portrayed in the schematic of Fig. 3.5. As described in Section 2.3.2, when designing the Q dispersion matrices for the ASTSK scheme, we optimize the position of a total of $M \cdot Q$ non-zero elements in the matrices, as well as each of the complex values. Therefore, the number of possible combinations for the non-zero elements positions is given by $\mathcal{O} = M^{MQ}$. By contrast, that of the ADSTSK scheme is unique, i.e. we have $\mathcal{O} = 1$, for the diagonal matrices of $\boldsymbol{A}_{q'}$ $(q' = 1, \cdots, Q)$. The associated lack of freedom may lead to a performance degradation in comparison to that of the ASTSK scheme.

Example 3.2: BPSK-modulated ADSTSK$(3, 2, 3, 4)$'s transmitter

Here, let us assume a BPSK-modulated $(M \times N) = (3 \times 2)$-element ADSTK transmitter having the $Q = 2$ dispersion matrices formulated as

$$\boldsymbol{A}_1 = \begin{bmatrix} 1.8176 & 0 & 0 \\ 0 & 2.4580 & 0 \\ 0 & 0 & -1.9670 \end{bmatrix},$$

$$\boldsymbol{A}_2 = \begin{bmatrix} -0.6621 & 0 & 0 \\ 0 & 0.4048 & 0 \\ 0 & 0 & -0.4276 \end{bmatrix},$$

where the transmission rate R is given by $R = \log_2(\mathcal{L} \cdot Q)/M = \log_2(2 \cdot 2)/3 = 0.67$ bits/symbol and $B = \log_2(\mathcal{L} \cdot Q) = 2$ bits are input at each block interval. As mentioned-above, the unitary matrix is generated according to the input bits B as well as Eqs. (3.19) and (3.20). Therefore, the legitimate space for the signals $\boldsymbol{X}$ is formulated as

$$\begin{aligned}
\boldsymbol{X}_{B=00} &= (\boldsymbol{I} - js_1\boldsymbol{A}_1)(\boldsymbol{I} + js_1\boldsymbol{A}_1)^{-1} \\
&= \begin{bmatrix} -0.5353 - j0.8447 & 0 & 0 \\ 0 & -0.7160 - j0.6981 & 0 \\ 0 & 0 & -0.5892 + j0.8080 \end{bmatrix}, \\
\boldsymbol{X}_{B=01} &= (\boldsymbol{I} - js_2\boldsymbol{A}_1)(\boldsymbol{I} + js_2\boldsymbol{A}_1)^{-1} \\
&= \begin{bmatrix} -0.5353 + j0.8447 & 0 & 0 \\ 0 & -0.7160 + j0.6981 & 0 \\ 0 & 0 & -0.5892 - j0.8080 \end{bmatrix}, \\
\boldsymbol{X}_{B=10} &= (\boldsymbol{I} - js_1\boldsymbol{A}_2)(\boldsymbol{I} + js_1\boldsymbol{A}_2)^{-1} \\
&= \begin{bmatrix} 0.3905 + j0.9206 & 0 & 0 \\ 0 & 0.7185 - j0.6956 & 0 \\ 0 & 0 & 0.6908 + j0.7230 \end{bmatrix}, \\
\boldsymbol{X}_{B=11} &= (\boldsymbol{I} - js_2\boldsymbol{A}_2)(\boldsymbol{I} + js_2\boldsymbol{A}_2)^{-1} \\
&= \begin{bmatrix} 0.3905 - j0.9206 & 0 & 0 \\ 0 & 0.7185 + j0.6956 & 0 \\ 0 & 0 & 0.6908 - j0.7230 \end{bmatrix},
\end{aligned}$$

each of which exhibits a diagonal form. Hence, provided that the previous space-time matrix $\boldsymbol{S}(i-1)$ has a diagonal structure, the current matrix $\boldsymbol{S}(i) = \boldsymbol{S}(i-1)\boldsymbol{X}(i)$ is also guaranteed to have a diagonal structure, which ensures that only one antenna element is activated at each symbol duration.

3.3.2 Computational Complexity

Let us now characterize the computational complexity imposed by the single-stream-based ML detection of our DSTSK scheme of Fig. 3.5. Since the single-stream-based ML detector employed for our DSTSK scheme is basically the same as that of the STSK scheme of Fig. 2.5 in Section 2.3, the associated computational complexity is given by

$$\frac{NTQ(4MT + 4\mathcal{L})}{\log_2(Q \cdot \mathcal{L})}, \tag{3.30}$$

similarly to that of the coherent STSK scheme, as shown in Eq. (2.33). The only difference in the computational complexity of the coherent STSK and of the DSTSK schemes is that in our DSTSK scheme real-valued symbols are employed for s_l, while the coherent STSK scheme employs complex-valued symbols. Here, the complexity is evaluated in terms of the number of real-valued multiplications, noting that a single complex-valued multiplication was considered equivalent to four real-valued multiplications.

For our DSTSK scheme, the equivalent channels $\bar{\boldsymbol{H}}(i)\chi$ have to be calculated for each DSTSK block, regardless of channel's coherence time $\tau \cdot T$, as required by the implementation of differential decoding. However, it is worth mentioning that since our DSTSK scheme does not impose a pilot overhead and eliminates the complexity associated with CSI estimation, hence its complexity may be significantly lower than those of the coherent STSK and SM schemes, especially when the corresponding MIMO channels change rapidly.

Additionally, the complexity of the ADSTSK scheme can be further simplified from Eq. (3.30) to

$$\frac{NTQ(4T + 4\mathcal{L})}{\log_2(Q \cdot \mathcal{L})}, \tag{3.31}$$

owing to the fact that each dispersion matrix of the ADSTSK scheme is sparse and hence the complexity required for the calculation of $\bar{\boldsymbol{H}}(i)\chi$ is reduced.

Similarly, the computational complexity per bit, imposed by the max-log approximated SISO detector of Eq. (2.43) invoked for the DSTSK scheme, is given by

$$\frac{NTQ(8MT + 6\mathcal{L})}{\log_2(Q \cdot \mathcal{L})}, \tag{3.32}$$

while that of the ADSTSK scheme may also be simplified to

$$\frac{NTQ(8T + 6\mathcal{L})}{\log_2(Q \cdot \mathcal{L})}. \tag{3.33}$$

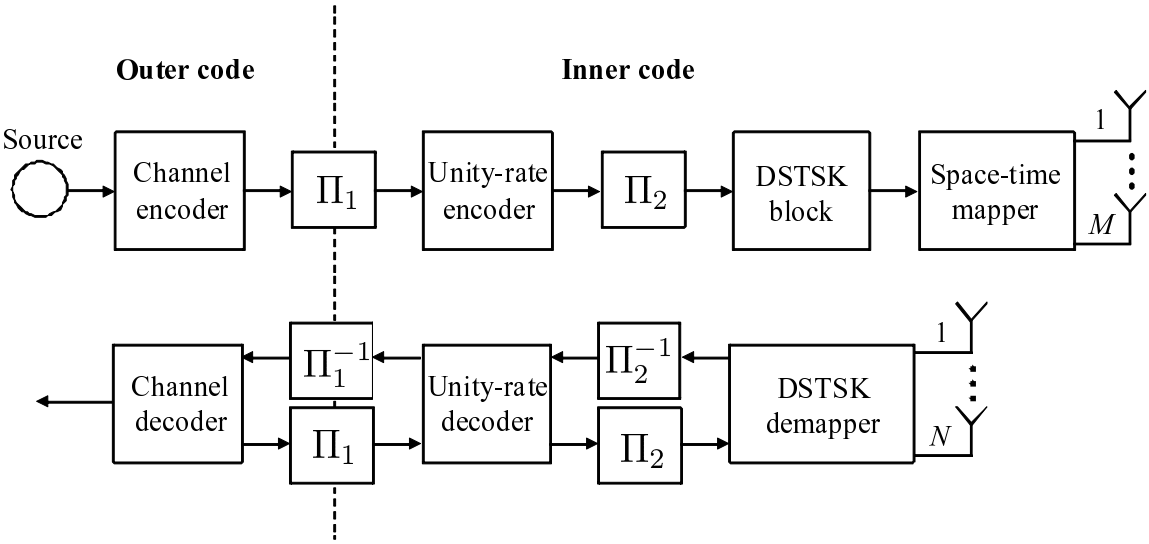

Figure 3.6: Schematic of a three-stage RSC- and URC-coded DSTSK scheme using iterative detection. The detailed schematic of the DSTSK scheme is seen in Fig. 3.5. The rationale of using the three-stage architecture was detailed in Section 2.4.

3.4 Three-Stage Concatenated Turbo DSTSK Scheme

Having introduced the DSTSK and ADSTSK schemes obeying the schematics of Fig. 3.5 in the context of uncoded scenarios, let us now consider their turbo-coded DSTSK counterpart, which is capable of achieving a near-capacity performance. Fig. 3.6 shows the architecture of the resultant three-stage serially-concatenated DSTSK scheme, employing a classic channel-encoder and a URC-encoder. The corresponding receiver iteratively detects the received signals, based on the turbo-decoding principle. We note that this arrangement constitutes the non-coherently detected counterpart of the coherent STSK scheme of Fig. 2.7 proposed in Section 2.4. Specifically, the STSK-mapper and STSK-demapper blocks of Fig. 2.7 were replaced by the DSTSK-mapper and DSTSK-demapper blocks, respectively.

Since the equivalent linearized system model of the DSTSK scheme formulated in Eq. (3.25) exhibited a similar structure to that of the coherent STSK scheme of Eq. (2.42), the soft demapper developed for the coherent STSK scheme of Fig. 2.7 may be directly applied to the DSTSK scheme of Fig. 3.6, by adjusting the noise variance component. Here, the noise variance N_0 in Eq. (2.42) may be simply replaced by the averaged equivalent noise $N_0 \left|\left|(\boldsymbol{I} + E\left[\boldsymbol{X}^2\right])\right|\right| / M$, formulated in Eq. (3.24).

3.5 Performance Results

This section will characterize the achievable performance of our DSTSK and ADSTK schemes for both uncoded and for channel coded scenarios.

3.5.1 Rank- and Determinant Criterion Aided Dispersion-Matrix Design

In this section, we briefly introduce the rank- and determinant-criterion [23], which were employed for optimizing the dispersion-matrix of our DSTSK scheme of Figs. 3.5 and 3.6. For the sake of convenience, let us revisit the Chernoff upper bound of Eq. (2.40), introduced in Section 2.3.5, which is given by

$$P(\boldsymbol{S} \rightarrow \boldsymbol{S}') \leq \underbrace{\left(\frac{1}{4N_0}\right)^{m'N}}_{\text{diversity gain}} \cdot \underbrace{\prod_{m=1}^{m'} \frac{1}{\mu_m^N}}_{\text{coding gain}}, \tag{3.34}$$

where m' represents the minimum rank of the difference matrix $\boldsymbol{R} = \boldsymbol{S} - \boldsymbol{S}'$ among all the possible combinations of

$$\begin{pmatrix} Q \cdot \mathcal{L} \\ 1 \end{pmatrix} = \frac{Q \cdot \mathcal{L}(Q \cdot \mathcal{L} - 1)}{2}. \tag{3.35}$$

Furthermore, μ_m denotes the mth non-zero eigenvalue of $\boldsymbol{R} \cdot \boldsymbol{R}^{\mathrm{H}}$. Therefore, as shown in Eq. (3.34), a dispersion-matrix set having the full-rank of $m' = \min(M, T)$ succeeds in achieving the maximum attainable transmit diversity order, by maintaining the first multiplicative term in Eq. (3.34). By contrast, a dispersion-matrix set exhibiting a high determinant value of $\nabla = \det\left[\boldsymbol{R} \cdot \boldsymbol{R}^{\mathrm{H}}\right] = \prod_{m=1}^{m'} \frac{1}{\mu_m^N}$ results in a high coding gain. Bearing this in mind, in this chapter we aimed for optimizing a set of Hermitian dispersion matrices by conducting a random search, so that the determinant value ∇ is maximized, while achieving the full-rank of $m' = \min(M, T)$. Furthermore, we note that as seen in Eq. (3.34) a higher Q value as well as a lower M value gives rise to an increased ST codeword set size, hence reducing the minimum distance between the two closest codewords.

Accordingly, a set of dispersion matrices employed for each $\mathcal{L}$-PAM aided DSTSK(M, N, M, Q) arrangement was optimized with the aid of the above-mentioned determinant-criterion, while maintaining full rank. To be more specific, for the DSTSK scheme, we randomly generate the element of a number of Hermitian dispersion matrices Q, where each matrix component obeys the Gaussian distribution. Similarly, for the ADSTSK scheme, a number of real-valued diagonal dispersion matrices Q having random are generated, whose non-zero components also obey the Gaussian distribution. Throughout our investigations, we found that 10^6–10^8 random dispersion-matrix generations are typically required in order to achieve a good BER, depending on the matrix-size employed.

Fig. 3.7 shows the results of our random search conducted over a dispersion-matrix-set of 10^8 generations of the BPSK-modulated DSTSK$(2, 2, 2, Q)$ and ADSTSK$(2, 2, 2, Q)$ schemes of Fig. 3.5, where the parameter Q was given by $Q = 1, 2, 4$ and 8. More specifically, Fig. 3.7(a) shows the determinant value $\nabla = \prod_{m=1}^{m'} \frac{1}{\mu_m^N}$ recorded for different Q values. Furthermore, Fig. 3.7(b) shows the coding gain on the left vertical axis and the normalized throughput on the right axis. Observe in Figs. 3.7(a) and 3.7(b) that upon increasing the

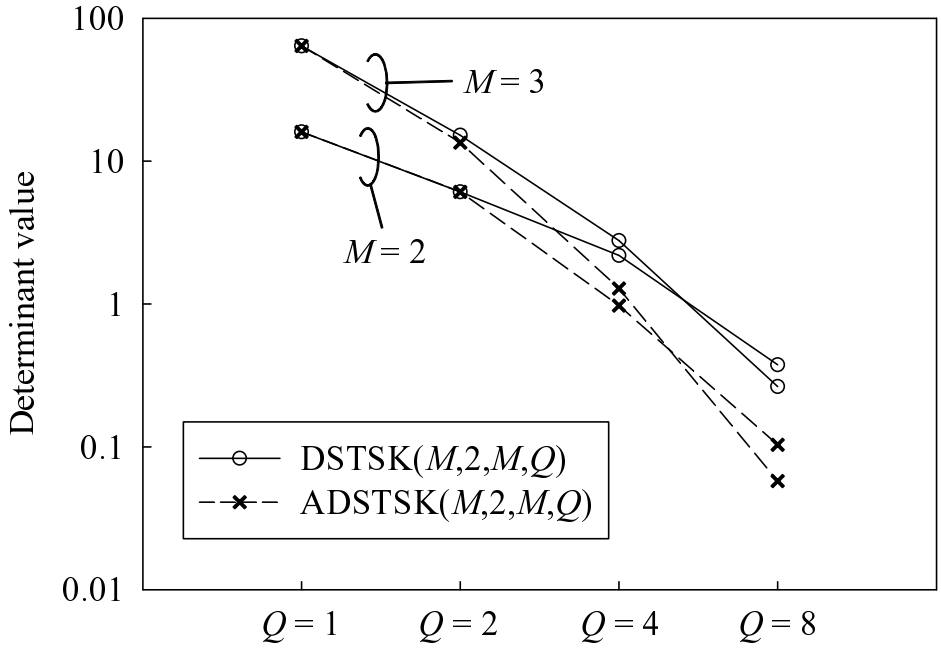

(a) Determinant value ∇, while having full rank

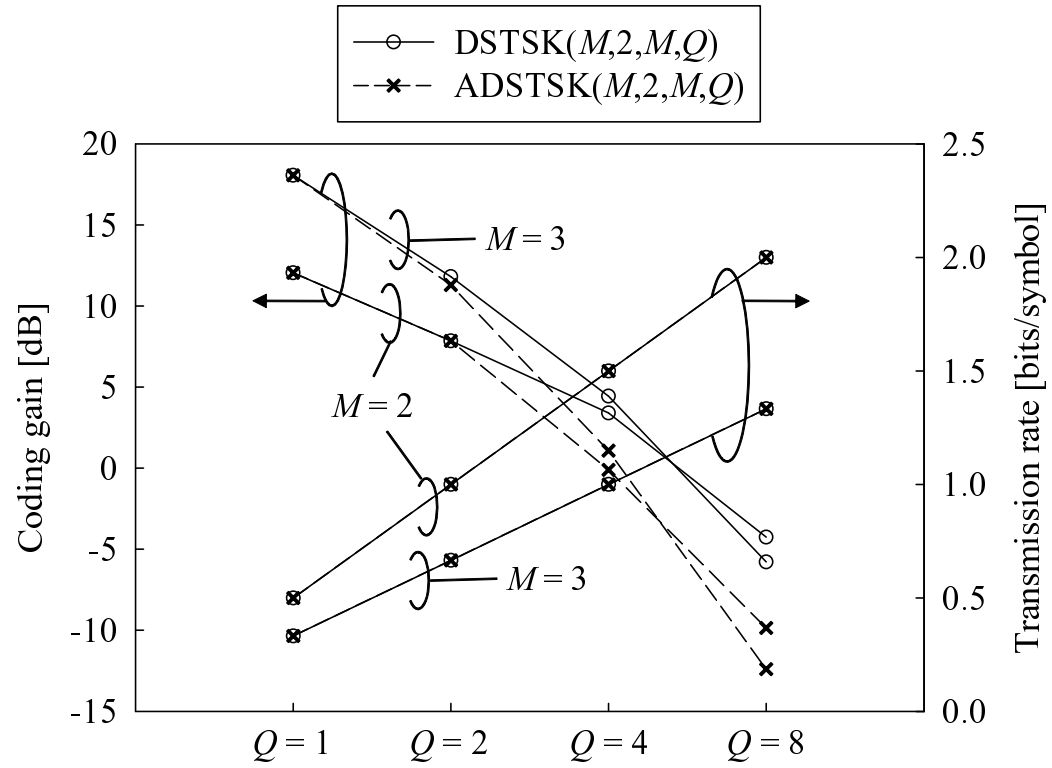

(b) Coding gain and transmission rate

Figure 3.7: Determinant-criterion assisted search results conducted over 10^8 dispersion-matrix generations for the BPSK-modulated DSTSK$(2, 2, 2, Q)$ and ADSTSK$(2, 2, 2, Q)$ schemes of Fig. 3.5, where the parameter Q is given by $Q = 1, 2, 4$ and 8. During the search the full-rank criterion was maintained.

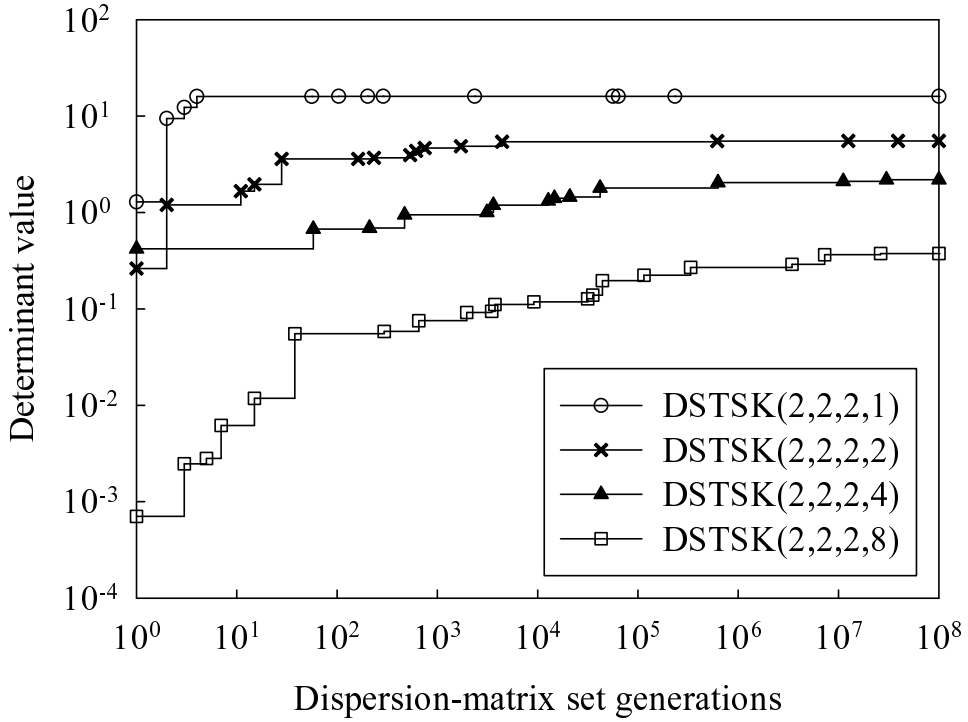

Figure 3.8: Convergence characterization of the search results over a search space of 10^8 dispersion-matrix generations for the BPSK-modulated DSTSK$(2, 2, 2, Q)$ scheme of Fig. 3.5, where the parameter Q is given by $Q = 1, 2, 4$ and 8. The corresponding effective throughput was $R = 0.5$, 1.0, 1.5 and 2.0 bits/symbol.

value of Q according to $Q = 1, 2, 4$ and 8, the achievable normalized transmission rate was increased from $R = 0.5$ bits/symbol to 2.0 bits/symbol for $M = 2$ antennas, as well as from $R = 0.33$ bits/symbol to 1.67 bits/symbol for $M = 3$ antennas. Observe in Fig. 3.7(a) that this was achieved at the cost of reducing the determinant value and hence the coding gain in Eq. (3.34), because a higher number of dispersion matrices Q results in a lower distance between the resultant ST signals $\boldsymbol{S}$. Furthermore, an increase in the number of transmit antennas from $M = 2$ to $M = 3$ tended to increase the value of the determinant and hence the diversity gain, except for the case of $Q = 8$. This is, because the search space of the DSTSK$(3, 2, 3, 8)$ scheme was very large and hence considering 10^8 dispersion-matrix generations was insufficient for the sake of finding an adequate dispersion-matrix set. Additionally, when comparing the DSTSK and ADSTSK schemes of Fig. 3.5, it was found that searching for a higher number of dispersion matrices Q resulted in a larger performance difference, although the ADSTSK scheme employing a small value of Q, such as $Q = 1, 2$, did not result in any substantial degradation over the DSTSK scheme.

Fig. 3.8 characterizes the convergence behavior of the search invoked to find a dispersion matrices for the DSTSK$(2, 2, 2, Q)$ scheme employing BPSK modulation, where we had $Q = 1, 2, 4$ and 8. Observe in the figure that a higher value of Q resulted in a reduced converged determinant value, while also requiring an increased search space for convergence.

Table 3.2: System parameters of the uncoded DSTSK scheme of Fig. 3.5

Number of transmit antennas	M
Number of receive antennas	N
Symbol durations per block	$T = M$
Number of dispersion matrices	Q
Modulation	$\mathcal{L}-$PAM
Channels	Frequency-flat Rayleigh fading
Channel's coherence-time	$\tau = 2$ block durations
Detector	ML detector of Eq. (3.10)

3.5.2 Uncoded System

Firstly, in Figs. 3.9, 3.10 and 3.11 we investigated the effects of the various DSTSK parameters on the achievable BER performance. Fig. 3.9 shows the BER performance, comparing a set of our DSTSK schemes, employing $M = 2, N = 2, T = 2$ and $Q = 1, 2, 4$ and 8. Similarly, Fig 3.10 considered the DSTSK schemes employing $M = 3, N = 2, T = 3$ and $Q = 1, 2, 4$ and 8. Observe in both the cases that as predicted from the determinant values of the dispersion-matrix optimization results of Fig. 3.7(a), an increase in the value of Q leads to an increased transmission rate R as well as to an increase in the SNR required to achieve a certain BER value. Observe in Fig. 3.11 that the achievable diversity gain monotonically increased with the number of transmit antennas M. We also note that in the high-SNR regime, each BER curve shown in Fig. 3.9 achieved the maximum attainable diversity order, which is expressed as $N \cdot \min(M, T) = N \cdot M$, as an explicit benefit of the rank- and determinant-criterion employed for the dispersion-matrix optimization.

Fig. 3.12 compares the BER curves of our BPSK-modulated DSTSK$(2, 2, 2, 2)$ scheme and those of the DOSTBC scheme employing $(M, N) = (2, 2)$ antenna elements, where the normalized Doppler frequency was 0.01. Here, the optimal ML detector of Eq. (2.32) was employed for the both schemes. As seen in Fig. 3.12, our DSTSK scheme marginally outperformed the DOSTBC scheme, where the BER of the DSTSK scheme recorded at BER $= 10^{-6}$, was 0.2 dB better than that of the DOSTBC scheme. This is the explicit benefit of the DSTSK's high design flexibility in terms of its throughput, coding gain and complexity.

In order to provide further insights, in Fig. 3.13 we investigated the achievable BER performance of our DSTSK scheme of Fig. 3.5, where we considered a 4–PAM assisted DSTSK$(2, 2, 2, 4)$ system, achieving a normalized throughput of $R = 2.0$ bits/symbol. Additionally, we also plotted the BER curves of the SM schemes suffering from different levels of CSI estimation errors, where the estimated channels were contaminated by the additive Gaussian noise of $\mathcal{CN}(0, \omega)$ having a power of 5, 10 and 15 dB below the signal power, hence

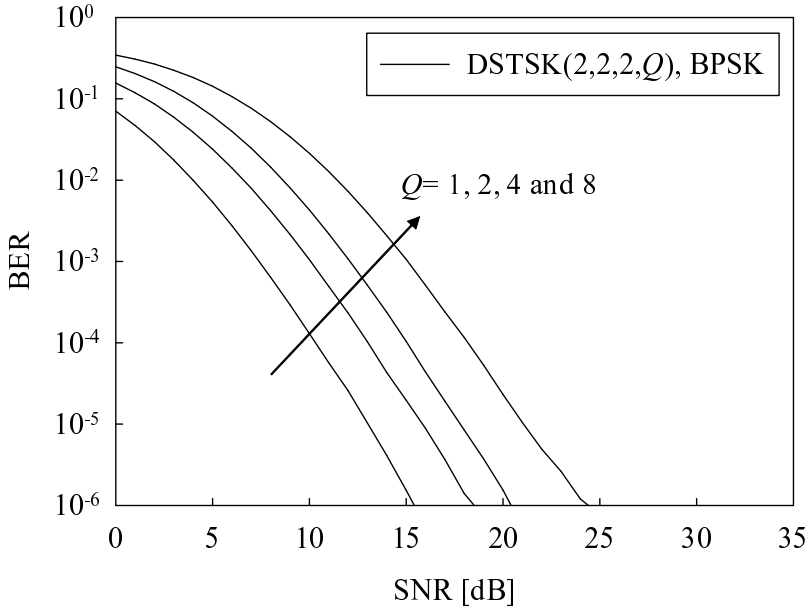

Figure 3.9: Achievable BER performance, comparing a set of our DSTSK schemes obeying the architecture of Fig. 3.5 and employing $M = 2, N = 2, T = 2$ and $Q = 1, 2, 4$ and 8, where the corresponding transmission rates are $R = 0.5, 1.0, 1.5$ and 2.0 bits/symbol, respectively. All other system parameters were summarized in Table 3.2.

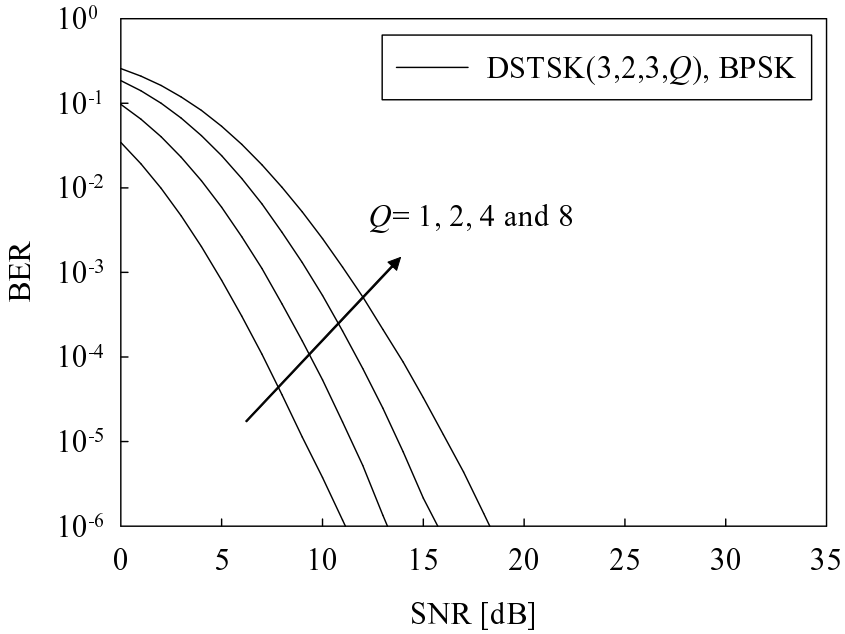

Figure 3.10: Achievable BER performance, comparing a set of our DSTSK schemes depicted in Fig. 3.5, employing $M = 3, N = 2, T = 3$ and $Q = 1, 2, 4$ and 8, where the corresponding transmission rates are $R = 0.33, 0.67, 1.0$ and 1.3 bits/symbol, respectively. All other system parameters were summarized in Table 3.2.

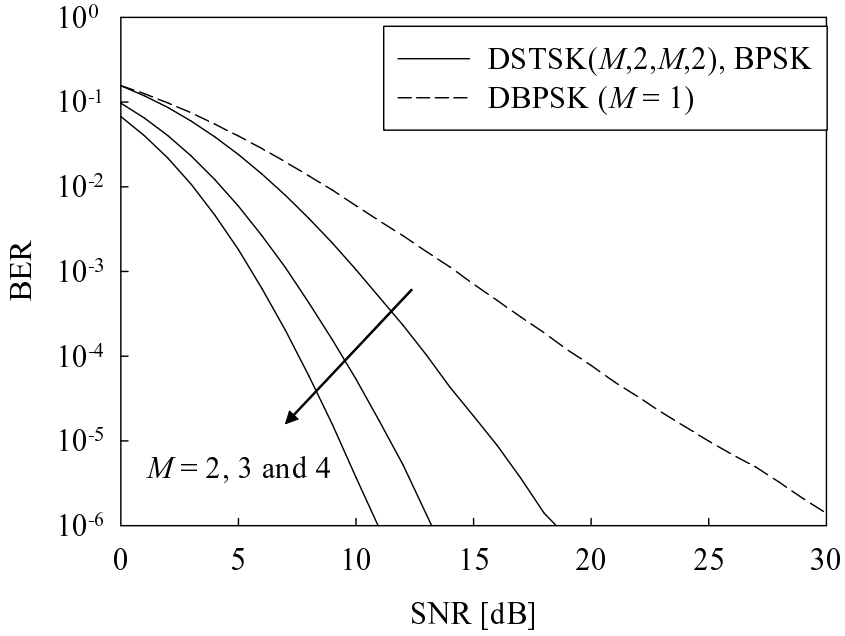

Figure 3.11: Achievable BER performance, comparing a set of our DSTSK schemes of Fig. 3.5 and employing $N = 2, Q = 2$ and $M = T = 2, 3, 4$. We also plotted the DBPSK scheme employing $(M, N) = (1, 2)$ antenna elements as the benchmarker. All other system parameters were summarized in Table 3.2.

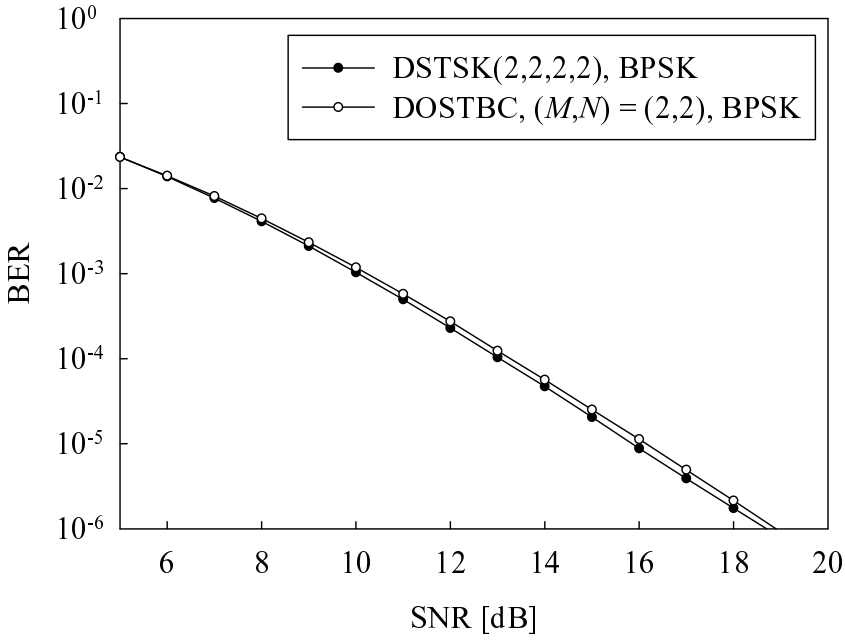

Figure 3.12: Achievable BER performance, comparing our BPSK-modulated DSTSK$(2, 2, 2, 2)$ scheme of Fig. 3.5 and the DOSTBC scheme of Fig. 3.1 employing $(M, N) = (2, 2)$ antenna elements, where the normalized Doppler frequency was 0.01. Here, the optimal ML detector of Eq. (3.10) was employed for the both schemes. All other system parameters were summarized in Table 3.2.

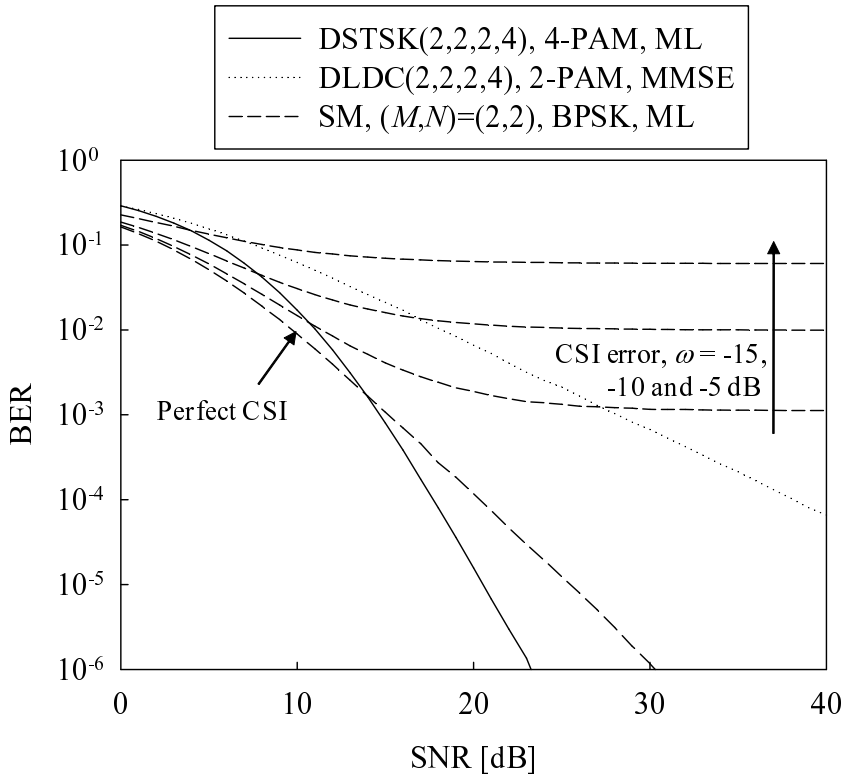

Figure 3.13: Achievable BER of our DSTSK scheme of Fig. 3.5, compared to the DLDC scheme of Fig. 3.2 as well as the SM scheme of Fig. 2.1 suffering from a CSI estimation error associated with an equivalent CSI-estimation SNR of $\omega = 5, 10$ and 15 dB. All other system parameters were summarized in Table 3.2.

yielding CSI-related equivalent SNRs of $\omega = -5$ dB, -10 dB and -15 dB. Furthermore, we employed the DLDC scheme of [89] as another benchmarker, where the MMSE criterion was employed for the DLDC's detection algorithm, noting that its complexity was higher than that of our DSTSK employing the single-antenna-based ML detector. Observe in Fig. 3.13 that as expected, our DSTSK scheme achieved a diversity order of four, hence outperforming both the DLDC scheme and the coherent SM scheme, which suffered from CSI estimation errors. Additionally, even for the case of no CSI error, the BER performance of our DSTSK scheme was better than that of the coherent SM scheme, when the SNR was higher than 14 dB.

The presence of Doppler spread may impose severe degradation on the achievable performance of the DSTSK scheme, since in the differential-encoding operation the current signal block is used as a reference for the next signal block. When the channel coefficients change substantially during the two consecutive block durations, the reference become inaccurate. To this end, in Fig. 3.14 we characterized the effects of the normalized Doppler frequency f_D on the attainable performance of our BPSK-modulated DSTSK$(2, 2, 2, 2)$ scheme, where we quantified the effective throughput recorded at BER $= 10^{-4}$, while f_D was varied from 10^{-6} to 0.06. Observe in Fig. 3.14 that when the normalized Doppler frequency was low, in particular $f_D < 10^{-2}$, the achievable performance remained unaffected by the Doppler shift.

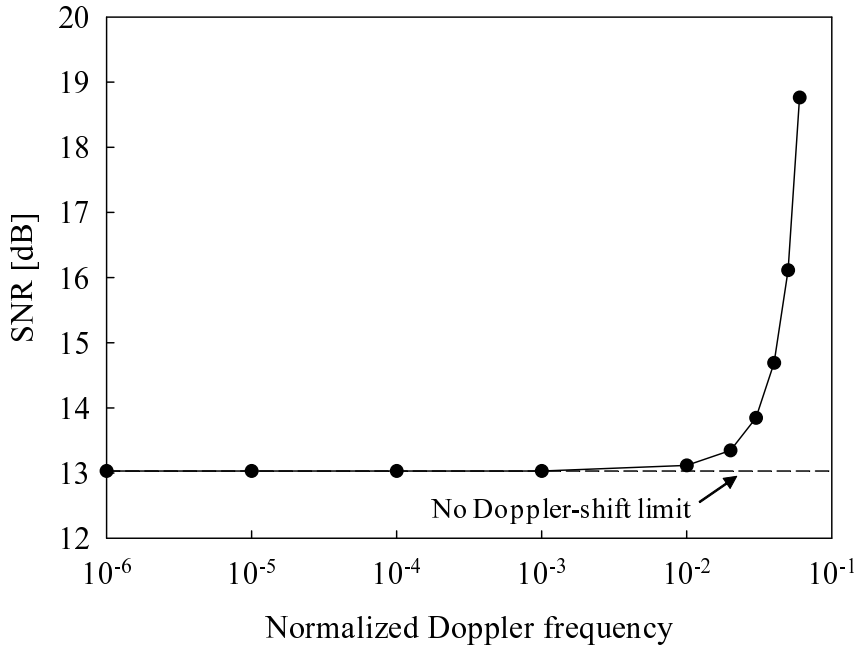

Figure 3.14: The SNR required by our BPSK-modulated DSTSK$(2, 2, 2, 2)$ scheme of Fig. 3.5 recorded at BER $= 10^{-4}$, where the normalized Doppler frequency $f_{\rm D}$ was varied from 10^{-6} to 0.06. All other system parameters were summarized in Table 3.2.

On the other hand, in the range of $f_{\rm D} \geq 10^{-2}$, its performance was substantially degraded, upon increasing the parameter $f_{\rm D}$. To be more quantitative, assuming a basic chip rate of $1/T_{\rm s} = 3.6864$ Mchips/s as well as a carrier frequency of $f = 2.0$ GHz, which are employed for cdma2000 [24], the maximum vehicular speed of $v = 100$ km/h ($= 27.78$ m/s) corresponds to the normalized Doppler frequency of $f_{\rm D} \simeq vT_{\rm s}\frac{f}{c} = 5.0 \times 10^{-5}$ [28]. For this reason, we mainly focused our attention on the zero Doppler-shift scenarios in this chapter, acknowledging that the increase in the number of symbols per block T, the sample duration $T_{\rm s}$ and the carrier frequency f may give rise to a non-negligible performance degradation due to the associated Doppler effect.

In order to offer further insights, in Fig. 3.15 we compared the achievable BER performance of our $\mathcal{L}$-PAM aided DSTSK and ADSTSK, where we varied the parameters according to $(\mathcal{L}, M, Q) = (2, 2, 2), (2, 3, 2), (4, 2, 4)$ and $(4, 3, 4)$, while maintaining a fixed number of receive antennas, namely $N = 2$. It was found that for $Q = 2$, the achievable BER curves of the DSTSK and ADSTSK schemes were almost identical for both $M = 2$ and $M = 3$. On the other hand, the achievable BER curves recorded for $Q = 4$ exhibited an SNR difference of 2.5 dB between the DSTSK and ADSTSK schemes for $M = 2$ and 1.2 dB for $M = 3$, as recorded at BER $= 10^{-4}$. This is because in uncoded scenarios the ADSTSK scheme's limited set of dispersion matrices may substantially reduce the achievable performance, especially for a higher Q value.

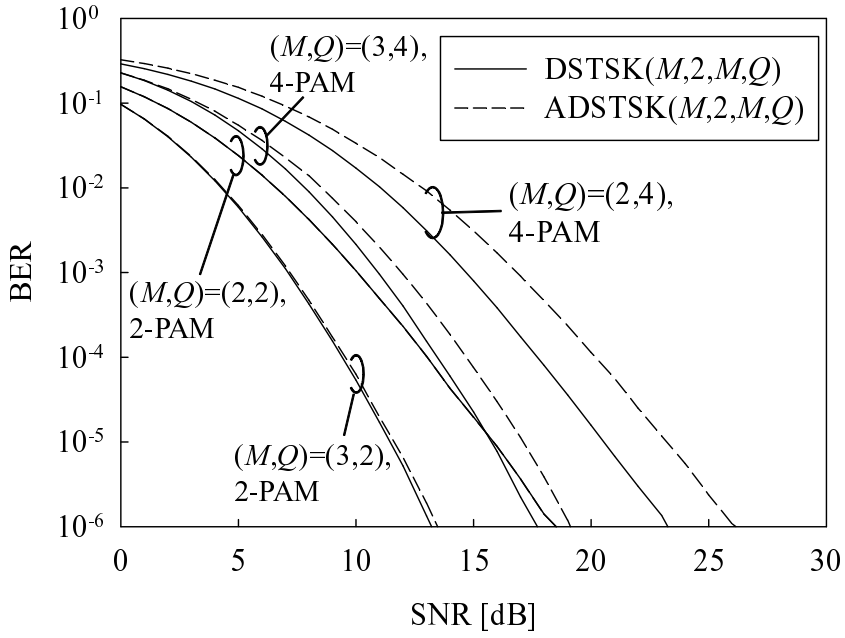

Figure 3.15: Achievable BER of our $\mathcal{L}$-PAM aided DSTSK and ADSTSK schemes of Fig. 3.5, where we varied the parameters $(\mathcal{L}, M, Q) = (2, 2, 2), (2, 3, 2), (4, 2, 4)$ and $(4, 3, 4)$, while having $N = 2$ receive antennas. All other system parameters were summarized in Table 3.2.

3.5.3 Coded System

Having discussed the uncoded system's performance, let us now characterize the performance of our turbo-coding assisted $\mathcal{L}$-PAM aided DSTSK$(M, N, T = M, Q)$ scheme, which is shown in Fig. 3.6. More specifically, we employed the half-rate Recursive Systematic Convolutional (RSC) code RSC(2,1,2) code having the generator polynomials of $(3, 2)_8$ in octal format for the channel encoder and the interleaver length of $\Pi_1 = \Pi_2 = 200\,000$ bits. Furthermore, the number of inner iterations was set to $I_{\text{in}} = 1$, while the number of outer iterations was varied from $I_{\text{in}} = 0$ to $I_{\text{in}} = 10$.

Firstly, we designed our DSTSK parameters with the aid of EXIT chart analysis. Fig. 3.16 shows the maximum achievable rates of our RSC- and URC-coded $\mathcal{L}$-PAM aided DSTSK(2, 2, 2, Q) scheme obeying the architecture of Fig. 3.3, exhibiting the inner code rate of $R = 2.0$ bits/symbol. As detailed in Section 2.7.2, the maximum achievable rates were calculated based on the associated EXIT charts. We note that in our DSTSK scheme, there are several combinations of $(\mathcal{L}, Q)$, achieving the targeted inner code rate, hence we simulated all of the four potential combinations, where $(\mathcal{L}, Q)$ were given by $(\mathcal{L}, Q) = (16, 1), (8, 2), (4, 4)$ and $(2, 8)$. Observe in Fig. 3.16 that depending on the choice of $(\mathcal{L}, Q)$, the capacity curve exhibited the different characteristics. More specifically, although the capacity curve printed in continuous line and corresponding to $(\mathcal{L}, Q) = (16, 1)$ exhibited the highest throughput in the low-SNR regime, i.e. below about -2 dB associated with $C \leq 0.30$ bits/symbol, the

Table 3.3: Basic system parameters of the coded DSTSK scheme of Fig. 3.6.

Number of transmit antennas	$M = 2$
Number of receive antennas	$N = 2$
Symbol durations per block	$T = 2$
Number of dispersion matrices	Q
Modulation	$\mathcal{L}-$PAM
Channels	Frequency-flat Rayleigh fading
Channel's coherence-time	$\tau = 2$ block durations
Detector	Max-log MAP detector of Eq. (2.43)
Interleaver blocklength	200 000 bits
Outer channel code	RSC$(2, 1, 2)$
Generator polynomials	$(G_\mathrm{r}, G) = (3,2)_8$
Precoder	URC
Number of inner iterations	$I_\mathrm{in} = 1$
Number of outer iterations	$I_\mathrm{in} = 10$
System bandwidth efficiency	1 bit per channel use

$(\mathcal{L}, Q) = (4, 4)$ scheme indicated by the dashed line outperformed the other three scenarios for higher SNRs. Since the effective transmission rate of our DSTSK system employing the half-rate RSC code is $R = 1.0$ bits/symbol, the DSTSK scheme associated with $(\mathcal{L}, Q) = (4, 4)$ may be selected from these four DSTSK arrangements as the most beneficial one. Fig. 3.17 portrays the EXIT curves of the four different DSTSK arrangements recorded at SNR = 4 dB, which represent the maximum achievable rates shown in Fig. 3.16. It was also found from Fig. 3.17 that the EXIT curves of the $\mathcal{L}$ = 4-PAM aided DSTSK$(2, 2, 2, 4)$ scheme exhibited the highest performance when comparing the four inner decoders' EXIT curves. Observe in Fig. 3.17 that it has the potential of achieving the fast convergence to the point $(I_\mathrm{in}, I_\mathrm{in}) = (1.0, 1.0)$, where an infinitesimally low BER may be attained. Furthermore, Fig. 3.18 shows the maximum achievable rates of the $\mathcal{L}$-PAM aided DSTSK$(2, 2, 2, Q)$ scheme, exhibiting the four different inner code rates of $R = 0.5, 1.0, 1.5$ and 2.0 bits/symbol. The corresponding overall throughputs after 1/2-rate coding become $R = 0.25, 0.5, 0.75$ and 1.0 bits/symbol. Naturally, the attainable throughput may always be improved with the aid of higher-order modulation schemes.

In Fig. 3.19 we plotted the EXIT chart of the three-stage RSC(2,1,2)- and URC coded DSTSK$(2, 2, 2, 4)$ of Fig. 3.6 employing BPSK modulation, in order to characterize its con-

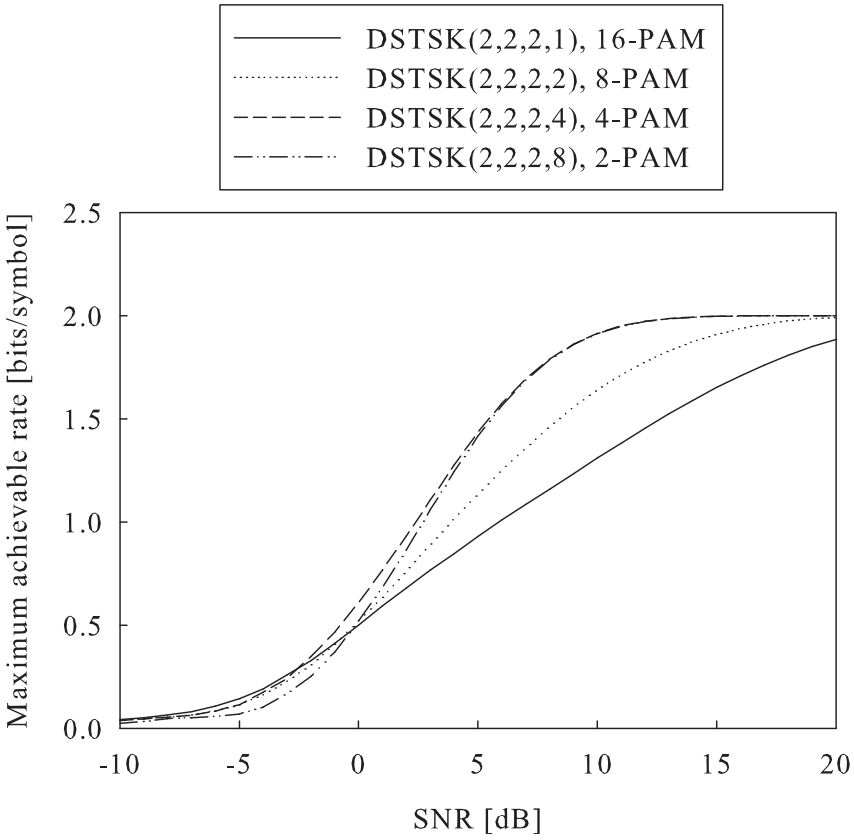

Figure 3.16: Maximum achievable rate of our $\mathcal{L}$-PAM aided DSTSK$(2, 2, 2, Q)$ scheme of Fig. 3.6 having the corresponding inner code rate of $R = 2.0$ bits/symbol, where the set of parameters $(\mathcal{L}, Q)$ was given by $(\mathcal{L}, Q) = (1, 16), (2, 8), (4, 4), (8, 2)$, while employing the single-stream-based ML detector. All other system parameters were summarized in Table 3.3. The achievable rate was extracted from the EXIT-chart of Fig. 3.17.

vergence behavior, where the SNR was varied from 1 dB to 6 dB. The Monte Carlo simulation based bit-by-bit decoding trajectory recorded at SNR = 3.5 dB as well as the outer EXIT curve of the URC code were also plotted, while assuming the employment of the single-stream-based ML detector. Observe in Fig. 3.19 that all the inner EXIT curves reached the point of perfect convergence at $(I_{\mathrm{A}}.I_{\mathrm{E}}) = (1.0, 1.0)$ as the explicit benefit of the URC encoder, which is capable of gleaning extrinsic information from all the bits within a frame. Additionally, upon increasing the SNR value, the corresponding inner EXIT curve shifted upwards, where an open EXIT tunnel appeared at SNR $>$ 3.0 dB. The decoding trajectory suggested that an infinitesimally low BER may be achieved with the aid of $I_{\mathrm{out}} = 9$ outer iterations, under the assumption of $I_{\mathrm{in}} = 1$ inner iteration.

Next, the achievable BER performance corresponding to the EXIT-chart of Fig. 3.19 was characterized in Fig. 3.20, where the number of outer iterations was varied from $I_{\mathrm{out}} = 0$ to $I_{\mathrm{out}} = 10$. Observe that upon increasing the number of outer iterations, the associated BER curve was substantially improved, gradually leading to an infinitesimally low BER at SNR = 3.5 dB. This result confirmed the EXIT-chart-aided iterative convergence prediction of Fig. 3.19. We note that a near-capacity performance was indeed achieved, exhibiting as

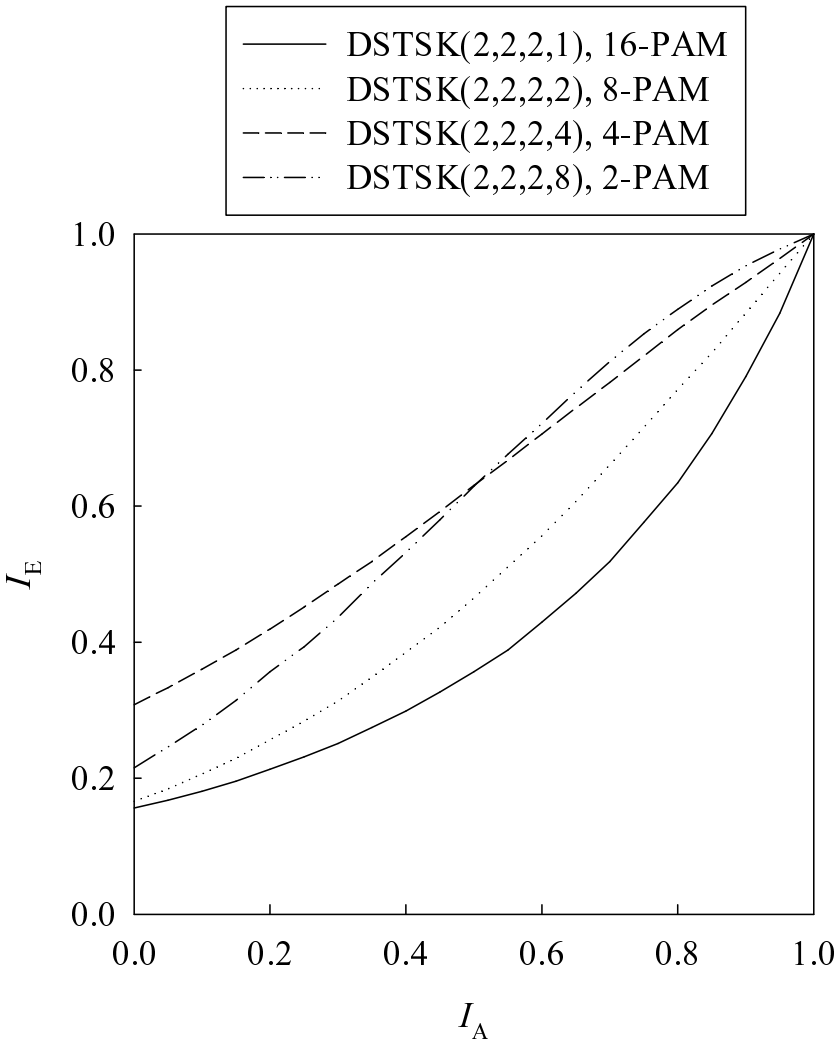

Figure 3.17: Inner EXIT curves of our $\mathcal{L}$-PAM aided DSTSK$(2, 2, 2, Q)$ scheme of Fig. 3.6 having the corresponding inner code rate of $R = 2.0$ bits/symbol, where the set of parameters $(\mathcal{L}, Q)$ was given by $(\mathcal{L}, Q) = (1, 16), (2, 8), (4, 4), (8, 2)$, while employing the single-stream-based ML detector. All other system parameters were summarized in Table 3.3.

low as 1.1 dB difference between the SNR where a vanishingly low BER may be attained at the specific effective throughput of $R = 1.0$ bits/symbol and that calculated by Monte-Carlo simulations. To expound a little further, in Fig. 3.21 we investigated the computational complexity imposed by our RSC-coded and URC-coded DSTSK$(2, 2, 2, 4)$ scheme of Fig. 3.6 and characterized in Fig. 3.20, which was derived by considering the number of iterations required to attain BER $= 10^{-5}$. For the sake of simplicity we assumed that the total complexity is dominated by that of the DSTSK's SISO detector block of Fig. 3.6, in comparison to those of the URC and RSC decoders. Observe in Fig. 3.21 that upon increasing the number of outer iterations I_{out}, the achievable performance improved at the expense of an increased complexity. It was also found that the first four iterations provided the highest gain, while any further iterations exhibited a modest gain at a substantial increase in the complexity.

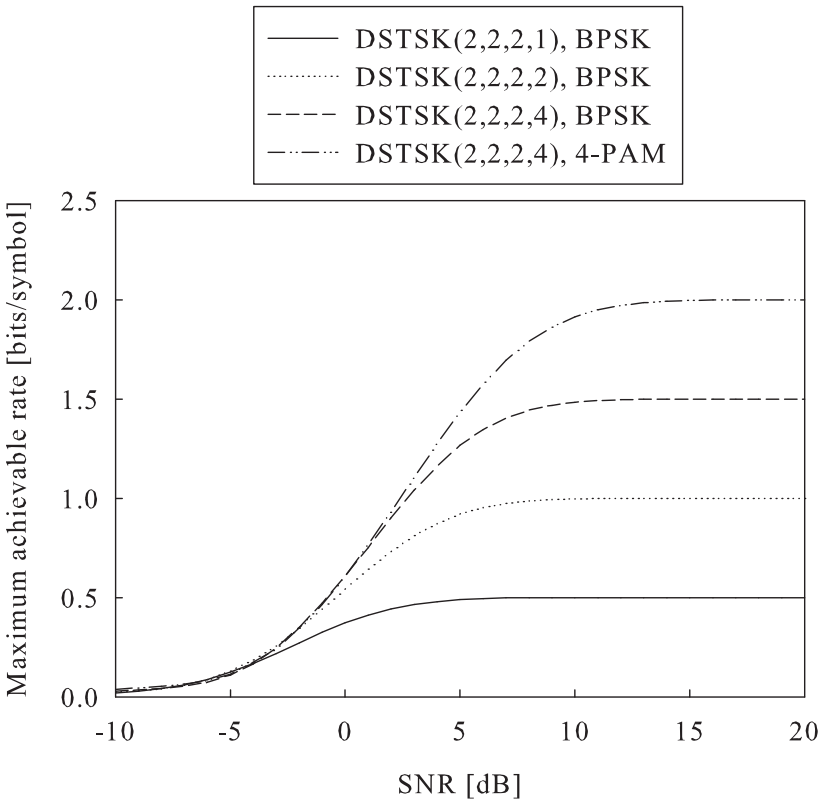

Figure 3.18: Maximum achievable rate of our $\mathcal{L}$-PAM aided DSTSK$(2, 2, 2, Q)$ scheme of Fig. 3.6, where the set of parameters $(\mathcal{L}, Q)$ was given by $(\mathcal{L}, Q) = (2, 1), (2, 2), (2, 4), (4, 4)$, while employing single-stream-based ML detector. The corresponding inner code rates are $R = 0.5, 1.0, 1.5$ and 2.0 bits/symbol. All other system parameters were summarized in Table 3.3. The achievable rate was extracted from the corresponding EXIT chart.

Fig. 3.22 compares the achievable BER performance of the coded/uncoded DSTSK(2, 2, 2, 4) and ADSTSK$(2, 2, 2, 4)$ schemes of Figs. 3.5 and 3.6 employing $\mathcal{L} = 4$-PAM and the single-stream-based ML detector, where the number of iterations $(I_{\text{in}}, I_{\text{out}})$ invoked by the coded systems was given by $(I_{\text{in}}, I_{\text{out}}) = (1, 10)$. It can be seen from Fig. 3.22 that the performance difference between the DSTSK and ADSTSK schemes became smaller, when turbo-coding was employed. More specifically, the SNR performance difference of the uncoded systems at BER $= 10^{-6}$ was 2.9 dB, while that of the coded systems was only 0.7 dB. This implies that the employment of the near-capacity turbo-coding principle makes our ADSTSK scheme more practical, even for the case of a higher Q value.

3.6 Chapter Conclusions

In Section 3.2, we commenced our discourse with a review of the conventional differentially-encoded STC arrangements, such as the DOSTBC and the DLDCs. In Section 3.3, motivated by the benefits of the coherent STSK scheme introduced in Section 2.3, we have proposed the novel differential modulation principle of DSTSK schemes of Fig. 3.5, which relies on the

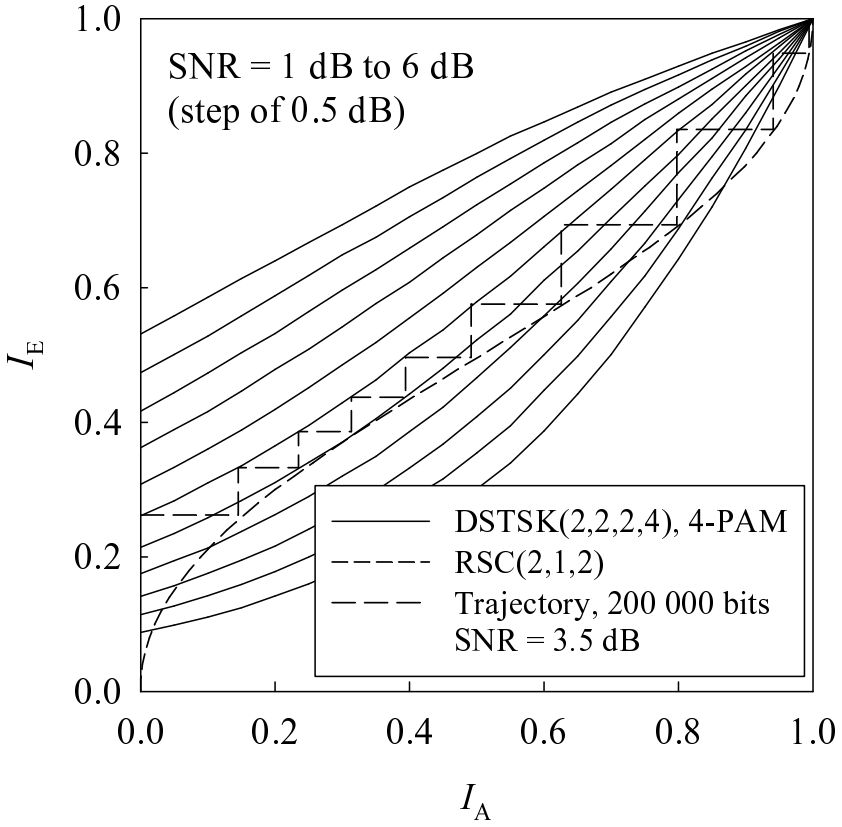

Figure 3.19: EXIT chart of our 4-PAM aided DSTSK$(2, 2, 2, 4)$ system of Fig. 3.6, employing an single-stream-based ML detector, where the SNR was changed from 1 dB to 6 dB. The outer EXIT curve of the half-rate RSC$(2, 1, 2)$ code as well as the decoding trajectory at SNR = 3.5 dB were also plotted. The interleaver-length was 200 000 bits for the Monte-Carlo simulation based decoding trajectory. All other system parameters were summarized in Table 3.3.

Cayley unitary transform. This concept enables us to strike the required tradeoff between the MIMO's diversity and multiplexing gains, similarly to the coherent STSK scheme, while dispensing with the requirement of CSI estimation. Hence, the achievable performance of our DSTSK scheme is not affected by the CSI estimation errors, although it is sensitive to the Doppler frequency. Additionally, in Section 3.3.1 we modified the DSTSK scheme so that it does not require any simultaneous transmissions from the multiple antenna elements and hence the usual symbol-level IAS is avoided. We referred to this arrangement as the ADSTSK scheme. Here, we derived the optimal single-stream ML detector for an uncoded scenario. Then, in Section 3.3.2 we characterized the associated computational complexity required for the single-stream-based ML detection of our uncoded DSTSK and ADSTSK schemes, which exhibited a realistic computational complexity, as a benefit of its single-stream-based ML search algorithm. Moreover, in Section 3.4 the proposed DSTSK scheme was extended to a three-stage serially concatenated arrangement for the sake of achieving a near-capacity performance, where we can directly utilize the previously derived soft demapper presented

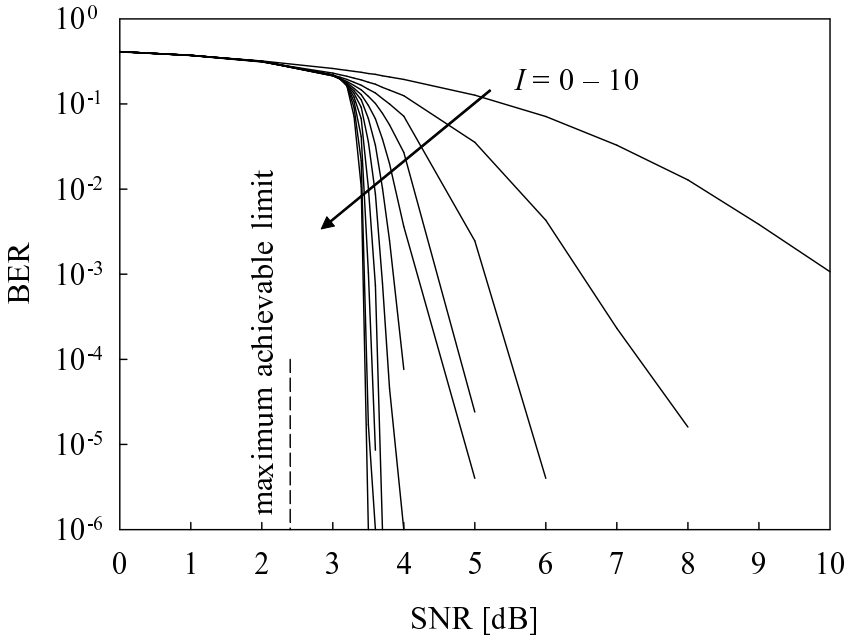

Figure 3.20: Achievable BER performance of our RSC-coded and URC-coded DSTSK$(2, 2, 2, 4)$ scheme of Fig. 3.6, using 4-PAM and an interleaver length of $\Pi_1 = \Pi_2 = 200\,000$ bits. All other system parameters were summarized in Table 3.3. The dashed-line indicates the lowest possible SNR, at which an infinitesimally low BER may be attained at the effective throughput of 1.0 bits/symbol.

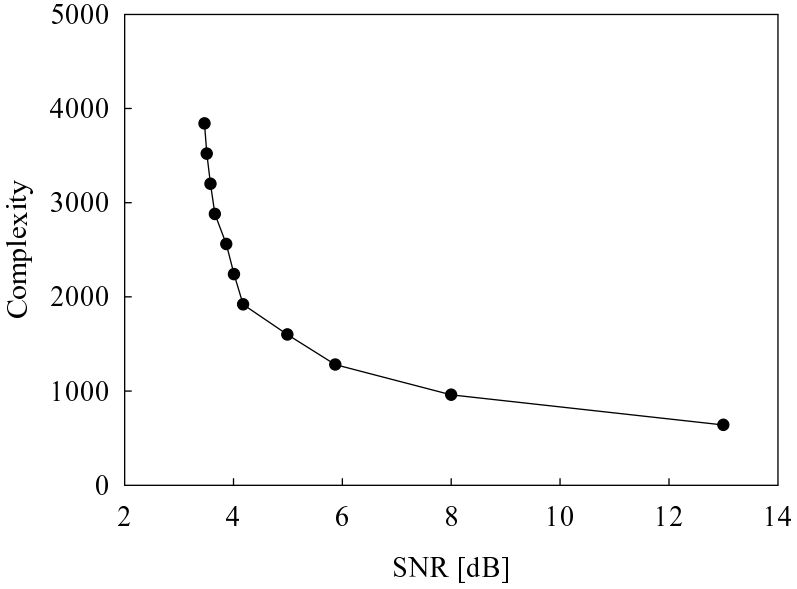

Figure 3.21: Computational complexity imposed by our RSC-coded and URC-coded DSTSK$(2, 2, 2, 4)$ scheme of Fig. 3.6, using 4-PAM and an interleaver length of $\Pi_1 = \Pi_2 = 200\,000$ bits recorded at the SNR value required to attain BER $= 10^{-5}$. Here, we varied the number of outer iterations from $I_{\text{out}} = 0$ to $I_{\text{out}} = 10$, while setting the number of inner iterations to $I_{\text{in}} = 1$. All other system parameters were summarized in Table 3.3.

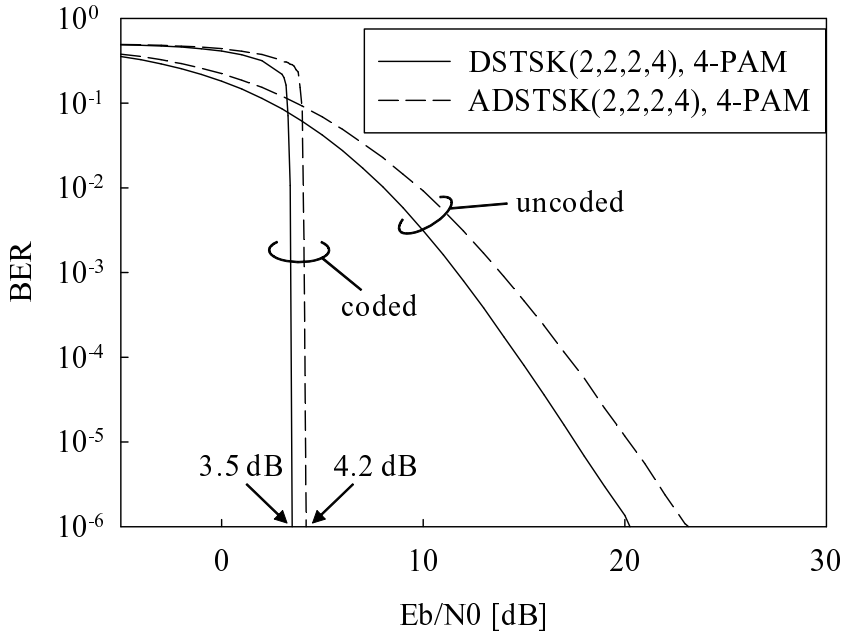

Figure 3.22: Achievable BER performance of both the coded and uncoded ADSTSK/DSTSK$(2, 2, 2, 4)$ schemes of Fig. 3.6 with the aid of $\mathcal{L}$ = 4-PAM, where the RSC(2,1,2) and URC codes are employed for the coded system in conjunction with an interleaver length of $\Pi_1 = \Pi_2 = 200\,000$ bits. All other system parameters were summarized in Table 3.3.

in Section 2.4.2.

The performance of our DSTSK scheme was characterized in Section 3.5, where the uncoded DSTSK and ADSTSK schemes of Fig. 3.5 were considered in Section 3.5.2. We then continued by investigating the coded DSTSK scheme of Fig. 3.6 with the aid of EXIT chart analysis in Section 3.5.3. In Fig. 3.23 we revisited our performance results recorded for the family of uncoded DSTSK schemes. Here, Fig. 3.23 summarizes the effective throughput recorded at BER $= 10^{-4}$ for the DSTSK$(2, 2, 2, Q)$ scheme of Fig 3.5, the ADSTSK$(2, 2, 2, Q)$ scheme of Fig. 3.5 and coherent STSK$(2, 2, 2, Q)$ scheme of Fig. 2.5, where the transmission rate was varied from 0.5 to 2.0 bits/symbol. Although in comparison to the coherent STSK scheme of Fig. 2.5, our DSTSK scheme of Fig. 3.5 suffered from the typical error-doubling effects of differential encoding, the corresponding achievable performance may not be affected by the CSI estimation errors, which potentially degrades the performance of the coherent STSK scheme. Additionally, the DSTSK scheme of Fig. 3.5 outperformed the ADSTSK scheme arrangement for higher values of Q, since the search space of the ADSTSK's dispersion matrices is constrained. However, the ADSTSK scheme has the benefit of dispensing with symbol-level IAS. Fig. 3.24 shows the effective throughput of our DSTSK scheme of Fig. 3.5 employing $M = 2$ transmit antennas and $N = 1, 2, 4$ receive antennas. We found in Fig. 3.24 that for each N an approximately 7.3 dB power was required to increase the effective throughput from 0.5 to 2.0 bits/symbol. We may this in the light of considering that a

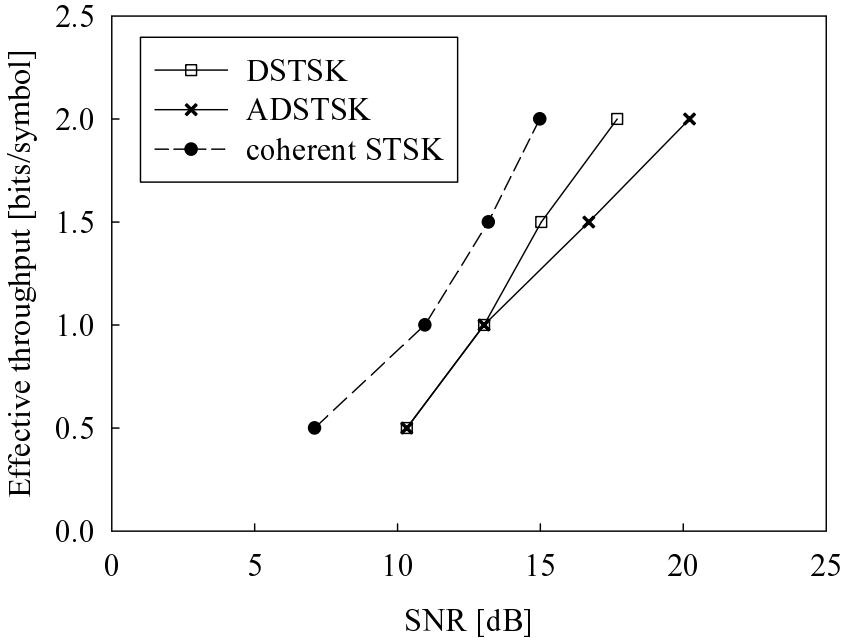

Figure 3.23: Effective throughput recorded at BER $= 10^{-4}$, comparing the $\mathcal{L}$-PAM aided and 1/2-rate coded DSTSK, ADSTSK and coherent STSK schemes of Figs. 3.6 and 2.7, which employ $M = 2$ transmit antennas and $N = 2$ receive antennas, while varying the parameters $(\mathcal{L}, Q)$. For each plot of the effective throughput, the best ones out of all possible combinations $(\mathcal{L}, Q)$ were selected. The system parameters are summarized in Table 3.2.

quadrupled throughput requires a minimum of quadrupled power, corresponding to 6 dB, hence our schemes may be deemed to be power-efficient.

In Chapters 2 and 3, we proposed the novel STSK and DSTSK architecture of Figs. 2.5 and 3.5, which facilitate low-complexity MIMO implementations, while achieving both flexible diversity-multiplexing gains tradeoffs as well as enabling single-stream-based ML detection. In the following chapter, we will further generalize the family of STSK schemes, in order to conceive more flexible system architectures in terms of the achievable diversity gain, transmission rate and computational complexity. Furthermore, we will link the STSK scheme to diverse other MIMO arrangements.

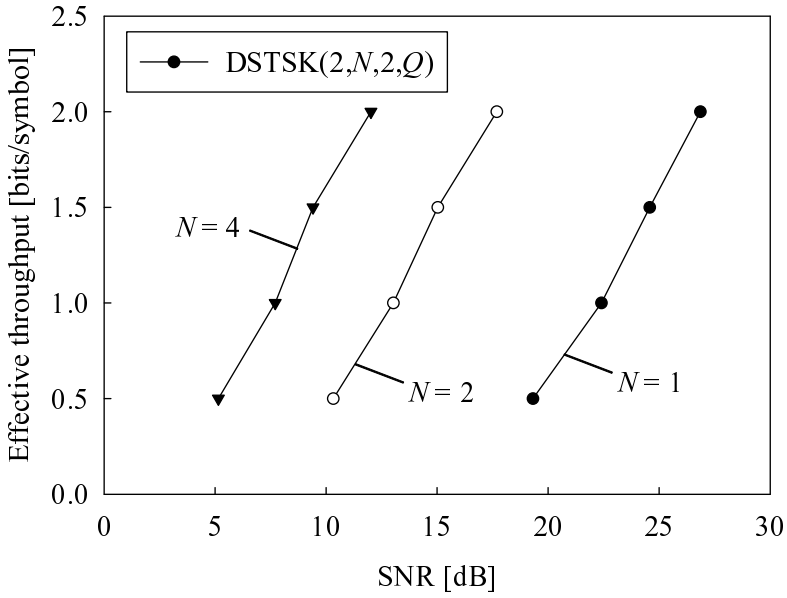

Figure 3.24: Effective throughput recorded at BER $= 10^{-4}$ of our $\mathcal{L}$-PAM aided and 1/2-rate coded DSTSK$(2, N, 2, Q)$ scheme of Fig. 3.5, which employ $M = 2$ transmit antennas and $N = 1, 2, 4$ receive antennas, while varying the parameters $(\mathcal{L}, Q)$. For each plot of the effective throughput, the best ones out of all possible combinations $(\mathcal{L}, Q)$ were selected. The system parameters are summarized in Table 3.2.

Table 3.4: Summary of the DSTSK and ADSTSK scheme, employing the system parameters of Table 3.3, where the system bandwidth efficiency was given by $R = 1.0$ bits/symbol.

	DSTSK	**ADSTSK**	**CSTSK**	**DLDC**
Schematic	Fig. 3.6	←	Fig. 2.7	Fig. 3.6[a]
CSI	No CSI	←	Perfect CSI	No CSI
IAS	Symbol-level	Relaxed	Symbol-level	←
Dispersion-matrix	Hermitian	Real-valued diagonal	Power constraint of Eq. (2.21)	Hermitian
Iterations $(I_{\text{in}}, I_{\text{out}})$	(1,10)			
FEC rate	0.5			
Complexity per iteration	$\frac{MNQ(8M^2+6\mathcal{L})}{\log_2(Q\cdot\mathcal{L})} = 224$	$\frac{MNQ(8M+6\mathcal{L})}{\log_2(Q\cdot\mathcal{L})} = 80$	$\frac{NTQ[(8MT+4\mathcal{L})/\tau+2\mathcal{L}]}{\log_2(Q\cdot\mathcal{L})} = 32+192/\tau$	$\frac{MN[8M^2Q+4(2Q+1)\mathcal{L}2^Q]}{Q\log_2\mathcal{L}} = 768$
Performance[a] $(M\times N)=(2\times 2)$	3.5 dB	4.2 dB	−0.8 dB	3.1 dB

[a] DSTSK block of Fig. 3.6 is replaced by the DLDC block of Fig. 3.2

[b] Performance is given by the SNR value required for achieving an infinitesimally BER.

Chapter 4

Generalized Space-Time Shift Keying for Co-Located MIMO Systems

4.1 Introduction

In Chapters 3 and 4, we proposed the new unified coherent and differential STSK MIMO modulation principles, which adopt the underlying concept of activating one out of Q dispersion matrices, whose matrix-activation process acts as an additional means of conveying information bits. This STSK concept enables us to invoke a realistic single-stream-based ML detection, since no spatial multiplexing is used. Hence its multiplexing gain is unity. By contrast, as described in Section 2.2.3, the classic LDC scheme may be viewed as another unified MIMO scheme, where all the Q preassigned dispersion matrices are linearly combined and the resultant multiplexed streams are transmitted simultaneously. Thus, the multiplexing gain of the LDC scheme corresponds to the value of Q, where the transmission rate can be linearly increased with Q at the cost of a substantially increased computational complexity.

Bearing in mind that both the STSK and LDC schemes are capable of striking flexible rate-diversity tradeoffs, a further generalized MIMO framework may be conceived by increasing the number of activated dispersion matrices in the STSK scheme, which amalgamates benefits of both the STSK scheme's dispersion-matrix activation as well as those of the LDC scheme's dispersed-symbol based multiplexing capability. The resultant arrangement is capable of achieving significantly flexible rate-, diversity- and complexity-tradeoffs. More specifically, in this chapter we will propose the so-called Generalized STSK (GSTSK) family, where P out of Q dispersion matrices are activated during each transmission interval. As shown in Fig. 4.1, owing to its high flexibility, the GSTSK framework subsumes most of

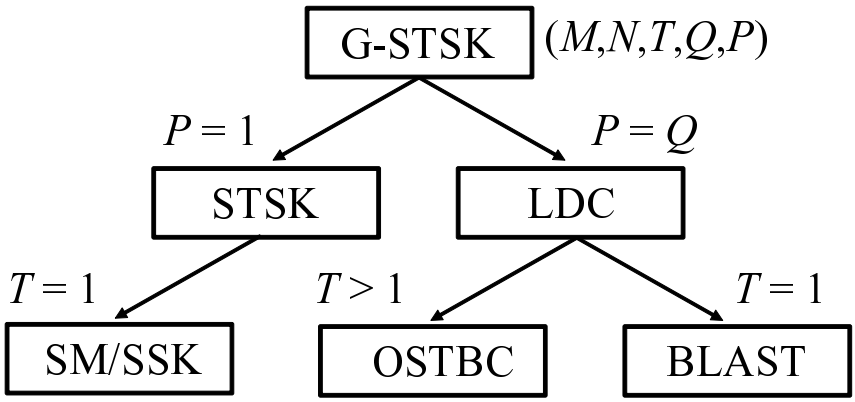

Figure 4.1: Relationship between our GSTSK scheme proposed in Chapter 4 and other MIMO schemes. The STSK, LDC, SM/SSK, OSTBC and BLAST were the subject of Chapter 2.

the above-mentioned MIMO arrangements, such as SM/SSK, LDC/DLDC, OSTBC as well as BLAST, and therefore has the potential of flexibly mimicking all of them. Additionally, we conceive the optimal ML detector designed for uncoded GSTSK systems and the soft-demodulator conceived for the coded GSTSK systems. Moreover, we also derive both the DCMC capacity [59] and the theoretical BER upper bound [138] of our GSTSK scheme, which serves as the unified capacity and BER, hence characterizing diverse MIMO arrangements. EXtrinsic Information Transfer (EXIT) chart analysis [130] is invoked for designing our GSTSK scheme and for characterizing its iterative detection process.

The remainder of this paper is organized as follows. Section 4.2 introduces the system model of our GSTSK scheme, and then both the corresponding hard- and soft-decision detectors are presented in Section 4.3. In Section 4.4 we derive the DCMC capacity of our GSTSK scheme, while Section 4.5 conceives the theoretical tight BER upper bound. Then, our performance results are provided in Section 4.6. Finally, the paper is concluded in Section 4.7.

4.2 System Model

In this section we introduce our GSTSK scheme and then demonstrate that it subsumes many MIMO schemes as its special cases.

Similarly to the CSTSK scheme, which was proposed in Chapter 2, let us first consider the general block-based space-time system model of [23]

$$\boldsymbol{Y}(i) \quad = \quad \boldsymbol{H}(i)\boldsymbol{S}(i) + \boldsymbol{V}(i), \tag{4.1}$$

where $\boldsymbol{Y}(i) \in \mathcal{C}^{N\times T}$ are the signals received at the receiver equipped with N AEs, while $\boldsymbol{S}(i) \in \mathcal{C}^{M\times T}$ represents the space-time codewords transmitted over T symbol durations from the transmitter having M AEs. Furthermore, transmission i represents the block index. It is

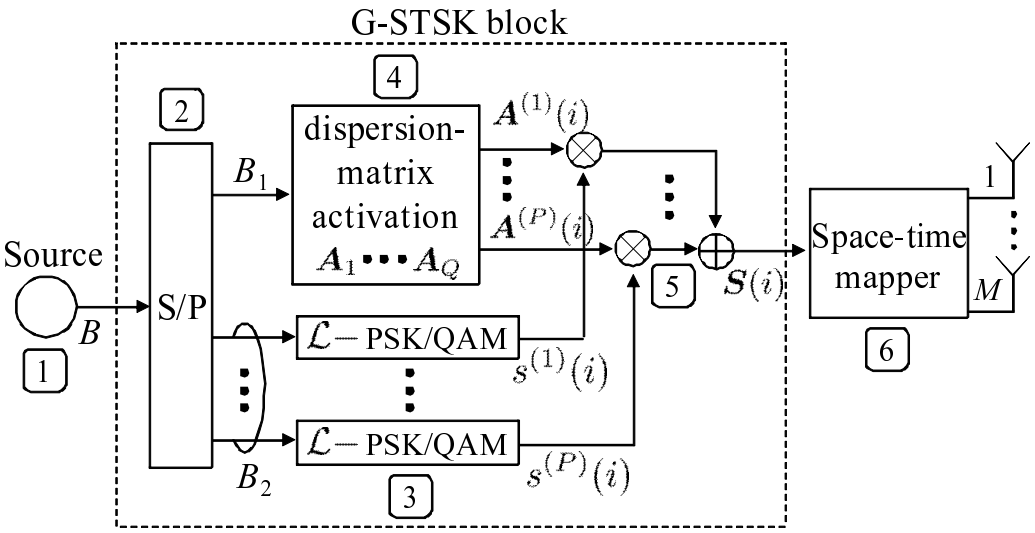

Figure 4.2: Transmitter structure of our GSTSK scheme, which was developed from the STSK architecture of Fig. 2.5.

also assumed that each component of the channel matrix $\boldsymbol{H}(i) \in \mathcal{C}^{N\times M}$ and the noise matrix $\boldsymbol{V}(i) \in \mathcal{C}^{N\times T}$ obeys the complex-valued Gaussian distribution of $\mathcal{CN}(0,1)$ and $\mathcal{CN}(0,N_0)$, respectively, where N_0 represents the noise variance.

4.2.1 GSTSK Modulation

Fig. 4.2 shows the schematic of our GSTSK's transmitter. In the GSTSK bit-to-symbol mapping scheme, $B = \log_2 f(Q,P) + P\log_2 \mathcal{L}$ bits per block are mapped to a space-time codeword $\boldsymbol{S}(i)$, where $f(Q,P)$ is calculated from Q and P as $f(Q,P) = 2^\iota$, while the integer ι satisfies the following inequality[1]

$$2^\iota \leq \begin{pmatrix} Q \\ P \end{pmatrix} < 2^{\iota+1}. \tag{4.2}$$

Firstly, $B = \log_2 f(Q,P) + P\log_2 \mathcal{L}$ input bits are S/P converted to $B_1 = \log_2 f(Q,P)$ bits and $B_2 = P\log_2 \mathcal{L}$ bits. Then, at the dispersion-matrix activation block of Fig. 4.2, P out of Q pre-assigned dispersion matrices $\boldsymbol{A}_{q'} \in \mathcal{C}^{M\times T}$ $(q' = 1,\cdots,Q)$ are activated according to $B_1 = \log_2 f(Q,P)$ input bits, in order to have $\boldsymbol{A}^{(p)}(i)$ $(p = 1,\cdots,P)$. By contrast, according to $B_2 = P\log_2 \mathcal{L}$ input bits, P number of $\log_2 \mathcal{L}$ bits are separately modulated by the classic $\mathcal{L}$-point PSK/QAM modulation scheme, giving rise to the symbols $s^{(p)}(i)$ $(p = 1,\cdots,P)$. Finally, the space-time codeword $\boldsymbol{S}(i)$ is generated as follows:

$$\boldsymbol{S}(i) = \sum_{p=1}^{P} s^{(p)}(i)\boldsymbol{A}^{(p)}(i), \tag{4.3}$$

[1]Although $f(Q,P)$ corresponds to P-out-of-Q dispersion-matrix selection process and can be given by $\begin{pmatrix} Q \\ P \end{pmatrix}$ at maximum, the relationship of Eq. (4.2) restricts $\log_2 f(Q,P)$ to be an integer number for simplicity of the input-bit treatment.

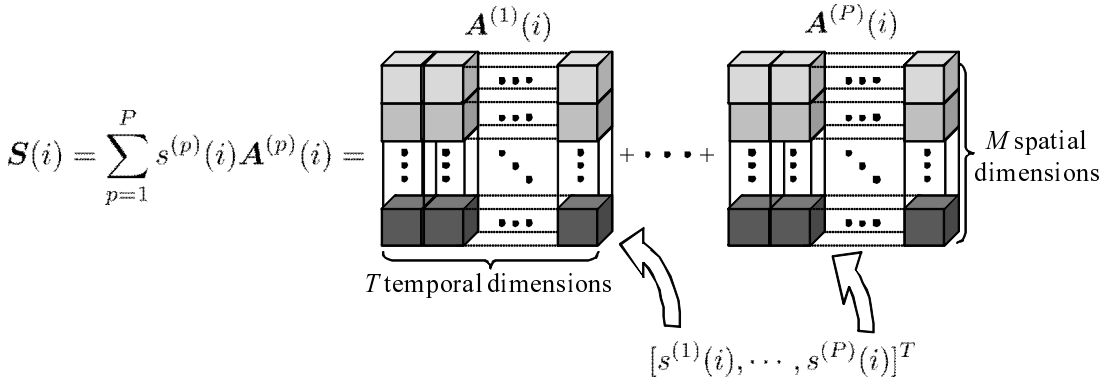

Figure 4.3: The space-time codeword $\boldsymbol{S}(i)$ of our GSTSK scheme obeying the architecture of Fig. 4.2, which is formulated based on Eq. (4.3).

where we have the power constraint of

$$\text{tr}\left[\boldsymbol{A}_{q'}\boldsymbol{A}_{q'}^{\text{H}}\right] = \frac{T}{P} \ (q' = 1, \cdots, Q), \tag{4.4}$$

in order to maintain a unity total transmission power per symbol. Here, tr[·] represents the trace operation. As seen by comparing Eqs. (2.21) and (4.4), the power transmitted by the GSTSK scheme of Fig. 4.2 is a factor P lower than that of the CSTSK scheme of Fig. 2.5. This is due to the fact that the GSTSK scheme simultaneously activates P dispersion matrices, rather than a single one. We note that as visualized in Fig. 4.3, each of the P PSK/QAM symbols $s^{(p)}(i)$ is dispersed both to the M spatial and T time dimensions, with the aid of the activated dispersion matrix $\boldsymbol{A}^{(p)}(i)$.

Hence, our GSTSK scheme has a set of parameters given by M, N, T, Q and P. Therefore we employ the parameter-based system description of GSTSK(M, N, T, Q, P) for simplicity. Additionally, the normalized throughput R of our GSTSK scheme is given by

$$R \ = \ \frac{B}{T} = \frac{\log_2 f(Q,P) + P\log_2 \mathcal{L}}{T} \text{ (bits/symbol)}. \tag{4.5}$$

To be more specific, in Table 4.1 we exemplify the bit-to-symbol mapping rule of BPSK-modulated ($\mathcal{L} = 2$) GSTSK$(M, N, T, 3, 2)$, where we have $f(Q,P) = 2^{\iota} = 2$, according to Eq. (4.2). As seen in Table 4.1, the $B = 4$ input bits are S/P converted to $B_1 = 2$ bits and $B_2 = 2$ bits. According to the B_1 bits, $P = 2$ out of $Q = 4$ dispersion matrices are selected as $\boldsymbol{A}^{(1)}(i), \boldsymbol{A}^{(2)}(i)$, while the B_2 bits generate the $P = 2$ BPSK symbols $s^{(1)}(i), s^{(2)}(i)$. Finally, the space-time codeword $\boldsymbol{S}(i)$ is generated as $\boldsymbol{S}(i) = s^{(1)}(i)\boldsymbol{A}^{(1)}(i) + s^{(2)}(i)\boldsymbol{A}^{(2)}(i)$.[2]

[2]To elaborate a little further, in the above-mentioned GSTSK scheme, we extended the CSTSK scheme by employing the new modulation principle that simultaneously activates multiple dispersion matrices, rather than a single one. This GSTSK philosophy can be readily applied to the differentially-encoded counterpart, i.e. the DSTSK scheme, which was proposed in Chapter 3, since both the CSTSK and DSTSK schemes share the underlying dispersion-matrix-activation concept. More specifically, in the differentially-encoded GSTSK scheme, the DSTSK's modulation operation $\tilde{\boldsymbol{X}}(i) = s(i)\boldsymbol{A}(i)$ of Eq. (3.19), whose block is placed before the Cayley transform may be replaced by $\sum_{p=1}^{P} s^{(p)}(i)\boldsymbol{A}^{(p)}(i)$ of Eq. (4.3), where the dispersion matrices

Table 4.1: Example of GSTSK$(2, 2, 2, 4, 2)$ modulation scheme of Fig. 4.2, mapping $B = 4$ bits per space-time block, with the aid of BPSK constellation

input bits $B = 4$		dispersion matrices	BPSK symbols	space-time codeword
B_1=2	B_2=2	$\boldsymbol{A}^{(1)}(i), \boldsymbol{A}^{(2)}(i)$	$s^{(1)}(i), s^{(2)}(i)$	$\boldsymbol{S}(i)$
00	00	$\boldsymbol{A}_1, \boldsymbol{A}_2$	$+1, +1$	$\boldsymbol{A}_1 + \boldsymbol{A}_2$
00	01	$\boldsymbol{A}_1, \boldsymbol{A}_2$	$+1, -1$	$\boldsymbol{A}_1 - \boldsymbol{A}_2$
00	10	$\boldsymbol{A}_1, \boldsymbol{A}_2$	$-1, +1$	$-\boldsymbol{A}_1 + \boldsymbol{A}_2$
00	11	$\boldsymbol{A}_1, \boldsymbol{A}_2$	$-1, -1$	$-\boldsymbol{A}_1 - \boldsymbol{A}_2$
01	00	$\boldsymbol{A}_1, \boldsymbol{A}_3$	$+1, +1$	$\boldsymbol{A}_1 + \boldsymbol{A}_3$
01	01	$\boldsymbol{A}_1, \boldsymbol{A}_3$	$+1, -1$	$\boldsymbol{A}_1 - \boldsymbol{A}_3$
01	10	$\boldsymbol{A}_1, \boldsymbol{A}_3$	$-1, +1$	$-\boldsymbol{A}_1 + \boldsymbol{A}_3$
01	11	$\boldsymbol{A}_1, \boldsymbol{A}_3$	$-1, -1$	$-\boldsymbol{A}_1 - \boldsymbol{A}_3$
10	00	$\boldsymbol{A}_2, \boldsymbol{A}_4$	$+1, +1$	$\boldsymbol{A}_2 + \boldsymbol{A}_4$
10	01	$\boldsymbol{A}_2, \boldsymbol{A}_4$	$+1, -1$	$\boldsymbol{A}_2 - \boldsymbol{A}_4$
10	10	$\boldsymbol{A}_2, \boldsymbol{A}_4$	$-1, +1$	$-\boldsymbol{A}_2 + \boldsymbol{A}_4$
10	11	$\boldsymbol{A}_2, \boldsymbol{A}_4$	$-1, -1$	$-\boldsymbol{A}_2 - \boldsymbol{A}_4$
11	00	$\boldsymbol{A}_3, \boldsymbol{A}_4$	$+1, +1$	$\boldsymbol{A}_3 + \boldsymbol{A}_4$
11	01	$\boldsymbol{A}_3, \boldsymbol{A}_4$	$+1, -1$	$\boldsymbol{A}_3 - \boldsymbol{A}_4$
11	10	$\boldsymbol{A}_3, \boldsymbol{A}_4$	$-1, +1$	$-\boldsymbol{A}_3 + \boldsymbol{A}_4$
11	11	$\boldsymbol{A}_3, \boldsymbol{A}_4$	$-1, -1$	$-\boldsymbol{A}_3 - \boldsymbol{A}_4$

Following the above-mentioned introductory elaborations, the encoding principle of our GSTSK scheme obeying the architecture of Fig. 4.2 can be formally summarized as follows:

Algorithm 4.1: Encoding principle of the GSTSK's transmitter of Fig. 4.2

1. Given the $\mathcal{L}$-PSK/QAM aided GSTSK(M, N, T, Q, P) scheme employing Q dispersion matrices $\boldsymbol{A}_1, \cdots, \boldsymbol{A}_Q \in \mathcal{C}^{M \times M}$, $B = \log_2(Q \cdot \mathcal{L})$ information bits are input to the GSTSK block of Fig. 4.2 in each of the space-time block durations T.

2. The $B = \log_2(Q \cdot \mathcal{L})$ information bits, input in *Step* 1, are Serial-to-Parallel (S/P) converted to $B_1 = P \log_2 \mathcal{L}$ bits and $B_2 = \log_2 f(Q, P)$ bits, where $f(Q, P)$ satisfies the relation of $f(Q, P) = 2^{\iota} \leq \begin{pmatrix} Q \\ P \end{pmatrix} < 2^{\iota+1}$.

$\boldsymbol{A}_{q'} \in \mathcal{C}^{M \times T}$ $(q' = 1, \cdots, Q)$ are Hermitian matrices, similarly to the DSTSK scheme. For example, when all the Q dispersion matrices are activated, i.e. for the case of $Q = P$, the system becomes equivalent to the conventional DLDC scheme [89]. The detailed investigation will be left for our future studies.

3. The $B_1 = \log_2 \mathcal{L}$ bits at the lower output of the S/P converter of Fig. 4.2 are then modulated to P complex-valued $\mathcal{L}$-PSK/QAM symbols $s^{(p)}$ $(p = 1, \cdots, P)$.

4. According to the $B_2 = \log_2 Q$ bits at the upper output of the S/P converter of Fig. 4.2 as well as to the corresponding lookup table provided in Appendix C, P out of the Q dispersion matrices $\boldsymbol{A}^{(1)}, \cdots, \boldsymbol{A}^{(P)} \in \mathcal{C}^{M \times T}$ are activated.

5. According to the modulated symbols $s^{(p)}$ $(p = 1, \cdots, P)$ generated in *Step* 3 as well as to the dispersion matrices $\boldsymbol{A}^{(p)}$ $(p = 1, \cdots, P)$ activated in *Step* 4, a matrix $\tilde{\boldsymbol{S}} \in \mathcal{C}^{M \times T}$ is computed as follows: $\tilde{\boldsymbol{S}} = \sum_{p=1}^{P} s^{(p)} \cdot \boldsymbol{A}^{(p)}$.

6. The ST matrix $\boldsymbol{S}$ generated in *Step* 7 is mapped to the space- and time-dimensions, where the components in the mth row and tth column of the matrix $\boldsymbol{S}$ are assigned to the mth antenna element in the tth symbol duration.

4.2.2 GSTSK Versus Conventional MIMO Arrangements

Next, we will demonstrate that our GSTSK scheme of Fig. 4.2 includes diverse MIMO arrangements.

4.2.2.1 Spatial Modulation/Space-Shift Keying

The conventional SM/SSK schemes [60, 61, 63, 66] of Section 2.2.4 may be derived by the GSTSK(M, N ,1, $Q = M$,1) scheme of Fig. 4.2 employing the dispersion matrices of

$$\boldsymbol{A}_1 = \begin{bmatrix} 1 \\ 0 \\ \vdots \\ 0 \end{bmatrix}, \boldsymbol{A}_2 = \begin{bmatrix} 0 \\ 1 \\ \vdots \\ 0 \end{bmatrix}, \cdots, \boldsymbol{A}_Q = \begin{bmatrix} 0 \\ 0 \\ \vdots \\ 1 \end{bmatrix}, \tag{4.6}$$

where the number of dispersion matrices Q is set to the number of the transmit antennas M. As also seen in Section 2.3.5, SM/SSK was not designed for exploiting any transmit diversity, due to the constraint of $T = 1$.

4.2.2.2 Linear Dispersion Code

According to the system model of [93], our GSTSK framework associated with $P = Q$ has an identical system model to that of LDCs reviewed in Section 2.2.3, where all of the Q pre-assigned dispersion matrices are used for the linear space-time dispersion of classic PSK/QAM symbols. We note here that as implied by the relation of $B_1 = \log_2 f(Q, P) = 0$ in Eq. (4.2), no additional information is transmitted with the aid of the dispersion-matrix activation process in the LDC arrangement. We note that as investigated for example in [88], the LDC multiplexing P dispersion matrices suffers from ICI.

4.2.2.3 Orthogonal Space-Time Block Code

A class of Orthogonal STBCs (OSTBCs) of Section 2.2.1 is also subsumed by the GSTSK scheme of Fig. 4.2 upon setting $P = Q$ and using appropriately designed dispersion matrices, depending on the space-time codewords employed. For example, consider an $(M \times N) = (2 \times 2)$ QPSK-modulated Alamouti STBC [20]. Then the space-time codeword $\boldsymbol{S}(i)$ of Eq. (4.1) may be expressed as

$$\boldsymbol{S}(i) = \frac{1}{\sqrt{2}} \begin{bmatrix} s_1 & s_2 \\ -s_2^* & s_1^* \end{bmatrix} \tag{4.7}$$

$$= \underbrace{\begin{bmatrix} \frac{1}{2} & 0 \\ 0 & \frac{1}{2} \end{bmatrix}}_{\boldsymbol{A}_1} \sqrt{2}\alpha_1 + j \underbrace{\begin{bmatrix} \frac{1}{2} & 0 \\ 0 & -\frac{1}{2} \end{bmatrix}}_{\boldsymbol{A}_2} \sqrt{2}\beta_1$$

$$+ \underbrace{\begin{bmatrix} 0 & \frac{1}{2} \\ -\frac{1}{2} & 0 \end{bmatrix}}_{\boldsymbol{A}_3} \sqrt{2}\alpha_2 + j \underbrace{\begin{bmatrix} 0 & \frac{1}{2} \\ \frac{1}{2} & 0 \end{bmatrix}}_{\boldsymbol{A}_4} \sqrt{2}\beta_2, \tag{4.8}$$

where $s_1 = \alpha_1 + j\beta_1$ and $s_2 = \alpha_2 + j\beta_2$ are two consecutive QPSK symbols per transmission block. As seen in Eq. (4.8), we may regard the QPSK-modulated Alamouti code as a BPSK-modulated GSTSK$(2, 2, 2, 4, 4)$ arrangement, employing $\boldsymbol{A}_{q'}$ $(q' = 1, \cdots, 4)$ of Eq. (4.8). By following a similar decomposition process, other OSTBCs may also be represented by our GSTSK system. Moreover, it may be readily shown that other STBCs, such as Quasi-OSTBCs (QOSTBCs), STBC employing Time Variant Linear Transformation (TVLT) and Threaded Algebraic STBCs (TASTBCs), are also described by our GSTSK structure, according to Section 7.3 of [23]. Here, the STBCs are designed so as to remain unaffected by ICI and to achieve a full transmit diversity, which is achieved at the cost of sacrificing the achievable multiplexing gain.

4.2.2.4 BLAST as a Subclass of GSTSK

We may also view the BLAST architecture of Section 2.2.2 as a certain form of our GSTSK scheme of Fig. 4.2, by setting $P = Q = M$, $T = 1$ and using Eq. (4.6). This BLAST arrangement does not provide any explicit transmit diversity gain, and this property is shared by the SM/SSK schemes. Since the resultant system suffers from Inter-Antenna Interference (IAI) imposed on the AEs, the computational complexity of mitigating it becomes inevitably high, which increases with the number of AEs M.

4.2.2.5 Coherent Space-Time Shift Keying

Furthermore, in this contribution we refer to the special case of our GSTSK scheme, employing $P = 1$, as STSK proposed in Section 2.3.1, where only one out of Q dispersion matrices is

activated, which results in lower B_1 and B_2 values in comparison to our GSTSK scheme for the case of $P > 1$. This STSK arrangement enables us to implement single-stream-based low-complexity ML detection, similarly to SM/SSK. Furthermore, an appropriately-constructed set of dispersion matrices $\boldsymbol{A}_{q'}$ $(q' = 1, \cdots, Q)$ enables us to dispense with symbol-level IAS. More specifically, the structure of each dispersion matrix $\boldsymbol{A}_{q'}$ is constructed so that there is a single non-zero element for each column of the dispersion matrix $\boldsymbol{A}_{q'}$. This constraint enables us to avoid any simultaneous transmission by multiple antennas, also similarly to SM/SSK.

4.2.3 Inter-Antenna Synchronization Issues in GSTSK

As proposed in Section 2.3.2, the ACSTSK scheme, which employed a specific dispersion-matrix structure in the context of the CSTSK scheme of Fig. 2.5, enables us to dispense with symbol-level IAS. Naturally, this ACSTSK arrangement is also subsumed by our GSTSK scheme of Fig. 4.2, when we have $P = 1$ as well as a specific sparse dispersion-matrix structure. On the other hand, it may be difficult to find a beneficial dispersion-matrix set, which performs well for an asynchronous version of the GSTSK scheme employing $P \geq 2$. Nevertheless, it is not impossible to find an asynchronous GSTSK structure by imposing the same non-zero element structure on all the dispersion matrices. This is due to the fact that the GSTSK scheme employing $P \geq 2$ simultaneously activates P dispersion matrices, rather than single one, and hence the resultant space-time modulated codewords $\boldsymbol{S}$ typically exhibit low distances from each other.

4.3 Detection Algorithm

In this section, we present both the optimal hard-decision ML detector and the soft-detector, which are derived for our GSTSK system of Fig. 4.2.

4.3.1 Optimal Hard-Decision ML Detector

Firstly, by applying the vectorial stacking operation $vec(\ )$ to the received signal block in Eq. (4.1), we arrive at

$$\bar{\boldsymbol{Y}}(i) = \bar{\boldsymbol{H}}(i)\boldsymbol{\chi}\boldsymbol{K}(i) + \bar{\boldsymbol{V}}(i), \tag{4.9}$$

where we have $\bar{\boldsymbol{Y}}(i) = vec[\boldsymbol{Y}(i)]$, $\bar{\boldsymbol{H}}(i) = \boldsymbol{I} \otimes \boldsymbol{H}$, $\boldsymbol{\chi} = [vec(\boldsymbol{A}_1), \cdots, vec(\boldsymbol{A}_Q)]$ and $\bar{\boldsymbol{V}}(i) = vec[\boldsymbol{V}(i)]$, while $\boldsymbol{I}$ is the identity matrix and $\otimes$ is the Kronecker product. Furthermore, the qth element of the equivalent transmit vector $\boldsymbol{K}(i)$ is assumed to be $k_q(i)$. Here, if the qth dispersion matrices $\boldsymbol{A}_q$ is selected in the ith block as $\boldsymbol{A}^{(p)}(i) = \boldsymbol{A}_q$, $k_q(i)$ is set to the corresponding PSK/QAM symbol $s^{(p)}(i)$. Otherwise, $k_q(i)$ is zero. It should be noted that the number of non-zero components in $\boldsymbol{K}(i) = [k_1(i), \cdots, k_Q(i)]^{\mathrm{T}}$ is equal to P.

Next, the conditional probability $P(\bar{\boldsymbol{Y}}|\boldsymbol{K})$ of the linearized equivalent system model of Eq. (4.9) is given by

$$P(\bar{\boldsymbol{Y}}|\boldsymbol{K}) = \frac{1}{(\pi N_0)^{NT}} \exp\left(-\frac{\left|\left|\bar{\boldsymbol{Y}} - \bar{\boldsymbol{H}}\boldsymbol{\chi}\boldsymbol{K}\right|\right|^2}{N_0}\right). \tag{4.10}$$

Accordingly, the ML detection criterion is formulated as

$$\begin{aligned}
(\hat{B}_1, \hat{B}_2) &= \arg \max_{(B_1,B_2)} P(\bar{\boldsymbol{Y}}|\boldsymbol{K}) && (4.11)\\
&= \arg \min_{(B_1,B_2)} \left|\left|\bar{\boldsymbol{Y}} - \bar{\boldsymbol{H}}\boldsymbol{\chi}\boldsymbol{K}\right|\right|^2 && (4.12)\\
&= \arg \min_{(B_1,B_2)} \left|\left|\bar{\boldsymbol{Y}} - \sum_{q=1}^{Q} k_q \left\{\bar{\boldsymbol{H}}\boldsymbol{\chi}\right\}_q\right|\right|^2, && (4.13)
\end{aligned}$$

where $\left\{\bar{\boldsymbol{H}}\boldsymbol{\chi}\right\}_q$ denotes the qth column of $\bar{\boldsymbol{H}}\boldsymbol{\chi}$. Note that the computational complexity imposed by calculating $\sum_{q=1}^{Q} k_q \left\{\bar{\boldsymbol{H}}\boldsymbol{\chi}\right\}_q$ in Eq. (4.13) linearly increases with the parameter P, because the number of non-zero elements in k_q $(q = 1, \cdots, Q)$ is P as mentioned above.

More specifically, the computational complexity per bit for the detection scheme of Eq. (4.13) is evaluated in terms of the number of real-valued multiplications, which may be shown to be

$$\frac{4MNT^2Q + (4NTP + 2NT)f(Q,P)\mathcal{L}^P}{B}. \tag{4.14}$$

Fig. 4.4 shows the relationship between the complexity and the throughput of our QPSK-modulated GSTSK$(2, 2, 2, 4, P)$ scheme designed for achieving the maximum diversity order of four, where the parameter P was varied from $P = 1$ to $P = 4$. As mentioned in Section 4.2, our GSTSK schemes employing $P = 1$ and $P = Q$ correspond to the STSK and LDC schemes, respectively. As seen in Fig. 4.4, the normalized throughput R tends to increase with the value of P at the cost of an increased computational complexity.

4.3.2 Soft MAP Demodulator

Although in Section 4.3.1 the optimal ML detector was derived for uncoded GSTSK systems, practical communication systems typically employ a powerful channel coding scheme, such as turbo coding [27]. Therefore, we hereby introduce the soft MAP demodulator of our GSTSK scheme, which can be used for iterative detection assisted by Soft-Input Soft-Output (SISO) decoders.

Considering that the equivalent received signal block $\bar{\boldsymbol{Y}}$ in Eq. (4.9) conveys channel-encoded binary bits $\boldsymbol{b} = [b_1, b_2, \cdots, b_B]$, the resultant extrinsic LLR value $L_e(b_k)$ of bit b_k

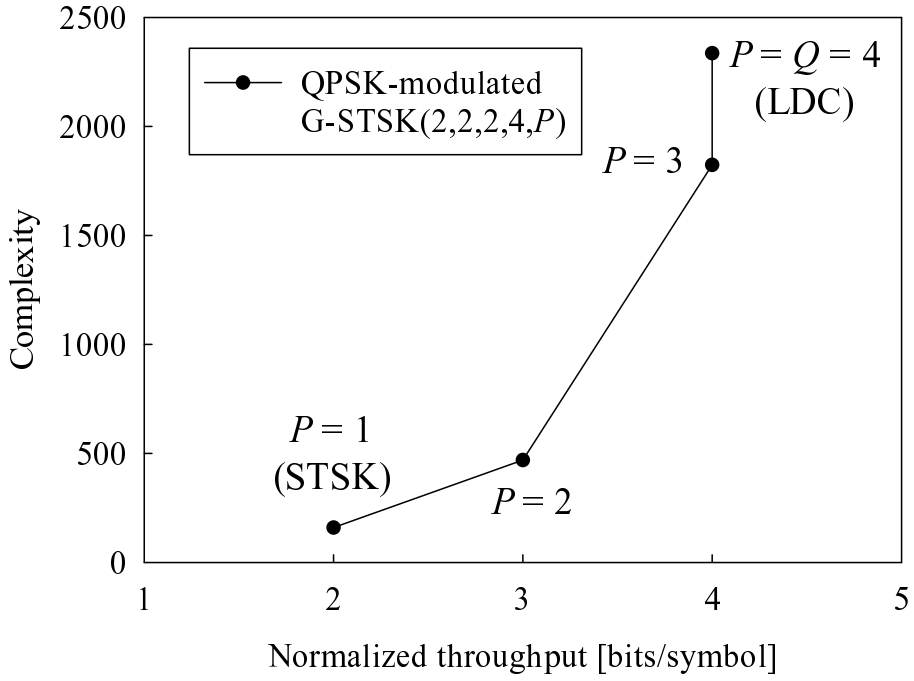

Figure 4.4: The relationship between complexity and throughput of our QPSK-modulated GSTSK$(2, 2, 2, 4, P)$ scheme of Fig. 4.2, achieving the maximum diversity order of four, where the parameter P was changed from $P = 1$ to $P = 4$.

for $k = 1, 2, \cdots, B$ may be expressed as [23]

$$L_{\mathrm{e}}(b_k) = \ln \frac{\sum_{\boldsymbol{K}_{\beta_1,\beta_2} \in K_1^k} P(\bar{\boldsymbol{Y}}|\boldsymbol{K}_{\beta_1,\beta_2}) \cdot \exp\left[\sum_{j \neq k} b_j L_{\mathrm{a}}(b_j)\right]}{\sum_{\boldsymbol{K}_{\beta_1,\beta_2} \in K_0^k} P(\bar{\boldsymbol{Y}}|\boldsymbol{K}_{\beta_1,\beta_2}) \cdot \exp\left[\sum_{j \neq k} b_j L_{\mathrm{a}}(b_j)\right]} \tag{4.15}$$

$$= \ln \frac{\sum_{\boldsymbol{K}_{\beta_1,\beta_2} \in K_1^k} \exp\left[-\left|\left|\bar{\boldsymbol{Y}} - \bar{\boldsymbol{H}}\boldsymbol{\chi}\boldsymbol{K}\right|\right|^2 / N_0 + \sum_{j \neq k} b_j L_{\mathrm{a}}(b_j)\right]}{\sum_{\boldsymbol{K}_{\beta_1,\beta_2} \in K_0^k} \exp\left[-\left|\left|\bar{\boldsymbol{Y}} - \bar{\boldsymbol{H}}\boldsymbol{\chi}\boldsymbol{K}\right|\right|^2 / N_0 + \sum_{j \neq k} b_j L_{\mathrm{a}}(b_j)\right]}, \tag{4.16}$$

where K_1^k and K_0^k represent the sub-space of the legitimate equivalent signals $\boldsymbol{K}$, which satisfy $K_1^k \equiv \{\boldsymbol{K}_{\beta_1,\beta_2} \in K : b_k = 1\}$ and $K_0^k \equiv \{\boldsymbol{K}_{\beta_1,\beta_2} \in K : b_k = 0\}$, respectively, while $\beta_1 \in \{1, \cdots, 2^{B_1}\}$ and $\beta_2 \in \{1, \cdots, 2^{B_2}\}$ are the variables corresponding to the S/P converted B_1 and B_2 input bits of Fig. 4.2.

Furthermore, Eq. (4.16) may be readily simplified by the well-known max-log approximation [27], giving rise to

$$L_{\mathrm{e}}(b_k) = \max_{\boldsymbol{K}_{\beta_1,\beta_2} \in K_1^k} \left[-\frac{\left|\left|\bar{\boldsymbol{Y}} - \bar{\boldsymbol{H}}\boldsymbol{\chi}\boldsymbol{K}\right|\right|^2}{N_0} + \sum_{j \neq k} b_j L_{\mathrm{a}}(b_j) \right] - \max_{\boldsymbol{K}_{\beta_1,\beta_2} \in K_0^k} \left[-\frac{\left|\left|\bar{\boldsymbol{Y}} - \bar{\boldsymbol{H}}\boldsymbol{\chi}\boldsymbol{K}\right|\right|^2}{N_0} + \sum_{j \neq k} b_j L_{\mathrm{a}}(b_j) \right]. \tag{4.17}$$

4.4 Unified DCMC Capacity

In this section we characterize the DCMC capacity [59] of our GSTSK framework. As mentioned above, members of the GSTSK family support many other MIMO arrangements, hence the resultant capacity equation is also applicable to diverse MIMOs.

According to [59], the DCMC capacity of our GSTSK scheme using $\mathcal{L}-$PSK/QAM signaling may be derived from that of the discrete memoryless channel as

$$\begin{aligned} C &= \frac{1}{T} \max_{P(\boldsymbol{K}_{1,1}),\cdots,P(\boldsymbol{K}_{2^{B_1},2^{B_2}})} \sum_{\beta_1,\beta_2} \int_{-\infty}^{\infty} \cdots \int_{-\infty}^{\infty} P(\bar{\boldsymbol{Y}}|\boldsymbol{K}_{\beta_1,\beta_2}) \\ &\cdot P(\boldsymbol{K}_{\beta_1,\beta_2}) \log_2 \left[\frac{P(\bar{\boldsymbol{Y}}|\boldsymbol{K}_{\beta_1,\beta_2})}{\sum_{\beta_1',\beta_2'} P(\bar{\boldsymbol{Y}}|\boldsymbol{K}_{\beta_1',\beta_2'}) P(\boldsymbol{K}_{\beta_1',\beta_2'})} \right] d\bar{\boldsymbol{Y}} \\ &\text{(bits/symbol)}. \end{aligned} \tag{4.18}$$

Since Eq. (4.18) is maximized under the assumption that all the signals $\boldsymbol{K}_{\beta_1,\beta_2}$ are equiprobable, i.e. when we have $P(\boldsymbol{K}_{1,1}) = \cdots = P(\boldsymbol{K}_{2^{B_1},2^{B_2}}) = 1/2^B$, Eq. (4.18) is simplified to [59]

$$C = \frac{1}{T} \left(B - \frac{1}{2^B} \sum_{\beta_1,\beta_2} E \left[\log_2 \left\{ \sum_{\beta_1',\beta_2'} \exp(\Psi_{\beta_1,\beta_2}^{\beta_1',\beta_2'}) \middle| \boldsymbol{K}_{\beta_1',\beta_2'} \right\} \right] \right), \tag{4.19}$$

where we have

$$\Psi_{\beta_1,\beta_2}^{\beta_1',\beta_2'} = -||\bar{\boldsymbol{H}}\chi(\boldsymbol{K}_{\beta_1,\beta_2} - \boldsymbol{K}_{\beta_1',\beta_2'}) + \bar{\boldsymbol{V}}||^2 + ||\bar{\boldsymbol{V}}||^2. \tag{4.20}$$

According to the unified capacity metric (Eq. (4.18)) derived above, we plotted in Figs. 4.5, 4.6, 4.7 and 4.8 the DCMC capacity curves associated with the diverse MIMO arrangements, i.e. the Alamouti, the BLAST, the SM and the GSTSK schemes, respectively. As seen in Fig. 4.5, upon increasing the number of receive antennas N, the associated Alamouti scheme's capacity curve improved, moving toward the left direction, while the achievable transmission rate at high SNRs remains constant, namely 2.0 bits/symbol. By contrast, as expected in Fig. 4.6 BLAST's capacity was enhanced, in accordance with the increased number of transmit antennas M, hence resulting in a beneficial multiplexing gain. Similarly, in the context of the corresponding SM scheme the rate was found to increase upon increasing in the number of transmit antennas M, noting that the associated decoding complexity of the receiver did not increase exponentially, unlike in the BLAST scheme. Furthermore, in Fig. 4.8 we portray the DCMC capacity curves of our QPSK-modulated GSTSK$(2, 2, 2, 4, P)$ scheme, where P was varied from $P = 1$ to $P = 4$. As seen in Fig. 4.8, upon increasing the SNR value, each capacity curve converged to the attainable normalized throughput R of Eq. (4.5). Additionally, observe in Fig. 4.8 that the capacity tended to be increased with the

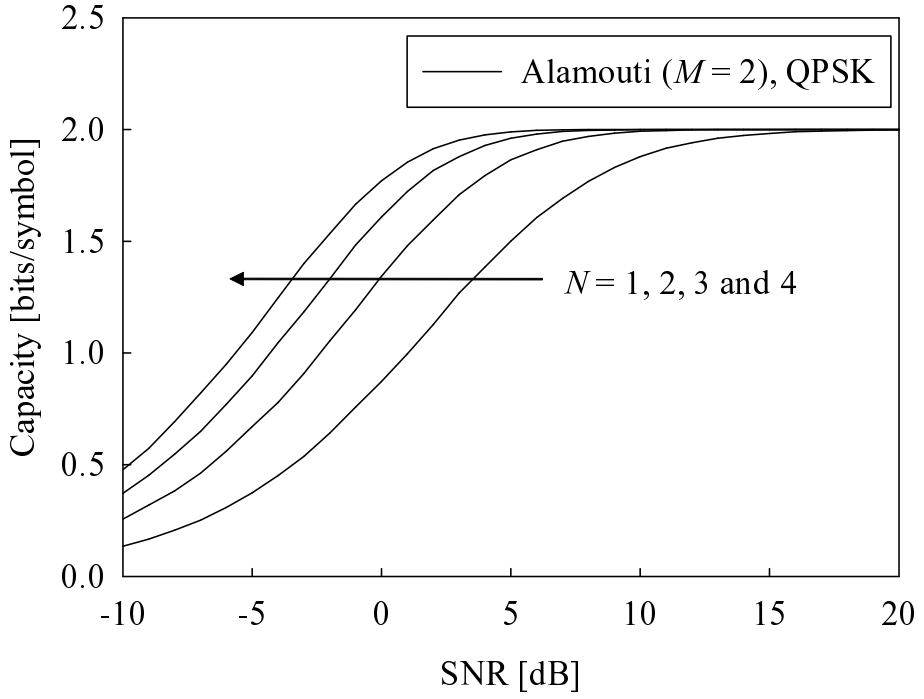

Figure 4.5: DCMC capacity of the QPSK-modulated Alamouti scheme of Section 2.2.1, employing $M = 2$ transmit antennas, where the number of receive antennas N was varied from $N = 1$ to $N = 4$.

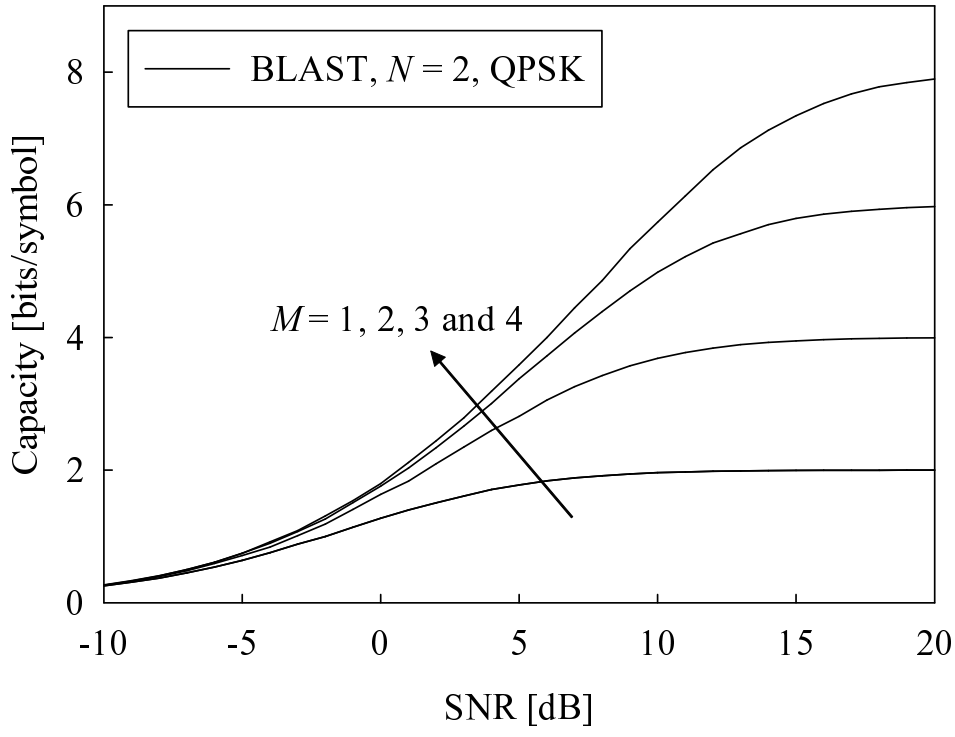

Figure 4.6: DCMC capacity of the QPSK-modulated BLAST scheme of Section 2.2.2, employing $M = 1, 2, 3$ and 4 transmit antennas and $N = 2$ receive antennas.

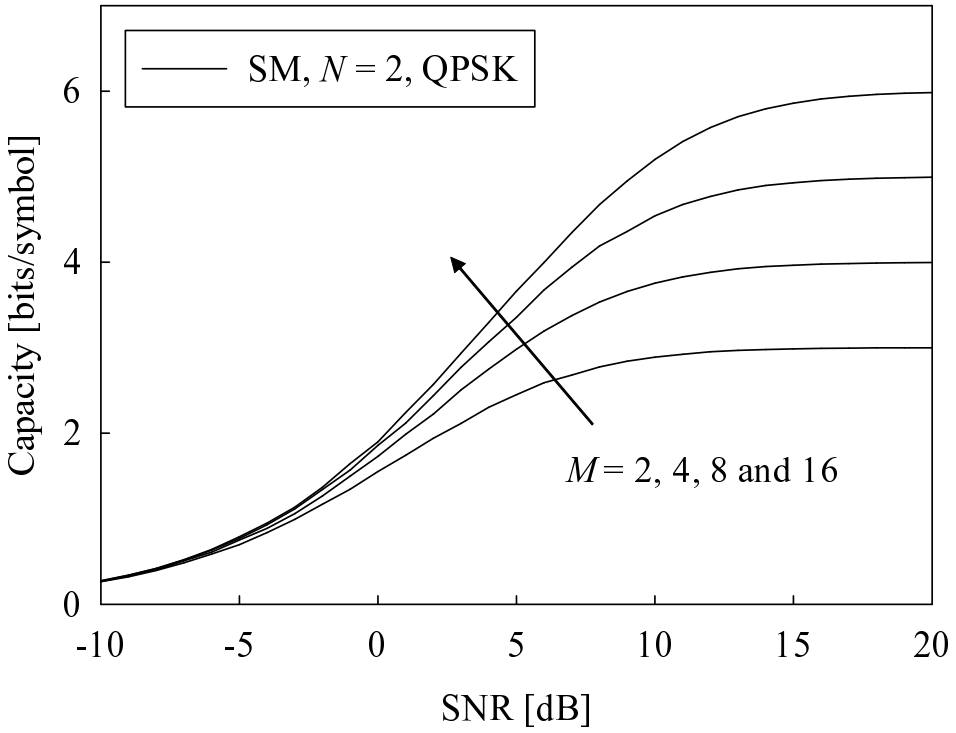

Figure 4.7: DCMC capacity of the QPSK-modulated SM scheme of Fig. 2.1, employing $M = 2, 4, 8$ and 16 transmit antennas and $N = 2$ receive antennas.

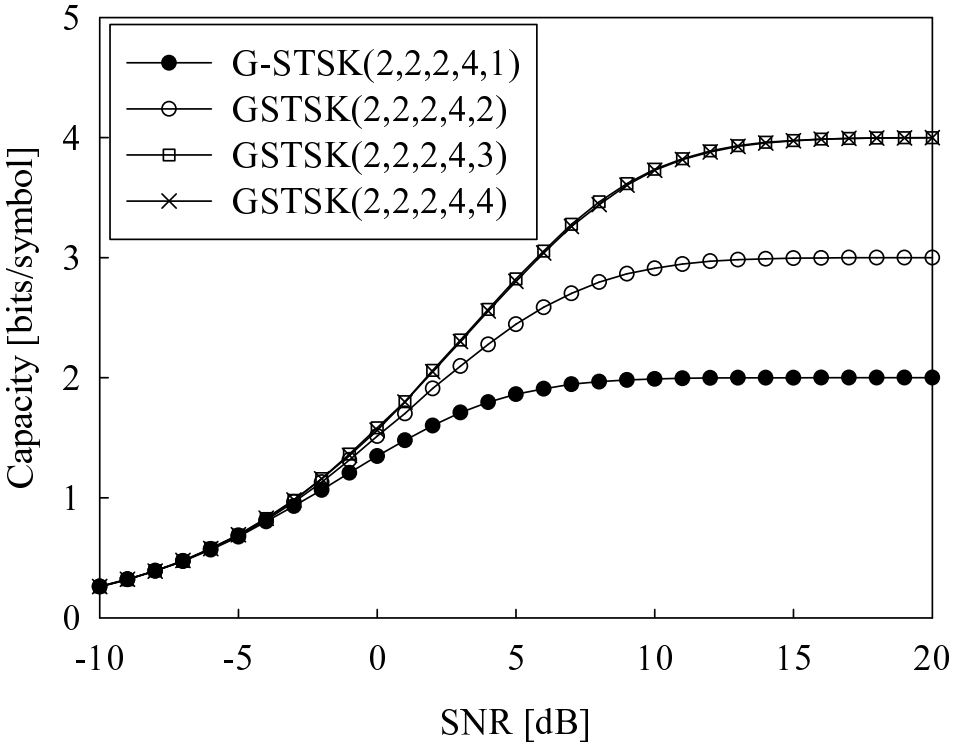

Figure 4.8: DCMC capacity of the QPSK-modulated GSTSK$(2, 2, 2, 4, P)$ of Fig. 4.2, where P was varied from $P = 1$ to $P = 4$.

parameter P, although the capacity curves corresponding to $P = 3$ and $P = 4$ were found to be almost identical. Accordingly, it was demonstrated that the DCMC capacity derived serves as a unified capacity limit of the diverse MIMO arrangements considered.

4.5 Achievable BER and Diversity Gain Analysis

In this section, we invoke the Moment Generating Functions (MGFs) [138] and derive exact BER curves for our GSTSK scheme for transmission over quasi-static Rayleigh fading channels, which serves as a tight upper bound of the achievable BER curve calculated with the aid of Monte Carlo simulations. Then, we will qualify the maximum achievable diversity order with the aid of the MGF-based BER bound. As mentioned, our GSTSK scheme subsumes diverse MIMO arrangements, hence the BER bound derived will also provide us with the unified analytical upper bound.

4.5.1 Unified BER Upper Bound

Let us define the PEP as $P(\boldsymbol{S} \rightarrow \boldsymbol{S}')$, which indicates the probability that a codeword $\boldsymbol{S}$ is erroneously decoded as $\boldsymbol{S}'$. According to the block-based system model of our GSTSK scheme, which was formulated in Eq. (4.1), we arrive at the corresponding PEP conditioned on the channel matrix $\boldsymbol{H}$ as follows:

$$\begin{aligned} P(\boldsymbol{S} \rightarrow \boldsymbol{S}'|\boldsymbol{H}) &= P\left(\left|\left|\boldsymbol{Y} - \boldsymbol{H}\boldsymbol{S}'\right|\right| - ||\boldsymbol{Y} - \boldsymbol{H}\boldsymbol{S}|| < 0\right) && (4.21)\\ &= P\left(\left|\left|\boldsymbol{H}(\boldsymbol{S} - \boldsymbol{S}') + \boldsymbol{Y}\right|\right| - ||\boldsymbol{V}|| < 0\right) && (4.22)\\ &= Q\left[\sqrt{\frac{||\boldsymbol{H}\Delta||^2}{2N_0}}\right], && (4.23) \end{aligned}$$

where we have $\Delta = \boldsymbol{S} - \boldsymbol{S}'$ and $Q[\cdot]$ represents the integral form of the Q-function of [138]

$$Q(x) = \frac{1}{\pi}\int_0^{\pi/2} \exp\left(-\frac{x^2}{2\sin^2\theta}\right) d\theta. \tag{4.24}$$

Accordingly, the conditional PEP of Eq. (4.23) may be expressed as

$$P(\boldsymbol{S} \rightarrow \boldsymbol{S}'|\boldsymbol{H}) = \frac{1}{\pi}\int_0^{\pi/2} \exp\left(-\frac{||\boldsymbol{H}\Delta||^2}{4N_0\sin^2\theta}\right) \mathrm{d}\theta. \tag{4.25}$$

Subsequently, we will obtain the unconditional PEP by averaging the conditional one over the legitimate range of potential channel components $||\boldsymbol{H}\Delta||^2$. Before delving into this derivation, let us first describe the basic characteristics of the MGF $\Phi(s)$.

MGF

The MGF is a useful tool that may be invoked to analyze digital communication systems communicating in fading environments, which enables us to arrive at the exact form

of the average error probability in a simplified way. More specifically, the MGF of a non-negative random variable $\gamma \geq 0$ obeying the distribution of $p_\gamma(\gamma)$ is defined as [28]

$$\Phi_\gamma(s) = \int_0^\infty p_\gamma(\gamma) \exp(s\gamma) \mathrm{d}\gamma, \tag{4.26}$$

which exhibits the same form as the Laplace transform. For example, the MGFs of the typical fading distributions, such as Rayleigh, Rician and Nakagami-m fading, may be computed in closed form [138]. This enables us to arrive at the unconditional PEP by integrating the probability over the legitimate range of the channel coefficients.

Furthermore, assuming a Hermitian matrix $\boldsymbol{A}$ and a circularly symmetric complex-valued Gaussian vector $\boldsymbol{u}$ having the mean of $\bar{\boldsymbol{u}}$ as well as the covariance matrix $\boldsymbol{R}_{\boldsymbol{u}}$, the MGF of the quadratic form $y = \boldsymbol{u}\boldsymbol{A}\boldsymbol{u}^{\mathrm{H}}$ is represented by [139]

$$\Phi_y(s) = \int_0^\infty p_y(y) \exp(sy) \mathrm{d}y = \frac{\exp(s\bar{\boldsymbol{u}}\boldsymbol{A}(\boldsymbol{I} - s\boldsymbol{R}_{\boldsymbol{u}}\boldsymbol{A})^{-1}\bar{\boldsymbol{u}}^{\mathrm{H}})}{|\boldsymbol{I} - s\boldsymbol{R}_{\boldsymbol{u}}\boldsymbol{A}|}. \tag{4.27}$$

We note that typically this relationship is advocated in the MGF-based PEP analysis of MIMO systems.

By averaging Eq. (4.25) over the legitimate range of $y = ||\boldsymbol{H}\Delta||^2$, namely over $0 < y < \infty$, we arrive at the unconditional PEP expression of:

$$\begin{aligned} P(\boldsymbol{S} \to \boldsymbol{S}') &= \frac{1}{\pi} \int_0^{\pi/2} \int_0^\infty \exp\left(-\frac{y^2}{4N_0 \sin^2\theta}\right) p_y(y) \mathrm{d}y \mathrm{d}\theta \\ &= \frac{1}{\pi} \int_0^{\pi/2} \Phi_y\left(-\frac{1}{4N_0 \sin^2\theta}\right) \mathrm{d}\theta. \end{aligned} \tag{4.28}$$

Here, $||\boldsymbol{H}\Delta||^2$ may be expressed as

$$\begin{aligned} ||\boldsymbol{H}\Delta||^2 &= \mathrm{tr}(\boldsymbol{H}\Delta\Delta^{\mathrm{H}}\boldsymbol{H}^{\mathrm{H}}) \\ &= \mathrm{vec}(\boldsymbol{H}^{\mathrm{H}})^{\mathrm{H}}(\boldsymbol{I} \otimes \Delta\Delta^{\mathrm{H}})\mathrm{vec}(\boldsymbol{H}^{\mathrm{H}}), \end{aligned} \tag{4.29}$$

where $\mathrm{vec}(\boldsymbol{H})$ is a zero-mean complex-valued Gaussian vector having the covariance matrix of $\boldsymbol{I}$ and $(\boldsymbol{I} \otimes \Delta\Delta^{\mathrm{H}})$ is a Hermitian matrix. Hence, by considering $\boldsymbol{u} = \mathrm{vec}(\boldsymbol{H})$, $\boldsymbol{R}\boldsymbol{u} = \boldsymbol{I}$ and $\boldsymbol{A} = \boldsymbol{I} \otimes \Delta\Delta^{\mathrm{H}}$ in Eq. (4.27), the MGF of $y = ||\boldsymbol{H}\Delta||^2$ can be rewritten as

$$\begin{aligned} \Phi_y(s) &= \left|\boldsymbol{I} - s(\boldsymbol{I} \otimes \Delta\Delta^{\mathrm{H}})\right|^{-1} \\ &= \prod_{m=1}^{M} (1 - s\mu_m)^{-N}, \end{aligned} \tag{4.30}$$

where μ_m is the mth eigenvalue of $\Delta\Delta^{\mathrm{H}}$. Therefore, the unconditional PEP of Eq. (4.28) becomes

$$P(\boldsymbol{S} \to \boldsymbol{S}') = \frac{1}{\pi} \int_0^{\pi/2} \prod_{m=1}^{M} \left(1 + \frac{\mu_m}{4N_0 \sin^2\theta}\right)^{-N} \mathrm{d}\theta. \tag{4.31}$$

Table 4.2: System parameters of the uncoded GSTSK scheme of Fig. 4.2

Number of transmit antennas	M
Number of receive antennas	N
Symbol durations per block	T
Number of dispersion matrices	Q
Number of activated dispersion matrices	P
Modulation	$\mathcal{L}-$PSK or $\mathcal{L}-$QAM
Channels	Frequency-flat Rayleigh fading
Channel's coherence-time	$\tau = 1$ block duration
Detector	ML detector of Eq. (4.13)

Having arrived at the exact PEP expression, we can now compute the tight upper bound on the average BER, by summing the PEP over all error events corresponding to a given transmitted codeword $\boldsymbol{S}$ [131], which is given by

$$P_{\text{e,bit}}(\boldsymbol{S}) \leq \frac{1}{B} \sum_{\boldsymbol{S} \neq \boldsymbol{S}'} d(\boldsymbol{S}, \boldsymbol{S}') P(\boldsymbol{S} \rightarrow \boldsymbol{S}'), \tag{4.32}$$

where $d(\boldsymbol{S}, \boldsymbol{S}')$ represents the Hamming distance between $\boldsymbol{S}$ and $\boldsymbol{S}'$. Finally, averaging over all the legitimate 2^B codewords $\boldsymbol{S}$, the upper bound of the averaged BER $\bar{P}_{\text{e,bit}}$ is given by

$$\begin{aligned} \bar{P}_{\text{e,bit}} &\leq E\left[\frac{1}{B} \sum_{\boldsymbol{S} \neq \boldsymbol{S}'} d(\boldsymbol{S}, \boldsymbol{S}') P(\boldsymbol{S} \rightarrow \boldsymbol{S}')\right] \\ &= \frac{1}{B \cdot 2^B} \sum_{\boldsymbol{S}} \sum_{\boldsymbol{S} \neq \boldsymbol{S}'} d(\boldsymbol{S}, \boldsymbol{S}') P(\boldsymbol{S} \rightarrow \boldsymbol{S}'). \end{aligned} \tag{4.33}$$

In order to verify the BER upper bound expression of Eq. (4.33), we investigated the BER curves of diverse MIMO arrangements, such as that of the BLAST-, the Alamouti-, the SM- and of the STSK schemes, comparing the bounds derived and the Monte Carlo simulation results in Figs. 4.9, 4.10, 4.11 and 4.12. It can be seen from these results that the theoretical curve served indeed, as the tight upper bound of the numerical simulation results. Upon increasing the SNR value, each bound asymptotically converged to the corresponding Monte Carlo curve. To be specific, the difference between the theoretical and numerical curves was found to be marginal, especially for the range of BER $< 10^{-2}$ in each case.

4.5.2 Achievable Diversity Order of Our GSTSK Scheme

In this section we derive the achievable diversity order of our GSTSK scheme, based on the above-mentioned unconditional PEP of Eq. (4.31). Considering the relationship of

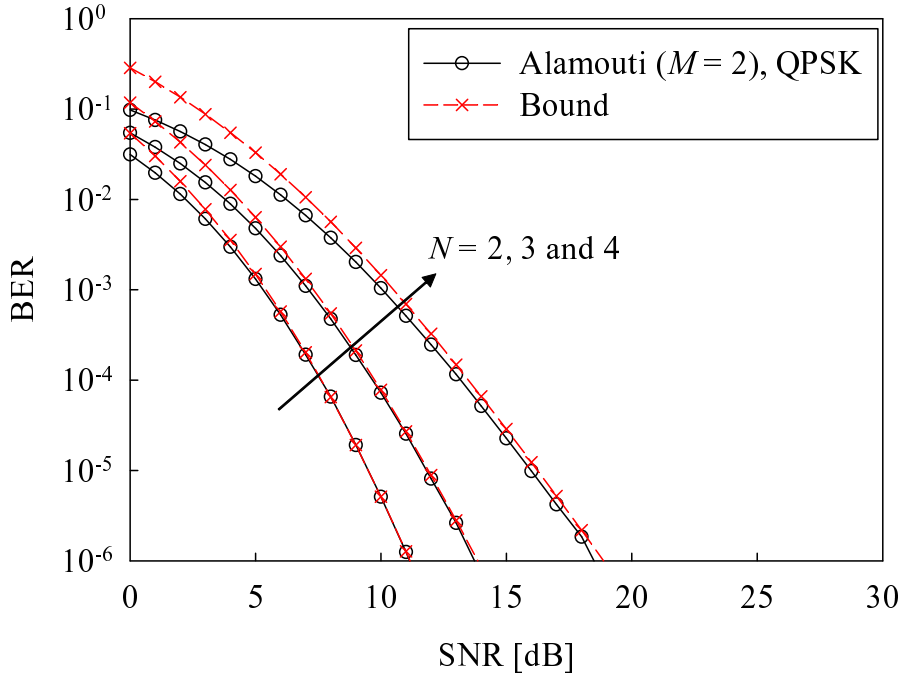

Figure 4.9: BER comparison of the theoretical upper bounds and the numerical results for the QPSK-modulated Alamouti scheme of Section 2.2.1, employing $M = 2$ transmit antennas and $N = 2, 3$ and 4 receive antennas. Here, the corresponding transmission rate was $R_{\mathrm{SM}} = 2$ bits/symbol. All other system parameters were summarized in Table 4.2.

$0 \leq \sin\theta \leq 1$ for $0 \leq \theta \leq \pi/2$, the PEP of Eq. (4.31) is loosely upper bounded by

$$P(\boldsymbol{S} \rightarrow \boldsymbol{S}') \leq \frac{1}{2} \prod_{m=1}^{M} \left(1 + \frac{\mu_m}{4N_0}\right)^{-N}, \tag{4.34}$$

by simply replacing $\sin\theta$ by 1. We note that this is widely-known as the Chernoff bound of the PEP. Moreover, in the high-SNR regime, the Chernoff bound of Eq. (4.34) can be further approximated by

$$P(\boldsymbol{S} \rightarrow \boldsymbol{S}') \leq \frac{1}{2} \underbrace{\left(\frac{1}{4N_0}\right)^{m'N}}_{\text{diversity gain}} \cdot \underbrace{\prod_{m=1}^{m'} \frac{1}{\mu_m^N}}_{\text{coding gain}}, \tag{4.35}$$

where m' is the rank of $\Delta\Delta^{\mathrm{H}}$. As seen from Eq. (4.35), the PEP can be divided into two components, namely the diversity gain and the coding gain. Furthermore, the achievable diversity order, which is typically defined as the slope of the PEP, is given by $m' \cdot N \leq \min(M, T) \cdot N$. This also indicates that the reduction in T may give rise to the reduction of the computational complexity, while increasing the normalized throughput in Eq. (4.5) at the cost of a reduced diversity gain.

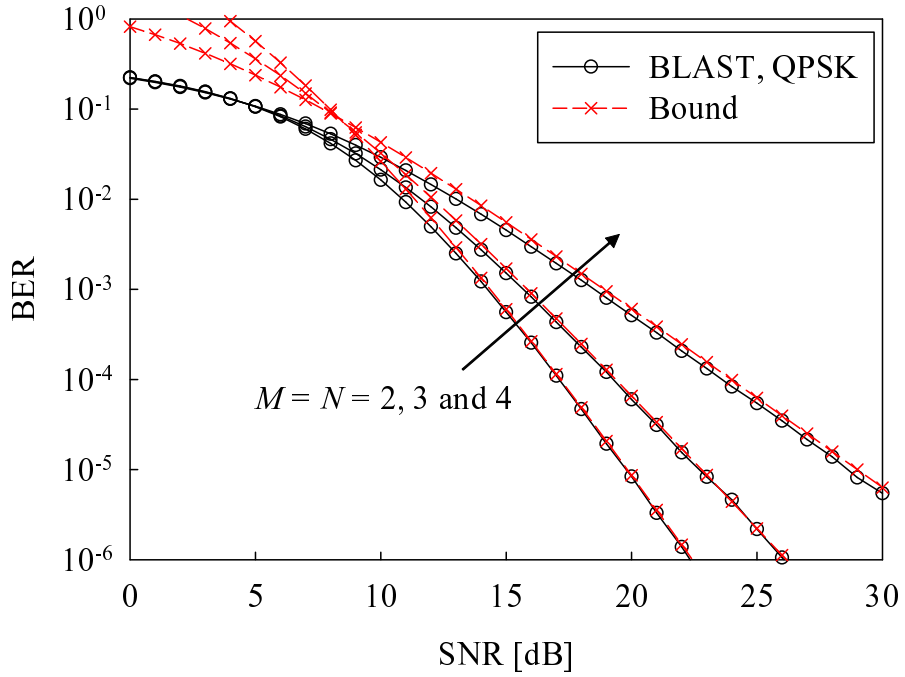

Figure 4.10: BER comparison of the theoretical upper bounds and the numerical results for the QPSK-modulated BLAST scheme of Section 2.2.2, employing $M = N = 2, 3$ and 4 antenna elements. Here, the corresponding transmission rate was $R_{\text{SM}} = 2$ bits/symbol. All other system parameters were summarized in Table 4.2.

4.6 Performance Results

In this section the performance of our uncoded and coded GSTSK systems of Figs. 4.2 and 4.17 is characterized, while comparing the effects of diverse GSTSK parameters. In this contribution, we generated an appropriate dispersion-matrix set capable of achieving a good BER performance for each GSTSK arrangement, which were designed based on the well-known rank- and determinant-criterion [23] for the sake of simplicity, although we may readily employ other design criteria, such as the BLock Error Ratio (BLER) minimization technique of [140] and the DCMC-capacity maximization technique of [23].

4.6.1 Uncoded Systems

Firstly, in Figs. 4.13, 4.14, 4.15 and 4.16 we compared the diverse GSTSK arrangements of Fig. 4.2 to other MIMOs, such as the CSTSK scheme of Fig. 2.5, the SM/SSK scheme of Fig. 2.1, the orthogonal STBC scheme of Section 2.2.1 and the BLAST scheme of Section 2.2.2.

More specifically, the system parameters employed in our simulations are listed in Table 4.3. In Figs. 4.13 and 4.14, $(M, N) = (3, 2)$ AEs were employed, where the transmission rates were given by $R = 2.0$ and 3.0 bits/symbol, respectively. In Figs. 4.15 and 4.16 we assumed having $(M, N) = (4, 3)$ AEs and the transmission rates were given by $R = 3.0$ and

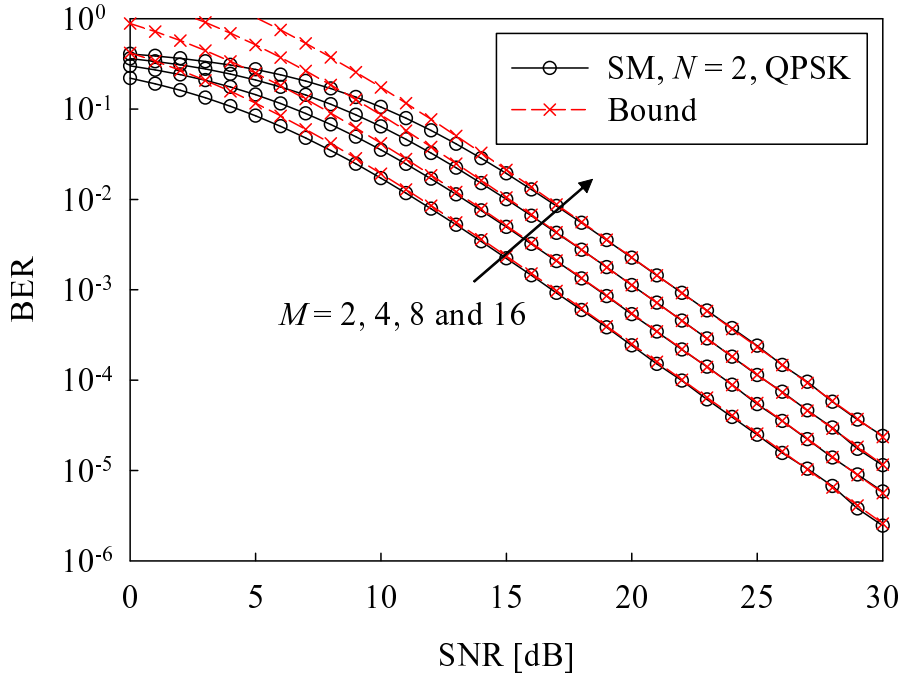

Figure 4.11: BER comparison of the theoretical upper bounds and the numerical results for the QPSK-modulated SM scheme of Fig. 2.1, employing $M = 2, 4, 8$ and 16 transmit antennas and $N = 2$ receive antennas. Here, the corresponding transmission rates were $R_{\text{SM}} = 3, 4, 5$ and 6 bits/symbol. All other system parameters were summarized in Table 4.2.

4.0 bits/symbol, respectively. Observe in Figs. 4.13, 4.14, 4.15 and 4.16 that our GSTSK scheme tended to outperform the CSTSK scheme, which was the explicit benefit of its more flexible system design. However, the GSTSK's performance advantage over the CSTSK scheme was at the expense of imposing on increased computational complexity invested in mitigating the effects of the P ICI contributions. Furthermore, it was also confirmed in Figs. 4.13, 4.14, 4.15 and 4.16 that our GSTSK scheme had a higher BER performance, than conventional MIMO arrangements, such as the SM/SSK, the OSTBC and the BLAST schemes. We also note that although the OSTBC schemes achieved the maximum achievable diversity order of $M \cdot N$, the corresponding BER curves of Figs. 4.13, 4.14, 4.15 and 4.16 were inferior in comparison to the GSTSK and the CSTSK schemes. This is mainly due to the fact that the OSTBC schemes had to employ a high modulation order, such as 64- and 256-QAM, in order to attain transmission rates that were comparable to those of the BLAST, GSTSK and CSTSK schemes.

4.6.2 Turbo Coded Systems

Next, we investigated the turbo coded GSTSK system as shown in Fig. 4.17, where we considered a serially concatenated three-stage turbo codec characterized for example in Section

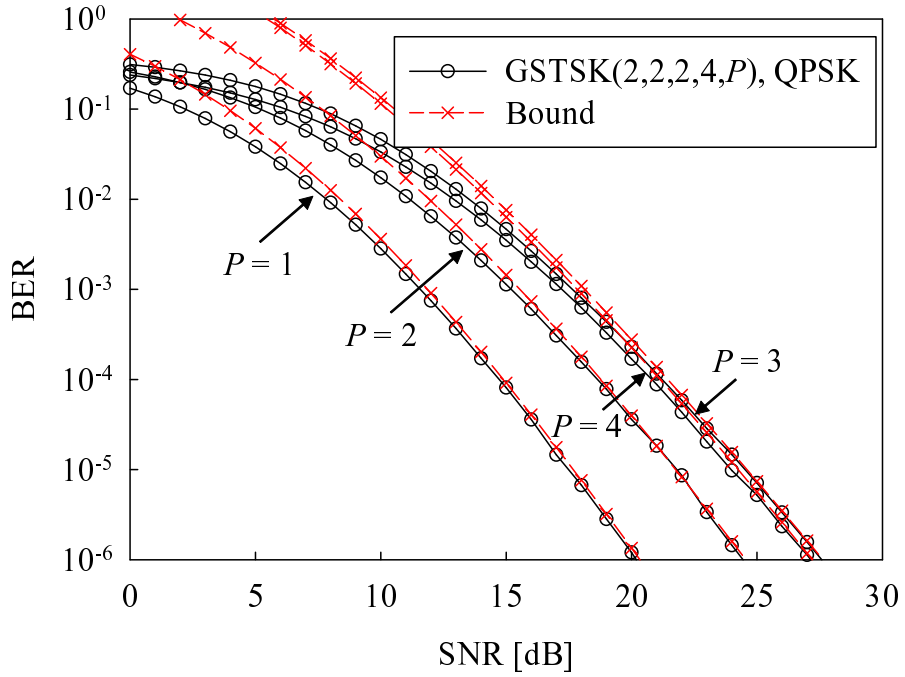

Figure 4.12: BER comparison of the theoretical upper bounds and the numerical results for the QPSK-modulated GSTSK$(2, 2, 2, 4, P)$ scheme of Fig. 4.2, where the parameter P was changed from $P = 1$ to $P = 4$. Here, the corresponding transmission rates were $R_{=}2, 3, 4$ and 4 bits/symbol. All other system parameters were summarized in Table 4.2.

7.4 of [23]. More specifically, the information bits are firstly channel-encoded by the half-rate Recursive Systematic Convolutional (RSC) code and then interleaved by the first random interleaver Π_1 of Fig. 4.17. Next, the interleaved bits are further encoded by the Unity-Rate Convolutional (URC) code and the URC-coded bits are then interleaved by another random interleaver Π_2 of Fig. 4.17. Finally, the interleaved bits are mapped to the AEs with the aid of our GSTSK mapping scheme of Fig. 4.2, in order to generate the space-time codewords $\boldsymbol{S}(i)$ to be transmitted to the receiver. By contrast, the receiver structure of Fig. 4.17 is constituted by a three-stage iterative detector, where three SISO decoders exchange their extrinsic information in the form of Log-Likelihood Ratios (LLRs). Let us assume that the RSC code is used as the *outer code*, while considering the amalgamated combination of the URC code and the GSTSK mapper to be the *inner code*.

Figs. 4.18(a)–4.18(d) show the EXIT charts of our RSC- and URC-coded GSTSK(4, 3, 2, 4, P) system employing QPSK modulation, comparing the effects of the parameter P, which was varied from $P = 1$ to $P = 4$. The associated inner code rates correspond to $R = 2, 3, 4$ and 4 bits/symbol. Furthermore, the corresponding SNR was varied from -3.0 dB to 3.0 dB with a step-size of 0.5 dB for generating the inner code's EXIT curves. Additionally, the outer code's EXIT curve of a half-rate RSC(2,1,2) scheme having the generator polynomials $(3, 2)_8$ was also plotted. Observe in Figs. 4.18(a)–4.18(d) that upon increasing the transmission rate

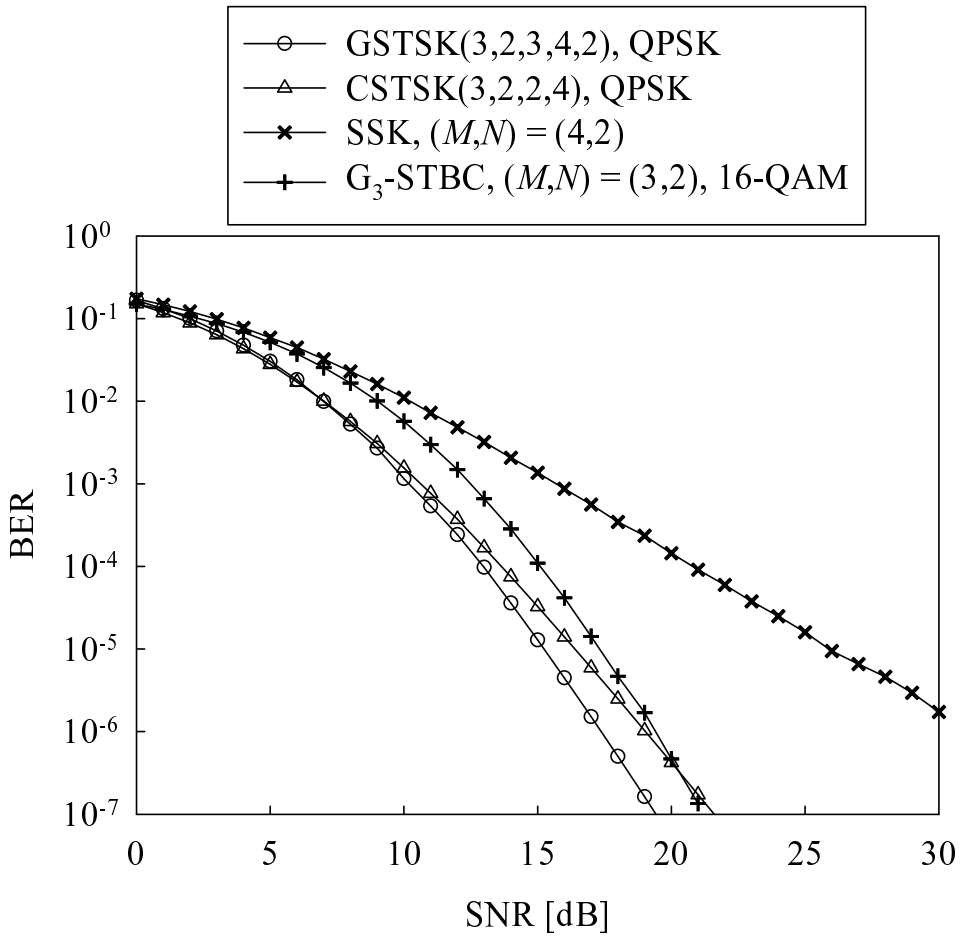

Figure 4.13: BER comparison of our uncoded QPSK-modulated GSTSK$(3, 2, 3, 4, 2)$ scheme of Fig. 4.2, the QPSK-modulated CSTSK$(3, 2, 2, 4)$ scheme of Fig. 2.5, the SSK scheme [66] of Fig. 2.1 having (M, N)=(4,2) antennas and the 16-QAM assisted G_3-STBC scheme [33] having (M, N)=(3,2) antennas. Here, each scheme exhibited a transmission rate of $R = 2.0$ bits/symbol, while employing the optimal ML detection. All other system parameters were summarized in Tables 4.2 and 4.3.

by changing the parameter P, the associated inner code's EXIT curve tended to be degraded, due to the increased IEI encountered. Furthermore, when comparing the GSTSK$(4, 3, 2, 4, 3)$ arrangement and the GSTSK$(4, 3, 2, 4, 4)$ arrangement, which have the same transmission rate of $R = 4$, the GSTSK$(4, 3, 2, 4, 4)$ scheme exhibited a slightly higher performance, since an open EXIT tunnel appeared for SNR > 0 dB. This is achieved at the cost of an increased computational complexity in comparison to that of the GSTSK$(4, 3, 2, 4, 3)$ scheme.

In order to provide further insights, in Figs. 4.19(a)–4.19(e) we show the EXIT charts of our RSC- and URC-coded GSTSK$(5, 2, T, 6, 3)$ system employing BPSK modulation, characterizing the effects of the parameter T, which was varied from $T = 1$ to $T = 5$, where the inner code rates correspond to $R = 7, 3.5, 2.33, 1.75$ and 1.4 bits/symbol. It was found that upon increasing the value T, the corresponding inner EXIT curve was shifted, as a benefit of an increase in the transmit diversity gain, which is commensurate with $\min(M, T)$. However, at the same time, the achievable inner code rate R was decreased from $R = 7$ to $R = 1.4$

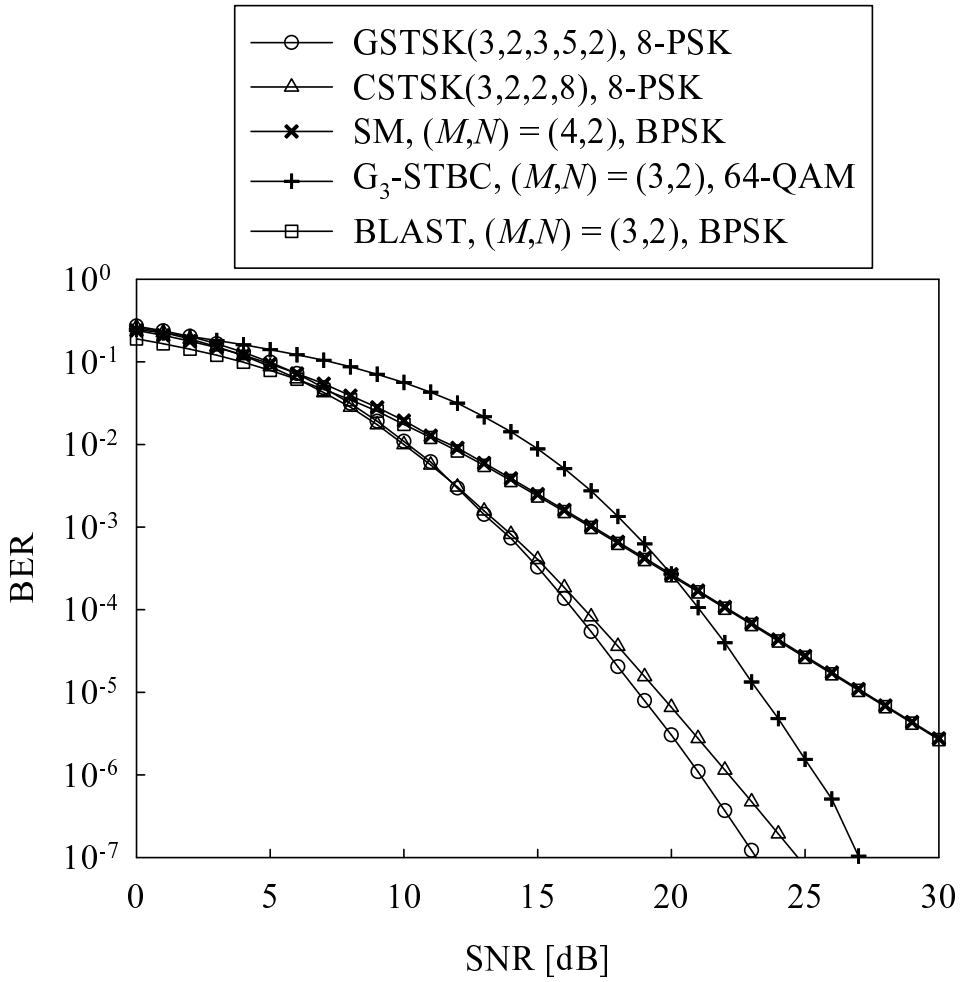

Figure 4.14: BER comparison of our uncoded 8-PSK modulated GSTSK$(3, 2, 3, 5, 2)$ scheme of Fig. 4.2, the 8-PSK modulated CSTSK$(3, 2, 2, 8)$ of Fig. 2.5, the BPSK-modulated SM scheme [63] of Fig. 2.1 having (M, N)=(4,2) antennas, the 64-QAM assisted G_3-STBC scheme [33] having (M, N)=(3,2) antennas and the BPSK-modulated BLAST scheme having (M, N)=(3,2) antennas. Here, each scheme achieved 3.0 bits/symbol, while employing the optimal ML detection. All other system parameters were summarized in Tables 4.2 and 4.3.

bits/symbol, according to Eq. (4.5).

Fig. 4.20 shows the EXIT curves of the QPSK-modulated GSTSK$(2, 2, 2, Q, P)$ arrangements at the SNR of 0 dB, where the parameters (Q, P) were varied. We also plotted the outer RSC(2,1,2) decoder's EXIT curve which employed the octal generator polynomials of $(3, 2)_8$, and the EXIT trajectory associated with the GSTSK$(2, 2, 2, 3, 2)$ scheme, where the interleaver length of both the interleavers Π_1 and Π_2 was set to 200 000 bits. This is a high interleaver length, which enables a good match between the EXIT-chart prediction and the Monte-Carlo simulation-based BER results, as detailed in [23]. Furthermore, the corresponding EXIT curves recorded for BLAST and for the Alamouti code were also shown. It can be seen in Fig. 4.20 that depending on the GSTSK parameters employed, the corresponding inner decoder's EXIT curve exhibited substantially different characteris-

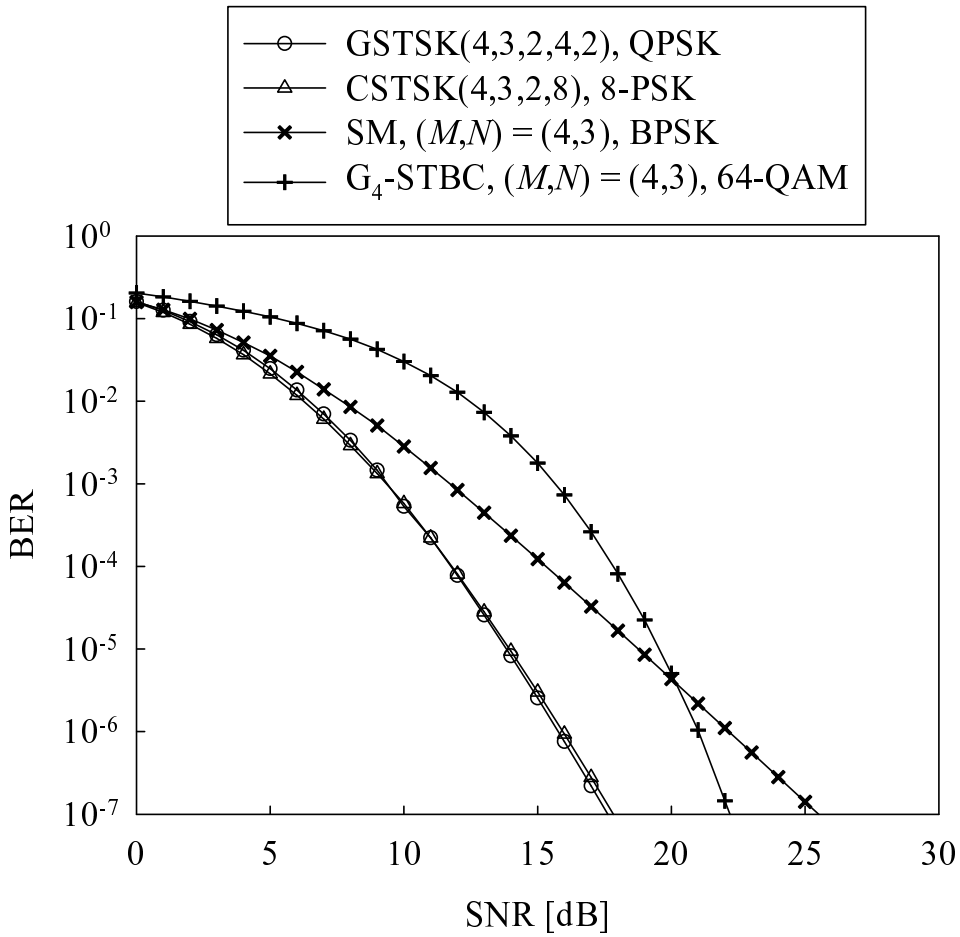

Figure 4.15: BER comparison of our uncoded QPSK-modulated GSTSK$(4, 3, 2, 4, 2)$ scheme of Fig. 4.2, the 8-PSK modulated CSTSK$(4, 3, 2, 8)$ scheme of Fig. 2.5, the BPSK-modulated SM scheme [63] of Fig. 2.1 having (M, N)=(4,3) antennas and the 64-QAM assisted G_4-STBC scheme [33] having (M, N)=(4,3) antennas. Here, each scheme achieved 3.0 bits/symbol, while employing the optimal ML detection. All other system parameters were summarized in Tables 4.2 and 4.3.

tics. The area within the open EXIT-tunnel determines how close the system may operate with respect to the DCMC capacity. Particularly, the inner decoder's EXIT curves of the GSTSK$(2, 2, 2, 3, 2)$ scheme exhibited the narrowest open tunnel at this SNR point, resulting in a performance which was the nearest to capacity for all the GSTSK arrangements. Furthermore, the Monte-Carlo simulation-based decoding trajectory demonstrated that the EXIT-chart prediction was quite accurate.

Finally, Fig. 4.21 shows the achievable BER performance of our RSC- and URC-coded GSTSK$(2, 2, 2, 3, 2)$ system employing QPSK modulation, achieving a total throughput of $R = 1.25$ bits/symbol. The number of iterations I between the *outer* and *inner codes* was varied from $I = 0$ to $I = 20$. As predicted from the EXIT chart of Fig. 4.20, the corresponding BER curve exhibited an infinitesimally low BER at the SNR point of 0 dB. This was within about 1 dB from the SNR corresponding to the DCMC capacity, namely from -1.0 dB.

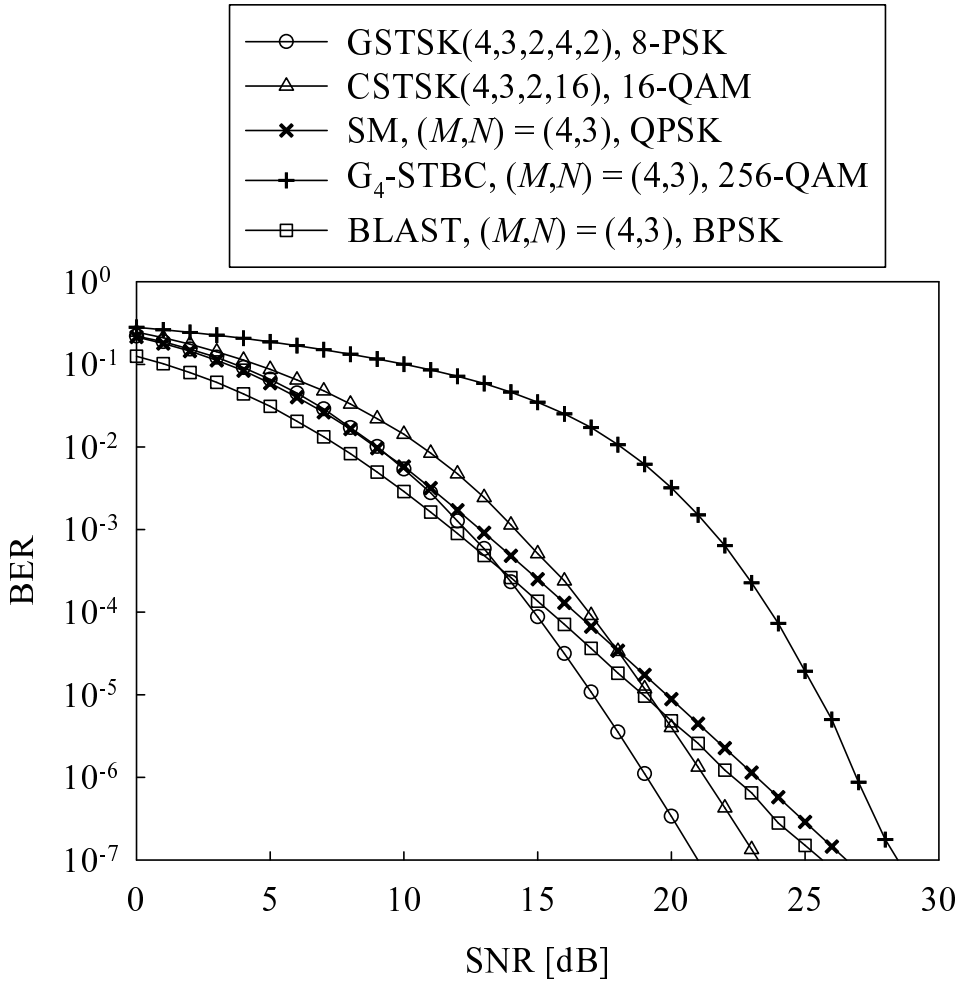

Figure 4.16: BER comparison of our uncoded 8-PSK modulated GSTSK$(4, 3, 2, 4, 2)$ scheme of Fig. 4.2, the 16-QAM modulated CSTSK$(4, 3, 2, 16)$ scheme of Fig. 2.5, the QPSK-modulated SM scheme [63] of Fig. 2.1, the 256-QAM assisted G_4-STBC scheme [33] and the BPSK-modulated BLAST scheme having (M, N)=(4,3) antennas. Here, each scheme achieved 4.0 bits/symbol, while employing the (M, N)=(4,3) antennas and optimal ML detection. All other system parameters were summarized in Tables 4.2 and 4.3.

In order to attain an even 'nearer-to-capacity' performance, the irregular inner- and outer-code concept [98] can be employed, where a set of EXIT curves corresponding to the diverse GSTSK parameters would allow us to create a narrower EXIT tunnel. However, it may be more practical to adaptively select one of the EXIT curves, in order to maintain an open EXIT tunnel, while increasing the achievable throughput R, depending on the instantaneous SNR. Additionally, we can also introduce a threshold for controlling the computational complexity imposed by the receiver, when appropriately designing the sets of GSTSK parameters configured for near-instantaneously adaptive operation. This is particularly beneficial for a downlink scenario, where the mobile receiver's affordable processing capability is limited.

Table 4.3: System parameters employed for the simulations of Figs. 4.13, 4.14, 4.15 and 4.16.

Figs.	rate [bps]	scheme	Tx AEs M	Rx AEs N	diversity order
Fig. 4.13	2.0	GSTSK of Fig. 4.2	3	2	6
		CSTSK of Fig. 2.5	3	2	4
		SSK of Fig. 2.1	4	2	2
		G_3-STBC [33]	3	2	6
Fig. 4.14	3.0	GSTSK of Fig. 4.2	3	2	6
		CSTSK of Fig. 2.5	3	2	4
		SM of Fig. 2.1	3	2	2
		G_3-STBC [33]	3	2	6
		BLAST [52]	3	2	2
Fig. 4.15	3.0	GSTSK of Fig. 4.2	4	3	6
		CSTSK of Fig. 2.5	4	3	6
		SM of Fig. 2.1	4	3	3
		G_4-STBC [33]	4	3	12
Fig. 4.16	4.0	GSTSK of Fig. 4.2	4	3	6
		CSTSK of Fig. 2.5	4	3	6
		SM of Fig. 2.1	4	3	3
		G_4-STBC [33]	4	3	12
		BLAST [52]	4	3	3

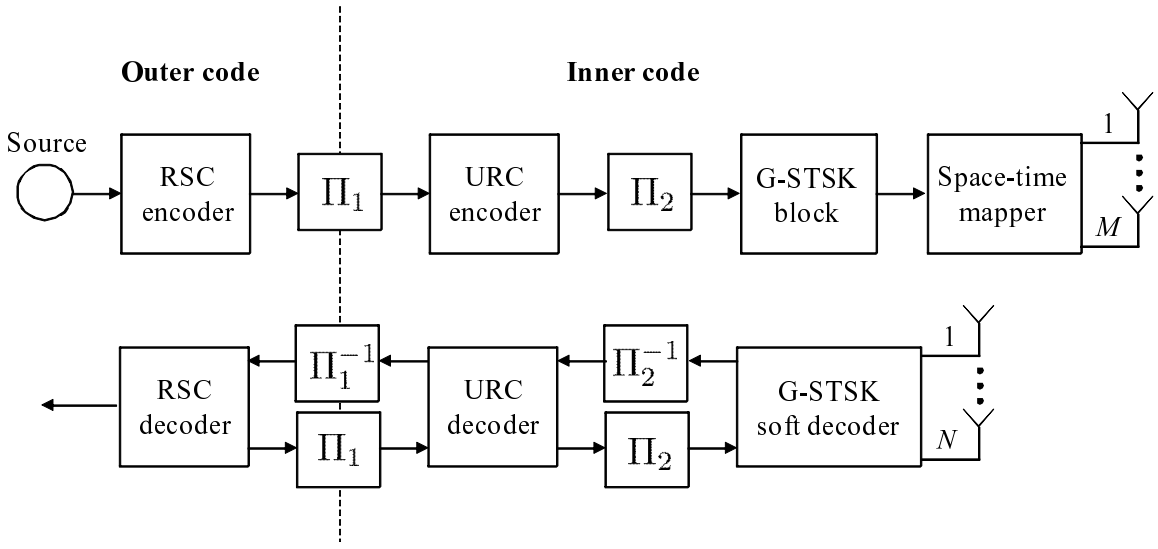

Figure 4.17: Schematic of a three-stage RSC- and URC-coded GSTSK scheme using iterative detection.

Table 4.4: Basic system parameters of the coded GSTSK scheme of Fig. 4.17.

Number of transmit antennas	$M = 2, 4, 5$
Number of receive antennas	$N = 2, 3$
Symbol durations per block	$T = 1$–5
Number of dispersion matrices	$Q = 2, 4, 6$
Number of activated dispersion matrices	$P = 1$–4
Modulation	$\mathcal{L}-$PSK or $\mathcal{L}-$QAM
Channels	Frequency-flat Rayleigh fading
Channel's coherence-time	$\tau = 1$ block duration
Detector	Max-log MAP detector of Eq. (4.17)
Interleaver blocklength	200 000 bits
Outer channel code	RSC$(2, 1, 2)$
Generator polynomials	$(G_\mathrm{r}, G) = (3,2)_8$
Precoder	URC
Number of inner iterations	$I_\mathrm{in} = 1$
Number of outer iterations	$I_\mathrm{in} = 0$–20

4.7 Chapter Conclusions

In this chapter, we proposed the novel GSTSK architecture, which acts as a unified MIMO framework, including many of the previously-developed MIMO arrangements, such as SM/SSK, LDC, STBC, BLAST and STSK as GSTSK's special cases. More specifically, based on the GSTSK's underlying concept, namely that P out of Q pre-allocated dispersion matrices are activated in conjunction with the P classic PSK/QAM symbols, we can strike a flexible trade-off between the achievable diversity order, throughput as well as computational complexity. Additionally, the unified DCMC capacity was derived for our GSTSK scheme, which also represents the capacity of other diverse MIMO arrangements. Our simulation results, including EXIT chart analysis and BER calculations, demonstrated that the proposed scheme was capable of near-capacity operation.

4.8 Chapter Summary

In this chapter, the STSK concept of Chapter 2, i.e. the single dispersion-matrix activation philosophy, has been extended to activate multiple dispersion matrices for the sake of a further increased system-design flexibility. Our GSTSK modulation technique was outlined

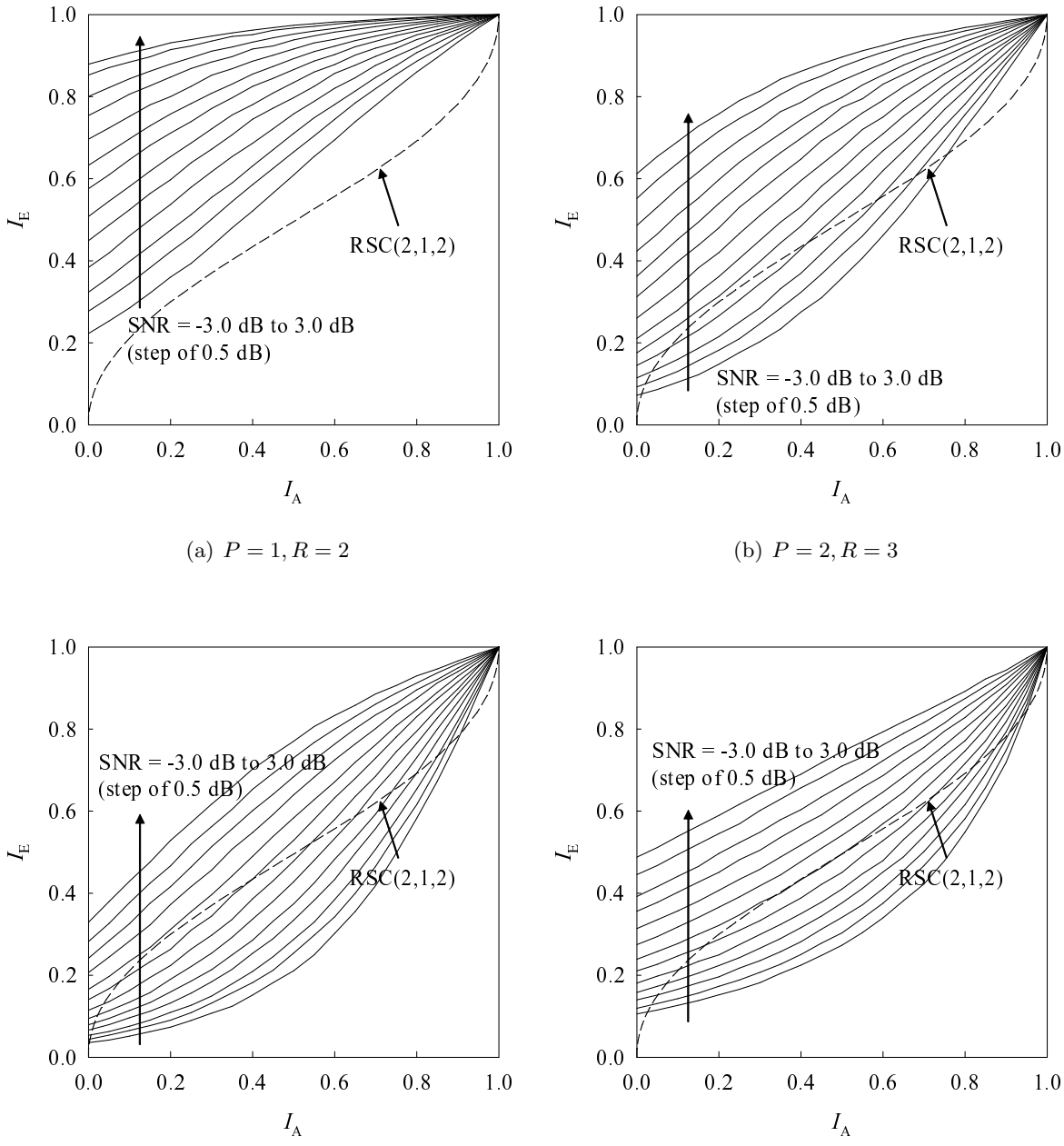

(a) $P = 1, R = 2$

(b) $P = 2, R = 3$

(c) $P = 3, R = 4$

(d) $P = 4, R = 4$

Figure 4.18: EXIT charts of our RSC- and URC-coded GSTSK$(4, 3, 2, 4, P)$ system of Fig. 4.17 employing QPSK modulation, where the parameter P was varied from $P = 1$ to $P = 4$ and the corresponding SNR was changed from -3.0 dB to 3.0 dB with a step of 0.5 dB for the inner EXIT curves. Additionally, the outer EXIT curve of a half-rate RSC(2,1,2) code having the generator polynomials $(3, 2)_8$ was also plotted. All other system parameters were summarized in Table 4.4.

in Section 4.2. It was demonstrated in Section 4.2.2 that since the GSTSK scheme is highly flexible, it subsumes diverse other MIMO schemes, such as the SM, SSK, LDC, STBC, BLAST and STSK schemes. Fig. 4.1 highlighted the linkage of the GSTSK's parameters (M, N, T, Q, P) to those of other MIMO schemes. In Section 4.3, we derived the optimal ML

Table 4.5: Simulation results of our uncoded BPSK-modulated GSTSK$(3, 2, T, 4, P)$ scheme.

Parameters (T, P)	Transmission rate	SNR at BER=10^{-5}	Complexity	Diversity order
$(1, 1)$ (=SM)	3.0 bps	27.1 dB	64	2
$(1, 2)$	4.0 bps	29.6 dB	104	2
$(1, 3)$	5.0 bps	32.0 dB	198	2
$(1, 4)$ (=LDC)	4.0 bps	29.0 dB	168	2
$(2, 1)$ (=CSTSK)	1.5 bps	15.0 dB	192	4
$(2, 2)$	2.0 bps	17.3 dB	256	4
$(2, 3)$	2.5 bps	19.6 dB	435	4
$(2, 4)$ (=LDC)	2.0 bps	16.7 dB	384	4
$(3, 1)$ (=CSTSK)	1.0 bps	11.4 dB	384	6
$(3, 2)$	1.3 bps	13.5 dB	456	6
$(3, 3)$	1.7 bps	16.0 dB	710	6
$(3, 4)$ (=LDC)	1.3 bps	13.1 dB	648	6

detector for uncoded GSTSK schemes, where the number of activated dispersion matrices P determines the amount of ICI imposed. Naturally, the associated complexity increases with P. Additionally, the SISO demodulator of coded GSTSK schemes was also introduced in Section 4.3.2, which is capable of exploiting the *a priori* information gleaned from the outer decoder.

Sections 4.4 and 4.5 analyzed the GSTSK's capacity and its tight BER bound, respectively. Both of these unified limits are applicable to diverse MIMO arrangements. More specifically, in Section 4.4 the DCMC capacity was derived, which takes into account the effects of the specific signaling scheme considered. In Section 4.5.1, the above-mentioned tight BER upper bound was introduced for transmission over Rayleigh fading channels, which was derived from the MGF-based analysis of the pairwise error probability. Based on the BER upper bound derived in Section 4.5.2, the attainable diversity order of our GSTSK scheme was characterized as $N \cdot \min(M, T)$.

Finally, in Section 4.6 our performance results were discussed, while comparing the effects of diverse GSTSK parameters as well as of the other MIMO arrangements considered. Section 4.6.1 provided our BER analysis for uncoded systems, where the GSTSK scheme was found to outperform the other MIMOs, such as the STBC, BLAST, SM/SSK and STSK schemes. Again, Table 4.5 provided a performance summary of our uncoded BPSK-modulated GSTSK$(3, 2, T, 4, P)$ scheme, where the value of T was varied from $T = 1$ to $T = 3$, while the value P was varied from $P = 1$ to $P = 4$. Here, upon increasing the value of T, both the achievable diversity order as well as the corresponding BER value improved

at the cost of an increased complexity. Observe in Table 4.5 that upon increasing the value of P in the rage of $1 \leq P \leq Q-1$, the attainable transmission rate increased. Furthermore, in Section 4.6.2 a three-stage concatenated RSC- and URC-coded GSTSK scheme was considered. Its EXIT chart analysis was conducted in Figs. 4.18, 4.19 and 4.20, in order to characterize the iterative decoding behaviour of our coded GSTSK scheme and to optimize its system parameters. The BER results of Fig. 4.21 suggested that our coded GSTSK scheme is capable of achieving a near-capacity performance, as predicted by the corresponding EXIT chart analysis of Fig. 4.20.

In Chapters 2, 3 and 4, we have proposed the novel STSK family in the context of co-located MIMO arrangements, assuming the presence of uncorrelated fading for the multipath channel components. However, when we cannot afford sufficient spacing between the AEs at the transmitter and/or receiver terminals, the achievable performance may be substantially degraded. To this end, in the following chapter we will invoke the recent concept of cooperative transmissions, which is combined with our STSK concept.

Table 4.6: Summary of the coded GSTSK, DSTSK/ADSTSK and CSTSK/ACSTSK schemes, employing the system parameters of Table 4.4, where the system bandwidth efficiency of the GSTSK scheme was given by $R = 1.5$ bits/symbol, while those of other schemes were represented by $R = 1.0$ bits/symbol.

	GSTSK	**DSTSK**	**ADSTSK**	**CSTSK**	**ACSTSK**
Schematic	Fig. 4.17	Fig. 3.6	←	Fig. 2.7	←
Parameters	(M, N, T, Q, P)	(M, N, Q)	←	(M, N, T, Q)	←
CSI	Perfect CSI	No CSI	←	Perfect CSI	←
IAS	Symbol-level	Symbol-level	Relaxed	Symbol-level	Relaxed
Dispersion-matrix	Power constraint of Eq. (4.4)	Hermitian	Real-valued diagonal	Power constraint of Eq. (2.21)	Power constraint of Eq. (2.21)
Iterations $(I_{\text{in}}, I_{\text{out}})$	(1,10)				
FEC rate	0.5				
Complexity	$\frac{NT[(8MTQ+8P\iota\mathcal{L}^Q)/\tau+4\iota\mathcal{L}^Q]}{Q\log_2\mathcal{L}+\iota} = 146 + 640/\tau$	$\frac{MNQ(8M^2+6\mathcal{L})}{\log_2(Q\cdot\mathcal{L})} = 224$	$\frac{MNQ(8M+6\mathcal{L})}{\log_2(Q\cdot\mathcal{L})} = 80$	$\frac{NTQ[(8MT+4\mathcal{L})/\tau+2\mathcal{L}]}{\log_2(Q\cdot\mathcal{L})} = 32 + 192/\tau$	$\frac{NTQ[(8T+4\mathcal{L})/\tau+2\mathcal{L}]}{\log_2(Q\cdot\mathcal{L})} = 32 + 126/\tau$
Performance[a] $(M \times N) = (2 \times 2)$	−1.0 dB	3.5 dB	4.2 dB	−0.8 dB	−0.7 dB

[a] Performance is characterized by the Eb/N0 value required for achieving an infinitesimally BER.

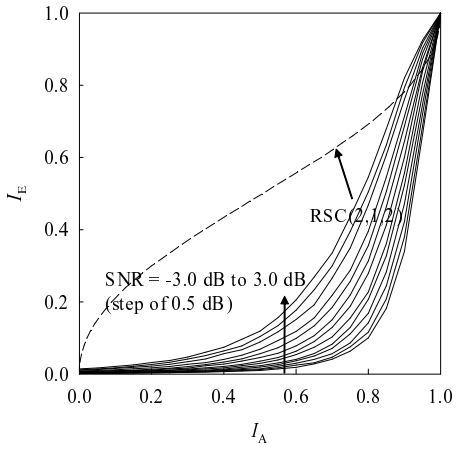

(a) $T = 1, R = 7$

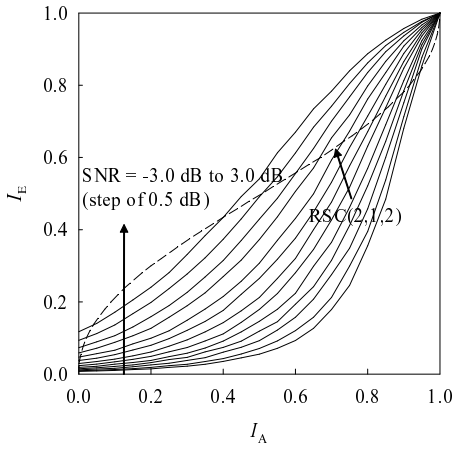

(b) $T = 2, R = 3.5$

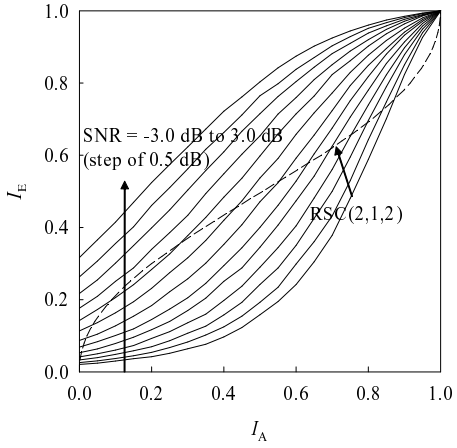

(c) $T = 3, R = 2.33$

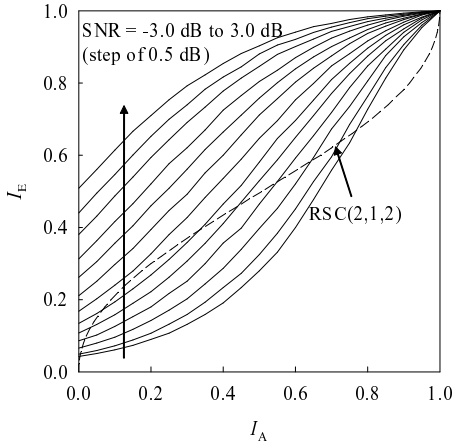

(d) $T = 4, R = 1.75$

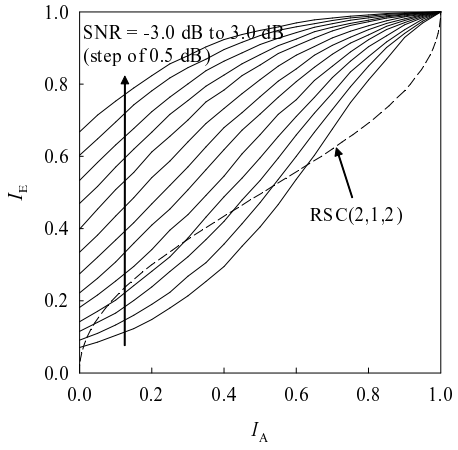

(e) $T = 5, R = 1.4$

Figure 4.19: EXIT charts of our RSC- and URC-coded GSTSK$(5, 2, T, 6, 3)$ system of Fig. 4.17 employing QPSK modulation, where the parameter T was varied from $T = 1$ to $T = 5$ and the corresponding SNR was changed from -3.0 dB to 3.0 dB with a step of 0.5 dB for the inner EXIT curves. Additionally, the outer EXIT curve of a half-rate RSC(2,1,2) code having the generator polynomials $(3, 2)_8$ was also plotted. All other system parameters were summarized in Table 4.4.

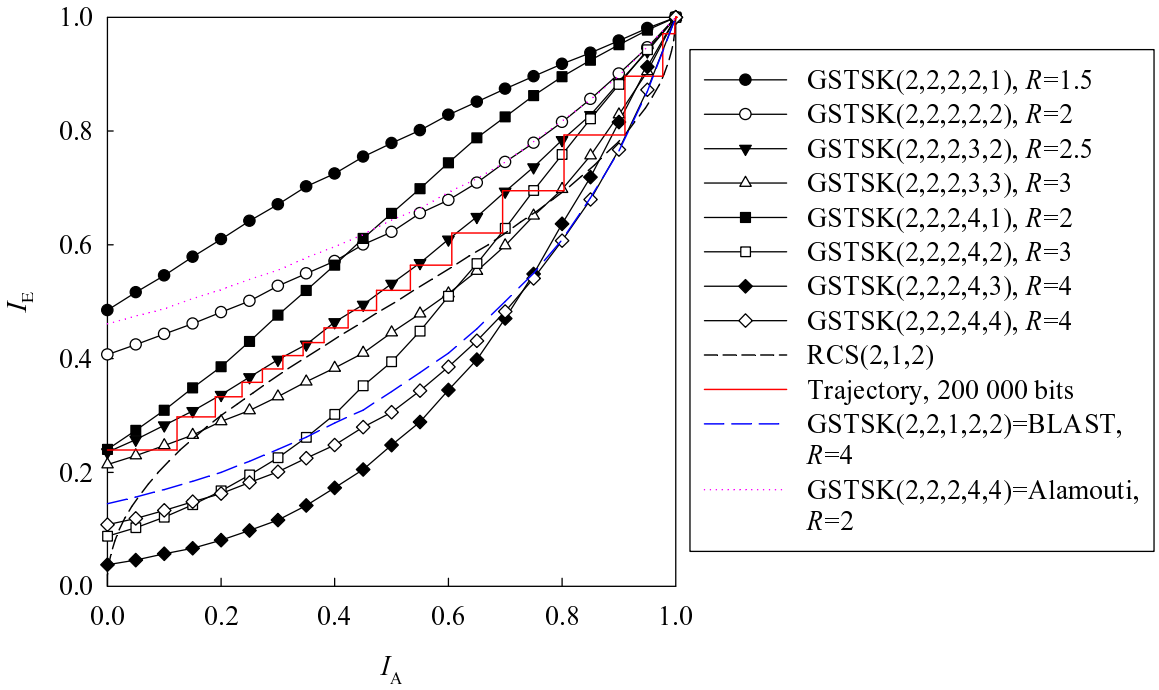

Figure 4.20: EXIT chart of our RSC- and URC-coded GSTSK$(2, 2, 2, T, P)$ system of Fig. 4.17. All other system parameters were summarized in Table 4.4.

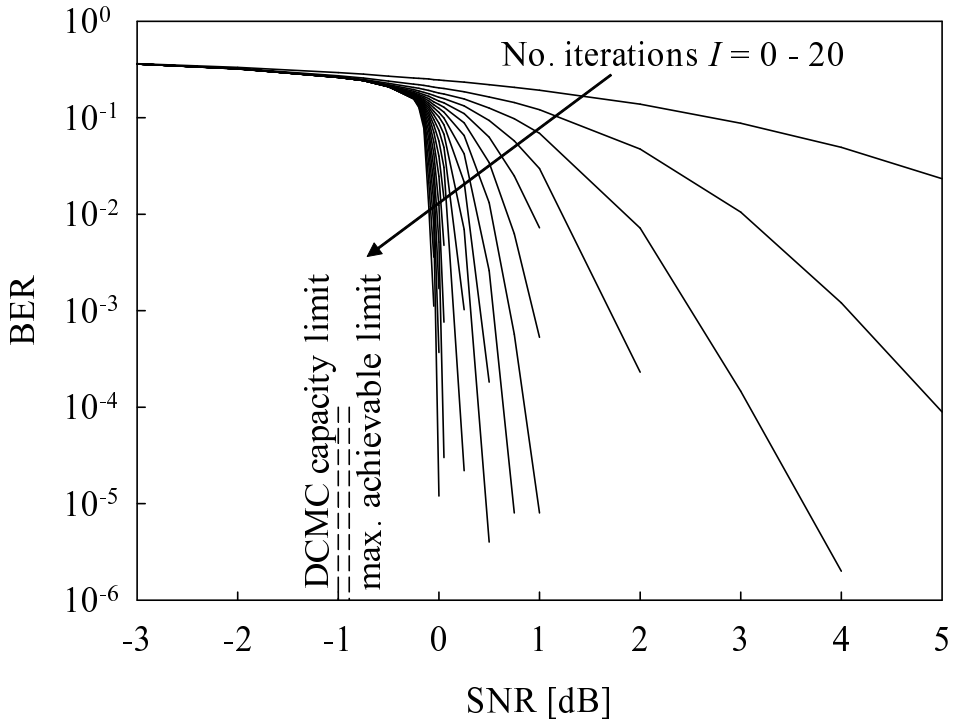

Figure 4.21: Achievable BER performance of our RSC- and URC-coded GSTSK$(2, 2, 2, 3, 2)$ system of Fig. 4.17 employing QPSK modulation, where the number of iterations I was changed from $I = 0$ to $I = 20$. All other system parameters were summarized in Table 4.4. The dashed-lines indicate the lowest possible SNRs, at which an infinitesimally low BER may be attained at the effective throughput of 1.25 bits/symbol, calculated from DCMC capacity and the maximum achievable rate.

Chapter 5

Cooperative STSK Scheme for Distributed MIMO Systems

5.1 Introduction

In Chapters 2, 3 and 4, we have investigated novel MIMO concepts, which included coherent STSK, differential STSK and generalized STSK schemes. In these chapters, we mainly focused our attention on co-located MIMO scenarios, where multiple antennas were accommodated at the transmitter and/or at the receiver, which may however suffer from the effects of inter-antenna correlation imposed by insufficient antenna separation. To this end, the recent philosophy of cooperative communication may be considered to be a promising approach, where the concept of Virtual Antenna Arrays (VAAs) enables us to exploit additional degrees of design freedom. More specifically, it is often claimed that cooperative MIMO systems are capable of attaining the maximum achievable diversity gain associated with uncorrelated fading. However, most of the previous studies related to cooperative MIMOs typically employed idealized assumptions, which are difficult to satisfy in practice.

In this chapter we propose a practical cooperative MIMO arrangement based on the above-mentioned CSTSK and DSTSK schemes, which considers the challenging problems of the relays' imperfect synchronization and channel estimation. The remainder of this chapter is organized as follows. Section 5.2 reviews the existing background, processes, literature and formulates our problem statement for cooperative MIMO systems. In Section 5.3 we describe the system model of our cooperative CSTSK scheme as well as the optimal IEI-free joint ML detector. By contrast, Section 5.4 presents our cooperative DSTSK scheme, which is the differentially-encoded counterpart of the above-mentioned cooperative CSTSK scheme. In Section 5.5 our simulation results characterize the achievable performance of our cooperative CSTSK and DSTSK schemes. Finally, this chapter is concluded in Section 5.6, which is then

followed by the chapter's summary in Section 5.7

5.2 Background and Problem Statement

As discussed in Chapters 2, 3 and 4, MIMO tranceiver design allows us to eliminate some of the limitations of reliable wireless communications. For example, the family of Space-Time Codes (STCs) constitute efficient diversity techniques that are capable of combating the time-varying fading effects of wireless channels. However, the antenna elements of co-located MIMO systems typically suffer from spatially correlated large-scale fading imposed by the shadowing effects [141]. In order to eliminate this correlation-induced diversity-gain erosion, cooperative STC schemes [105, 109, 112] were proposed to achieve the best attainable diversity gain of uncorrelated elements, where a collection of single-antenna-aided nodes act as a VAA, having widely separated distributed antenna elements. Additionally, this cooperative MIMO arrangement enables us to circumvent the physical limitations of installing multiple antennas on a mobile handset.

To briefly clarify the benefits of cooperative STCs, here we provides a comparison of co-located and cooperative STC schemes, focusing on Alamouti's scheme [20] employing $M = 2$ transmit antennas and $N = 1$ receive antenna in frequency-flat Rayleigh fading environments. Fig. 5.1 shows the achievable BER performance of the co-located and cooperative STCs. Here we assumed that while the two channel components of the cooperative STC were uncorrelated, those of the co-located STC were correlated, where the spatial correlation factor $\rho_s = E[h_1 h_2^*]$ was varied from 0.1 to 0.9. We also characterized in Fig 5.1 the 'no diversity' scenario, where the transmitter was equipped with a single antenna element, which we hence referred to as the single-antenna scenario. Observe in Fig. 5.1 that as expected, the cooperative STC achieved the full diversity order of two, while that of the single-antenna scenario was only one owing to the absence of any diversity effect. By contrast, the diversity order of the co-located STC deteriorated from two to one, upon increasing the correlation factor ρ_s. Thus, it was confirmed that the cooperative MIMO arrangement may be capable of combating the co-located MIMO channel's correlation caused by typical shadow-fading channels and/or by the insufficient antenna element separation.

On the other hand, attaining a high cooperative space-time diversity gain in a practical relay-aided network imposes further challenges. Firstly, many of the previously-proposed cooperative STC schemes assumed that perfect CSI of the Source-Relay (SR) links and/or of the Relay-Destination (RD) links is available at the destination receiver. However, the rapidly changing topology of vehicles travelling at high speeds makes it challenging to acquire accurate CSI, which results in a severe degradation of the achievable performance. Since each of the MIMO subchannels has to be sampled above the Doppler frequency, at high speeds an increased pilot overhead is added for the sake of accurately estimating each MIMO channel component, which also gives rise to a substantial increase of the complexity.

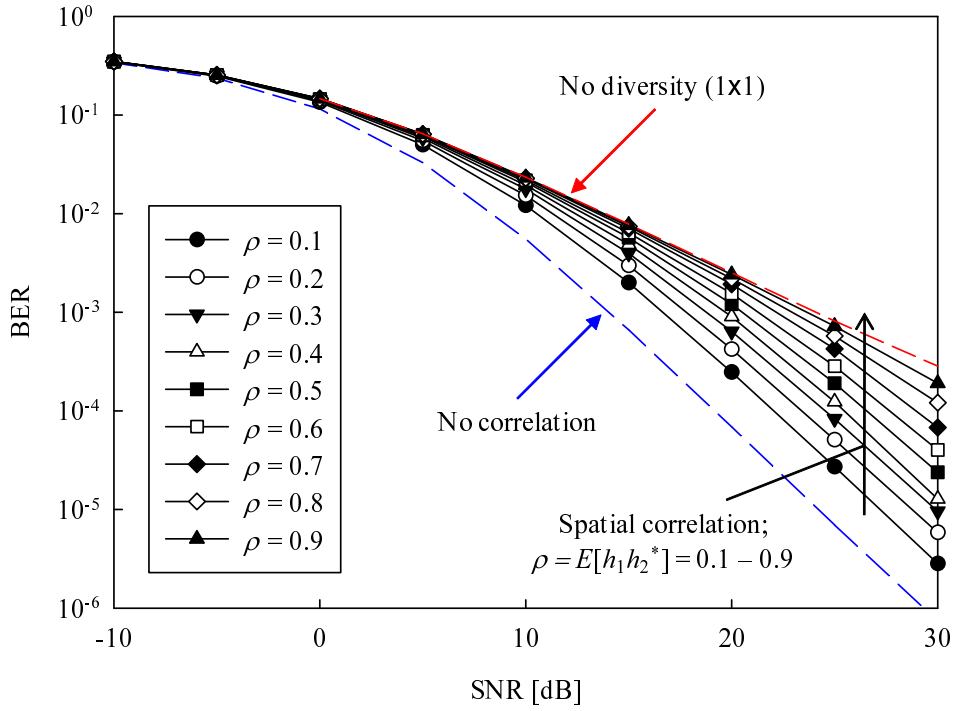

Figure 5.1: Comparison of co-located and cooperative MIMO systems, employing 2×1 Alamouti scheme, where spatial correlation $\rho_s = E[h_1 h_2^*]$ between the two channels was changed from $\rho_s = 0.1$ to $\rho_s = 0.9$, while the cooperative MIMO exhibited the no-correlation result.

While the majority of the cooperative STC studies assumed availability of perfect CSI, a number of Cooperative Differential STCs (CDSTCs) were proposed in [6, 110, 116, 119] in order to achieve reliable symbol detection without any CSI, inspired by the differential STC philosophy developed for collocated MIMO systems [42, 136].

Another major challenge is the asynchronous nature of relay nodes in the network. The aforementioned cooperative STCs are all based on the assumption of perfect timing synchronization between the relay nodes, although in practice it is difficult to acquire accurate symbol-level time synchronization, without imposing a high additional synchronization overhead and implementation complexity. As noted in [142], the resultant time synchronization errors impose a significant performance degradation. Additionally, the propagation delays arising both from the different node locations and from the multipath-induced delayspread also contribute to the sampling offset errors, which further aggravates the effect of synchronization errors. To this end, a number of asynchronous cooperative STCs were proposed [143–147], which invoke space-time equalization or multi-carrier transmission techniques, assuming that the perfect CSI and/or the relative transmission delays of the mobiles are available at the destination. However, a relatively high computational complexity is imposed at the destination receiver. More importantly, these schemes do not provide attractive solution to the above-mentioned CSI problem.

From a practical point of view, it is important to combat both the problems associated with the CSI estimation errors and the time synchronization errors, in order to achieve a realistic cooperative space-time diversity gain. Having briefly described the background and the challenges of cooperative MIMOs, we then propose a new CSTSK-assisted cooperative MIMO arrangement in the following section.

5.3 Cooperative CSTSK Scheme

In this section, inspired by the matrix-activation concept of the STSK scheme proposed in Chapter 2, we present a cooperative CSTSK scheme, which potentially outperforms the conventional cooperative OSTBCs. The co-located CSTSK scheme of Fig. 2.5 was found to attain a higher BER performance than those of OSTBCs due to the CSTSK scheme's capability of striking a flexible tradeoff between the diversity and multiplexing gains for an arbitrary number of transmit and receive AEs. Additionally, we also modify the cooperative CSTSK scheme in order to realize its asynchronous counterpart, which is developed with the aid of the ACSTSK concept introduced in Section 2.3.2.

Considering that the SM scheme can be operated without perfect Inter-Antenna Synchronization (IAS), our proposition is that this arrangement may also be suitable for cooperative communication scenarios, although no cooperative SM scheme has been presented in the open literature. However, since SM was not designed for providing transmit diversity gain, increasing the number of RNs would not increase the cooperative diversity order.

5.3.1 System Model

This section describes our cooperative STSK scheme. As seen in Fig. 3.5, we consider a two-phase relay network, which is constituted by a single Source Node (SN), M RNs and a DN, each having a single antenna element. We note that the proposed scheme can be readily extended to the multiple-antenna-element assisted DN scenario. Here, it is assumed that a Time Division Multiple Access (TDMA) protocol is used and that the cooperating relays attempt to loosely-synchronize their timings under the BS's control,[1] but nevertheless, we will demonstrate that the proposed regime is resilient against Inter-Relay Synchronization (IRS) errors. We also assume that each node is operated in a half-duplex mode, either receiving or transmitting in a given time slot.

[1]The synchronization accuracy achieved by the Medium Access Control (MAC) layer is typically lower than the symbol-synchronized simultaneous transmissions of the relays.

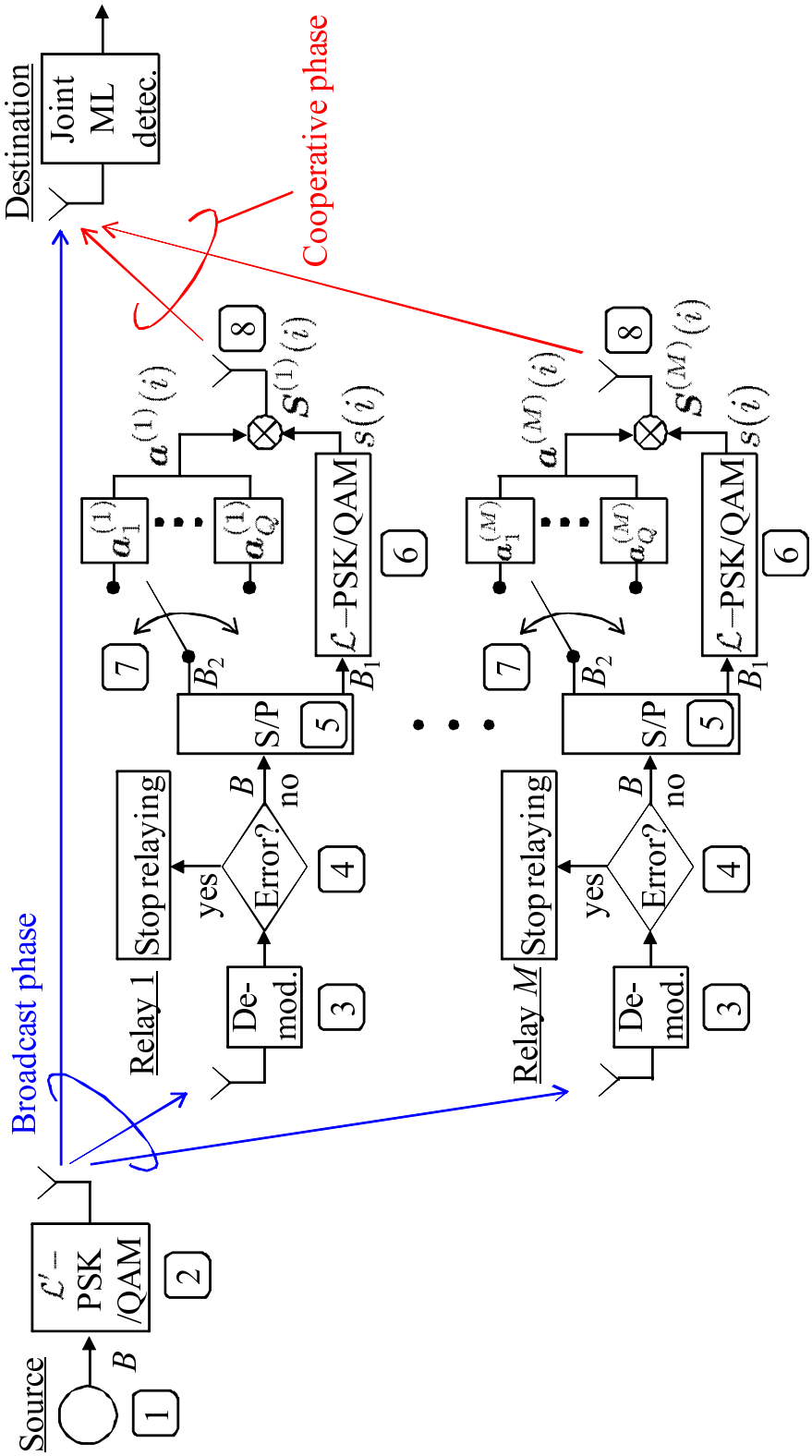

Figure 5.2: Schematic of our cooperative CSTSK scheme assisted by selective DF relaying, which was developed from the CSTSK architecture of Fig. 2.5.

5.3.1.1 Source Model

During the broadcast phase of Fig. 3.5, the SN transmits its information to the M RNs as well as to the DN. As noted in [148], the SN first attaches Cyclic Redundancy Check (CRC) bits to its information bits in order for the RNs to be able to detect the potential decoding errors and hence to avoid the propagation of DF errors to the DN. Then the CRC-encoded bits are mapped to the $\mathcal{L}'-$constellation point PSK/QAM scheme in order to generate the symbols $\boldsymbol{S}_{\rm s}(i) = [s_1(i), \cdots, s_b(i)]^{\rm T} \in \mathcal{C}^{b\times 1}$, where i represents the block index and $B = b\log_2 \mathcal{L}'$ bits are transmitted in each block. Let us assume that the SN transmits the symbols $\boldsymbol{S}_{\rm s}(i)$ over b time slots, and the corresponding signals received at the mth RN as well as at the DN are given by

$$\boldsymbol{Y}_{\rm sr}^{(m)}(i) = h_{\rm sr}^{(m)}(i)\boldsymbol{S}_{\rm s}(i) + \boldsymbol{V}_{\rm r}^{(m)}(i) \tag{5.1}$$

and

$$\boldsymbol{Y}_{\rm sd}(i) = h_{\rm sd}(i)\boldsymbol{S}_{\rm s}(i) + \boldsymbol{V}_{\rm d}(i), \tag{5.2}$$

respectively, where the channel coefficients $h_{\rm sr}^{(m)}$ and $h_{\rm sd}(i)$ obey the complex-valued Gaussian distributions of $\mathcal{CN}(0, \sigma_{\rm sd}^2)$ and of $\mathcal{CN}(0, \sigma_{\rm sr}^2)$, while each component of the noise vectors $\boldsymbol{V}_{\rm r}^{(m)}(i)$ and $\boldsymbol{V}_{\rm d}(i)$ is a complex-valued Gaussian variable of $\mathcal{CN}(0, N_0)$. Finally, N_0 represents the noise variance.

5.3.1.2 Relay Model

Let us now describe the cooperative phase of Fig. 3.5, where the M RNs employ CRC-activated DF transmission with the aid of our cooperative CSTSK scheme. Let us consider the mth RN to be the node of interest, which first decodes the received signals $\boldsymbol{Y}_{\rm sr}^{(m)}(i)$ of Eq. (5.1). If any decoding error is identified by the CRC, the RN refrains from relaying the signals to the DN without requiring any negotiation with the other nodes. By contrast, if there are no decoding errors, the mth relay re-encodes the decoded bits and transmits them using the cooperative CSTSK scheme as follows. The $B = b\log_2 \mathcal{L}'$ decoded bits per b-slot block are Serial-to-Parallel (S/P) converted to $B_1 = \log_2 \mathcal{L}$ and $B_2 = \log_2 Q$ bits, assuming the relationship of $b\log_2 \mathcal{L}' = \log_2(Q \cdot \mathcal{L})$.[2] Here, we will represent each of the corresponding S/P converted bits as (q, l) in decimal representation. Then, as shown in Fig. 3.5, the bits decoded at the mth RN are mapped to a $T-$length symbol vector $\boldsymbol{S}_{\rm r}^{(m)}(i) \in \mathcal{C}^{1\times T}$, which is given by

$$\boldsymbol{S}_{\rm r}^{(m)}(i) = s(i)\boldsymbol{a}^{(m)}(i), \tag{5.3}$$

where according to the input bits q, $\boldsymbol{a}^{(m)}(i)$ is selected from the Q pre-assigned dispersion vectors $\boldsymbol{a}_{q'}^{(m)} \in \mathcal{C}^{1\times T}$ $(q' = 1, 2, \cdots, Q)$, while $s(i)$ is selected from an $\mathcal{L}$–point PSK/QAM

[2] To expound a little further, this constraint was employed only for the sake of maintaining bits per block during the broadcast phase to be equal to that of the cooperative phase, having the relation $B = B_1 + B_2$.

Table 5.1: Example of mth Relay's STSK Modulation Scheme, Mapping 3 Bits Per Space-Time Block, with the Aid of BPSK Constellation

		$Q=4,\ \mathcal{L}=2$		
Input bits		Mapped symbols		
(q,l)		$\boldsymbol{a}^{(m)}(i)$	$s(i)$	$\boldsymbol{S}_{\mathrm{r}}^{(m)}(i)$
00	0	$\boldsymbol{a}_1^{(m)}$	$+1$	$\boldsymbol{a}_1^{(m)}$
00	1	$\boldsymbol{a}_1^{(m)}$	-1	$-\boldsymbol{a}_1^{(m)}$
01	0	$\boldsymbol{a}_2^{(m)}$	$+1$	$\boldsymbol{a}_2^{(m)}$
01	1	$\boldsymbol{a}_2^{(m)}$	-1	$-\boldsymbol{a}_2^{(m)}$
10	0	$\boldsymbol{a}_3^{(m)}$	$+1$	$\boldsymbol{a}_3^{(m)}$
10	1	$\boldsymbol{a}_3^{(m)}$	-1	$-\boldsymbol{a}_3^{(m)}$
11	0	$\boldsymbol{a}_4^{(m)}$	$+1$	$\boldsymbol{a}_4^{(m)}$
$\underbrace{11}_{\log_2 Q}$	$\underbrace{1}_{\log_2 \mathcal{L}}$	$\boldsymbol{a}_4^{(m)}$	-1	$-\boldsymbol{a}_4^{(m)}$

constellation according to the input bits l. We note that the input bit-dependent selection of a dispersion vector from a set of Q provides an additional implicit means of transmitting $\log_2 Q$ bits of information, similarly to the antenna selection philosophy of SM [61, 63, 66]. To elaborate a little further, the mth relay's bit-to-symbol mapping regime of our cooperative CSTSK scheme employing $Q=4$ and $\mathcal{L}=2$ is shown in Table 5.1. Given $B=\log_2(Q\cdot\mathcal{L})$ input bits per block, there are several potential combinations of Q and $\mathcal{L}$, for instance, $(Q,\mathcal{L})$ $=(8,1)$, $(4,2)$, $(2,4)$ and $(1,8)$ for the above-mentioned case of conveying $\log_2(Q\cdot\mathcal{L})=3$ input bits.

Having generated the STSK-modulated signal vector $\boldsymbol{S}_{\mathrm{r}}^{(m)}(i)$, the corresponding signals received at the DN may be expressed as

$$\boldsymbol{Y}_{\mathrm{rd}}(i) = \sum_{m=1}^{M} \alpha_m h_{\mathrm{rd}}^{(m)}(i)\boldsymbol{S}_{\mathrm{r}}^{(m)}(i) + \boldsymbol{V}'_{\mathrm{d}}(i) \tag{5.4}$$

$$= s(i)\boldsymbol{H}_{\mathrm{rd}}(i)\boldsymbol{A}(i) + \boldsymbol{V}'_{\mathrm{d}}(i), \tag{5.5}$$

where we have

$$\boldsymbol{H}_{\mathrm{rd}}(i) = \left[\alpha_1 h_{\mathrm{rd}}^{(1)}(i), \cdots, \alpha_M h_{\mathrm{rd}}^{(M)}(i)\right] \in \mathcal{C}^{1\times M}, \tag{5.6}$$

$$\boldsymbol{A}(i) = \begin{bmatrix} \boldsymbol{a}^{(1)}(i) \\ \vdots \\ \boldsymbol{a}^{(M)}(i) \end{bmatrix} \in \mathcal{C}^{M\times T}. \tag{5.7}$$

Here, $\alpha_m \in \{1,0\}$ represents the activation/deactivation of the mth relay, where α_m is 0, if any decoding error is identified by the CRC scheme of the mth relay. Otherwise α_m is set to 1. Furthermore, the RN-DN channel coefficients $h_{\mathrm{rd}}^{(m)}(i)$ $(m=1,\cdots,M)$ and the

destination's noise components $\boldsymbol{V}'_{\mathrm{d}}(i)$ follow the complex-valued Gaussian distributions of $\mathcal{CN}(0, \sigma_{\mathrm{rd}}^2)$ and $\mathcal{CN}(0, N_0)$, respectively. In order to maintain a unity transmission power per time slot, the $M \cdot Q$ pre-assigned dispersion vectors $\boldsymbol{a}_q^{(m)}$ $(1 \leq m \leq M, 1 \leq q \leq Q)$ have to satisfy

$$\mathrm{tr}(\boldsymbol{A}_{q'} \boldsymbol{A}_{q'}^{\mathrm{H}}) = T \ (q' = 1, \cdots, Q), \tag{5.8}$$

where tr( ) represents the trace of a matrix and

$$\boldsymbol{A}_{q'} = \begin{bmatrix} \boldsymbol{a}_{q'}^{(1)} \\ \vdots \\ \boldsymbol{a}_{q'}^{(M)} \end{bmatrix} \in \mathcal{C}^{M \times T}. \tag{5.9}$$

Additionally, the normalized throughput per each of the b time slots or per PSK/QAM symbol duration for the broadcast phase is R_1 and that of the cooperative phase is R_2, which are given by

$$R_1 = \log_2 \mathcal{L}' \quad [\text{bits/symbol}] \tag{5.10}$$

$$R_2 = \frac{\log_2(Q \cdot \mathcal{L})}{T} \quad [\text{bits/symbol}], \tag{5.11}$$

leading to the total normalized throughput of

$$R = \frac{bR_1 + TR_2}{2(b+T)} = \frac{\log_2(Q \cdot \mathcal{L})}{b+T} \ [\text{bits/symbol}]. \tag{5.12}$$

It can be seen from Eq. (5.11) that upon increasing either the number of dispersion vectors Q or the classic PSK/QAM constellation size $\mathcal{L}$, the transmission rate of the cooperative phase increases. Moreover, as detailed in Section 2.3.5, the maximum achievable transmit diversity order of the cooperative CSTSK scheme is upper-bounded by $\min(M, T)$, according to the well-known pairwise-error probability analysis based on the Chernoff upper bound [93].

Again, since the matrices $\boldsymbol{A}_{q'}$ $(q' = 1, \cdots, Q)$ of our cooperative CSTSK(M, N, T, Q) scheme have the size of $(M \times T)$, their search space increases upon increasing the number of relay nodes M, the number of symbols T per block and the number of dispersion-vector sets Q, in addition to the constellation points $\mathcal{L}$. According to the rank- and determinant-criterion discussed in Section 3.5.1, an random search may be implemented in order to optimize Q dispersion-vector sets $\boldsymbol{A}_{q'}$ $(q' = 1, \cdots, Q)$. As the result, any two of the $Q \cdot \mathcal{L}$ virtual space-time matrices $s_l \boldsymbol{A}_q$ $(1 \leq q \leq Q, 1 \leq l \leq \mathcal{L})$ typically exhibit a low correlation, which offers a good detection performance at the receiver.

Following the above-mentioned introductory elaborations, the encoding principle of our cooperative CSTSK scheme obeying the architecture of Fig. 5.2 may be formally summarized as follows:

Algorithm 5.1: Cooperative CSTSK scheme of Fig. 5.2

The source node's actions during the broadcast phase

1. Given the $\mathcal{L}'$-PSK/QAM constellation employed for a source node as well as the $\mathcal{L}$-PSK aided cooperative CSTSK(M, N, T, Q) scheme employing Q dispersion matrices $\boldsymbol{A}_1, \cdots, \boldsymbol{A}_Q \in \mathcal{C}^{M\times M}$ for M relay nodes, $B = b\log_2 \mathcal{L}'$ information bits are input to the PSK/QAM block of the source node. Here, the information bits are CRC-encoded over B bits.

2. The $B = b\log_2 \mathcal{L}'$ input bits are modulated to the b $\mathcal{L}'$-PSK/QAM symbols of $\boldsymbol{S}_{\rm s}(i) = [s_1(i), \cdots, s_b(i)]^{\rm T} \in \mathcal{C}^{b\times 1}$. Then the modulated PSK/QAM symbols $\boldsymbol{S}_{\rm s}(i)$ are transmitted to both the source node and to the M relay nodes over b symbol durations.

The mth relay node's actions during the cooperative phase

3. The mth relay node decodes the received symbols corresponding to B bits.

4. If any decoding errors are detected by the CRC-check in *Step* 3, the mth relay node does not join the cooperation. Otherwise, go to *Step* 5.

5. The $B = b\log_2 \mathcal{L}' = \log_2(Q \cdot \mathcal{L})$ information bits input during *Step* 4 are then Serial-to-Parallel (S/P) converted to $B_1 = \log_2 \mathcal{L}$ bits and $B_2 = \log_2 Q$ bits, where we have the relation of $B = B_1 + B_2$.

6. The $B_1 = \log_2 \mathcal{L}$ bits at the lower output of the S/P converter of Fig. 5.2 are then modulated to $\mathcal{L}$-PSK/QAM symbols $\{s_l(i);\ l = 1, \cdots \mathcal{L}\}$.

7. The $B_2 = \log_2 Q$ bits at the upper output of the S/P converter of Fig. 5.2 are then mapped to one out of the Q dispersion vectors $\boldsymbol{a}_m^{(1)}, \cdots, \boldsymbol{a}_m^{(Q)} \in \mathcal{C}^{1\times T}$, which we refer to as the activated vector $\{\boldsymbol{a}_m^{(q)}(i)\ ; q = 1, \cdots Q\}$.

8. According to the modulated symbol $s_l(i)$ generated in *Step* 6 as well as to the dispersion matrix $\boldsymbol{a}_m^{(q)}(i)$ activated in *Step* 7, a matrix $\boldsymbol{S}(i) \in \mathcal{C}^{M\times T}$ is computed as follows: $\boldsymbol{S}^{(m)}(i) = s_l(i) \cdot \boldsymbol{a}_m^{(q)}(i)$. Then, the signal vector $\boldsymbol{S}^{(m)}(i)$ is transmitted from the mth relay to the destination node over T symbol durations.

As mentioned, Algorithm 5.1 of our cooperative CSTSK scheme obeying the structure of Fig. 5.2 was developed from Algorithm 2.1 of the CSTSK scheme seen in Fig 2.5. More specifically, while the creation of the STSK codeword $\boldsymbol{S}(i)$ takes place during *Steps* 1–5 of Algorithm 2, the corresponding STSK codeword $\boldsymbol{S}^{(m)}(i)$ in our cooperative CSTSK scheme is generated according to *Steps* 3–8, in a distributed manner during the cooperative phase, where the mth RN generates the mth row components of the STSK codeword $\boldsymbol{S}(i)$ as $\boldsymbol{S}^{(m)}(i)$ without any negotiation with other RNs.

Having formulated the cooperative CSTSK scheme, we then conceive a modified cooperative CSTSK arrangement, which does not require the RNs to synchronize with each other at a symbol-duration accuracy.

5.3.2 Cooperative Asynchronous CSTSK Scheme

It is implied in Eq. (5.5) that the RNs typically have to synchronize with each other within a fraction of the symbol duration, owing to the requirement of their simultaneous transmissions. However, as mentioned above, it is a challenging task to acquire accurate IRS. Therefore, in order to relax this IRS-related limitation, hereby we impose a further constraint on the Q dispersion matrices of $\boldsymbol{A}_{q'}$ $(q' = 1, \cdots, Q)$ in addition to the power constraint of Eq. (5.8), with the aid of asynchronous CSTSK concept proposed in Section 2.3.2. More specifically, $\boldsymbol{A}_{q'}$ is generated by ensuring that in each column of $\boldsymbol{A}_{q'}$ only one component has a complex non-zero value, while the others become zero. By obeying this constraint, only one of the M RNs transmits its signal during each symbol interval, and hence we can avoid the requirement of symbol-synchronized simultaneous relay transmissions.

5.3.3 IEI-Free Joint ML Detection at the Destination Receiver

At the DN, the directly transmitted signals of Eq. (5.2) and the relayed signals of Eq. (5.5) are jointly detected using a low-complexity single-stream ML detector.

Firstly, by applying the vectorial stacking operation $vec()$ to both sides of Eq. (5.5), we arrive at the linearized relay-destination system's output in the form of [93]

$$\bar{\boldsymbol{Y}}_{\mathrm{rd}}(i) = \bar{\boldsymbol{H}}_{\mathrm{rd}}(i)\boldsymbol{\chi}\boldsymbol{K}(i) + \bar{\boldsymbol{V}'}_{\mathrm{d}}(i), \tag{5.13}$$

where we have

$$\bar{\boldsymbol{Y}}_{\mathrm{rd}}(i) = vec[\boldsymbol{Y}_{\mathrm{rd}}(i)] \in \mathcal{C}^{T\times 1}, \tag{5.14}$$

$$\bar{\boldsymbol{H}}_{\mathrm{rd}}(i) = \boldsymbol{I} \otimes \boldsymbol{H}_{\mathrm{rd}}(i) \in \mathcal{C}^{T\times MT}, \tag{5.15}$$

$$\bar{\boldsymbol{V}'}_{\mathrm{d}}(i) = vec[\boldsymbol{V}'_{\mathrm{d}}(i)] \in \mathcal{C}^{T\times 1}, \tag{5.16}$$

$$\boldsymbol{\chi} = [vec(\boldsymbol{A}_1), \cdots, vec(\boldsymbol{A}_Q)] \in \mathcal{C}^{MT\times Q}, \tag{5.17}$$

and

$$\boldsymbol{K}(i) = [\underbrace{0, \cdots, 0}_{q-1}, s(i), \underbrace{0, \cdots, 0}_{Q-q}]^{\mathrm{T}} \in \mathcal{C}^{Q\times 1}. \tag{5.18}$$

Furthermore, $\boldsymbol{I}$ is the identity matrix and $\otimes$ is the Kronecker product. It is worth mentioning that the linearized relay-destination system model of Eq. (5.13) does not contain any IEI, because the equivalent signal vector $\boldsymbol{K}(i)$ has only a single non-zero symbol component, similarly to SM [61, 63, 66].

Finally, the joint system model, combining the broadcast phase of Eq. (5.2) and the cooperative phase of Eq. (5.13), may be formulated as

$$\hat{\boldsymbol{Y}}(i) = \begin{bmatrix} \boldsymbol{Y}_{\mathrm{sd}}(i) \\ \bar{\boldsymbol{Y}}_{\mathrm{rd}}(i) \end{bmatrix} \in \mathcal{C}^{(b+T)\times 1} \tag{5.19}$$

$$= \hat{\boldsymbol{H}}(i)\hat{\boldsymbol{S}}(i) + \hat{\boldsymbol{V}}(i), \tag{5.20}$$

where we have

$$\hat{\boldsymbol{H}}(i) = \left[\begin{array}{c:c} h_{\mathrm{sd}}(i)\boldsymbol{I}_b & \mathbf{0} \\ \hdashline \mathbf{0} & \bar{\boldsymbol{H}}_{\mathrm{rd}}(i)\boldsymbol{\chi} \end{array}\right] \in \mathcal{C}^{(b+T)\times(b+Q)} \tag{5.21}$$

$$\hat{\boldsymbol{S}}(i) = \left[\begin{array}{c} \boldsymbol{S}_{\mathrm{s}}(i) \\ \boldsymbol{K}(i) \end{array}\right] \in \mathcal{C}^{(b+Q)\times 1},\ \hat{\boldsymbol{V}}(i) = \left[\begin{array}{c} \boldsymbol{V}_{\mathrm{d}}(i) \\ \bar{\boldsymbol{V}}'(i) \end{array}\right] \in \mathcal{C}^{(b+T)\times 1}. \tag{5.22}$$

Let us then consider the conditional probability of

$$P\left(\hat{\boldsymbol{Y}}(i)\middle|\,\hat{\boldsymbol{H}}(i), \hat{\boldsymbol{S}}^{(q,l)}\right) = \frac{1}{(\pi N_0)^{b+T}} \exp\left(-\frac{||\hat{\boldsymbol{Y}}(i) - \hat{\boldsymbol{H}}(i)\hat{\boldsymbol{S}}^{(q,l)}||^2}{N_0}\right), \tag{5.23}$$

where

$$\hat{\boldsymbol{S}}^{(q,l)} = \left[\begin{array}{c} \boldsymbol{S}_{\mathrm{s}}^{(q,l)} \\ \boldsymbol{K}^{(q,l)} \end{array}\right] \in \mathcal{C}^{(b+Q)\times 1}. \tag{5.24}$$

with

$$\boldsymbol{K}^{(q,l)} = [\underbrace{0, \cdots, 0}_{q-1}, s_l, \underbrace{0, \cdots, 0}_{Q-q}]^{\mathrm{T}}. \tag{5.25}$$

Here, s_l denotes the lth constellation point of $\mathcal{L}$–PSK/QAM, employed during the cooperative phase and $\boldsymbol{S}_{\mathrm{s}}^{(q,l)}$ represents the modulated symbols of the broadcast phase, corresponding to the bits of the set (q, l).

Then, the optimal ML detector of our cooperative CSTSK scheme may be formulated with the assistance of [63] as

$$(\hat{q}, \hat{l}) = \arg\max_{q,l} P\left(\hat{\boldsymbol{Y}}(i)\middle|\,\hat{\boldsymbol{H}}(i), \hat{\boldsymbol{S}}^{(q,l)}\right) \tag{5.26}$$

$$= \arg\min_{q,l} ||\hat{\boldsymbol{Y}}(i) - \hat{\boldsymbol{H}}(i)\hat{\boldsymbol{S}}^{(q,l)}||^2 \tag{5.27}$$

$$= \arg\min_{q,l} \left(||\boldsymbol{Y}_{\mathrm{sd}}(i) - h_{\mathrm{sd}}(i)\boldsymbol{S}_{\mathrm{s}}^{(q,l)}||^2 + ||\bar{\boldsymbol{Y}}_{\mathrm{rd}}(i) - s_l\left(\bar{\boldsymbol{H}}_{\mathrm{rd}}(i)\boldsymbol{\chi}\right)_q||^2\right), \tag{5.28}$$

where $\left(\bar{\boldsymbol{H}}_{\mathrm{rd}}(i)\boldsymbol{\chi}\right)_q$ is the qth column of $\bar{\boldsymbol{H}}_{\mathrm{rd}}(i)\boldsymbol{\chi}$. The first term of Eq. (5.28) indicates the detection of the source-destination signals, while the second term corresponds to that of the relay-destination signals, where all the signal components are independent of each other and hence no IEI is imposed.

The computational complexity per bit imposed by calculating Eq. (5.28) for the cooperative CSTSK scheme may be evaluated in terms of the number of real-valued multiplications, which is given by

$$\frac{4MQT^2 + 6TQ\mathcal{L} + 4\mathcal{L}' + 2bQ\mathcal{L}}{\log_2(Q \cdot \mathcal{L})}. \tag{5.29}$$

Furthermore, that of the cooperative ACSTSK scheme may be simplified to

$$\frac{4QT^2 + 6TQ\mathcal{L} + 4\mathcal{L}' + 2bQ\mathcal{L}}{\log_2(Q \cdot \mathcal{L})}. \tag{5.30}$$

This complexity is as low as those of the OSTBC [21] and SM schemes [63] used in an identical cooperative scenario. In the rest of this paper, we employ the parameter-based system notation of CSTSK(M, N, T, Q) for the cooperative phase.

5.4 Cooperative Differential STSK Scheme

Having introduced our cooperative CSTSK scheme in Section 5.3, we now conceive its differentially-encoded counterpart with the aid of the DSTSK scheme of Fig. 3.5, which we refer to as the cooperative DSTSK scheme. Here, we aim for designing a simplified cooperative system, dispensing with any CSI estimation at the nodes, while still retaining the cooperative STSK scheme's fundamental benefits.

Fig. 5.3 shows the schematic of our cooperative DSTSK system, which was developed from the DSTSK scheme of Fig. 3.5 and from the cooperative CSTSK scheme of Fig. 5.2. More specifically, in our cooperative DSTSK scheme DPSK modulation is employed at the source node, instead of the PSK/QAM scheme of the cooperative CSTSK arrangement seen in Fig. 5.2. Moreover, in Fig. 5.3 we employed the DSTSK-encoding principle at each relay node, which is replaced by CSTSK in the cooperative CSTSK scheme of Fig. 5.3.

Similarly to the algorithmic summary shown in Algorithm 5.1, the encoding principle of our cooperative DSTSK scheme obeying the architecture of Fig. 5.3 may be formally summarized as follows:

Algorithm 5.2: Cooperative DSTSK scheme of Fig. 5.3

The source node's actions during the broadcast phase

1. Given the $\mathcal{L}'$-DPSK modulation scheme of the source node as well as the $\mathcal{L}$-PAM aided cooperative DSTSK(M, N, T, Q) arrangement employing Q Hermitian dispersion matrices $\boldsymbol{A}_1, \cdots, \boldsymbol{A}_Q \in \mathcal{C}^{M\times M}$ for M relay nodes, $B = b\log_2 \mathcal{L}'$ information bits are input to the DPSK block of the source node. Here, the information bits are CRC-encoded over B bits.

2. The $B = b\log_2 \mathcal{L}'$ input bits are modulated to b $\mathcal{L}'$-DPSK symbols with the aid of differentially-encoded modulation, which is given by $\boldsymbol{S}_{\rm s}(i) = [s_1(i), \cdots, s_b(i)]^{\rm T} \in \mathcal{C}^{b\times 1}$. Then, the modulated DPSK symbols $\boldsymbol{S}_{\rm s}(i)$ are transmitted to both the source node and to the M relay nodes over b symbol durations.

The mth relay node's actions during the cooperative phase

3. The mth relay node decodes the received symbols corresponding to B bits.

4. If any decoding errors are detected by the CRC-check during *Step* 3, the mth relay node does not join the cooperation. Otherwise, go to *Step* 5.

5. The $B = b\log_2 \mathcal{L}' = \log_2(Q\cdot\mathcal{L})$ information bits input during *Step* 4 are then Serial-to-Parallel (S/P) converted to $B_1 = \log_2 \mathcal{L}$ and $B_2 = \log_2 Q$ bits, where we have the relation of $B = B_1 + B_2$.

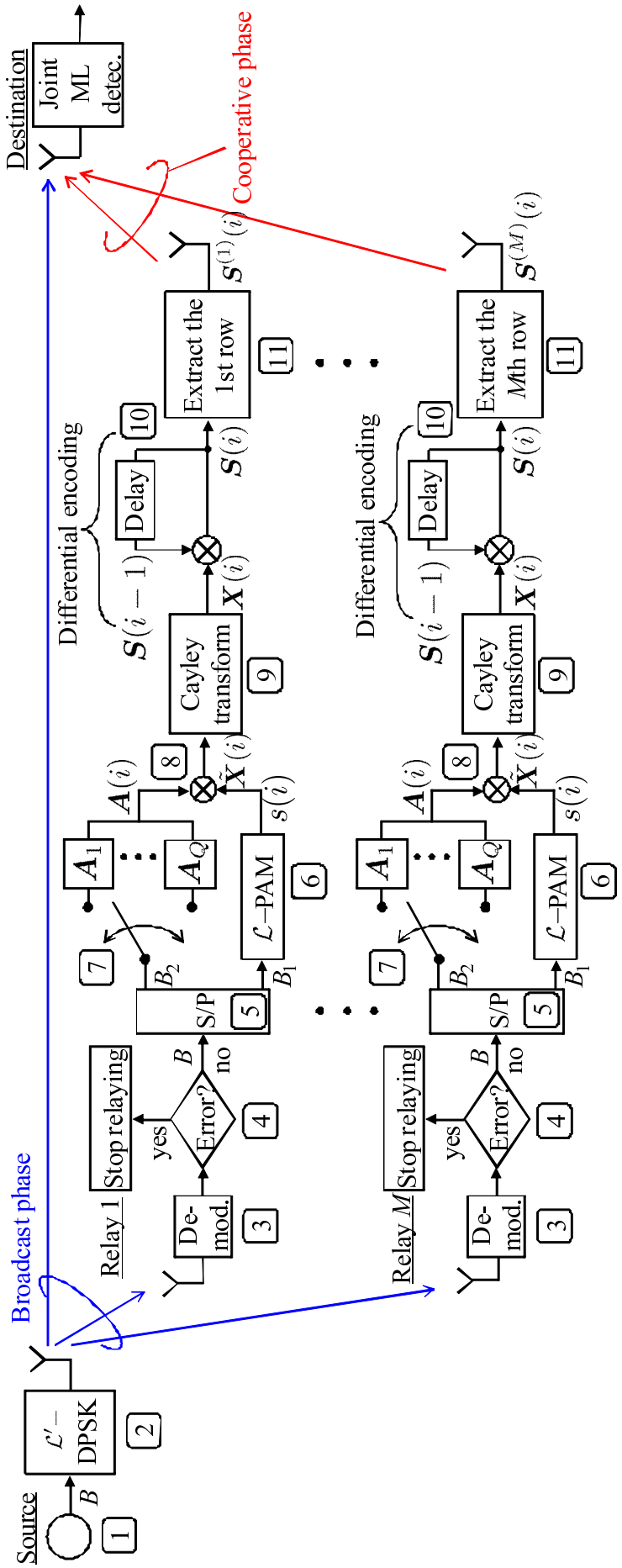

Figure 5.3: Schematic of our distributed DSTSK scheme assisted by selective DF relaying, which was developed from the DSTSK scheme of Fig. 3.5 and the cooperative CSTSK scheme of Fig. 5.3.

6. The $B_1 = \log_2 \mathcal{L}$ bits emerging at the lower output of the S/P converter of Fig. 5.3 are then modulated to the $\mathcal{L}$-PAM symbols of $\{s_l(i);\ l = 1, \cdots \mathcal{L}\}$.

7. According to the $B_2 = \log_2 Q$ bits seen at the upper output of the S/P converter of Fig. 5.3 are mapped to one out of the Q dispersion vectors $\boldsymbol{A}_1, \cdots, \boldsymbol{A}_M \in \mathcal{C}^{1\times T}$, which we refer to as the activated matrix $\{\boldsymbol{A}(i)\ ; q = 1, \cdots Q\}$.

8. According to the modulated symbol $s_l(i)$ generated in *Step* 6 as well as to the dispersion matrix $\boldsymbol{A}_q(i)$ activated in *Step* 7, a matrix $\tilde{\boldsymbol{X}}(i) \in \mathcal{C}^{M\times T}$ is computed as follows: $\tilde{\boldsymbol{X}}^{(m)}(i) = s_l(i) \cdot \boldsymbol{A}(i)$.

9. Then a unitary matrix $\boldsymbol{X}(i)$ is computed from the matrix $\tilde{\boldsymbol{X}}(i)$ obtained in *Step* 8, using the Cayley transform of $\boldsymbol{X}(i) = [\boldsymbol{I} - j\tilde{\boldsymbol{X}}(i)][\boldsymbol{I} + j\tilde{\boldsymbol{X}}(i)]^{-1}$.

10. In order to generate a ST codeword $\boldsymbol{S}(i)$ for the current ST block, the unitary matrix $\boldsymbol{X}(i)$ generated in *Step* 9 is differentially encoded as follows: $\boldsymbol{S}(i) = \boldsymbol{S}(i-1)\boldsymbol{X}(i)$.

11. The mth row of the ST matrix $\boldsymbol{S}(i)$ generated in *Step* 10 is transmitted from the mth relay to the destination node over T symbol durations.

As mentioned, the cooperative DSTSK scheme of Fig. 5.3 is the differentially encoded counterpart of the cooperative CSTSK scheme of Fig. 5.2, where *Steps* 6–8 of Algorithm 5.1 are replaced by *Steps* 6–11 of Algorithm 5.2.

5.4.1 Cooperative Asynchronous DSTSK Scheme

Similarly to the co-located ACSTSK scheme of Section 2.3.2 employing a specific dispersion-matrix structure, in this section we conceive the cooperative Asynchronous DSTSK (AD-STSK) scheme. More specifically, in order to relax this IRS-related limitation, a real-valued diagonal constraint may be imposed on the Q dispersion matrices of $\boldsymbol{A}_{q'}$ $(q' = 1, \cdots, Q)$, as motivated by the asynchronous DSTSK concept proposed in Section 3.3.1. Due to this constraint, only one of the M RNs transmits its signal during each symbol interval and hence we can avoid the requirement of symbol-synchronized simultaneous relay transmissions.

5.4.2 IEI-Free Joint ML Detection at the Destination Receiver

As seen in Section 3.3, the DSTSK codeword can be detected in a similar manner to that of the CSTSK scheme, since both the system models of the CSTSK and DSTSK receivers may be formulated as the linearized IEI-free signal model of Eqs. (2.25) and (3.25). Therefore, our cooperative DSTSK signal is readily detected according to the ML detection of the cooperative CSTSK scheme formulated in Eq. (5.28).

Table 5.2: System parameters of the cooperative CSTSK(M, N, T, Q) scheme of Fig. 5.2

Number of relay nodes	$M = 2$–6
Number of receive antennas	$N = 1$
Symbol durations per block	$T = 2, 3$
Number of dispersion matrices	$Q = 1, 2, 4, 8, 16$
Modulation during broadcast phase	$\mathcal{L}'-$PSK/QAM
Modulation during cooperative phase	$\mathcal{L}-$PSK/QAM
Channels	Frequency-flat Rayleigh fading
Channel's coherence-time	$\tau = 1$ block duration
Geometrical channel gains	$(\sigma_{\rm sd}^2, \sigma_{\rm sr}^2, \sigma_{\rm rd}^2) = (1, 4, 2)$
Detector	Joint ML detector of Eq. (5.28)

More specifically, the equivalent signals received at the DN during the broadcast phase of Fig. 5.3 may be formulated after the differential-decoding operation as

$$\begin{aligned} \boldsymbol{Y}'_{\rm sd}(i) &= {\rm diag}[\boldsymbol{Y}^*_{\rm sd}(i-1) \cdot \boldsymbol{Y}^{\rm T}_{\rm sd}(i)] && (5.31) \\ &= h_{\rm sd}\boldsymbol{S}_{\rm S}(i) + \boldsymbol{V}_{\rm d}. && (5.32) \end{aligned}$$

Furthermore, the linearized equivalent signal model of the cooperative phase of Fig. 5.3 formulated after the differential decoding operation of Eq. (3.23) is represented by

$$\bar{\boldsymbol{Y}}'_{\rm rd}(i) = \bar{\boldsymbol{H}}_{\rm rd}(i)\boldsymbol{\chi}\boldsymbol{K}(i) + \bar{\boldsymbol{V}}'(i). \quad (5.33)$$

Here, the variance of $\boldsymbol{V}_{\rm d}(i)$ and $\bar{\boldsymbol{V}}'(i)$ is given by $2N_0$, which is twice that of the cooperative CSTSK scheme. Based on the differentially-decoded equivalent signals of Eqs. (5.32) and (5.33), we may be able to employ the IEI-free joint ML detector of Eq. (5.28), which is the same as that derived for the cooperative CSTSK scheme of Fig. 5.2.

5.5 Performance Results

In this section we provide our performance results, comparing different DF scenarios as well as different cooperative schemes. Basic system parameters employed for the simulations are listed in Tables 5.2 and 5.3 In line with [4], we considered independent Rayleigh block-fading environments, having the geometrical distance-reduction based channel gains of $\sigma_{\rm sd}^2 = 1$, $\sigma_{\rm sr}^2 = 4$ and $\sigma_{\rm rd}^2 = 2$, which remains constant over $(b + T)$ cooperative CSTSK/DSTSK symbol durations. Furthermore, the SN was assumed to employ QPSK modulation, which indicates $\mathcal{L}' = 4$. In the simulations, the dispersion-matrix sets optimized for the co-located CSTSK and DSTSK schemes of Figs. 2.5 and 3.5 were reused for our cooperative CSTSK and DSTSK schemes of Figs. 5.2 and 5.3, which are given in Appendices A and B.

Table 5.3: System parameters of the cooperative DSTSK(M, N, T, Q) scheme of Fig. 5.3

Number of relay nodes	$M = 2$
Number of receive antennas	$N = 1$
Symbol durations per block	$T = M$
Number of dispersion matrices	$Q = 1, 2, 4, 8$
Modulation during broadcast phase	$\mathcal{L}'-$DPSK
Modulation during cooperative phase	$\mathcal{L}-$PAM
Channels	Frequency-flat Rayleigh fading
Channel's coherence-time	$\tau = 2$ block durations
Geometrical channel gains	$(\sigma_{\text{sd}}^2, \sigma_{\text{sr}}^2, \sigma_{\text{rd}}^2) = (1, 4, 2)$
Detector	Joint ML detector of Eq. (5.28)

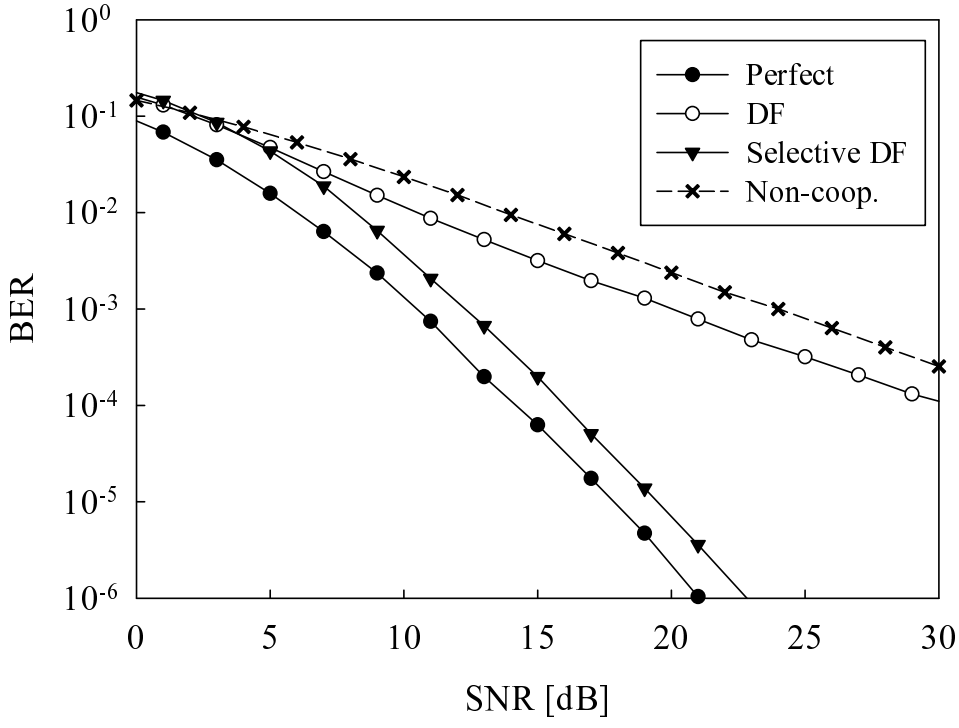

Figure 5.4: Achievable BER performance of our cooperative CSTSK$(2, 1, 2, 4)$ system obeying the architecture of Fig. 5.2, comparing different DF relaying schemes, such as perfect DF, conventional DF and CRC-activated DF schemes. Here, the QPSK modulation scheme was employed both at the SN and at the RNs, where the normalized transmission rate was given by $R = 1.0$ bits/symbol. All other system parameters are summarized in Table 5.2. We also characterized the non-cooperative scenario employing BPSK modulation.

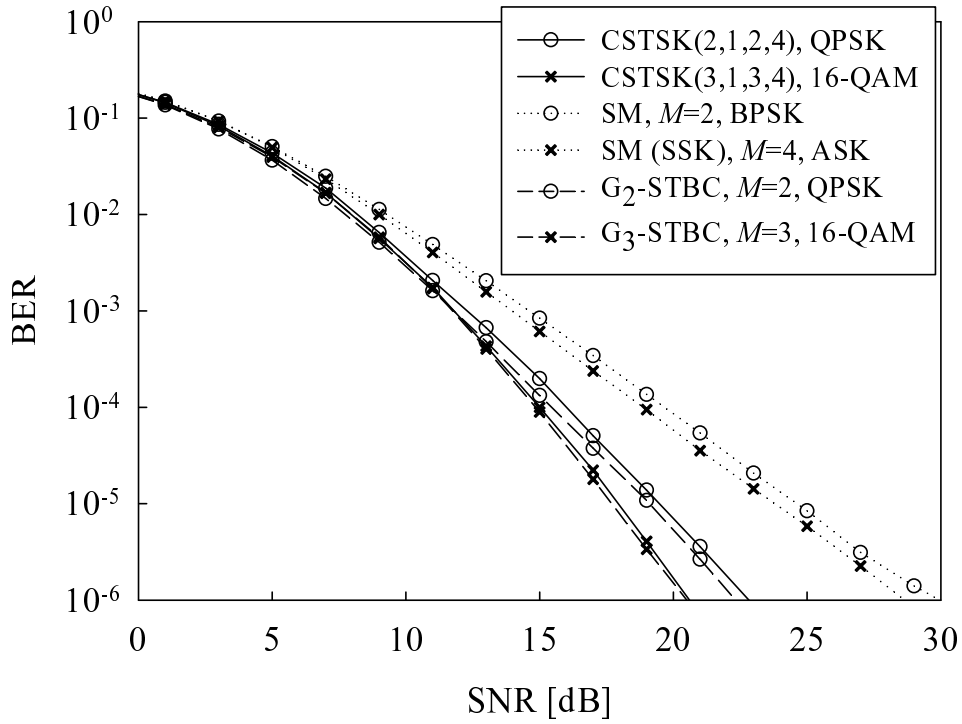

Figure 5.5: Achievable BER performance of our $\mathcal{L} = 4$ PSK-modulated cooperative CSTSK$(2, 1, 2, 4)$ and $\mathcal{L} = 16$ QAM cooperative CSTSK$(3, 1, 3, 4)$ schemes obeying the architecture of Fig. 5.2, while $\mathcal{L}' = 4$ PSK was employed at the SN for both the schemes. Here, the normalized transmission rate was given by $R = 1.0$ bits/symbol. All other system parameters are summarized in Table 5.2. The corresponding BER curves of the SM scheme employing $M = 2$ and $M = 4$ RNs and the G_2 and G_3 STBC schemes were also calculated as benchmarkers.

Fig. 5.4 shows the achievable BER performance of our cooperative CSTSK$(2, 1, 2, 4)$ scheme obeying the architecture of Fig. 5.2, where QPSK modulation was employed both at the SN and at the RNs, hence the normalized transmission rate was $R = 1.0$ bits/symbol. We compared three different DF schemes, namely the perfect decision based DF, the conventional DF and the proposed CRC-activated DF schemes, where the perfect decision aided DF scheme assumed having perfect source-relay channels, hence imposing no errors by the relays' decoders, while in the conventional DF scheme all the M RNs were assumed to join the cooperative transmission regime, regardless of the presence or absence of decoding errors. We also plotted the BER curve of the corresponding non-cooperative scenario, assuming the employment of BPSK modulation at the SN. Observe in Fig. 5.4 that the perfect and the selective DF schemes attained a transmit diversity order of three, hence both outperformed the conventional DF scheme and the non-cooperative scenario. Here, it should be emphasized that the selective DF scheme achieved a reduced-overhead distributed operation at each RN. On the other hand, the BER curves of the conventional DF scheme and of the non-cooperative scenario did not exhibit any additional transmit diversity gain.

Next, in Fig. 5.5 our cooperative CSTSK arrangement of Fig. 5.2 was compared to the distributed SM and OSTBC benchmarkers, both using the selective CRC-activated DF scheme presented in this chapter and have the same normalized transmission rate of $R = 1.0$ bits/symbol. More particularly, for the distributed OSTBC scheme, we considered two different relaying arrangements, namely the $M = 2$ relay-assisted G_2 STBC [20] employing QPSK modulation as well as the $M = 3$ relay-aided G_3 STBC [21] employing 16–QAM. For the distributed SM scheme, we also simulated two arrangements, namely the $M = 2$ relay-aided SM scheme [61] using BPSK modulation and the $M = 4$ relay-aided SM scheme employing two-level Amplitude Shift Keying (ASK), which was also referred to as Space-Shift Keying (SSK) in [66].[3] To be more specific, while our cooperative CSTSK and the SM schemes did not require simultaneous relay transmissions, the OSTBC scheme necessitated perfect IRS, noting that the potential synchronization errors may cause severe performance degradations [142]. As seen in Fig. 5.5, our cooperative CSTSK arrangement achieved a BER performance, which was comparable to that of the corresponding OSTBC benchmarker for both $M = 2$ and $M = 3$. Observe furthermore in Fig. 5.5 that as expected the diversity order increased with the number of RNs. On the other hand, the SM scheme did not attain any additional cooperative diversity gain upon increasing the number of the RNs, since the original SM scheme designed for co-located MIMO systems was also unable to provide any transmit diversity gain.

Fig. 5.6 shows the achievable BER performance of our $\mathcal{L} = 4$ PSK-modulated cooperative CSTSK$(M, 1, 2, 4)$ scheme obeying the architecture of Fig. 5.2, while $\mathcal{L}' = 4$-PSK was employed at the SN, where the number of relays was varied from $M = 2$ and $M = 6$. Each scenario exhibited the same transmission rate of $R = 1.0$ bits/symbol. Observe in Fig. 5.6 that upon increasing the number of RNs, the associated BER curve improved. Since diversity gain during the cooperative STSK transmission was fixed to $\min(M, T) = 2$, this improvement was benefit of the increased coding gain.

In order to provide further insights, in Figs. 5.7, 5.8 and 5.9 we compared our cooperative CSTSK and ACSTSK schemes of Fig. 5.2 to other cooperative OSTBC arrangements, having the corresponding bandwidth efficiency. Fig. 5.7 investigated the scenario of a normalized transmission rate of $R = 1.0$ bits/symbol, where $M = 4$ RNs were considered. Observe in Fig. 5.7 that all the three cooperative schemes achieved a useful diversity gains in comparison to the non-cooperative scenario. The cooperative CSTSK scheme outperformed the cooperative OSTBC scheme, as predicted from the results characterized by the co-located STSK arrangements in Section 2.7. Additionally, the cooperative ACSTSK scheme exhibited a slightly lower performance than those of the cooperative CSTSK and OSTBC schemes, due to the restricted dispersion matrix structure discussed in Section 5.3.2. Nevertheless, the cooperative ACSTSK scheme's benefit of dispensing with symbol-level IRS may be especially

[3]Note that the proposed D–STSK scheme includes the distributed SM and SSK schemes as its special cases, which satisfies the relations of $\boldsymbol{A}_1 = [1, 0, \cdots, 0]^{\mathrm{T}}$, $\boldsymbol{A}_2 = [0, 1, 0, \cdots, 0]^{\mathrm{T}}$, $\boldsymbol{A}_Q = [0, \cdots, 0, 1]^{\mathrm{T}}$, $M = Q$ and $T = 1$.

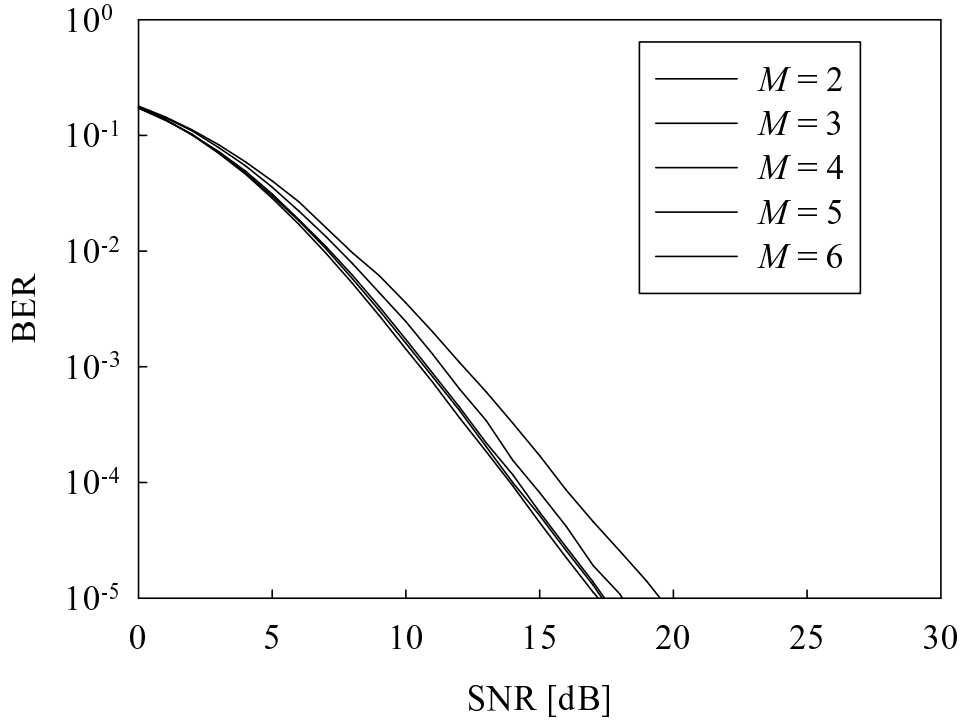

Figure 5.6: Achievable BER performance of our $\mathcal{L} = 4$ PSK-modulated cooperative CSTSK$(M, 1, 2, 4)$ scheme obeying the architecture of Fig. 5.2, while $\mathcal{L}' = 4$ PSK was employed at the SN, where the number of relays was varied from $M = 2$ and $M = 6$. Each scheme exhibited a transmission rate of $R = 1.0$ bits/symbol. All other system parameters are summarized in Table 5.2.

useful for the scenario suffering from a rapid topology change, where perfect IRS is hard to achieve.

Furthermore, when increasing the normalized transmission rate R, the performance advantage of our CSTSK and ACSTSK schemes becomes more explicit, as observed in Figs. 5.8 and 5.9, which correspond to the scenarios of the normalized transmission rates of $R = 1.3$ bits/symbol and of $R = 1.5$ bits/symbol. To expound a little further, it was found in Figs. 5.8 and 5.9 that our CSTSK and ACSTSK schemes outperformed the corresponding BER of the cooperative OSTBC scheme. This is mainly owing to the fact that the cooperative OSTBC scheme is typically required to employ power-hungry high order modulation, in order to attain an increased transmission rate.

In Fig. 5.10, we characterized the achievable BER performance of our $\mathcal{L} = 4$ PSK-modulated cooperative DSTSK$(2, 1, 2, 4)$ scheme of Fig. 5.3, compared to the $\mathcal{L} = 4$ PSK-modulated cooperative CSTSK$(2, 1, 2, 4)$ scheme of Fig. 5.2. Furthermore, the cooperative DSTSK and CSTSK schemes employed $\mathcal{L}' = 4$ PSK and $\mathcal{L}' = 4$ DPSK at the SN, respectively, where both the cooperative schemes exhibited a normalized transmission rate of $R = 1.0$ bits/symbol. In order to characterize the effects of the CSI estimation errors associated

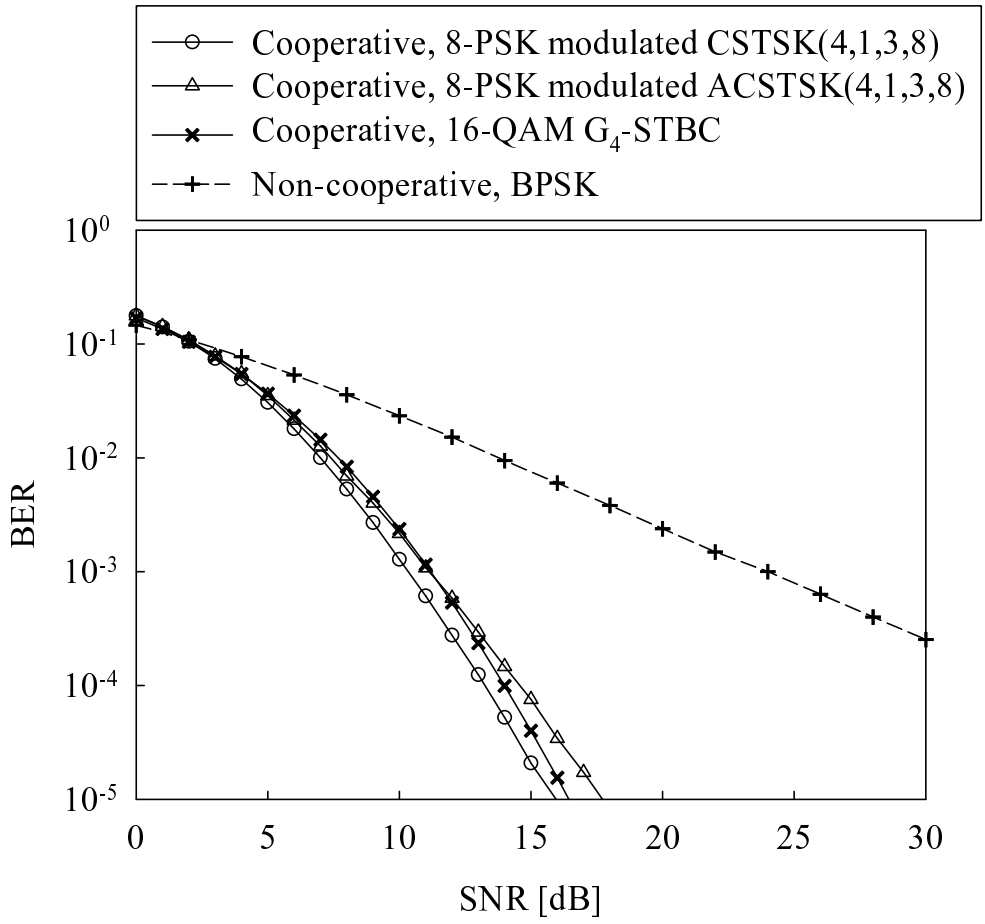

Figure 5.7: Achievable BER performance of our $\mathcal{L} = 8$ PSK-modulated CSTSK$(4, 1, 3, 8)$ and $\mathcal{L} = 8$ PSK-modulated ACSTSK$(4, 1, 3, 8)$ schemes obeying the architecture of Fig. 5.2, while $\mathcal{L}' = 8$ PSK was employed for the source node. The corresponding BER curves of the G_4-STBC scheme as well as BPSK-modulated non-cooperative scheme were also calculated as benchmarkers. Here, each scheme exhibited a normalized transmission rate of $R = 1.0$ bits/symbol. All other system parameters were summarized in Table 5.2.

with coherent detection, we used an equivalent CSI-estimation SNR of $\omega = 5, 10$ and 15 dB. For example, a CSI SNR of 10 dB indicates that the CSI error power is a factor ten lower than the received signal power. Observe in Fig. 5.10 that since the equivalent noise variance of the cooperative DSTSK scheme was doubled, the system suffered from a 3 dB performance penalty in comparison to its coherently-detected counterpart. On the other hand, as expected, the cooperative CSTSK scheme's performance was severely degraded upon introducing the CSI estimation errors, hence exhibiting an error floor. This emphasized the benefits of non-coherent detection at our cooperative DSTSK scheme's receiver.

Finally, we compared the achievable BER performance of our cooperative $\mathcal{L}$-PAM DSTSK(2, 1,2,Q) and ADSTSK$(2, 1, 2, Q)$ schemes obeying the architecture of Fig. 5.3, while employing $\mathcal{L}' = \mathcal{L}$ DPSK at the SN. Here, the sets of the parameters of $(\mathcal{L}, Q)$ were given by $(2, 2)$, $(4, 4)$ and $(8, 8)$, achieving the normalized transmission rates of $R = 0.5, 1$ and 1.5 bits/symbol,

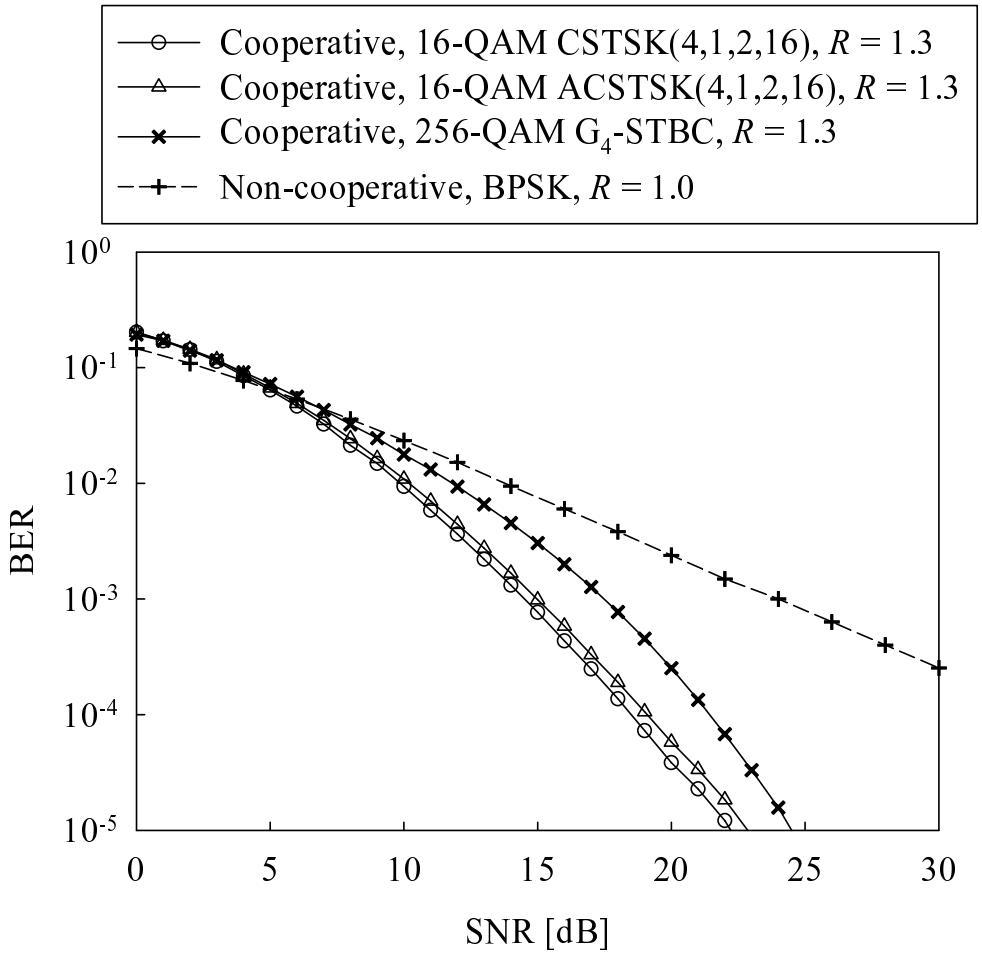

Figure 5.8: Achievable BER performance of our $\mathcal{L} = 16$ QAM CSTSK$(4, 1, 2, 16)$ and $\mathcal{L} = 16$ QAM ACSTSK$(4, 1, 2, 16)$ schemes obeying the architecture of Fig. 5.2, while $\mathcal{L}' = 4$ PSK was employed for the source node. The corresponding BER curves of the $\mathcal{L} = 256$ QAM G_4-STBC cooperative scheme as well as BPSK-modulated non-cooperative scheme were also calculated as benchmarkers. Here, each of the cooperative schemes exhibited a normalized transmission rate of $R = 1.3$ bits/symbol. All other system parameters were summarized in Table 5.2.

respectively. It was found in Fig. 5.11 that while the cooperative DSTSK and ADSTSK schemes having the parameters of $(2, 2)$ exhibited a similar BER, a performance difference emerged and became higher upon increasing the values of $(\mathcal{L}, Q)$. This is owing to real-valued diagonal constraint imposed by the cooperative DSTSK scheme, similarly to its co-located STSK counterpart discussed in Section 3.3.1.

5.6 Chapter Conclusions

Motivated by the philosophy of the CSTSK and DSTSK schemes proposed in Chapters 2 and 3, in this chapter we proposed novel cooperative CSTSK and DSTSK schemes, where each RN uses CRC-activated DF relaying employing STSK during the cooperative phase of Figs.

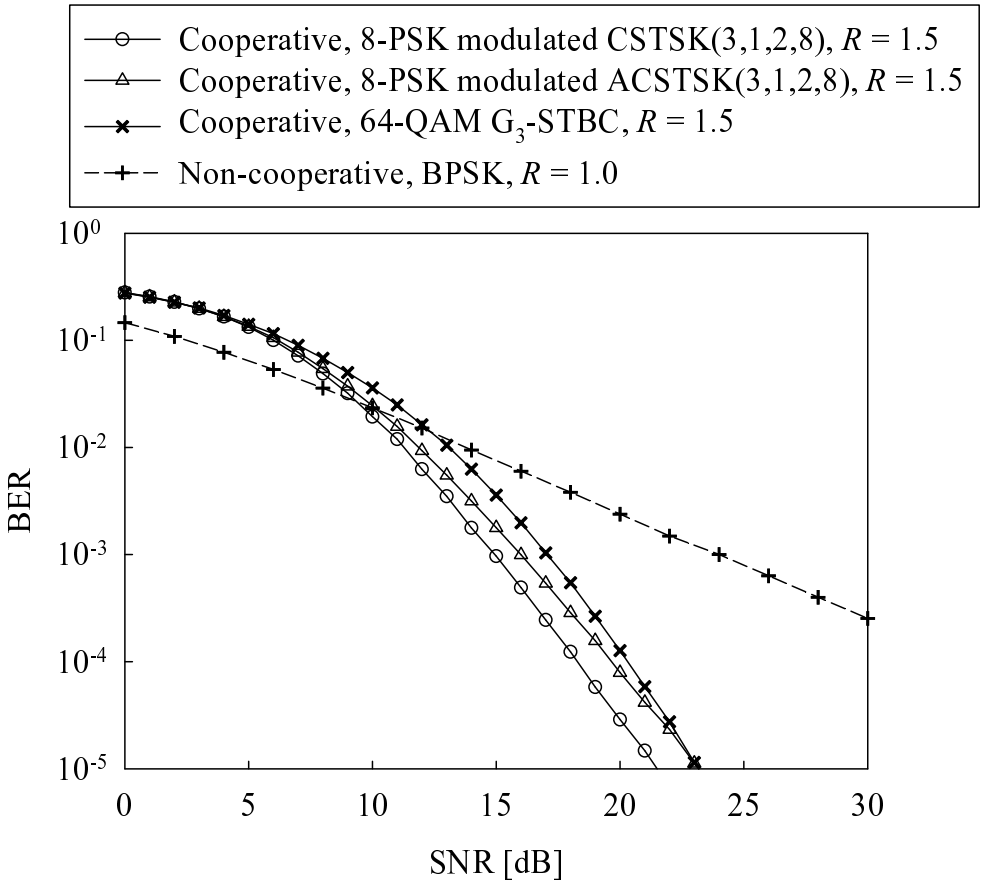

Figure 5.9: Achievable BER performance of our $\mathcal{L} = 8$ PSK modulated CSTSK$(3, 1, 2, 8)$ and $\mathcal{L} = 8$ PSK modulated ACSTSK$(3, 1, 2, 8)$ schemes obeying the architecture of Fig. 5.2, while $\mathcal{L}' = 8$ PSK was employed for the source node. The corresponding BER curves of the $\mathcal{L} = 64$ QAM G_3-STBC cooperative scheme as well as BPSK-modulated non-cooperative scheme were also calculated as benchmarkers. Here, each of the cooperative schemes exhibited a normalized transmission rate of $R = 1.5$ bits/symbol. All other system parameters were summarized in Table 5.2.

5.2 and 5.3, which is capable of attaining an attractive cooperative diversity gain. Here, the RNs do not require symbol-synchronization owing to the additional restriction which we imposed on the dispersion vector design. At the receiver, the received signals of the direct source-destination link and the relay-destination links are jointly detected using IEI-free low-complexity single-stream ML detection. More importantly, owing to its design flexibility, our cooperative STSK arrangement enables us to adapt the number of RNs, the transmission rate as well as the achievable diversity order, depending on the associated system requirements and channel conditions.

5.7 Chapter Summary

Section 5.2 reviewed the background of cooperative communications, where we showed that VAA arrangements have the potential of combating the performance degradation imposed by

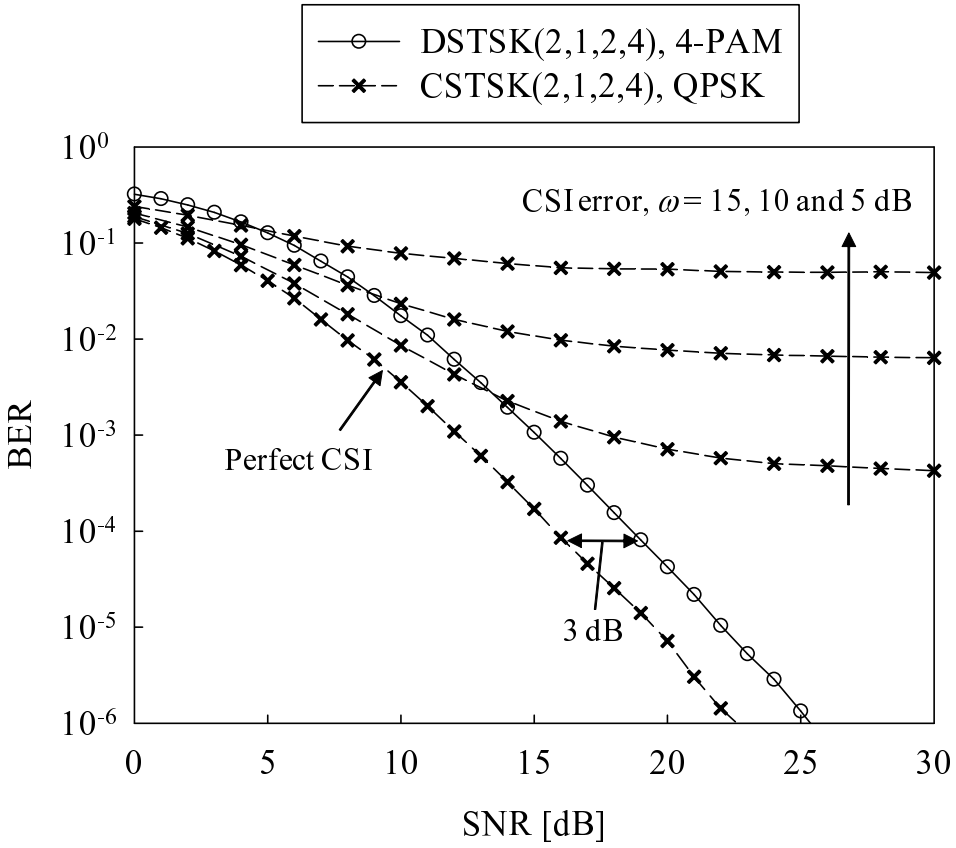

Figure 5.10: Achievable BER performance of our $\mathcal{L} = 4$ PSK-modulated cooperative CSTSK$(2, 1, 2, 4)$ scheme of Fig. 5.2 and $\mathcal{L} = 4$ PAM-modulated cooperative DSTSK$(2, 1, 2, 4)$ scheme of Fig. 5.3, employing $\mathcal{L}' = 4$ PSK and $\mathcal{L}' = 4$ DPSK at the SN, respectively. Here, both the cooperative CSTSK and ACSTSK schemes exhibited a normalized transmission rate of $R = 1.0$ bits/symbol. All other system parameters were summarized in Tables 5.2 and 5.3. The effects of the CSI estimation errors associated with the cooperative CSTSK scheme was characterized by an equivalent CSI-estimation SNR of $\omega = 5, 10$ and 15 dB.

the inter-antenna correlation of the co-located MIMO systems. In Section 5.3 we proposed a novel cooperative CSTSK scheme, which was developed from the co-located CSTSK scheme of Fig. 2.5. Here, the proposed cooperative CSTSK scheme was designed to dispense with any negotiations between the relay nodes and hence to be able to construct their CSTSK codeword in a distributed manner with the aid of the CRC code employed. Additionally, motivated by the ACSTSK scheme proposed in Section 2.3.2, we developed the cooperative asynchronous CSTSK scheme of Section 5.3.2, which does not require symbol-level IRS during the cooperative phase. Then, in Section 5.3.3 we described the optimal joint ML detector of our cooperative CSTSK and ACSTSK schemes, which facilitates low-complexity operation as a benefit of the IEI-free system model of Eq. (5.20). In contrast to the cooperative CSTSK scheme of Fig. 5.2, in Fig 5.3 of Section 5.4 we proposed its differentially encoded counterpart, namely the cooperative DSTSK arrangement. Similarly to the above-mentioned cooperative ACSTSK scheme, we also presented a cooperative ADSTSK scheme in Section

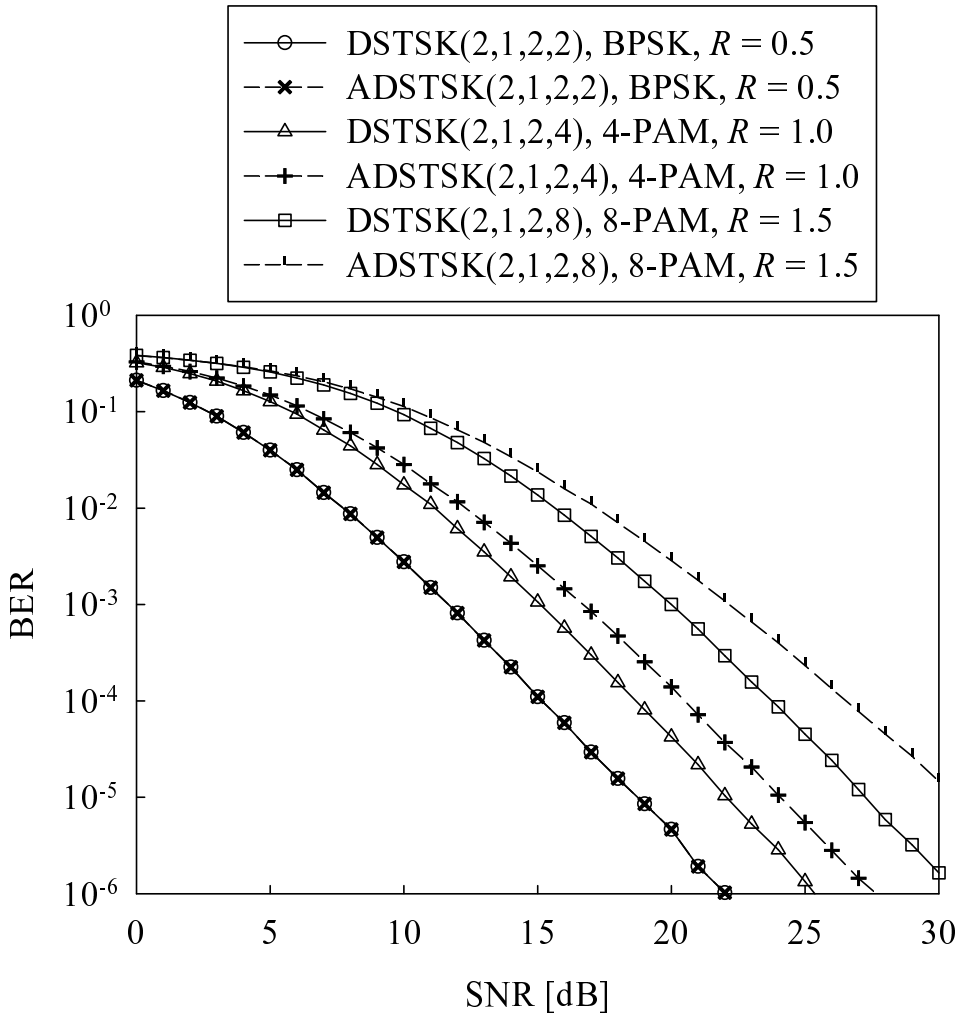

Figure 5.11: Comparison of our cooperative $\mathcal{L}$-PAM DSTSK$(2,1,2,Q)$ and ADSTSK$(2,1,2,Q)$ schemes obeying the architecture of Fig. 5.3, while employing $\mathcal{L}' = \mathcal{L}$ DPSK at the SN. Here, the sets of the parameters of $(\mathcal{L}, Q)$ were given by $(2,2)$, $(4,4)$ and $(8,8)$, achieving the normalized transmission rates of $R = 0.5, 1.0$ and 1.5 bits/symbol, respectively. All other system parameters were summarized in Table 5.3.

5.4.1.

The attainable performance of our cooperative CSTSK, ACSTSK, DSTSK and ADSTSK schemes was characterized in Section 5.5, while varying the diverse system parameters. It was demonstrated that our cooperative CSTSK and ACSTSK schemes of Fig. 5.2 tended to outperform the cooperative OSTBC and SM schemes. Furthermore, our cooperative DSTSK and ADSTSK arrangements of Fig. 5.3 were found to remain unaffected by the CSI estimation errors, while maintaining the fundamental benefits of their coherently-detected counterparts. Figs. 5.12(a) and 5.12(b) summarize the effective throughput recorded at BER $= 10^{-4}$, comparing the co-located CSTSK scheme of Fig. 2.5, the cooperative CSTSK regime of Fig. 5.2 and the cooperative DSTSK arrangement of Fig. 5.3, while employing $M = 3$ transmit and $N = 1$ receive antennas for the co-located CSTSK scheme and $M = 2$ RNs and $N = 1$ receive antenna for the cooperative CSTSK and DSTSK schemes. Observe in Fig. 5.12(a) that our

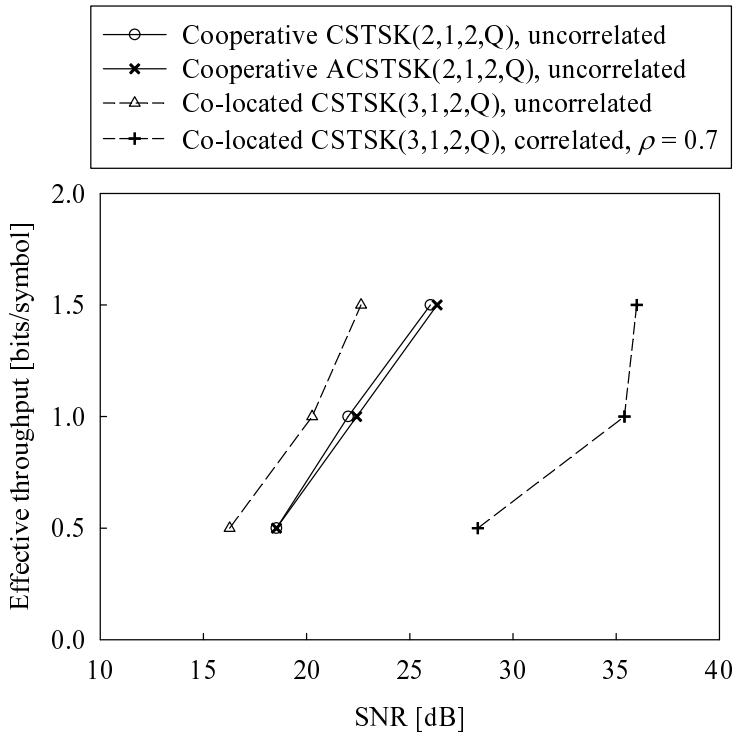

(a) Co-located CSTSK versus cooperative CSTSK

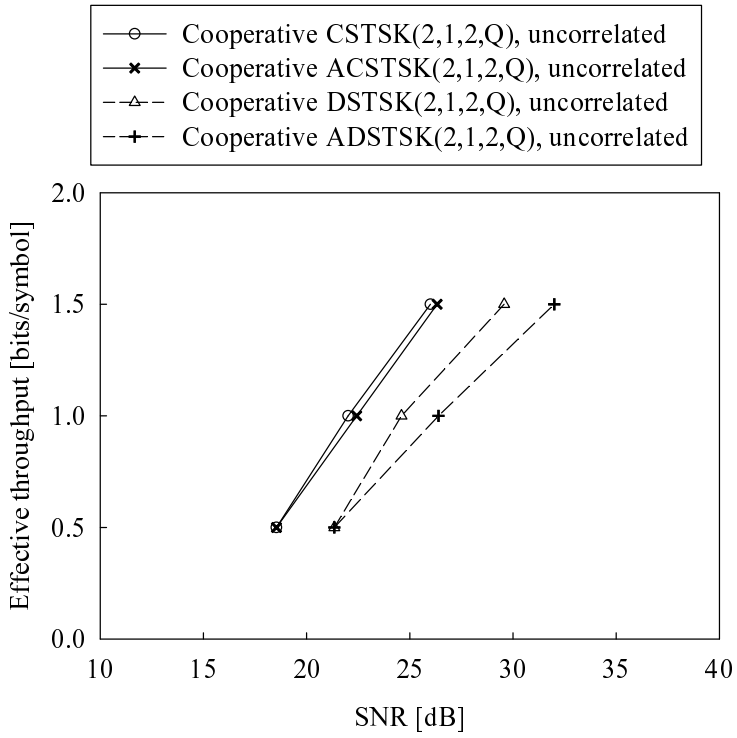

(b) Cooperative CSTSK versus cooperative DSTSK

Figure 5.12: Effective throughput recorded at BER = 10^{-4}, comparing the co-located CSTSK scheme of Fig. 2.5, the cooperative CSTSK scheme of Fig. 5.2 and the cooperative DSTSK scheme of Fig. 5.3, while employing $M = 3$ transmit and $N = 1$ receive antennas for the co-located CSTSK scheme and $M = 2$ RNs and $N = 1$ receive antenna for the cooperative CSTSK and DSTSK schemes. The system parameters are summarized in Tables 2.2, 5.2 and 5.3.

cooperative CSTSK and ACSTSK schemes did not exhibit any performance advantage over the co-located CSTSK scheme assuming no inter-antenna correlation between the AEs. On the other hand, upon introducing shadowing-induced inter-antenna correlation, our cooperative CSTSK and ACSTSK schemes outperformed the co-located CSTSK arrangement, which is the explicit benefit of VAAs. Furthermore, Fig. 5.12(b) compares the effective throughput of the cooperative CSTSK, ACSTSK, DSTSK and ADSTSK schemes. As expected, due to the error-doubling property of non-coherent detection, the cooperative CSTSK and ACSTSK schemes outperformed the cooperative DSTSK and ADSTSK arrangements. We note that as shown in Fig. 5.10, upon introducing CSI estimation errors, the cooperative CSTSK and ACSTSK schemes exhibited error floors, which underlined the benefits of the cooperative DSTSK and ADSTSK schemes.

Table 5.4: Summary of the co-located CSTSK and DSTSK schemes as well as the cooperative CSTSK/ACSTSK and DSTSK/ADSTSK schemes, employing the system parameters of Tables 2.5, 3.2, 5.2 and 5.3, where the system bandwidth efficiency was given by $R = 1.0$ bits/symbol.

	Co-located MIMO		Cooperative MIMO			
	CSTSK	**DSTSK**	**CSTSK**	**ACSTSK**	**DSTSK**	**ADSTSK**
Schematic	Fig. 2.5	Fig. 3.5	Fig. 5.2	←	Fig. 5.3	←
Tx AEs M	Arbitrary Tx AEs	←	Arbitrary RNs	←	←	←
Rx AEs N	Arbitrary Rx AEs	←	Arbitrary DN's AEs	←	←	←
Symbol durations T	Arbitrary durations	$T = M$	Arbitrary durations	←	$T = M$	←
Dispersion matrices Q	Arbitrary matrices	←	←	←	←	←
CSI	Perfect CSI	No CSI	Perfect CSI	←	No CSI	←
IAS	Symbol-level	←	←	Relaxed	Symbol-level	Relaxed
Dispersion-matrix	Power constraint of Eq. (2.21)	Hermitian and sparse structure	Power constraint of Eq. (5.8)	←	Hermitian	Real-valued diagonal
Complexity	$\frac{NTQ[(4MT+4\mathcal{L})/\tau+2\mathcal{L}]}{\log_2(Q\cdot\mathcal{L})} = 8+64/\tau$	$\frac{NTQ(4MT+4\mathcal{L})}{\log_2(Q\cdot\mathcal{L})} = 208$	$\frac{4[(M+\mathcal{L})QT+\mathcal{L}']/\tau}{\log_2(Q\cdot\mathcal{L})} + \frac{2(b+T)Q\mathcal{L}}{\log_2(Q\cdot\mathcal{L})} = 24+52/\tau$	$\frac{4[(1+\mathcal{L})QT+\mathcal{L}']/\tau}{\log_2(Q\cdot\mathcal{L})} + \frac{2(b+T)Q\mathcal{L}}{\log_2(Q\cdot\mathcal{L})} = 24+44/\tau$	$\frac{TQ(4M+6\mathcal{L})+4\mathcal{L}'+2bQ\mathcal{L}}{\log_2(Q\cdot\mathcal{L})} = 76$	$\frac{TQ(4+6\mathcal{L})+4\mathcal{L}'+2bQ\mathcal{L}}{\log_2(Q\cdot\mathcal{L})} = 68$
Performance[a,b]	No corr.: 16.4 dB $\rho = 0.7$: 31.4 dB	No corr.: 18.9 dB $\rho = 0.7$: 34.3 dB	21.8 dB	22.4 dB	24.6 dB	26.4 dB

[a] Performance is characterized by the SNR value recorded for the BER $= 10^{-4}$.

[b] $(M \times N) = (3 \times 1)$ AEs are employed for the co-located CSTSK and DSTSK schemes, while $(M \times N) = (2 \times 1)$ AEs are employed for the cooperative CSTSK, ACSTSK, DSTSK and ADSTSK schemes.

Chapter 6

Cooperative Differential Space-Time Spreading for Large-Delay Relay Networks

6.1 Introduction

In Chapter 5, we have proposed the family of cooperative STSK schemes, namely the cooperative CSTSK, ACSTSK, DSTSK and ADSTSK schemes, based on the STSK concept that activates one out of Q dispersion matrices, where we can exploit a useful diversity gain, while combating the effects of correlated large-scale fading. More specifically, the cooperative ACSTSK and ADSTSK schemes enable us to dispense with symbol-level Inter-Relay Synchronization (IAS), since only a single relay node is activated within each symbol duration of the cooperative transmission phase. Nevertheless, these cooperative schemes cannot avoid suffering from a severe performance degradation, when the IRS error exceeds the symbol duration, hence destroying the structure of the STSK codeword.

Let us note again that from a practical point of view, it is important to combat both the problems associated with the CSI estimation errors and the time synchronization errors, in order to achieve an effective cooperative space-time diversity gain. In addition to the above-mentiond ACSTSK and ADSTSK schemes, a number of asynchronous cooperative STCs have been proposed [144, 146], which invoke space-time equalization or multi-carrier transmission techniques, assuming that the perfect CSI and/or the relative transmission delays of the mobiles are available at the destination. However, a relatively high computational complexity is imposed at the destination receiver. Against this background, the main contribution of this chapter is that we first propose a practical CDSTC scheme designed for large-delay asynchronous relay networks, where neither channel estimation, IRS nor *prior* knowledge of the relays' synchronization delays are required at any of the nodes. More specifically, our

system employs differential encoding during the broadcast phase and STS-based scheme during the cooperative phase in conjunction with interference rejection spreading codes, namely Loosely Synchronized (LS) spreading codes. The LS codes exhibit a so-called Interference Free Window (IFW), where both the auto-correlation and cross-correlation values of the codes become zero, and hence have the capability of eliminating the MUIs as well as the orthogonality degradation of the cooperative STC, which are imposed by the asynchronous nature of the relay nodes. Furthermore, the destination node can detect both the transmitted symbols received from the direct Source-Destination (SD) link as well as from the RD link based on a low-complexity correlation operation, while using a hard-decision decoder, rather than exhaustive ML search.

To be more specific, we will propose the following two CDSTS architectures for asynchronous relay networks:

- Firstly, we propose a new cooperative space-time diversity protocol, invoking our LS code-based STS scheme relying on cooperating asynchronous nodes, while the destination node simultaneously decodes both the direct SD signal as well as the relayed STS-encoded symbols based on a low-complexity correlation operation.
- Next, we incorporate the three-stage Distributed Turbo Coding (DTC) scheme into the above-mentioned asynchronous CDSTS system, for the sake of achieving an infinitesimally low BER at a low SNR. Furthermore, the associated iterative decoding behaviour and the achievable performance are characterized with the aid of EXIT charts.

The remainder of this chapter is organized as follows. In Section 6.2 we describe the system model of our uncoded CDSTS system designed for asynchronous relay networks, while outlining our CDSTS system's detection algorithm. Section 6.3 highlights the concept of LS codes employed as the DS spreading codes in our CDSTS arrangement. In Section 6.4 we characterize the achievable performance of the uncoded CDSTS system. Furthermore, we describe the system model of the DTC-CDSTS scheme in Section 6.6. Our iterative detection algorithm is detailed in Section 6.6.3. In Section 6.7 the design and analysis of the proposed scheme is provided, while our performance results are summarized in Section 6.8. Finally, our conclusions are offered in Section 6.9.

6.2 System Overview of Cooperative Differential STS

Consider a collection of $N_{\text{total}} = N_{\text{TDMA}} \times N_{\text{CDMA}}$ nodes, each having a single antenna element and communicating with each other or with a specific destination node via frequency-flat fading channels, which corresponds to an uplink (UL) scenario or that of an ad hoc network. We assume the employment of a Time Division aided CDMA (TD-CDMA) based channel allocation scheme, where a single TD transmission frame is divided into N_{TDMA} time slots, where N_{CDMA} DS-CDMA source nodes are supported in each of the N_{TDMA} time slots

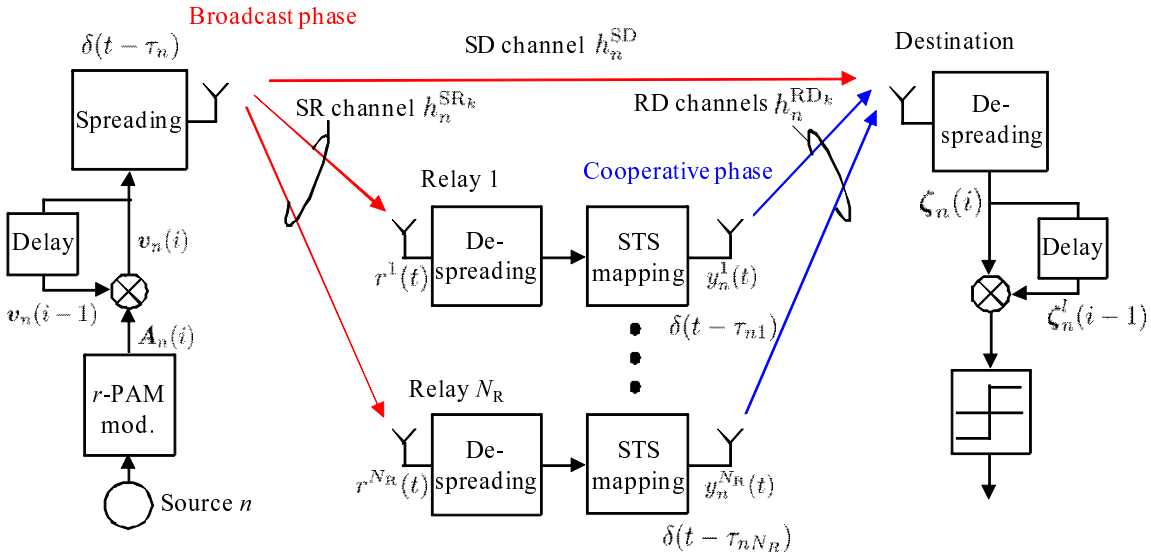

Figure 6.1: Dual-phase transmission model of our CDSTS.

with the aid of N_{CDMA} unique, user-specific DS-CDMA spreading codes. More specifically, each transmission of the N_{CDMA} source nodes is assisted by the preassigned source-specific M relay nodes, and the signal transmission involves two phases, i.e. the broadcast phase and the cooperative phase, assuming that the system is operated in a half-duplex mode. Additionally, in order to quantify the effects of asynchronously transmitting nodes on our CDSTS system, we introduce node-specific delays caused by their time synchronization errors, where the delays of the nth source node and that of the associated kth relay node are represented by τ_n and τ_{nk}, respectively. Furthermore, the Channel Impulse Responses (CIRs) of the Source-Relay (SR) channels, the SD channel and the Relay-Destination (RD) channels are described by $h_n^{\text{SR}_k}\exp(j\theta_n^{\text{SR}_k})$, $h_n^{\text{SD}}\exp(j\theta_n^{\text{SD}})$ and $h_n^{\text{RD}_k}\exp(j\theta_n^{\text{RD}_k})$, respectively, where $h_n^{\text{SR}_k}$, h_n^{SD} and $h_n^{\text{RD}_k}$ are the corresponding fading envelopes, while $\theta_n^{\text{SR}_k}$, θ_n^{SD} and $\theta_n^{\text{RD}_k}$ are the uniformly distributed phase-shift components.

Without loss of generality, we focus our attention on the first time slot, where each of the N_{CDMA} sources communicates with a certain destination node with the aid of the M source-specific cooperating nodes selected from all the nodes, as illustrated in Fig. 6.1. To be specific, we consider the case of $M = 4$ relay nodes, where the resultant maximum space-time diversity order provided by the relay nodes is also four. Note that a single node may simultaneously act as the relay supporting different source nodes.

6.2.1 Transmitted Signal

During the broadcast phase of Fig. 6.1, each of the N_{CDMA} source nodes transmits the differentially-encoded symbols both to the $M = 4$ relay nodes and to the destination node. Let the nth source node be the source-of-interest in this system model. First, the source

bits $b_n(q)$ are mapped to r-bit PAM-modulated symbols and then the modulated symbols are Serial-to-Parallel (S/P) converted to the symbol blocks $\boldsymbol{a}_n(i)$, each containing four modulated symbols formulated as $\boldsymbol{a}_n(i) = [a_n^1(i)\ a_n^2(i)\ a_n^3(i)\ a_n^4(i)]^{\mathrm{T}}$, where q and i represent the symbol and the block indices, respectively. Then, based on the symbol blocks $\boldsymbol{a}_n(i)$, the corresponding differentially-encoded symbol blocks $\boldsymbol{v}_n(i) = [v_n^1(i)\ v_n^2(i)\ v_n^3(i)\ v_n^4(i)]^{\mathrm{T}}$ are generated as follows [149]: $\boldsymbol{v}_n(i) = \boldsymbol{A}_n(i)\boldsymbol{v}_n(i-1)/||\boldsymbol{v}_n(i-1)||$ with

$$\boldsymbol{A}_n(i) = \begin{bmatrix} a_n^1(i) & a_n^2(i) & a_n^3(i) & a_n^4(i) \\ -a_n^2(i) & a_n^1(i) & a_n^4(i) & -a_n^3(i) \\ -a_n^3(i) & -a_n^4(i) & a_n^1(i) & a_n^2(i) \\ -a_n^4(i) & a_n^3(i) & -a_n^2(i) & a_n^1(i) \end{bmatrix}, \tag{6.1}$$

where the first block $\boldsymbol{v}_n(0) = [1\ 1\ 1\ 1]^{\mathrm{T}}$ is transmitted as a reference of the next differentially-encoded block, hence the first one does not containing any useful information. To relate the block index i to the symbol index q, let us define the qth differentially-modulated symbol as $\bar{v}_n(q)$, having the relation of $\bar{v}_n(4i+k-1) = v_n^k(i)$. Furthermore, the time-domain waveform transmitted by the nth source can be written as $s_n(t) = \sum_{q=-\infty}^{\infty} \bar{v}_n(q)\psi_{T_s^{\mathrm{S}}}(t - qT_s^{\mathrm{S}})$, where $\psi_\alpha(t)$ is the rectangular waveform, which is defined over the interval $[0, \alpha)$ and T_s^{S} represents the symbol duration of the broadcast phase.

Next, the differentially-modulated symbols $\bar{v}_n(t)$ are spread with the aid of the source's node-specific spreading code $c_n(t) = \sum_{i=0}^{L_{\mathrm{S}}-1} c_{ni}\psi_{T_c}(t - iT_c)$, where L_{S} is the code length of the spreading code and T_c is the chip duration, while c_{ni} represents the ith chip value. Here, we have the relation of $T_s^{\mathrm{S}} = L_{\mathrm{S}}T_c$. Note that the spreading factor G_{S} of the spreading code is given by the number of non-zero chips.

Having obtained the transmitted time-domain waveform $y_n(t)$ as

$$y_n(t) = \sqrt{\frac{P_{\mathrm{S}}}{G_{\mathrm{S}}}} \sum_{q=0}^{\infty} s_n(t)c_n(t - qT_s^{\mathrm{S}}), \tag{6.2}$$

the corresponding symbols received at the kth relay $r^k(t)$ and at the destination $r^{\mathrm{SD}}(t)$ are written as:

$$r^k(t) = \sum_{n=1}^{N} h_n^{\mathrm{SR}_k} y_n(t - \tau_n) \exp\left\{j(2\pi f_c t + \phi_n^{\mathrm{SR}_k})\right\} + n_k(t) \tag{6.3}$$

$$r^{\mathrm{SD}}(t) = \sum_{n=1}^{N} h_n^{\mathrm{SD}} y_n(t - \tau_n) \exp\left\{j(2\pi f_c t + \phi_n^{\mathrm{SD}})\right\} + n_{\mathrm{SD}}(t), \tag{6.4}$$

where we have $\phi_n^{\mathrm{SR}_k} = \theta_n^{\mathrm{SR}_k} - 2\pi f_c\tau_n$ and $\phi_n^{\mathrm{SD}} = \theta_n^{\mathrm{SD}} - 2\pi f_c\tau_n$, each given by the uniformly distributed random phase, while f_c is the operating carrier frequency. The noise components $n_k(t)$ of the kth relay and of the destination, namely $n_{\mathrm{SD}}(t)$ has a zero mean and variances of N_{0k} and $N_{0\mathrm{D}}$. Furthermore, P_{S} represents the transmission power of the source node, while $P_{\mathrm{R}}/4 = (1 - P_{\mathrm{S}})/4$ is that of each relay node, where the total transmission power

is considered to be unity. It should be noted here that the Eqs. (6.3) and (6.4) take into account the effects of the asynchronous relationship between the source nodes by introducing the delay terms τ_n.

6.2.2 Relayed Signal

During the cooperative phase of Fig. 6.1, the $M = 4$ relay nodes *amplify-and-forward* the received signals to the destination node with the aid of the STS scheme. More specifically, each relay node constructs the STS codeword based on the preassigned four spreading codes $c_n^l(t)$ $(l = 1, 2, 3, 4)$, corresponding to the nth source, which are expressed as $c_n^l(t) = \sum_{i=0}^{L_{\rm R}-1} c_{ni}^l \psi_{T_c}(t - iT_c)$, where $L_{\rm R}$ is the code length of the spreading code and the symbol duration of the cooperating phase $T_s^{\rm R} = L_{\rm R}T_c$. Let us furthermore define the spreading factor of the codes $c_n^l(t)$ as $G_{\rm R}$.

First, the kth relay node despreads the received signal $r^k(t)$ with the aid of the classic correlation operation using the spreading code $c_n(t)$, in order to obtain the despread symbol $\bar{d}_n^{{\rm SR}_k}(q)$ corresponding to the transmitted symbols $\bar{v}_n(q)$, which is given by[1]

$$\bar{d}_n^{{\rm SR}_k}(q) = \sqrt{P_{\rm S}} h_n^{{\rm SR}_k} \bar{v}_n(q) + J_n^{{\rm SR}_k}(q) + N_n^{{\rm SR}_k}(q), \tag{6.5}$$

where $J_n^{{\rm SR}_k}(q)$ is the MUI-related term induced by the other source nodes' signals, which is given by

$$\begin{aligned} J_n^{{\rm SR}_k}(q) &= \frac{1}{T_c} \sum_{n' \neq n} \sum_{q=0}^{\infty} \frac{\sqrt{P_{\rm S}}}{G_{\rm S}} h_{n'}^{{\rm SR}_k} \exp\left\{ j(\phi_{n'}^{{\rm SR}_k} - \phi_n^{{\rm SR}_k}) \right\} \\ &\times \int_{qT_s^{\rm S}+\tau_n}^{(q+1)T_s^{\rm S}+\tau_n} s_{n'}(t - \tau_{n'}) c_{n'}(t - qT_s^{\rm S} - \tau_{n'}) c_n(t - \tau_n) dt \end{aligned} \tag{6.6}$$

and $N_n^{{\rm SR}_k}(q)$ is the AWGN-related term formulated as

$$N_n^{{\rm SR}_k}(q) = \frac{1}{T_c \sqrt{G_{\rm S}}} \int_{qT_s^{\rm S}+\tau_n}^{(q+1)T_s^{\rm S}+\tau_n} n_k(t) c_n(t - \tau_n) e^{-j(2\pi f_c t + \phi_n^{{\rm SR}_k})} dt. \tag{6.7}$$

Here, $N_n^{{\rm SR}_k}(q)$ is a Gaussian distributed complex variable having a zero mean and a variance of N_{0k}.

Let us then S/P convert the despread symbols $\bar{d}_n^{{\rm SR}_k}(q)$ to generate the block-indexed vector $\boldsymbol{d}_n^{{\rm SR}_k}(i) = [d_n^{{\rm SR}_k 1}(i), \cdots, d_n^{{\rm SR}_k 4}(i)]^{\rm T}$ with the aid of the relation $d_n^{{\rm SR}_k l}(i) = \bar{d}_n^{{\rm SR}_k}(4i + l - 1)$. Furthermore, the time domain waveform of the despread symbols $d_n^{{\rm SR}_k l}(i)$ is given by $\hat{s}_n^{kl}(t) = \sum_{i=-\infty}^{\infty} d_n^{{\rm SR}_k l}(i) \psi_{T_s^{\rm R}}(t - iT_s^{\rm R})$.

Finally, the kth relay constructs the following STS-related signals $y_n^k(t)$ with the aid of

[1]The delay estimation is not necessary, since we can identify the correlation peak of the locally stored and received spreading sequence with the aid of an appropriate threshold value in order to accomplish code acquisition.

the STS mapping and the spreading blocks of Fig. 6.1, which are given by

$$y_n^1(t) = \alpha_1\sqrt{\frac{P_{\mathrm{R}}}{4G_{\mathrm{R}}}}\sum_{q=0}^{\infty}\big\{\hat{s}_n^{11}(t)c_n^1(t-qT_s^{\mathrm{R}}) - \hat{s}_n^{12}(t)c_n^2(t-qT_s^{\mathrm{R}}) - \hat{s}_n^{13}(t)c_n^3(t-qT_s^{\mathrm{R}}) - \hat{s}_n^{14}(t)c_n^4(t-qT_s^{\mathrm{R}})\big\} \tag{6.8}$$

$$y_n^2(t) = \alpha_2\sqrt{\frac{P_{\mathrm{R}}}{4G_{\mathrm{R}}}}\sum_{q=0}^{\infty}\big\{\hat{s}_n^{22}(t)c_n^1(t-qT_s^{\mathrm{R}}) + \hat{s}_n^{21}(t)c_n^2(t-qT_s^{\mathrm{R}}) + \hat{s}_n^{24}(t)c_n^3(t-qT_s^{\mathrm{R}}) - \hat{s}_n^{23}(t)c_n^4(t-qT_s^{\mathrm{R}})\big\} \tag{6.9}$$

$$y_n^3(t) = \alpha_3\sqrt{\frac{P_{\mathrm{R}}}{4G_{\mathrm{R}}}}\sum_{q=0}^{\infty}\big\{\hat{s}_n^{33}(t)c_n^1(t-qT_s^{\mathrm{R}}) - \hat{s}_n^{34}(t)c_n^2(t-qT_s^{\mathrm{R}}) + \hat{s}_n^{31}(t)c_n^3(t-qT_s^{\mathrm{R}}) + \hat{s}_n^{32}(t)c_n^4(t-qT_s^{\mathrm{R}})\big\} \tag{6.10}$$

$$y_n^4(t) = \alpha_4\sqrt{\frac{P_{\mathrm{R}}}{4G_{\mathrm{R}}}}\sum_{q=0}^{\infty}\big\{\hat{s}_n^{44}(t)c_n^1(t-qT_s^{\mathrm{R}}) + \hat{s}_n^{43}(t)c_n^2(t-qT_s^{\mathrm{R}}) - \hat{s}_n^{42}(t)c_n^3(t-qT_s^{\mathrm{R}}) + \hat{s}_n^{41}(t)c_n^4(t-qT_s^{\mathrm{R}})\big\}, \tag{6.11}$$

with the aid of the normalization factor $\alpha_k = \sqrt{\frac{1}{P_{\mathrm{S}}\sigma_k^2+N_{0k}}}$, where σ_k^2 represents a variance of the kth SR channel. As a result of the quasi-simultaneous cooperative transmission of the STS codeword of Eqs. (6.8)–(6.11), the corresponding received symbols at the destination node $r^{\mathrm{RD}}(t)$ can be expressed as

$$r^{\mathrm{RD}}(t) = \sum_{n=1}^{N}\sum_{k=1}^{4} h_n^{\mathrm{RD}_k} y_n^k(t-\tau_{nk}) e^{j(2\pi f_c t + \phi_n^{\mathrm{RD}_k})} + n_{\mathrm{RD}}(t), \tag{6.12}$$

where $\phi_n^{\mathrm{RD}_k} = \theta_n^{\mathrm{RD}_k} - 2\pi f_c \tau_{nk}$ and $n_{\mathrm{RD}}(t)$ has a zero mean and a variance of $N_{0\mathrm{D}}$. Note here that Eq. (6.12) represents the waveform superimposition of the $4N_{\mathrm{CDMA}}$ asynchronous relay nodes, corresponding to the N_{CDMA} STS codewords.

6.2.3 Hard-Decision CDSTS Detection Algorithm

At the destination node of Fig. 6.1, the symbols transmitted from the nth source node are detected in a low-complexity manner based both on the direct SD link and on the RD links, so that a high diversity gain is achieved without any CSI estimation.

First, the signals received at the broadcast phase $r^{\mathrm{SD}}(t)$ in Eq. (6.4) are despread similarly to Eq. (6.5), which is expressed as

$$\bar{d}_n^{\mathrm{SD}}(q) = \sqrt{P_{\mathrm{S}}} h_n^{\mathrm{SD}} \bar{v}_n(q) + J_n^{\mathrm{SD}}(q) + N_n^{\mathrm{SD}}(q), \tag{6.13}$$

where we have the MUI-related component $J_n^{\mathrm{SD}}(q)$ and the AWGN-related component $N_n^{\mathrm{SD}}(q)$,

such as

$$J_n^{\mathrm{SD}}(q) = \frac{1}{T_c}\sum_{n'\neq n}\sum_{q=0}^{\infty}\frac{\sqrt{P_{\mathrm{S}}}}{G_{\mathrm{S}}}h_{n'}^{\mathrm{SD}}\exp\left\{j(\phi_{n'}^{\mathrm{SD}}-\phi_n^{\mathrm{SD}})\right\} \times \int_{qT_s^{\mathrm{S}}+\tau_n}^{(q+1)T_s^{\mathrm{S}}+\tau_n} s_{n'}(t-\tau_{n'})c_{n'}(t-qT_s^{\mathrm{S}}-\tau_{n'})c_n(t-\tau_n)dt \quad (6.14)$$

$$N_n^{\mathrm{SD}}(q) = \frac{1}{T_c\sqrt{G_{\mathrm{S}}}}\int_{qT_s^{\mathrm{S}}+\tau_n}^{(q+1)T_s^{\mathrm{S}}+\tau_n} n_{\mathrm{SD}}(t)c_n(t-\tau_n)e^{-j(2\pi f_c t+\phi_n^{\mathrm{SD}})}dt. \quad (6.15)$$

For simplicity of the treatment, the despread symbols $\bar{d}_n^{\mathrm{SD}}(q)$ are then rearranged at the detector into the following vectorial form

$$\begin{aligned}\boldsymbol{\xi}_n^{\mathrm{SD}}(i) &= \left[\begin{array}{cccc}\xi_n^{\mathrm{SD}_1}(i) & \xi_n^{\mathrm{SD}_2}(i) & \xi_n^{\mathrm{SD}_3}(i) & \xi_n^{\mathrm{SD}_4}(i)\end{array}\right]^{\mathrm{T}} \\ &= \frac{1}{\sqrt{4}}\left[\begin{array}{c} d_n^{\mathrm{SD}_1}(i)+d_n^{\mathrm{SD}_2}(i)+d_n^{\mathrm{SD}_3}(i)+d_n^{\mathrm{SD}_4}(i) \\ -d_n^{\mathrm{SD}_2}(i)+d_n^{\mathrm{SD}_1}(i)-d_n^{\mathrm{SD}_4}(i)+d_n^{\mathrm{SD}_3}(i) \\ -d_n^{\mathrm{SD}_3}(i)+d_n^{\mathrm{SD}_4}(i)+d_n^{\mathrm{SD}_1}(i)-d_n^{\mathrm{SD}_2}(i) \\ -d_n^{\mathrm{SD}_4}(i)-d_n^{\mathrm{SD}_3}(i)+d_n^{\mathrm{SD}_2}(i)+d_n^{\mathrm{SD}_1}(i)\end{array}\right], \end{aligned} \quad (6.16)$$

with the aid of the symbol-to-block transformation $d_n^{\mathrm{SD}_l}(i)=\bar{d}_n^{\mathrm{SD}}(4i+l-1)$. Next, the signals received during the cooperative phase $r^{\mathrm{RD}}(t)$ in Eq. (6.12) are despread to form $\boldsymbol{\xi}_n^{\mathrm{RD}}(i) = [\xi_n^{\mathrm{RD}_1}(i)\ \xi_n^{\mathrm{RD}_2}(i)\ \xi_n^{\mathrm{RD}_3}(i)\ \xi_n^{\mathrm{RD}_4}(i)]^{\mathrm{T}}$, which is given by

$$\begin{aligned}\xi_n^{\mathrm{RD}_l}(i) &= \frac{1}{T_c\sqrt{G_{\mathrm{R}}}}\sum_{k=1}^{4}\int_{iT_s^{\mathrm{R}}+\tau_{nk}}^{(i+1)T_s^{\mathrm{R}}+\tau_{nk}} r^{\mathrm{RD}}(t)c_n^l(t-\tau_{nk})e^{-j(2\pi f_c t+\phi_n^{\mathrm{RD}_k})}dt \\ &= D_n^{\mathrm{RD}_l}(i)+J_n^{\mathrm{RD}_l}(i)+N_n^{\mathrm{RD}_l}(i), \end{aligned} \quad (6.17)$$

where $\boldsymbol{D}_n^{\mathrm{RD}}(i) = [D_n^{\mathrm{RD}_1}(i)\ D_n^{\mathrm{RD}_2}(i)\ D_n^{\mathrm{RD}_3}(i)\ D_n^{\mathrm{RD}_4}(i)]^{\mathrm{T}}$ can be expressed as $\boldsymbol{D}_n^{\mathrm{RD}}(i) = \boldsymbol{\Xi}_n(i)\boldsymbol{\chi}_n$ with the relations of

$$\begin{aligned}\boldsymbol{\Xi}_n(i) &= \left[\begin{array}{cccc} d_n^{\mathrm{SR}_1 1}(i) & d_n^{\mathrm{SR}_2 2}(i) & d_n^{\mathrm{SR}_3 3}(i) & d_n^{\mathrm{SR}_4 4}(i) \\ -d_n^{\mathrm{SR}_1 2}(i) & d_n^{\mathrm{SR}_2 1}(i) & -d_n^{\mathrm{SR}_3 4}(i) & d_n^{\mathrm{SR}_4 3}(i) \\ -d_n^{\mathrm{SR}_1 3}(i) & d_n^{\mathrm{SR}_2 4}(i) & d_n^{\mathrm{SR}_3 1}(i) & -d_n^{\mathrm{SR}_4 2}(i) \\ -d_n^{\mathrm{SR}_1 4}(i) & -d_n^{\mathrm{SR}_2 3}(i) & d_n^{\mathrm{SR}_3 2}(i) & d_n^{\mathrm{SR}_4 1}(i)\end{array}\right] \\ \boldsymbol{\chi}_n &= [\alpha_1 h_n^{\mathrm{RD}_1}\ \alpha_2 h_n^{\mathrm{RD}_2}\ \alpha_3 h_n^{\mathrm{RD}_3}\ \alpha_4 h_n^{\mathrm{RD}_4}]^{\mathrm{T}}, \end{aligned}$$

and the corresponding MUI component $J_n^{\mathrm{RD}}(i)$ and the noise component $N_n^{\mathrm{RD}_l}(i)$ are as follows:

$$\begin{aligned}J_n^{\mathrm{RD}}(i) &= \frac{1}{T_c\sqrt{G_{\mathrm{R}}}}\sum_{k=1}^{4}\int_{iT_s^{\mathrm{R}}+\tau_{nk}}^{(i+1)T_s^{\mathrm{R}}+\tau_{nk}} c_n^l(t-\tau_{nk})e^{-j(2\pi f_c t+\phi_n^{\mathrm{RD}_k})} \\ &\times \left[\sum_{n'\neq n}\sum_{k'=1}^{4} h_{n'}^{\mathrm{RD}_{k'}}y_{n'}^{k'}(t-\tau_{n'k'})e^{j(2\pi f_c t+\phi_{n'}^{\mathrm{RD}_{k'}})}\right. \\ &+ \left.\sum_{k'\neq k}^{4} h_n^{\mathrm{RD}_{k'}}y_n^{k'}(t-\tau_{nk'})e^{j(2\pi f_c t+\phi_n^{\mathrm{RD}_{k'}})}\right]dt \end{aligned} \quad (6.18)$$

$$N_n^{\mathrm{RD}_l}(i) = \frac{1}{T_c\sqrt{G_{\mathrm{R}}}}\sum_{k=1}^{4}\int_{iT_s^{\mathrm{R}}+\tau_{nk}}^{(i+1)T_s^{\mathrm{R}}+\tau_{nk}} n_{\mathrm{RD}}(t)c_n^l(t-\tau_{nk})e^{-j(2\pi f_c t+\phi_n^{\mathrm{RD}_k})}dt. \quad (6.19)$$

According to [149], let us denote the rearranged vectorial form of the despread signals as follows:

$$\boldsymbol{\zeta}_n^{X_1}(i) = [\ \xi_n^{X_1}(i) \quad \xi_n^{X_2}(i) \quad \xi_n^{X_3}(i) \quad \xi_n^{X_4}(i)]^{\mathrm{T}} \tag{6.20}$$

$$\boldsymbol{\zeta}_n^{X_2}(i) = [-\xi_n^{X_2}(i) \quad \xi_n^{X_1}(i) \quad \xi_n^{X_4}(i) \ -\xi_n^{X_3}(i)]^{\mathrm{T}} \tag{6.21}$$

$$\boldsymbol{\zeta}_n^{X_3}(i) = [-\xi_n^{X_3}(i) \ -\xi_n^{X_4}(i) \quad \xi_n^{X_1}(i) \quad \xi_n^{X_2}(i)]^{\mathrm{T}} \tag{6.22}$$

$$\boldsymbol{\zeta}_n^{X_4}(i) = [-\xi_n^{X_4}(i) \quad \xi_n^{X_3}(i) \ -\xi_n^{X_2}(i) \quad \xi_n^{X_1}(i)]^{\mathrm{T}}, \tag{6.23}$$

where we have $X = \mathrm{SD}$ or RD. Finally, based on Eqs. (6.20)–(6.23), the detector evaluates

$$\begin{aligned} &\Re\left[\left\{\boldsymbol{\zeta}_n^{\mathrm{SD}_1}(i+1)\right\}^{\mathrm{T}}\left\{\boldsymbol{\zeta}_n^{\mathrm{SD}_l}(i)\right\}^{*} + \left\{\boldsymbol{\zeta}_n^{\mathrm{RD}_1}(i+1)\right\}^{\mathrm{T}}\left\{\boldsymbol{\zeta}_n^{\mathrm{RD}_l}(i)\right\}^{*}\right] \\ &= \left\{4P_{\mathrm{S}}\left(h_n^{\mathrm{SD}}\right)^2 + \sum_{k=1}^{4}\frac{P_{\mathrm{S}}P_{\mathrm{R}}}{P_{\mathrm{S}}\sigma_k^2 + N_{0k}}\left(h_n^{\mathrm{SR}_k}h_n^{\mathrm{RD}_k}\right)^2\right\}||\boldsymbol{v}_n(i)||a_n^l(i) + J_n(i) + N_n(i), \end{aligned} \tag{6.24}$$

where the operator $\Re[\bullet]$ indicates the real part of $\bullet$ and $J_n(i)$ represents the MUI-related term, originated from Eqs. (6.6), (6.14) and (6.18), while $N_n(i)$ is the AWGN-related term obeying Eqs. (6.7), (6.15) and (6.19). Finally, the symbols $a_n^l(i)$ are detected by the low-complexity hard decision decoder evaluating Eq. (6.24). It can be seen from Eq. (6.24) that if the multiuser interference is efficiently suppressed, our system may benefit from a maximum diversity order of five.

6.3 Basic Properties of LS Codes

As represented by the term $J_n(i)$ in Eq. (6.24), the attainable performance of our CDSTS system is affected by the MUI, therefore dependent on the spreading codes employed. In order to mitigate the performance degradation due to the MUI, we employ LS codes [24] as the spreading codes in our CDSTS system, which exhibit a so-called IFW, where the off-peak aperiodic auto-correlation values as well as the aperiodic cross-correlation values become zero, resulting in zero ISI and zero MAI, provided that the maximum delay of the asynchronous transmissions is within the width of the IFW.

Here we only highlight the basic characteristics and the parameters of the LS codes employed, since the design of LS codes was detailed for example in [150] and in the references therein. To be specific, LS codes are constructed with the aid of a $(P_{\mathrm{LS}} \times P_{\mathrm{LS}})$-dimensional Walsh-Hadamard matrix as well as an orthogonal complementary code set of length N_{LS}. More specifically, by inserting W_0 zeros both at the beginning and in the center of the complementary code pair, we can generate P_{LS} LS codes having an IFW of $\min\{N_{\mathrm{LS}}-1, W_0\}$ chip durations, where the corresponding code length of the LS codes is $L = N_{\mathrm{LS}}P_{\mathrm{LS}} + 2W_0$. According to [150], the parameter-based notation of LS codes is given by LS(N_{LS}, P_{LS}, W_0).

On the other hand, a particular drawback of LS codes is that they have a limited code set. For example, consider the set of LS codes LS(N_{LS}, P_{LS}, W_0) = (4, 8, 3), having an

IFW of $W_0 = 3$ chip durations and the code length of $L = N_{\mathrm{LS}}P_{\mathrm{LS}} + 2W_0 = 38$ chips. In this case the corresponding number of LS codes becomes as low as $P_{\mathrm{LS}} = 6$, while that of the Gold codes having a similar code length of $L = 31$ chips is 33. Therefore, considering the employment of LS codes in a practical system, it is generally beneficial to combine DS-CDMA using LS codes with other multiple access schemes. For example, we may combine LS-code based CDMA with Frequency Division Multiple Access (FDMA), Time Division Multiple Access (TDMA) and Spatial Division Multiple Access (SDMA). For this reason, a hybrid TD-CDMA based channel allocation scheme is employed in our LS code-aided CDSTS system, which is reminiscent of the TDMA/CDMA philosophy of the 3G systems [24].

In our CDSTS scheme the effects of asynchronous relay nodes are eliminated under the ideal assumption that the despreading operation at the destination receiver is capable of sufficiently suppressing both the asynchronous MUI as well as the multi-path-induced Inter-Symbol Interference (ISI). This indicates that low cross-correlations as well as auto-correlations are required for the spreading codes employed. However, the conventional spreading codes, such as Walsh codes and Gold codes, normally suffer from both MUI and from Multi-Path Interference (MPI) due to the non-negligible auto- and/or cross-correlation values. To this end, we employ here the above-mentioned LS codes as the spreading codes in our CDSTS system, according to the proposal in [4]. The family of LS codes exhibits a so-called Interference-Free Window (IFW), resulting in zero ISI and zero Multiple-Access Interference (MAI), provided that the maximum delay of the asynchronous transmissions including all MPI components is within the width of the IFW.[2]

6.4 Performance Results

In this section we provide our performance results in order to characterize our CDSTS system. The basic system parameters used in our simulations are listed in Table 6.1. We consider a CDSTS system supporting $N_{\mathrm{CDMA}} = 4$ source nodes, each of which are supported by $M = 4$ source-specific relay nodes that are allocated prior to communications. The synchronization delays τ_n of the source nodes and those of the associated kth relay nodes τ_{nk} are uniformly distributed in $[0, \tau_{\max}]$, where $\tau_{\max}$ is the maximum delay value, ranging from 0 to $7T_c$ in our simulations. We assumed that the SD and the RD channels were non-dispersive Rayleigh fading channels, while the SR channels were either Rayleigh fading or perfect channels. We note here that the term 'perfect channel' indicates a lossless channel, leading to the ideal relaying performance in the context of the decode-and-forward scheme. As mentioned above,

[2] Although the effects of MUI and MPI arriving within the IFW are perfectly eliminated, the number of LS codes exhibiting a sufficiently wide IFW is limited. In order to extend the degree of design freedom and hence to accommodate large synchronous delays, Multi-Carrier (MC) transmission can be invoked in our CDSTS system, as described in [150]. More specifically, the IFW duration of the LS codes can be extended by a factor given by the number of subcarriers, since the chip duration of each subcarrier is proportionately increased.

Table 6.1: Basic system parameters of the uncoded CDSTS scheme of Fig. 6.1

Number of source nodes per time slot N_{CDMA}	4
Number of relay nodes per source node M	4
Modulation Scheme	BPSK
Power allocation (P_{S}, P_{R})	(0.5, 0.5)
Spreading codes of source nodes	LS codes of LS(8,4,7)
Spreading codes of relay nodes	LS codes of LS(8,16,7)
SR channel	Perfect or Rayleigh fading channel
SD and RD channels	Rayleigh fading channel
Maximum delay $\tau_{\max}$	0 to $7T_c$
Detector at the destination	Hard-decision decoder of Eq. (6.24)

LS codes are employed as our spreading codes, where the source nodes have the LS codes of LS(N_{LS}, P_{LS}, W_0) = LS(8,4,7), while the relay nodes employ LS(N_{LS}, P_{LS}, W_0) = LS(8,16,7), indicating that the corresponding width of the IFW is $7T_c$. For instance, assuming that the system has a chip rate of 1.2288 Mchips/sec, the width of the IFW becomes $7T_c$ = 5.7 μs. Furthermore, the power allocated to the source and to the relay nodes was set to $P_{\mathrm{S}} = P_{\mathrm{R}} = 0.5$, as suggested in [116].

Figs. 6.2 and 6.3 show the achievable BER performance of our CDSTS system in conjunction with the different maximum delay values of $\tau_{\max} = T_c$, $2T_c$, $4T_c$ and $7T_c$, where the SR channels were assumed to be perfect in Fig. 6.2, while those were assumed to be the frequency-flat Rayleigh fading channels in Fig. 6.3. In addition to the above-mentioned LS codes, Gold codes are also considered as spreading codes in order to show the effects of the diverse spreading codes on the achievable performance, noting that Gold codes constitute well-known spreading code having relatively good asynchronous cross-correlation properties. Furthermore, we also characterized the non-cooperative differential transmission scenario associated with $P_{\mathrm{S}} = 1$, where the source nodes communicate with the destination node without any cooperating nodes. Observe in Figs. 6.2 and 6.3 that regardless of the maximum delay values $\tau_{\max}$, the LS code-based CDSTS system attained a high diversity gain, outperforming the non-cooperative case, although an error floor was exhibited for the high-delay scenario of $\tau_{\max} = 8T_c > W_0$ due to the effects of the unsuppressed interfering signal components arriving outside the IFW.. This also implies that the MUI-induced degradations were overcome by the LS code's IFW. On the other hand, it can be seen that the performance of the Gold code-based CDSTS system is seriously deteriorated by the effects of synchronization errors. In fact, the performance became even worse than that of the non-cooperative system.

Fig. 6.4 compares our CDSTS with the CDSTC benchmarker presented by Jing and Ja-

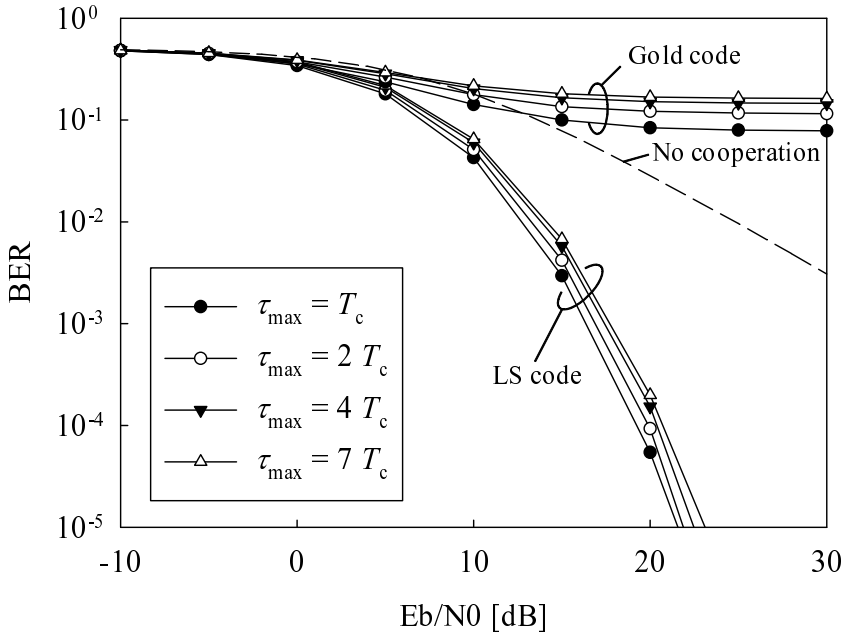

Figure 6.2: Achievable BER performance of our CDSTS system obeying the architecture of Fig. 6.1 for the maximum delay values of $\tau_{\max} = T_c$, $2T_c$, $4T_c$ and $7T_c$ for both LS codes and Gold codes. Here, we assumed the perfect channels for the SR channels and frequency-flat Rayleigh fading channels for the RD channels. The BER curve of non-cooperative scenario employing LS codes was also plotted. All other system parameters were summarized in Table 6.1.

farkhani [116], which employs a TDMA-based orthogonal channel allocation scheme. Therefore, unlike the TD-CDMA based channel allocation scheme of our CDSTS, Jing's CDSTC does not cause any MUI, although the relay nodes' asynchronous nature was not taken into account. We assumed in Jing's CDSTC benchmark scheme that the symbol duration was T_c and a (4×4)-element real-valued square system-matrix contained the orthogonal codes [116] employed for the STC scheme, while employing the ML detector at the destination node. Additionally, since the direct SD link was not considered in the benchmark system [116], the SD link in our CDSTS system was also ignored in order to enable a fair comparison, although this gives rise to a reduction in the resultant diversity order of our system. Also, the SR channels were assumed to be Rayleigh fading channels. Observe in Fig. 6.4 that our CDSTS and Jing's CDSTC [116] exhibited an identical BER performance in the case of $\tau_{\max} = 0$, implying that our CDSTS can indeed perfectly eliminate the effects of synchronous MUI, and hence reached the BER performance of Jing's CDSTC benchmark using a TDMA-based orthogonal multiple access scheme. Furthermore, upon introducing the asynchronous relays, Jing's CDSTC exhibited an error floor due to deteriorating the orthogonality of the cooperative space-time codeword. By contrast, our LS code-based CDSTS system retained its high diversity gain in all the cases considered, although naturally the performance was degraded to some extent upon increasing the maximum delay $\tau_{\max}$.

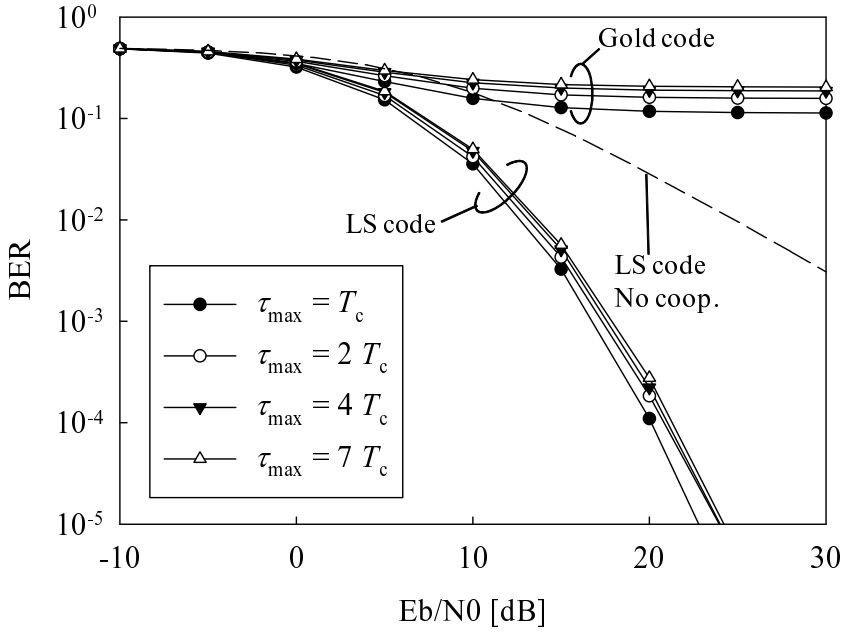

Figure 6.3: Achievable BER performance of our CDSTS system obeying the architecture of Fig. 6.1 for the maximum delay values of $\tau_{\max} = T_c$, $2T_c$, $4T_c$ and $7T_c$ for both LS codes and Gold codes. Here, we assumed frequency-flat Rayleigh fading channels both for the SR channels and for the RD channels. The BER curve of non-cooperative scenario employing LS codes was also plotted. All other system parameters were summarized in Table 6.1.

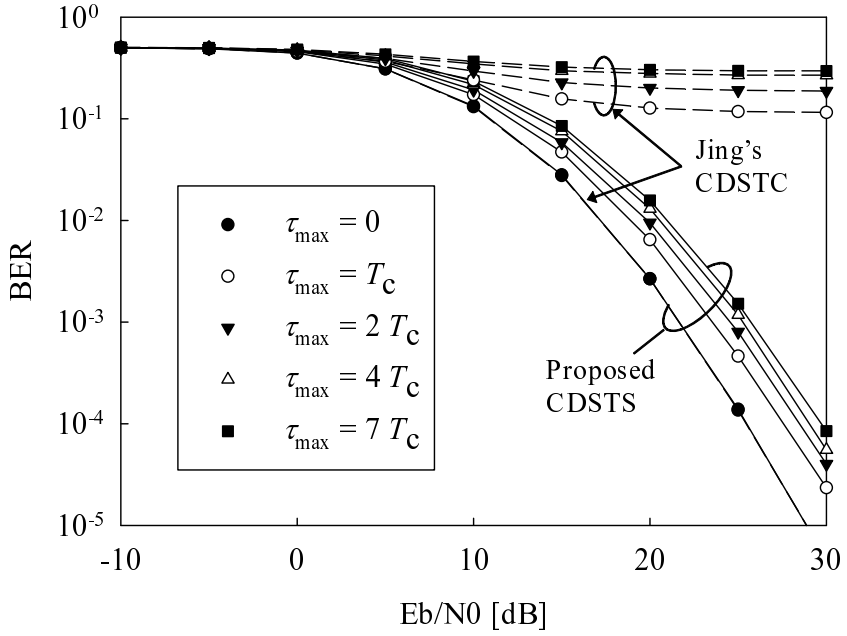

Figure 6.4: Comparison of our CDSTS scheme obeying the architecture of Fig. 6.1 and Jing's CDSTC scheme [116] for the maximum delay values of $\tau_{\max} = 0$, T_c, $2T_c$, $4T_c$ and $7T_c$. Here, we assumed frequency-flat Rayleigh fading channels both for the SR channels and for the RD channels. All other system parameters were summarized in Table 6.1.

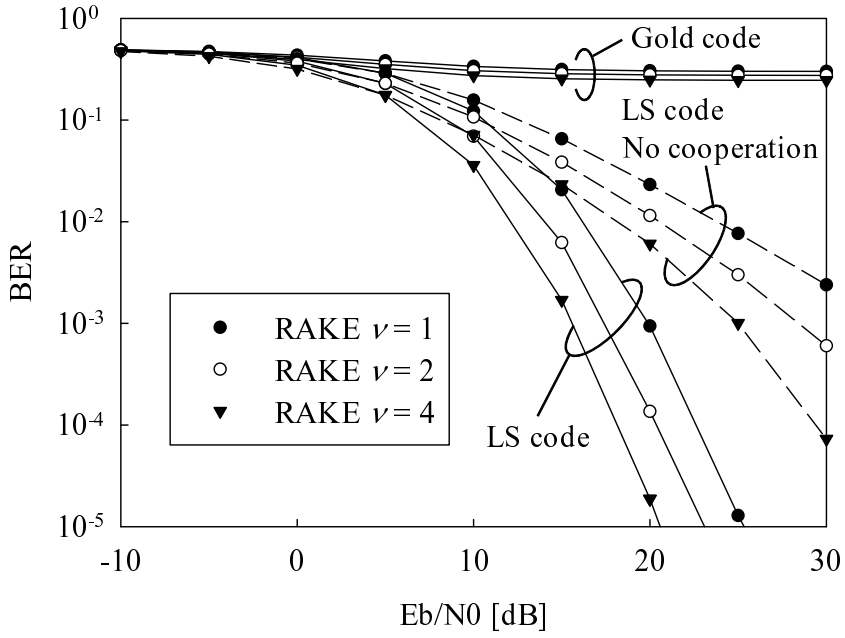

Figure 6.5: Achievable BER performance of our CDSTS scheme obeying the architecture of Fig. 6.1, assuming the perfect channels for the SR channels nd the frequency-selective Rayleigh fading channels for the RD channels. Different number of RAKE fingers $\nu = 1$, 2 and 4 at the destination receiver were compared, where we also considered a correlated tapped line channel model associated with $L_{\text{tap}} = 4$ taps and the tap correlation factor of $\rho = 0.5$. The maximum delay value was set to $\tau_{\max} = 3T_c$. All other system parameters were summarized in Table 6.1.

Although the aforementioned systems assumed the presence of narrowband frequency-flat channels, our CDSTS system can be readily employed for transmission over broadband frequency-selective channels by introducing the concept of (RAKE) combining in Eq. (6.24). Figs. 6.5 and 6.6 show the achievable BER performance of our CDSTS assuming the frequency-selective Rayleigh fading RD channels in conjunction with different number of RAKE fingers $\nu = 1$, 2 and 4, where the perfect channels were assumed for the SR channels in Fig. 6.5, while the frequency-selective Rayleigh fading channels were assumed for both the SR and RD channels in Fig. 6.6. Here we assumed that the maximum delay value was set to $\tau_{\max} = 3T_c$. Furthermore, we considered a correlated tapped delay line channel model for each channel [151], where the number of CIR taps was $L_{\text{tap}} = 4$ and the correlation factor ρ_{ij} between the ith tap and the jth tap was set to $\rho_{ij} = 0.5$. For comparison, we also simulated the non-cooperative differentially-encoded transmission scheme using LS codes and the Gold code-based CDSTS benchmark scheme. In this case, the corresponding total maximum delay, namely the sum of the maximum synchronization delay $\tau_{\max}$ and of the tap length L_{tap}, becomes $7T_c$, which is within the IFW. The SR channels were assumed to be perfect. It is seen in Fig. 6.5 that both our LS code-based CDSTS arrangement and the non-cooperative scenario using LS codes benefitted from an increased path diversity gain upon increasing the

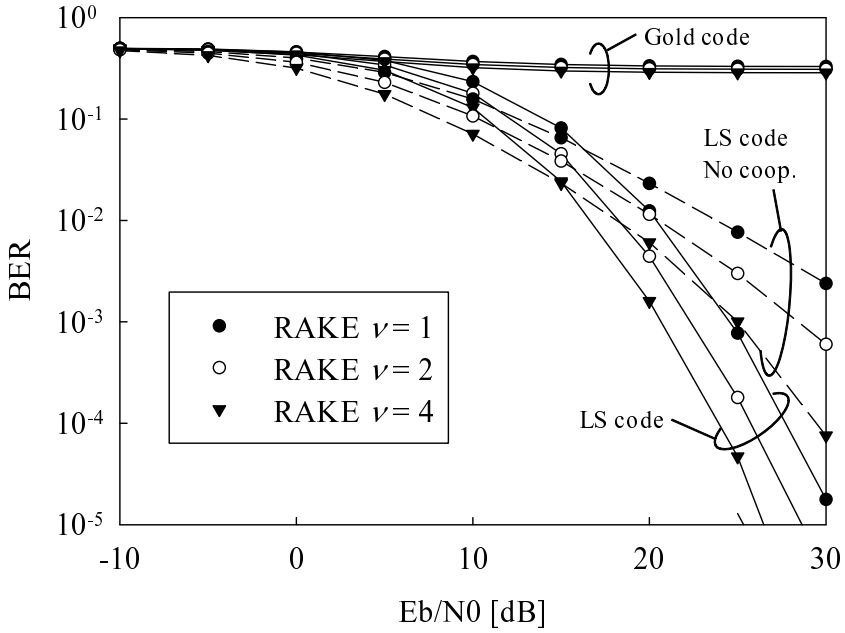

Figure 6.6: Achievable BER performance of our CDSTS scheme obeying the architecture of Fig. 6.1, assuming the frequency-selective Rayleigh fading channels for both the SR and RD channels. Different number of RAKE fingers $\nu = 1$, 2 and 4 at the destination receiver were compared, where we also considered a correlated tapped line channel model associated with $L_{\text{tap}} = 4$ taps and the tap correlation factor of $\rho = 0.5$. The maximum delay value was set to $\tau_{\max} = 3T_c$. All other system parameters were summarized in Table 6.1.

number of RAKE fingers ν owing to the ideal auto-correlation characteristics of the LS codes. More specifically, our LS code-based CDSTS is capable of gleaning both space-time diversity gain as well as path diversity gain, and hence outperformed both the non-cooperative scenario as well as the Gold code-based CDSTS benchmark scheme.

6.5 Distributed Turbo-Coded CDSTS

Having introduced the uncoded CDSTS of Fig. 6.1 exhibiting improved robustness against large-delay IRS, we now conceive its Distributed-Turbo-Coded (DTC) counterpart for the sake of achieving a near-capacity performance.

The DTC philosophy was presented in [106, 108, 113], where the turbo coding principle [27] was applied to a single-relay-assisted cooperative system. Whilst in general cooperative STCs have the capability of achieving the maximum attainable diversity order in the high SNR regime, the DTC aims for achieving an additional *turbo processing gain*, and therefore it is particularly suitable for operation at low SNRs. Here we note that most of the previous DTC schemes proposed in the open literature [106, 108, 113] are based on a two-stage parallel-concatenated arrangement assisted by a single relay node, assuming that there is a perfect link

between the cooperating nodes. More recently, a sophisticated three-component distributed turbo trellis coded modulation scheme was proposed in [152], also assuming the assistance of a single relay node.

Against this background, the novel contributions and rationale of our DTC-CDSTS system are as follows.

1. We present a cooperative STC protocol, intrinsically amalgamating the concepts of asynchronous cooperation, of non-coherent detection as well as of DTC, which is capable of achieving beneficial spatial-diversity and iterative-processing gains. More specifically, in our CDSTS scheme a multi-relay-assisted three-stage DTC is employed in order to take maximum advantage of the potentially available relay nodes, unlike the family of conventional single-relay-assisted DTCs [108, 113, 152]. We emphasize that the asynchronous cooperation technique employed plays a beneficial role.

2. In contrast to the uncoded CDSTS of Fig. 6.1, where the CDSTS codewords were designed based on the orthogonal STBC philosophy[3], the STC blocks of our CDSTS are constructed based on Differential Linear Dispersion Codes (DLDCs) [89], which have the capability of striking a flexible diversity versus multiplexing tradeoff, depending on the number of relay nodes as well as on the target transmission rate. Additionally, as mentioned above, we invoke the multiple-relay-assisted DTC technique, in order to conceive a practical Forward Error Correction (FEC)-assisted cooperative system.

3. A Unity Rate Code (URC) and a Recursive Systematic Convolutional (RSC) code are incorporated into our CDSTS system for the sake of maximizing the interleaver gain achieved by iterative decoding. The system parameters are optimized with the aid of EXtrinsic Information Transfer (EXIT) chart analysis [130] for the sake of approaching the Rayleigh fading channel's capacity.

6.6 System Overview of Distributed Turbo-Coded CDSTS

In this section we present the system model of our cooperative transmission scheme. Consider the cooperative network of Fig. 6.7, which comprises a source node, M relay nodes and a destination node.[4] Here, it is assumed that each node has a node-specific synchronization delay, which is uniformly distributed from 0 to $\tau_{\max}$, where $\tau_{\max}$ denotes the maximum delay.

[3]To expound a little further, the number of antenna elements supported by orthogonal STBCs is limited [22]. Hence, when orthogonal STBCs are employed for cooperative transmissions, the number of relay nodes is equally limited.

[4]For example, we may consider a Time Division-Code Division Multiple Access (TD-CDMA) based channel allocation scheme supporting $(N_{\rm T} \times N_{\rm C})$ source nodes, namely supporting $N_{\rm C}$ source nodes in each of the $N_{\rm T}$ time slots.

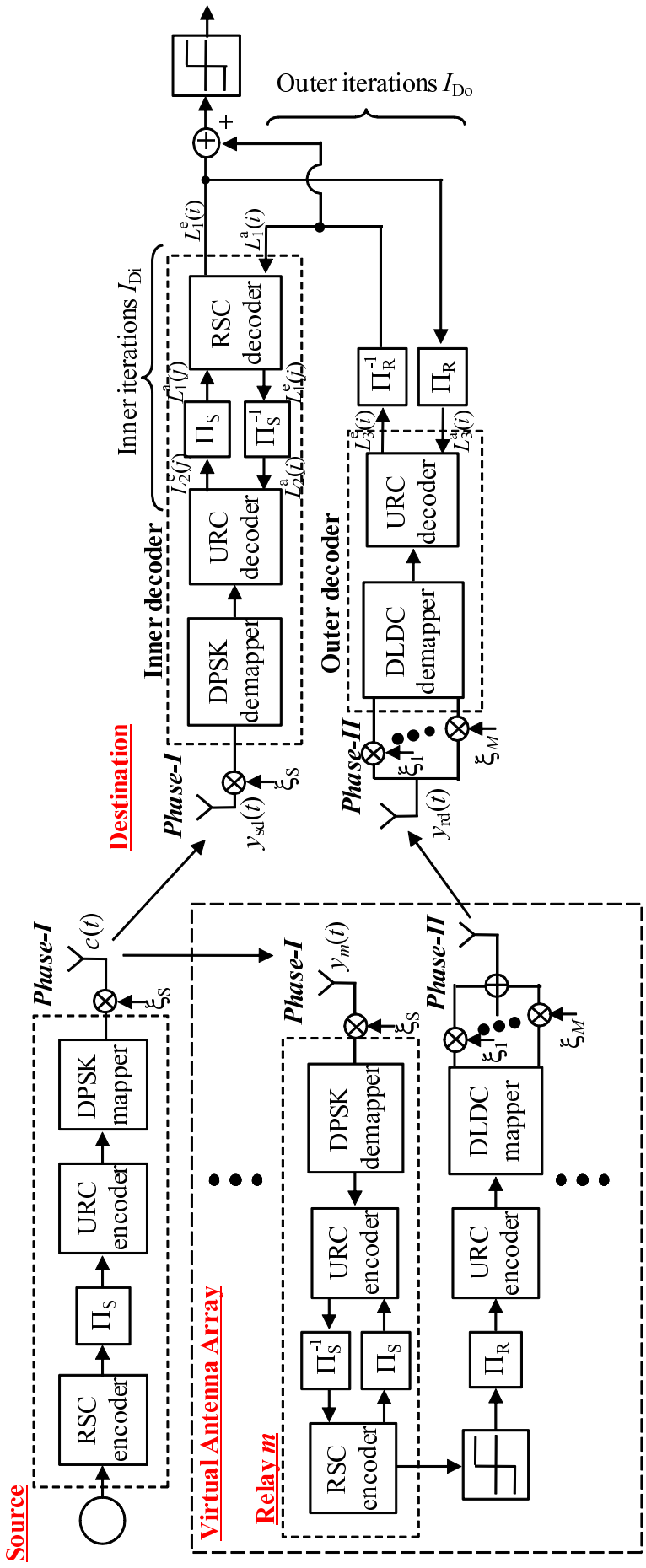

Figure 6.7: Schematic of the source and relay nodes based on three-stage encoded cooperative transmission and the three-stage iterative detector at the destination node.

The source node transmits its signals to the destination node with the aid of the source-specific relay nodes. More specifically, each transmission is composed of two phases, i.e. a broadcast phase-I and a cooperative phase-II. While the source node broadcasts the signals to the associated M relay nodes and to the destination node during phase-I, the relay nodes retransmit the decoded signals to the destination node based on our CDSTS scheme during phase-II. Although in this paper we assume that each node is equipped with a single antenna element, our system can be readily extended to the scenario of multiple-antenna-element assisted cooperative networks. Additionally, we assume that a unity total power is shared by the collaborating nodes, where the power values P_{S} and P_{R} are allocated to the source node and the corresponding relay nodes, respectively, while maintaining the relation of $P_{\mathrm{S}}+P_{\mathrm{R}} = 1$. For the sake of simplicity, we set $P_{\mathrm{S}} = P_{\mathrm{R}} = 0.5$, noting that power optimization remains an open problem at this stage.

Furthermore, let us define d_{sd}, d_{sr} and d_{rd}, as the average geometrical distances of the SD link, of the SR links and of the RD links, respectively. Here, each path-loss value of the corresponding links can be modeled by $P(\mathrm{ab}) = K \cdot d_{\mathrm{ab}}^{-\alpha}$ $(\mathrm{a,b} = \mathrm{s,d,r})$, where K is the constant element and α is the path loss exponent. Considering a free-space propagation model of $\alpha = 2$, the power gain G_{sr} of the SR link and that of the RD link G_{rd} over the SD link is given by $G_{\mathrm{sr}} = (d_{\mathrm{sd}}/d_{\mathrm{sr}})^2$ and $G_{\mathrm{rd}} = (d_{\mathrm{sd}}/d_{\mathrm{rd}})^2$, respectively.

6.6.1 Source Model

During the broadcast phase-I, the source node transmits its differentially-encoded signals to the corresponding M relay nodes as well as to the destination node. As shown in Fig. 6.7, the source node first channel-encodes the source bits $b(i)$ with the aid of a half-rate RSC code, and then interleaves the channel-encoded bits by using the source-specific interleaver Π_{S}. Furthermore, the interleaved bits are further encoded by a recursive URC[5], and then the coded bits are input to the Differential Phase-Shift Keying (DPSK) mapper block. Finally the DPSK-modulated symbols $c(k)$ are spread with the aid of the source-specific direct sequence spreading code $\xi_{\mathrm{S}}(t)$, having the code length of L_{S} and the chip durations of T_{c}.

Under the condition of frequency-selective Rayleigh fading channels having a maximum number of resolvable paths L_{p}, the time-domain signals $y_m(t)$ received at the mth relay node

[5]The role of the URC is to impose an Infinite Impulse Response (IIR), which improves the achievable iterative decoding performance by efficiently spreading the extrinsic information without requiring a longer interleaver. More specifically, as detailed in [129] a recursive inner code is necessary for the sake of maximizing the interleaver gain and for avoiding the formation of a BER floor, when employing iterative decoding.

and the destination node $y_{\rm sd}(t)$ are expressed, respectively, as

$$y_m(t) = \sqrt{P_{\rm S}G_{\rm sr}}\sum_{k=0}^{N_{\rm M}-1}\sum_{l=1}^{L_{\rm P}} h_{{\rm sr}_m}^{(l)} c(k)\xi_{\rm S}(t-kL_{\rm S}T_{\rm c}) + n_m(t) \quad (6.25)$$

$$y_{\rm sd}(t) = \sqrt{P_{\rm S}}\sum_{k=0}^{N_{\rm M}-1}\sum_{l=1}^{L_{\rm P}} h_{\rm sd}^{(l)} c(k)\xi_{\rm S}(t-kL_{\rm S}T_{\rm c}) + n_{\rm d}(t), \quad (6.26)$$

where $h_{{\rm sr}_m}^{(l)}$ and $h_{\rm sd}^{(l)}$ are the corresponding Rayleigh fading coefficients associated with the lth path, while n_m and $n_{\rm d}$ are the noise components having a zero mean and a variance of $N_0/2$ per dimension. Furthermore, $N_{\rm M}$ indicates the number of modulated symbols. Here, the SNRs at the relay nodes, namely $\text{SNR}_{\rm sr}$, and at the destination node $\text{SNR}_{\rm sd}$ have the relation of $\text{SNR}_{\rm sr} = \text{SNR}_{\rm sd} + 10\log_{10}(G_{\rm sr})$ expressed in dB due to the geometrical power-gain effect [152]. Furthermore, the transmission rate of the phase-I $R_{\rm S}$ is given by $R_{\rm S} = \frac{r}{2}$ bits/symbol, where r is the number of bits/symbol for the DPSK modulation scheme employed.

6.6.2 Relay Model

During the cooperative phase-II, the M relay nodes implement the decode-and-forward CD-STC transmission scheme based on the DLDC-coded STS concept, where each of the M relay nodes use all the M spreading codes according to the DSTS principle [39]. The M spreading codes have a code length of $L_{\rm R}$. Letting the mth relay node be the node of interest, the received signals $y_m(t)$ are first despread by the source node's spreading code $\xi_{\rm S}(t)$, and then iteratively decoded according to the turbo principle. Next, the estimated bits $\hat{b}(i)$ are interleaved and coded by the interleaver $\Pi_{\rm R}$ and the URC encoder, which are common for the associated M relay nodes. Then, the coded bits are mapped to DLDC blocks [89], which is represented by $\boldsymbol{S}^{(k)} = [s_{ij}^{(k)}] \in \mathcal{C}^{M\times M}$, where $s_{ij}^{(k)}$ indicates the ith-row and jth-column element of the codeword $\boldsymbol{S}^{(k)}$ and k is the block index. Here, Q BPSK symbols are multiplexed in each of the codewords $\boldsymbol{S}^{(k)}$. It should be emphasized that the DLDC has the capability of striking a balance between the attainable diversity and multiplexing gain [89], enabling us to generate a set of M codewords while having a multiplexing order Q, without exhibiting a substantial information rate loss in comparison to the theoretical upper bound.[6] This high degree of freedom enables the flexible adjustment of the number of cooperating relay nodes and the resultant phase-II throughput, depending on the rate of change in the network topology and the propagation environment.

Instead of arranging for each relay node to transmit each row of the DLDC codeword

[6]To elaborate a little further, Q BPSK symbols $[v_1^{(k)}, \cdots, v_Q^{(k)}]$ are mapped to or multiplexed into a DLDC codeword $\boldsymbol{S}^{(k)}$ with the aid of the Hermitian dispersion-matrix set $\boldsymbol{A}_1, \cdots, \boldsymbol{A}_Q \in \mathcal{C}^{M\times M}$, which is given by the following equations [89]: $\tilde{\boldsymbol{X}}^{(k)} = \sum_{q=1}^{Q} v_q^{(k)}\boldsymbol{A}_q$, $\boldsymbol{X}^{(k)} = [\boldsymbol{I} - j\tilde{\boldsymbol{X}}^{(k)}][\boldsymbol{I} + j\tilde{\boldsymbol{X}}^{(k)}]^{-1}$ and $\boldsymbol{S}^{(k)} = \boldsymbol{S}^{(k-1)}\boldsymbol{X}^{(k)}$. Increasing the number of multiplexed layers Q leads to a linear increase in the normalized transmission rate R, which may be formulated as $R = Q/M$ for BPSK modulation.

$\boldsymbol{S}^{(k)}$ during M symbol durations in the conventional way [105], here we apply the concept of STS [39] during the phase-II transmissions with the aid of the M spreading codes seen in Fig. 6.7. This operation assists the destination receiver to rearrange the received DLDC space-time codeword, hence eliminating the effect of synchronization errors between the relay nodes, provided that the spreading sequences have ideal cross-correlation properties. To be specific, the mth relay node spreads each component of the mth row in $\boldsymbol{S}^{(k)}$ with the aid of a different spreading code for each component, and transmits the linear combination of the spread symbols in a concerted action with the other relay nodes, as closely synchronized as possible. Therefore, the time-domain signals $y_{\mathrm{rd}}(t)$ received at the destination node during phase-II of Fig. 6.7 is represented by

$$y_{\mathrm{rd}}(t) = \sqrt{\frac{P_{\mathrm{R}}G_{\mathrm{rd}}}{M}} \sum_{k=0}^{N_{\mathrm{B}}-1} \sum_{l=1}^{L_{\mathrm{p}}} \sum_{m=1}^{M} \sum_{j=1}^{M} h_{\mathrm{rd}_m}^{(l)} s_{m,j}^{(k)} \xi_j(t - kL_{\mathrm{R}}T_{\mathrm{c}} - \tau_{m,l}) + n_{\mathrm{d}}(t), \quad (6.27)$$

where $h_{\mathrm{rd}_m}^{(l)}$ is the Rayleigh channel coefficient between the mth relay node and the destination node, associated with the lth path, while $\tau_{m,l}$ is the delay component corresponding to the mth user and the lth path. Furthermore, $\xi_j(t)$ is the normalized signature sequence of the jth spreading code. Note that the corresponding transmission rate R_{R} of phase-II is given by $R_{\mathrm{R}} = Q$ bits/symbol. Similarly to the SR SNR of $\mathrm{SNR}_{\mathrm{sr}}$, the RD SNR of $\mathrm{SNR}_{\mathrm{rd}}$ and the SD SNR of $\mathrm{SNR}_{\mathrm{sd}}$ have the relation of $\mathrm{SNR}_{\mathrm{rd}} = \mathrm{SNR}_{\mathrm{sd}} + 10\log_{10}(P_{\mathrm{R}}G_{\mathrm{rd}}/P_{\mathrm{S}})$ in dB.

At the destination node, the source bits are iteratively detected based on the signals $y_{\mathrm{sd}}(t)$ in (6.26) received during phase-I as well as the signals $y_{\mathrm{rd}}(t)$ in (6.27) received during phase-II, which will be detailed in the following section.

6.6.3 Three-Stage Iterative CDSTS Detector Structure

In this section, we present the destination receiver's structure for our CDSTS scheme, where a three-stage iterative decoding algorithm is employed, as illustrated in Fig. 6.7. For ease of treatment we refer to the DPSK demapper, the URC decoder and the RSC decoder of phase-I as an *inner decoder*, while the DLDC demapper and the URC decoder of phase-II are considered as an *outer decoder*. To be specific, the Soft-Input Soft-Output (SISO) decoders at the receiver iteratively exchange soft extrinsic information L_i^e in the form of Log Likelihood Ratios (LLRs). At the *inner decoder* of Fig. 6.7, the destination receiver decodes the signals broadcast from the source node during phase-I, in order to output the extrinsic LLR $L_1^e(i)$. The same procedure is followed by the relays' iterative decoders seen in Fig. 6.7, with the sole difference that the RSC decoder block of the above-mentioned *inner decoder* can make use of the *apriori* information $L_1^a(i)$ gleaned from the *outer decoder*. The number of inner iterations between the two decoders within the *inner decoder* is represented by I_{Di}.

By contrast, at the *outer decoder* of Fig. 6.7, the destination receiver first despreads the signals, which are received during phase-II. We note here that at this despreading stage the effects of the synchronization errors between the relay nodes are eliminated. Then, the DLDC

demapper produces soft information, where a conventional low-complexity linear Multiple-Input Multiple Output (MIMO) decoder can be employed due to the linearization operation of [89]. Then, the resultant soft information is input to the URC decoder of Fig. 6.7 in order to output the extrinsic LLR $L_3^e(i)$ of the *outer decoder*. Furthermore, the soft LLRs are iteratively exchanged between the *inner decoder* and the *outer decoder*, where the associated number of outer iterations is denoted as I_{Do}. Note that in this three-stage iterative decoding process, the total number of iterations is given by $(I_{\mathrm{Di}} \times I_{\mathrm{Do}})$. Finally, the estimated bits are calculated from the LLRs $L_1^a(i)$ and $L_1^e(i)$ with the aid of the hard-decision operation.

6.7 EXIT chart analysis

In this section we investigate the effects of diverse system parameters on our CDSTS system with the aid of EXIT charts [130]. Here, the number of source nodes allocated to each time slot is set to $N_{\mathrm{C}} = 4$. Let us define here the equivalent transmit SNR ρ as $\rho = (P_{\mathrm{S}} + P_{\mathrm{R}})/N_0$, which relates the total source-power P_{S} plus relay-power P_{R} to the noise-power N_0 at the receiver. Additionally, we consider frequency-selective block-fading Rayleigh channels, where the channel coefficients can be regarded as constant during two DLDC block durations, while the number of resolvable paths L_{p} as well as the number of RAKE combiner fingers ν is four.

First, we investigated the decoding characteristics of the destination receiver of Fig. 6.7 in our CDSTS system, where each source node was assisted by $M = 2$ relay nodes and $Q = 2$ BPSK symbols were multiplexed per each DLDC codeword. We assumed that the each node's geometrical relationship, defined in Section 6.6, was given by $G_{\mathrm{sr}} = 8$ and $G_{\mathrm{rd}} = 2$. Furthermore, the LS(8,4,7) and LS(8,8,7) codes were preassigned for the source and relay nodes, respectively. Fig. 6.8 shows the EXIT curves of both the *inner decoder* and of the *outer decoder*, where the transmit SNR was varied from SNR = 0 dB to 7 dB in 1 dB steps, while satisfying the maximum synchronization delay range of $\tau_{\max} = 3T_{\mathrm{c}}$. Furthermore, a half-rate RSC code having the octally-represented generator polynomials of $(g_{\mathrm{r}}, g) = (7,5)_8$ was employed as our channel encoder at the source nodes. As we can see from Fig. 6.8, upon increasing the transmit SNR, the open EXIT tunnel between the EXIT curves of the *inner* and *outer decoders* becomes wider, potentially leading to a fast convergence of the iterative process, although the Monte-Carlo-simulation based bit-by-bit decoding trajectories are not shown here.

Furthermore, in Fig. 6.9 we investigated the effect of different modulation orders for both the source and relay nodes at the equivalent transmit SNR of 4 dB, where we considered DBPSK, DQPSK, 8–DPSK and 16–DPSK modulation schemes for the source nodes as well as the DLDC multiplexing factors of $Q = 1$, 2, 3 and 4 for the relay nodes. Here, we also employed Gold codes as the benchmark spreading codes of the LS codes, noting that Gold codes constitute well-known spreading sequences having relatively good asynchronous cross-correlation properties. Observe in Fig. 6.9 that our LS code-based CDSTS scheme created

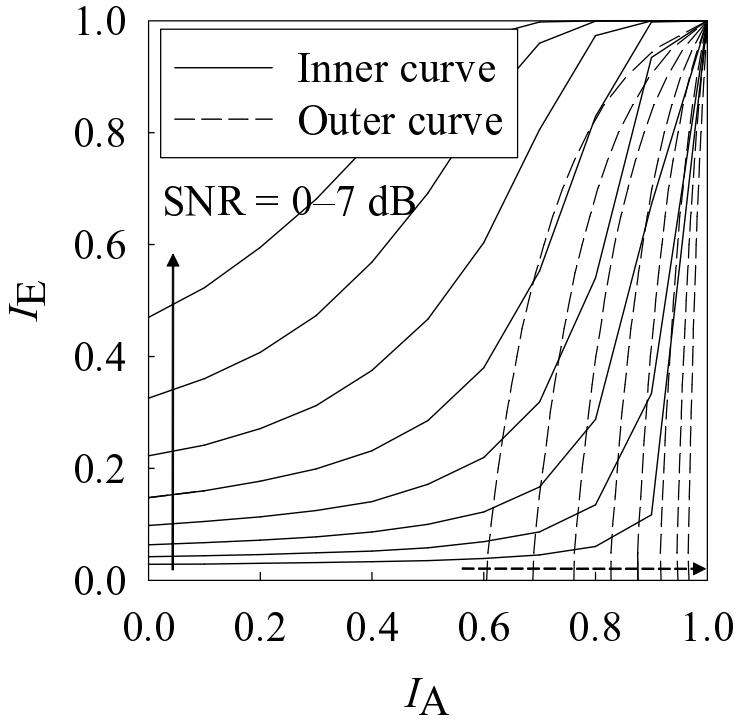

Figure 6.8: The EXIT curves of the *inner decoder* and *outer decoders* of our CDSTS system seen in Fig. 6.7, supporting $N_C = 4$ source nodes in each time slot and employing DQPSK modulation at each source nodes and BPSK multiplexing associated with $Q = 2$ per DLDC block at the corresponding $M = 2$ relay nodes. The equivalent transmit SNR was varied from SNR = 0 dB to 7 dB, while the maximum synchronization delay was $\tau_{max} = 3T_c$. All other system parameters were summarized in Table 6.2.

open tunnels between the inner and outer EXIT curves in the cases of low modulation orders, such as DBPSK, DQPSK and 8–DPSK as well as DLDC multiplexing factors of $Q = 1$, 2 and 3. By contrast, the employment of 16–DPSK or of $Q = 4$ gives rise to the closure of the EXIT tunnel. On the other hand, as shown in Fig. 6.9, the EXIT curves of the Gold code-based CDSTS arrangement did not exhibit an open tunnel for every combination of the inner EXIT curve and the outer EXIT curve. This is because the LS codes' IFW successfully eliminated the effects of the synchronization errors between the relay nodes, while suppressing the MUIs imposed by the other source and relay nodes, also having synchronization errors. To be specific, upon increasing the modulation order for the source or the relay nodes, the corresponding EXIT tunnel becomes narrower or closed for both the LS and Gold spreading codes, implying that as expected, a higher SNR is required to attain a good BER performance in comparison to the lower modulation orders. Additionally, we note that the outer decoder's EXIT curves in Figs. 6.8 and 6.9 did not emerge from the origin of the coordinate system at $(I_A, I_E) = (0, 0)$, which is different from that of a typical serially-concatenated turbo-coded system. This is because the source-relay-destination links of our CDSTS system seen in Fig. 6.7 may be viewed as a parallel-concatenated branch, rather than that of the classic

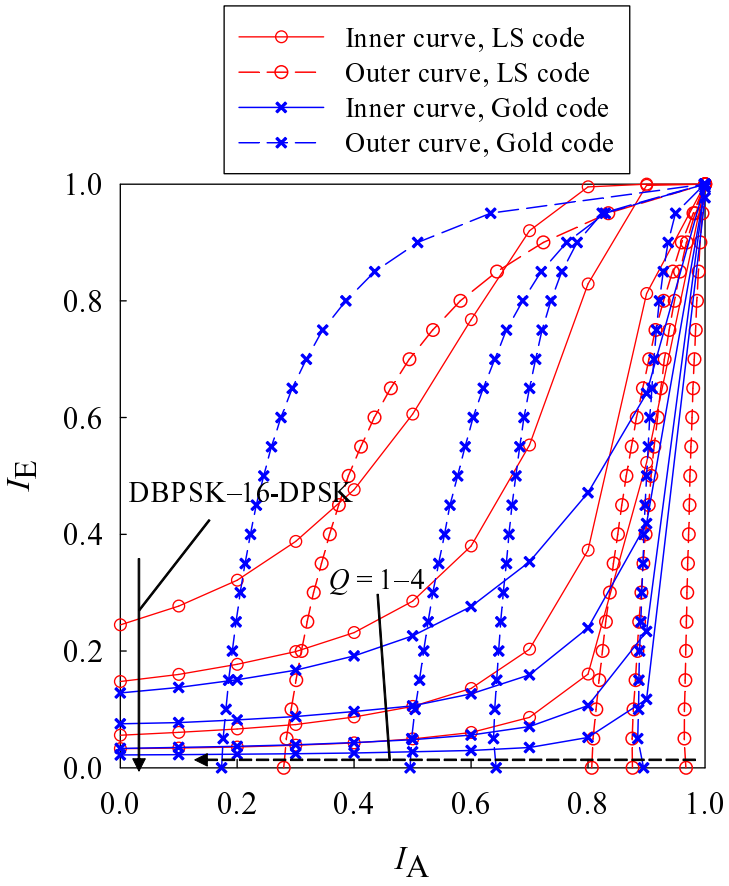

Figure 6.9: The EXIT curves of the *inner* and *outer decoders* of our CDSTS system seen in Fig. 6.7, comparing different modulation schemes, such as DBPSK, DQPSK, 8–DPSK and 16–DPSK for the source nodes as well as for DLDC multiplexing factors of $Q = 1$, 2, 3 and 4 for the relay nodes, while an equivalent transmit SNR = 4 dB and a maximum synchronization delay of $\tau_{\max} = 3T_c$. All other system parameters were summarized in Table 6.2.

serially-concatenated turbo coding scheme. Hence the corresponding inner decoder's EXIT curve acted similarly to that of parallel-concatenated turbo coding, which does not emerge from the point of $(I_A, I_E) = (0, 0)$.

6.8 Performance Results

In this section we provide performance results for the CDSTS system. The basic system parameters employed in our simulations are listed in Table 6.2, which we derived with the aid of our EXIT chart analysis of the previous section.[7] A DQPSK modulation scheme and an interleaver Π_S having the length of 20 000 bits were employed at the N_C source nodes, each of which was assisted by $M = 2$ relay nodes employing a DLDC multiplexing factor of

[7]More specifically, in our EXIT-chart aided system design, we jointly optimized the related parameters, such as the source node's modulation alphabet size, the relay nodes M as well as the number of multiplexing order Q of DLDCs.

Table 6.2: Basic system parameters of the distributed turbo-coded CDSTS scheme obeying the architecture of Fig. 6.7

Source node	
Number of source nodes per time slot N_C	4
Modulation scheme	DQPSK
Interleaver block length of Π_S	20 000 bits
Spreading codes	LS codes of LS(8,4,7)
Outer channel code	RSC with generator polynomials $(7,5)_8$
Precoder code	URC $G(D) = 1/(1+D)$ with a delay element D
Power allocation P_S	0.5
Relay node	
Number of relay nodes per source node M	$M = 2$
Modulation scheme	BPSK-modulated DLDC [89]
DLDC's multiplexed factor Q	$Q = 2$
Interleaver block length of Π_R	10 000 bits
Spreading codes	LS codes of LS(8,8,7)
Precoder code	URC $G(D) = 1/(1+D)$ with a delay element D
DPSK demapper	Soft demapper of [153]
Number of iterations I_R	5
Power gain of SR links G_{sr}	8
Power allocation P_R	0.5
Destination node	
DPSK demapper	Soft demapper of [153]
DLDC demapper	SISO-MMSE detector [154]
Number of inner iterations I_{Di}	2
Number of outer iterations I_{Do}	5
Power gain of RD links G_{rd}	2

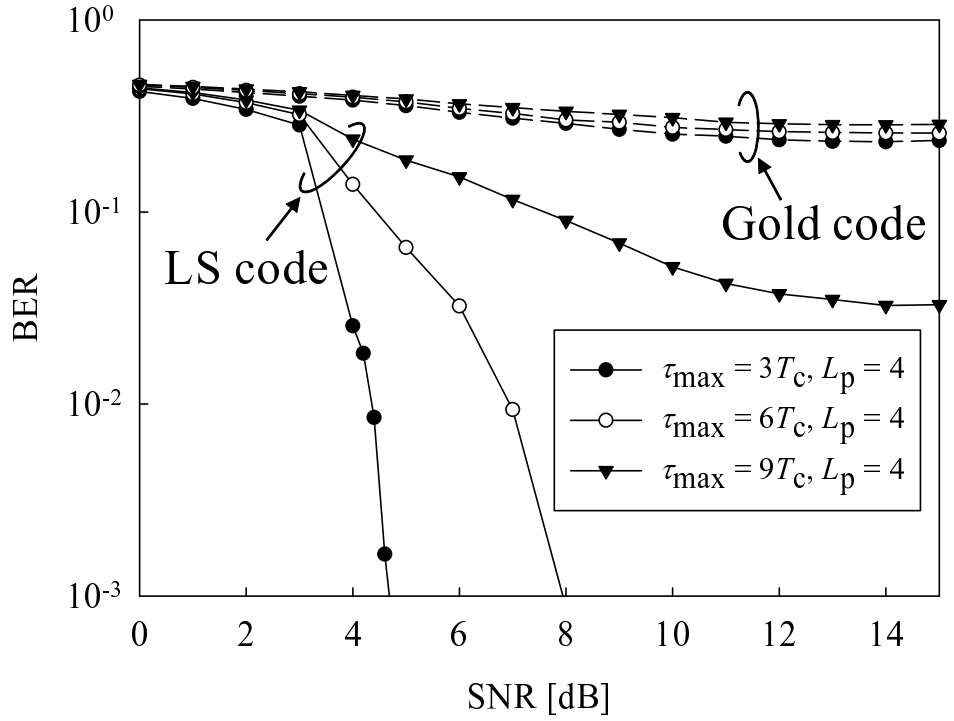

Figure 6.10: Achievable BER performance of our LS code-aided CDSTS and the Gold code-aided CDSTS schemes, both obeying the architecture of Fig. 6.7. Here, we compared the maximum synchronization delays of $\tau_{max} = 3T_c$, $6T_c$ and $9T_c$, while having $L_p = 4$ delay spread-induced paths. All other system parameters were summarized in Table 6.2.

$Q = 2$ and an interleaver Π_S having a length of 10 000 bits. The number of iterations at each relay node I_R was set to $I_R = 2$, while the number of inner and outer iterations at the destination node was given by $I_{Di} = 2$ and $I_{Do} = 5$, respectively. Furthermore, the maximum synchronization delay τ_{max} was set to $\tau_{max} = 3T_c$.

Here, the total transmission rate of our CDSTS R_{total} was given by

$$R_{total} = L_S / \left(\frac{L_S}{R_S} + \frac{L_R}{R_R} \right) \quad \text{[bits/symbol]}, \tag{6.28}$$

where L_S and L_R are the code lengths of the spreading codes during phase-I and phase-II, respectively, and the rate R_{total} was normalized by the phase-I code length L_S. Based on these relationships, the transmission rate of our CDSTS was given by $R_{total} = 0.54$, while for instance that of the DBPSK-modulated non-cooperative scenario was $R_S = 0.5$.

Fig. 6.10 shows the achievable BER performance of our LS code-aided and Gold code-aided CDSTS schemes, where the maximum synchronization delays τ_{max} were set to $\tau_{max} = 3T_c$, $6T_c$ and $9T_c$, while having $L_p = 4$ resolvable paths and $\nu = 4$ RAKE combiner fingers. It can be seen from Fig. 6.10 that the BER curve of our LS code-based CDSTS system recorded for the case of $\tau_{max} = 3T_c$ exhibited a good BER performance, as expected on the basis of the EXIT chart analysis of Fig. 6.8 in the previous section. On the other hand, for

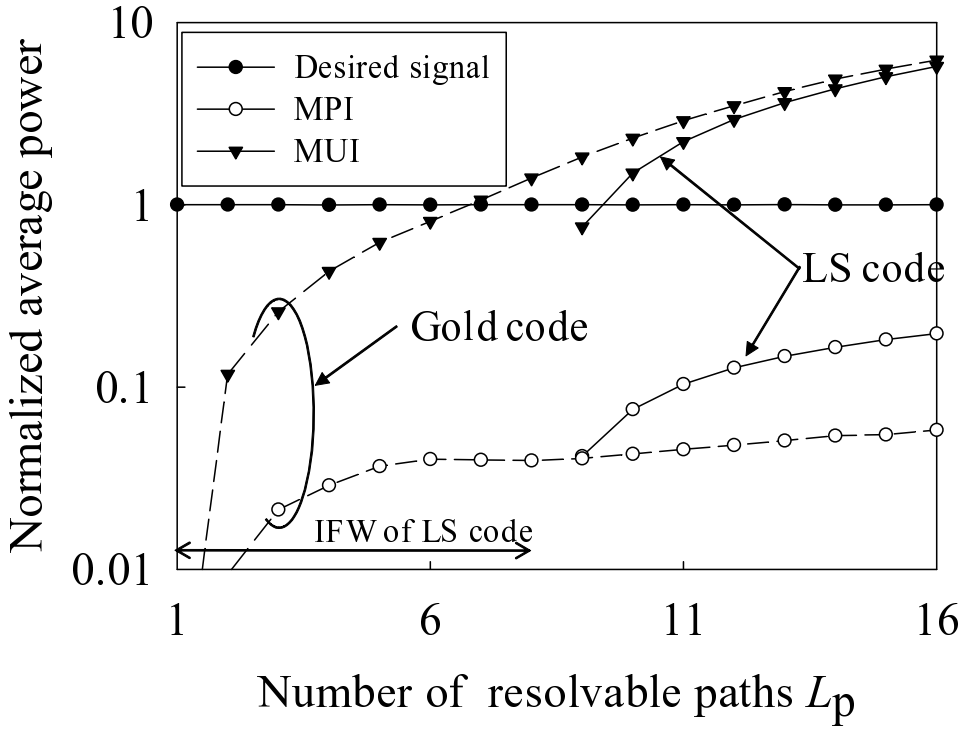

Figure 6.11: Effect of the number of resolvable paths L_p on the average power of the desired signal, on the MPI and on the MUI. All other system parameters were summarized in Table 6.2.

the high-delay scenarios of $\tau_{max} = 6T_c$ and $9T_c$, where the sum of the maximum delay τ_{max} and the delay spread $(L_p - 1)$ is higher than the LS code's IFW, the corresponding BER was substantially deteriorated due to the residual MUIs and MPIs, although it was still better than that of the Gold codes for any of the delays considered.

Next, in Fig. 6.11 we evaluated the effects of both the MPI and of the MUI during the cooperative phase-II, assuming that the number of resolvable paths L_p was varied from $L_p = 1$ to $L_p = 16$, while maintaining a maximum delay of $\tau_{max} = 0$ for the sake of simplicity. We note here that the $(N_C \times M)$ relay nodes were quasi-synchronously transmitting their signals. Fig. 6.11 shows the average powers of the desired signals, of the MPI and of the MUI, while comparing the performance of LS codes and Gold codes. Firstly, it was confirmed that our LS code-aided CDSTS was capable of perfectly suppressing both the MUI and the MPI, provided that the delay-spread associated with the $(L_p - 1)$ delayed paths was within the designed IFW of W_0, while the Gold code-aided system suffered from their residual MUI and MPI owing to the non-zero auto-correlation and cross-correlations.

Finally, we investigated a more practical scenario, namely that of employing the shorter interleaver lengths of $\Pi_S = 2\,000$ bits and of $\Pi_R = 1\,000$ bits. Here we assumed quasi-static Rayleigh fading environments. Furthermore, the LS code of LS(8,16,7) was employed for the case of $M = 3$ relay nodes, in order to generate the required number of LS codes

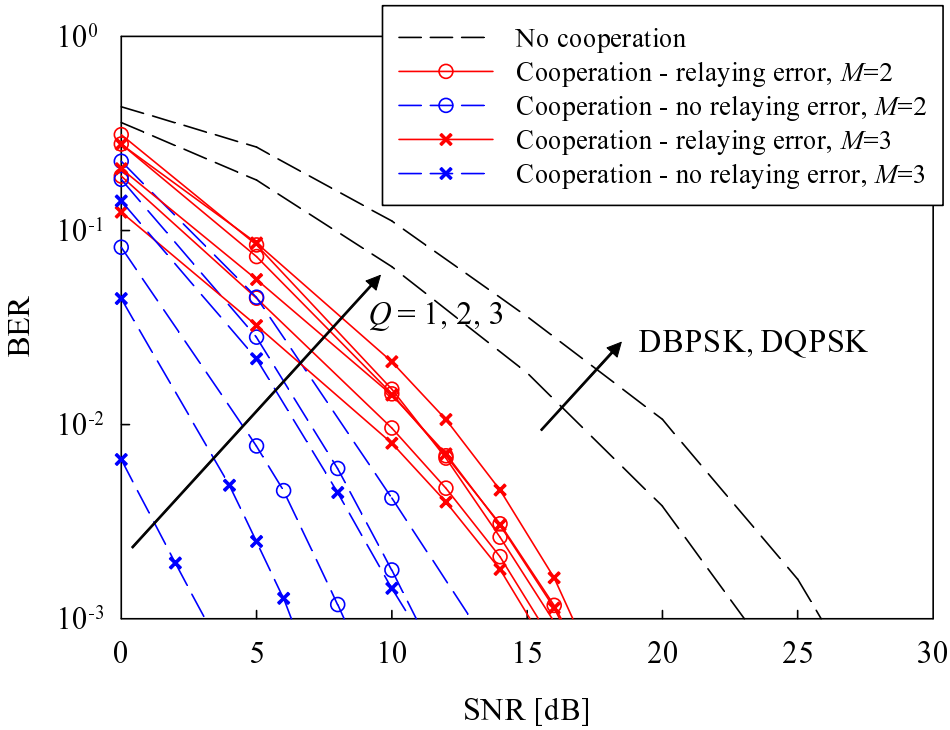

Figure 6.12: Achievable BER performance of our LS code-aided CDSTS scheme obeying the architecture of Fig. 6.7, employing $M = 2$ and 3 cooperating nodes for each source node, where the DLDC's multiplexing factor Q is changed from $Q = 1$ to $Q = 3$. We also plotted here the corresponding BER curves of our system suffering from no relaying errors, as well as those of non-cooperative system having the modulations of DBPSK and DQPSK. All other system parameters were summarized in Table 6.2.

having an IFW of 7 chip durations. It is predicted that since no *time diversity gain* can be exploited in this block-fading scenario, the spatial diversity order, determined by the number of relay nodes dominantly affects the attainable performance improvement. Hence our multi-relay-assisted DTC has the potential to exhibit a better performance than those of the conventional single-relay-assisted DTCs [106, 108, 113, 152]. Fig. 6.12 shows the achievable BER performance of our LS code-aided CDSTS scheme, employing $M = 2$ and $M = 3$ cooperating nodes, respectively, where the DLDC's multiplexing factor Q was varied from $Q = 1$ to $Q = 3$. Additionally, we plotted here the BER curves of our benchmark CDSTS system assuming the idealized scenario of having no decoding errors at the relay nodes, in order to benchmark the effects of the relays' decoding errors and their error propagation. Observe in Fig. 6.12 that while the proposed CDSTS system achieved a better performance than the non-cooperative scheme as a benefit of its cooperative spatial diversity gain, it was severely degraded by the relays' decoding errors, when compared to those of the no-relaying error scenario. Therefore, it was found that in order to exploit the designed diversity-multiplexing tradeoff, it is important to overcome the effects of error propagation by employing Cyclic Redundancy Checks (CRC) for the sake of identifying the relays' decoding errors, or by in-

troducing the concept of [155], where the relays' decoding errors are compensated for at the destination receiver by exploiting each relay's average BER estimated for the received LLRs. Furthermore, it can also be seen that upon increasing the number of relay nodes from $M = 2$ to $M = 3$, the potential diversity gain improves for each multiplexing factor Q, provided that the relays' decoding errors are successfully eliminated.

6.9 Chapter Conclusions

In this chapter we firstly proposed a practical cooperative differential space-time diversity protocol, where neither channel estimation nor symbol-level synchronization is required at the nodes. More specifically, the source node transmits differentially encoded symbols to the relay nodes and the destination node at the broadcast phase, and then a cooperating cluster transmits the STS-encoded symbols with the aid of LS codes, having the IFW at the cooperative phase. As a result, cooperative space-time diversity is achieved with the aid of our LS code-based STS scheme relying on cooperating asynchronous nodes, while the destination node simultaneously decodes both the direct SD signal as well as the relayed STS-encoded symbols based on the low-complexity correlation operation. Our simulation results of Section 6.4 demonstrate that unlike the previously-proposed CDSTC of [116], the proposed CDSTS scheme is capable of combating the effects of asynchronous transmissions, provided that the maximum synchronization delay of the relay nodes is within the width of the IFW. Furthermore, our CDSTS scheme is capable of gleaning path diversity gain in addition to space-time diversity gain with the aid of RAKE combining at the destination receiver.

Next, we extended the above-mentioned cooperative transmission protocol to exploit the advantages of asynchronous cooperation, non-coherent detection and multi-relay-assisted DTC. The DLDC scheme employed for our cooperative STC has the potential of adapting our CDSTS arrangement, such as the number of relay nodes and the transmission rate, depending on the network's topology and on the propagation environment encountered. Our simulation results of Section 6.8 demonstrated that the proposed LS code-aided CDSTS scheme is capable of both achieving spatial diversity and turbo processing gains aided time-diversity, while combating the effects of the relays' synchronization errors and CSI estimation errors.

Table 6.3: Summary of the uncoded LS-code and Gold-code assisted CDSTS schemes as well as the uncoded cooperative DSTSK scheme, employing the system parameters of 6.1.

	LS-coded CDSTS	**Gold-coded CDSTS**	**Cooperative DSTSK**
Schematic	Fig. 6.1	←	Fig. 5.3
Relaying scheme	amplify-and-forward	amplify-and-forward	CRC-activated selective decode-and-forward
CSI	No CSI	←	←
IAS	Relaxed (within IFW of LS code)	Symbol-level	Symbol-level
Cooperative STC structure	G_4-OSTBC	G_4-OSTBC	DSTSK$(4, 1, 4, 2)$
Complexity[a]	$\frac{8M}{\log_2 \mathcal{L}} + \text{comp}_{\text{despread}}$	$\frac{8M}{\log_2 \mathcal{L}} + \text{comp}_{\text{despread}}$	$\frac{TQ(4M+6\mathcal{L})+4\mathcal{L}'+2bQ\mathcal{L}}{\log_2(Q\cdot\mathcal{L})}$
Detector	ML detector of Eq. (6.24)	ML detector of Eq. (6.24)	ML detector of Eq. (5.28)
Performance[b,c]	23.1 dB	error floor	error floor

[a] The value of '$\text{comp}_{\text{despread}}$' represents the complexity imposed by the despreading operation at the DN, which is shown in Fig. 6.1.

[b] $M = 4$ RNs as well as maximum synchronization delay of $\tau_{\max} = 7T_c$ were assumed.

[c] Performance is given by the SNR value required for achieving BER $= 10^{-5}$.

Chapter 7

Conclusions and Future Research

In this concluding chapter, we will provide our overall summary and conclusions in Section 7.1. Then several research topics concerning potential future studies will be presented in Section 7.2.

7.1 Summary and Conclusions

In this thesis, we have provided detailed MIMO transceiver designs employing the novel STSK encoding concept for enhancing their achievable performance. More specifically, we proposed the diverse STSK arrangements, investigating the pros and cons of coherent-versus-differential, synchronous-versus-asynchronous and co-located-versus-distributed MIMO techniques.

- **Chapter 1:** In Chapter 1, we provided a generic overview of MIMO techniques, commencing with their historical development in Tables 1.1–1.7. More specifically, in Section 1.1 we introduced the MIMO channels and our block-based MIMO system model. In Section 1.2 we described four different co-located MIMO functions, namely the spatial diversity, spatial multiplexing, SDMA and beamforming concepts, as shown in Fig. 1.1. Section 1.3 detailed the diversity-versus-multiplexing tradeoffs. Furthermore, in Section 1.4 we discussed the cooperative MIMO concept, in contrast to the above-mentioned co-located MIMO arrangements. Finally, Section 1.5 highlighted the organization as well as the main findings of this thesis.

- **Chapter 2 [1, 11]:** In Chapter 2, the novel STSK concept invoking dispersion-matrix activation was proposed in the context of co-located MIMO systems employing coherent detection. This design philosophy facilitated the full exploitation of the space-

and time-dimensions, hence had the potential of outperforming other classic MIMO arrangements, such as OSTBCs, BLAST, SM and SSK schemes. Furthermore, Since the STSK receiver does not suffer from multiplexing-induced ICI, which is an exclusive benefit of the STSK codeword's specific structure, the employment of low-complexity single-stream-based optimal ML detection becomes realistic at the receiver.

In Section 2.2 we briefly reviewed the family of conventional MIMO arrangements, such as the OSTBCs of Section 2.2.1, the SDM scheme of Section 2.2.2, the LDCs of Section 2.2.3 and the SM/SSK scheme of Section 2.2.4, while quantifying their computational complexity detected by the ML algorithm in each section. Table 7.1 of this chapter summarizes the diversity gain/order, complexity and throughput of these MIMO schemes, where the complexity was evaluated in terms of the number of real-valued multiplications required for implementing ML detection at each scheme's detector. It was shown in Table 7.1 that the SDM and the SM/SSK schemes are capable of achieving a high normalized throughput, which increases upon increasing the number of transmit AEs M, although the maximum achievable diversity order relies only on the number of receiver AEs N. By contrast, while the OSTBC are capable of attaining the maximum achievable diversity order of $(M \cdot N)$, the achievable normalized transmission rate/throughput is limited by the constellation size $\mathcal{L}$, since no multiplexing gain is attained. The LDCs are capable of striking a flexible tradeoff between the achievable diversity and multiplexing gains, which include the OSTBCs and the SDM scheme as special cases. However, similarly to the SDM scheme, the complexity of the LDCs includes the exponential component of $\mathcal{L}^Q$ in Table 7.1, where the employment of exhaustive ML search may be unrealistic for high values of Q. In order to expound a little further, in Table 7.2 we exemplified the complexity and the SNR recorded at BER = 10^{-4} for the G_3 OSTBCs having (M, N) = (3,2) AEs, the SDM scheme having (M, N) = (3,2) AEs, the SM scheme having (M, N) = (4,2) AEs and for the CSTSK$(3, 2, 2, 8)$ scheme, which exhibited the same normalized transmission rate of $R = 3$ bits/symbol. Although the CSTSK scheme's complexity was higher than that of other schemes in this scenario, this is because of an increased diversity gain. It may be seen in Table 7.2 that the CSTSK scheme achieved the highest BER performance, as the benefit of its capability of striking a flexible rate-diversity tradeoff.

Section 2.3 proposed the new CSTSK concept in the context of an uncoded scenario. More specifically, in Section 2.3.1 the CSTSK transmitter's bit-to-space-time-symbol mapping scheme was described in Fig. 2.5 and Eq. (2.20), while its step-by-step algorithmic explanations were provided in Algorithm 2.1. In this scheme, one out of Q dispersion matrices is activated according to having $B_2 = \log_2 Q$ input bits, while the activated matrix spreads by the $\mathcal{L}$-PSK/QAM symbol conveying $B_1 = \log_2 \mathcal{L}$ bits. We also demonstrated that our CSTSK arrangement subsumes the SM/SSK scheme by employing the specific dispersion matrix set, which was formulated in Eq. (2.23). To be specific, the explicit benefits of our CSTSK scheme can be found in Table 7.1. For

Table 7.1: Diversity, rate and complexity for various coherently-detected MIMO arrangements, i.e. the OSTBCs, the SDM scheme, the LDCs, the SM/SSK scheme, the CSTSK scheme and the ACSTSK scheme.

Scheme	Criterion	Diversity	Complexity	Rate
OSTBC	Section 2.2.1	$M \cdot N$	$\mathcal{O}\left(\frac{MN\mathcal{L}}{\log_2 \mathcal{L}}\right)$	$\leq \log_2 \mathcal{L}$
SDM	Section 2.2.2	N	$\mathcal{O}\left(\frac{N\mathcal{L}^M}{\log_2 \mathcal{L}}\right)$	$M \log_2 \mathcal{L}$
LDC	Section 2.2.3	$N \cdot \min(M,T)$	$\mathcal{O}\left(\frac{NT\mathcal{L}^Q}{\log_2 \mathcal{L}}\right)$	$Q \log_2 \mathcal{L}/T$
SM/SSK	Section 2.2.4	N	$\mathcal{O}\left(\frac{MN\mathcal{L}}{\log_2(M\cdot\mathcal{L})}\right)$	$\log_2(M \cdot \mathcal{L})$
CSTSK	Section 2.3.1	$N \cdot \min(M,T)$	$\mathcal{O}\left(\frac{MNT^2Q\mathcal{L}}{\log_2(Q\cdot\mathcal{L})}\right)$	$\log_2(Q \cdot \mathcal{L})/T$
ACSTSK	Section 2.3.2	$N \cdot \min(M,T)$	$\mathcal{O}\left(\frac{NT^2Q\mathcal{L}}{\log_2(Q\cdot\mathcal{L})}\right)$	$\log_2(Q \cdot \mathcal{L})/T$

example, the CSTSK arrangement is capable of striking a flexible rate-diversity tradeoff, hence having the potential of achieving a transmit diversity gain, unlike the BLAST, SM and SSK schemes. Additionally, the normalized throughput of the CSTSK scheme may be increased without an exponential increase in the ML-detection complexity, while those of the OSTBCs are limited to less than unity.

Additionally, in Section 2.3.2 we conceived the modified CSTSK arrangement, which was termed as the ACSTSK scheme, where each dispersion matrix of the CSTSK scheme was constrained to have a sparse structure, allowing us to dispense with symbol-level IAS. The ACSTSK scheme's dispersion matrices were also exemplified in Eq. (2.24). In Section 2.3.3 the optimal single-stream-based ML detection of Eq. (2.32) was proposed. Then, Section 2.3.4 characterized the computational complexity imposed by the CSTSK's ML detector, where the complexity may be reduced upon increasing the channel's coherence time τ. In Section 2.3.5, it was shown that the maximum achievable diversity order of the CSTSK scheme was represented by $N \cdot \min(M,T)$, which was derived with the aid of the classic Chernoff upper bound formulated in Eq. (2.38).

The design guidelines of our CSTSK scheme relying on the parameters $(\mathcal{L}, M, N, T, Q)$ as well as on the Q dispersion matrices $\boldsymbol{A}_q$ $(q = 1, \cdots, Q)$ are summarized as follows:

- The values of (M, N) specify the number of transmit and receive AEs.
- The values of $(\mathcal{L} \cdot Q, T)$ are chosen so as to satisfy the desirable rate-diversity tradeoff characterized by the rate of $R = \log_2(Q \cdot \mathcal{L})/T$ and the maximum attainable diversity order of $N \cdot \min(M,T)$. We note that several combinations of $(\mathcal{L}, Q)$ are possible at a given throughput, which impose different complexity and exhibit a different BER performance.
- For all the potential $(\mathcal{L}, Q)$ combinations, the Q dispersion matrices $\boldsymbol{A}_q$ $(q =$

Table 7.2: Complexity and SNR recorded at BER = 10^{-4} for the G_3 OSTBC having $(M, N) = (3,2)$ AEs, the SDM scheme having $(M, N) = (3,2)$ AEs, the SM scheme having $(M, N) = (4,2)$ AEs and for the CSTSK$(3, 2, 2, 8)$ scheme, which exhibited the normalized transmission rate of $R = 3$ bits/symbol.

Scheme	Complexity	SNR recorded for BER = 10^{-4}
G_3-OSTBC	≈128	21.0 dB
SDM	≈16	22.1 dB
SM	≈5	22.1 dB
CSTSK	≈256	16.7 dB

$1, \cdots, Q$) are calculated based on the criterion of DCMC capacity maximization, which was detailed in Section 2.6.

– The best set of $(\mathcal{L}, Q)$ is identified by comparing the BER or EXIT curves corresponding to all the potential $(\mathcal{L}, Q)$ combinations.

Furthermore, in Section 2.4 the three-stage concatenated turbo STSK concept was introduced as the extension of the uncoded CSTSK arrangement of Fig. 2.5. The architectural overview of the turbo-coded STSK scheme was provided in Section 2.4.1 and Fig. 2.7, while in Section 2.4.2 the SISO MAP detector was formulated as Eq. (2.42). Then, Section 2.5 defined the DCMC capacity of our CSTSK scheme, as represented by Eq. (2.44). Moreover, the dispersion-matrix design criterion of our CSTSK scheme was provided in Section 2.6, where the DCMC capacity was adopted as the optimization criterion to be maximized.

In Section 2.7 we characterized the performance of both uncoded and turbo coded scenarios, where the basic system parameters employed for the simulations were listed in Tables 2.5 and 2.6. Finally, in order to consider practical environments, the typical interference-limited scenario was considered in Section 2.7.3, where we varied the number of interfering users.

- **Chapter 3 [1, 11]:** In Chapter 2, coherently-detected co-located MIMO scenarios were considered, assuming that perfect CSI is available at the receiver. However, typically a high complexity is imposed by the MIMO channels' estimation, while also imposing a high pilot overhead. Furthermore, the resultant CSI estimation errors at the receiver may give rise to severe performance degradation. Inspired by the CSTSK scheme of Fig. 2.5 conceived in Chapter 2 and by the DSTC scheme, in Chapter 3 we proposed a novel DSTSK scheme, which dispenses with CSI estimation at the DSTSK receiver,

while retaining the fundamental benefits of the CSTSK scheme.

Section 3.1 briefly described the differential encoding and decoding operation for single-antenna-aided systems. Section 3.2 reviewed the classic DSTBC schemes designed for co-located MIMO systems, where we considered the differential unitary modulation concept of Eq. (3.6) and the ML detection philosophy formulated in Eq. (3.10). More specifically, in Section 3.2.1 we described DOSTBCs, which were developed from the coherently-detected OSTBCs seen in Section 2.2.1. Then, in Fig. 3.2 of Section 3.2.2 DLDCs were introduced, where the LDC scheme of Section 2.2.3 was extended to include differential USTM schemes with the aid of the Cayley transform of Eq. (3.17). Hence, similarly to the LDCs, the DLDCs are also capable of striking a flexible diversity- and multiplexing-gain tradeoff, owing to the fact that the Q dispersion matrices were linearly combined with the Q real-valued modulated symbols, as summarized in Algorithm 3.1.

In Section 3.3, we proposed the novel DSTSK encoding scheme of Fig. 3.5 and its architectural details were summarized in Algorithm 3.2. The DSTSK scheme was developed from the CSTSK scheme of Fig. 2.5, where dispersion-matrix activation is followed by the Cayley transform and the differential unitary encoding operation, as portrayed in Fig. 3.5. Since the linearized signal model of Eq. (3.25) exhibits a structure similar to that of the CSTSK scheme of Fig. 2.5 and of Eq. (2.25), the single-stream-based optimal ML detector developed for the CSTSK scheme may also be invoked for the DSTSK scheme. Furthermore, Section 3.3.1 conceived the ADSTSK scheme, which dispenses with symbol-level IAS, similarly to the ACSTSK scheme of Section 2.3.2. In the ADSTSK scheme, the 'diagonal-structure' constraint of Eq. (3.29) was imposed by the dispersion matrices, although this may degrade the achievable performance in comparison to the unconstrained DSTSK scheme, which is a consequence of having a the limited search space for the dispersion matrices. In Section 3.3.2 the computational complexity imposed by the DSTSK's single-stream-based ML detector was characterized. Section 3.4 considered the three-stage concatenated turbo DSTSK scheme of Fig. 3.6, as the extension of the uncoded DSTSK scheme of Fig. 3.5, aiming for achieving a near-capacity performance. Section 3.5.1 described the dispersion matrix design criterion employed for our DSTSK scheme. More specifically, the dispersion matrices were optimized according to the rank- and determinant criterion, which maximizes the coding gain expressed in Eq. (3.5.1), while maintaining the maximum achievable diversity order.

Section 3.5 characterized our DSTSK scheme's performance both for the uncoded and turbo coded scenarios in Sections 3.5.2 and 3.5.3, respectively. The basic system parameters employed for our simulations were listed in Tables 3.2 and 3.3. In Table 7.3, we summarized the BER performance characterized for the uncoded DSTSK scheme of Fig. 3.5, where we varied the diverse DSTSK system parameters. Section 3.5.3 characterized the achievable BER and the EXIT charts of our three-stage concate-

Table 7.3: BER summary of the DSTSK family obeying the architecture of Fig. 3.5, considering the basic system parameters listed in Table 3.2.

DSTSK$(M, N, T = M, Q)$	BER
Effects of the value of M	Figs. 3.11 and 3.15
Effects of the value of N	Fig. 3.24
Effects of the value of Q	Figs. 3.9, 3.10 and 3.15
Effects of fading	Fig. 3.14
Comparison between DSTSK and ADSTSK	Figs. 3.15 and 3.23
Comparison with the DOSTBC scheme	Fig. 3.12
Comparison with the CSTSK scheme	Fig. 3.23
Comparison with the SM and DLDC schemes	Fig. 3.13

nated DSTSK scheme of Fig. 3.6. More specifically, in Fig. 3.20 the DSTSK$(2, 2, 2, 4)$ scheme exhibited an infinitesimally low BER at SNR = 3.5 dB, as predicted from the corresponding EXIT chart of Fig. 3.19. This was 1.1 dB away from the achievable limit, which was estimated from the area property of the inner code's EXIT curve. It was also found in Fig. 3.22 that the performance difference between the three-stage concatenated DSTSK and ADSTSK schemes of Fig. 3.6 became lower than that of its uncoded counterparts of Fig. 3.5. Finally, Table 3.6 provided the overall summary of the uncoded DSTSK, ADSTSK, CSTSK and ACSTSK schemes, comparing their schematics, dispersion-matrix structures, computational complexity and achievable BER performance.

- **Chapter 4 [10, 15]:** In Chapter 4, we further generalized the STSK concept proposed in Chapter 2, so that P out of Q dispersion matrices are activated, rather than a single one out of Q dispersion matrices, which was the case for the CSTSK scheme. Owing to this generalization, the proposed GSTSK arrangement constituted a flexible ST framework, hence subsuming diverse MIMO arrangements, such as the OSTBCs, the BLAST scheme, the LDCs, the SM, the SSK and the CSTSK schemes, as depicted in Fig. 4.1. Another contribution of this chapter was that we derived the unified capacity and theoretical BER bounds for our GSTSK scheme. As mentioned above, the GSTSK scheme subsumes many MIMO arrangements, therefore these capacity and BER bounds serve as the unified limits.

  Section 4.2 proposed the system model of our GSTSK scheme obeying the architecture of Fig. 4.2. As compared to the system model of the CSTSK scheme of Fig. 2.5, the

GSTSK scheme linearly combines P out of Q dispersion matrices with P PSK/QAM symbols spreading them to all the ST dimension available. Therefore, the GSTSK scheme is capable of increasing the transmission rate, at the cost of an increased ICI. Additionally, the step-by-step algorithmic operations of the GSTSK scheme's transmitter were detailed in Algorithm 4.1.

In Section 4.2.2 we demonstrated that the GSTSK scheme subsumes diverse MIMO arrangements, which is achieved by appropriately setting the GSTSK scheme's parameters (M, N, T, Q, P) and dispersion matrices $\boldsymbol{A}_q$ $(q = 1, \cdots, Q)$. Specifically, Section 4.2.2.2 showed that our GSTSK scheme is identical to LDCs, when all the Q dispersion matrices are activated, i.e. for $P = Q$. By contrast, in Section 4.2.2.5 the GSTSK scheme having $P = 1$ was shown to be equivalent to the CSTSK scheme of Fig. 2.5. As shown in Chapter 2, LDCs include OSTBCs and the BLAST scheme, while the CSTSK scheme subsumes the SM/SSK schemes. Hence, our GSTSK scheme was found to serve as the unified MIMO arrangement, as shown in Fig. 4.1.

In order to design our GSTSK architecture, the related six parameters, namely ($\mathcal{L}$, M, N, T, Q, P) as well as the Q dispersion matrices $\boldsymbol{A}_q$ $(q = 1, \cdots, Q)$ are determined according to the following steps.

- The values of (M, N) represent the number of transmit and receive AEs.
- The values of $(\mathcal{L}, T, Q, P)$ are chosen so as to satisfy the desirable rate-, diversity- and complexity-tradeoffs characterized by the rate of $R = \frac{\log_2 f(Q,P) + P \log_2 \mathcal{L}}{T}$, the maximum attainable diversity order of $N \cdot \min(M, T)$ and the computational complexity of $[4MNT^2Q + (4NTP + 2NT)f(Q, P)\mathcal{L}^P/B]$.
- The Q dispersion matrices $\boldsymbol{A}_q$ $(q = 1, \cdots, Q)$ are designed based on the DCMC-capacity maximization criterion or the rank- and determinant-criterion.

Since in practice we may have several potential options for ($\mathcal{L}$, M, N, T, Q, P), their performance comparison is required in order to choose the most appropriate set.

Section 4.3.1 presented the optimal ML detector of Eq. (4.13) designed for the uncoded GSTSK scheme, which suffers from P number of ICI-contributions, because P substreams are multiplexed. Furthermore, the corresponding computational complexity was characterized by Eq. (4.14), which contains an exponentially increasing complexity component associated with the P multiplexed substreams. Then, in Section 4.3.2 we also introduced the SISO-MAP detector of the GSTSK scheme, as formulated in Eq. (4.16).

The DCMC capacity of our GSTSK scheme was defined in Eq. (4.18) of Section 4.4. For example, this unified capacity limit was used for calculating the DCMC capacity limit of Alamouti's scheme, of the BLAST scheme, of the SM scheme and of the GSTSK scheme in Figs. 4.5–4.8. Next, in Section 4.5 we derived the tight theoretical BER upper bound of our GSTSK scheme based on the concept of the MGFs. It was found

from Figs. 4.9–4.12 that the MGF-based BER bound derived asymptotically converged to the simulated BER curves for various MIMO arrangements.

Section 4.6 characterized the performance of our uncoded and turbo coded GSTSK schemes. Figs. 4.13–4.16 compared the achievable BER of our uncoded GSTSK scheme to those of other MIMO arrangements, such as the OSTBCs, BLAST, the SM scheme and the CSTSK arrangement. As a benefits of the GSTSK scheme's flexibility, it was found to outperform other MIMO arrangements, although this was achieved at the cost of an increased decoding complexity in comparison to that of the CSTSK scheme. Finally, in Table 4.6 the fundamental characteristics of our coded GSTSK scheme of Fig. 4.17, such as its schematic, parameters, computational complexity and the achievable BER, were compared to those of the CSTSK, the ACSTSK, the DSTSK and the ADSTSK schemes.

- **Chapter 5 [12, 13]:** In Chapters 2, 3 and 4 the family of STSKs was proposed for co-located MIMO systems, where having an insufficient antenna separation may suffer from shadowing-induced large-scale fading, hence leading to a performance degradation. To this end, in Chapter 5 we applied the STSK concept of Fig. 2.5 in cooperative communications, which we referred to as the cooperative STSK scheme.

  Section 5.2 provided the brief background and problem statement of cooperative MIMO techniques. Fig. 5.1 showed the effects of inter-antenna correlation on the (2×1)-element Alamouti scheme, where the diversity gain decreased upon increasing the correlation value, gradually approaching the no-diversity scenario. In this section, we also noted that both CSI estimation errors as well as IRS errors may severely degrade the achievable performance of cooperative systems.

  In Section 5.3 we proposed the CRC-activated cooperative CSTSK concept relying on the DF protocol at the relay nodes, whose schematic and algorithmic procedure were described in Fig. 5.2 and Algorithm 4.1, respectively. As shown in Fig 2.14, the CSTSK scheme outperformed OSTBCs, hence the cooperative CSTSK scheme has the potential of achieving a higher performance than conventional cooperative OSTBCs. Furthermore, in Section 5.3.2 we conceived the cooperative ACSTSK scheme, which was developed from the cooperative CSTSK scheme of Fig. 5.2 and the ACSTSK scheme of Section 2.3.2, in order to dispense with symbol-level IRS, which exhibited robustness against IRS errors. Then, Section 5.3.3 introduced the IEI-free SR- and RD-joint ML detection algorithm employed at the DN, as formulated in Eq. (5.28).

  Section 5.4 proposed the cooperative DSTSK scheme of Fig. 5.3, which was the differentially-encoded counterpart of the above-mentioned cooperative CSTSK scheme of Fig. 5.2, emerging from the DSTSK scheme of Fig. 3.5. The resultant architecture was detailed in Algorithm 5.2. The corresponding cooperative ADSTSK scheme was

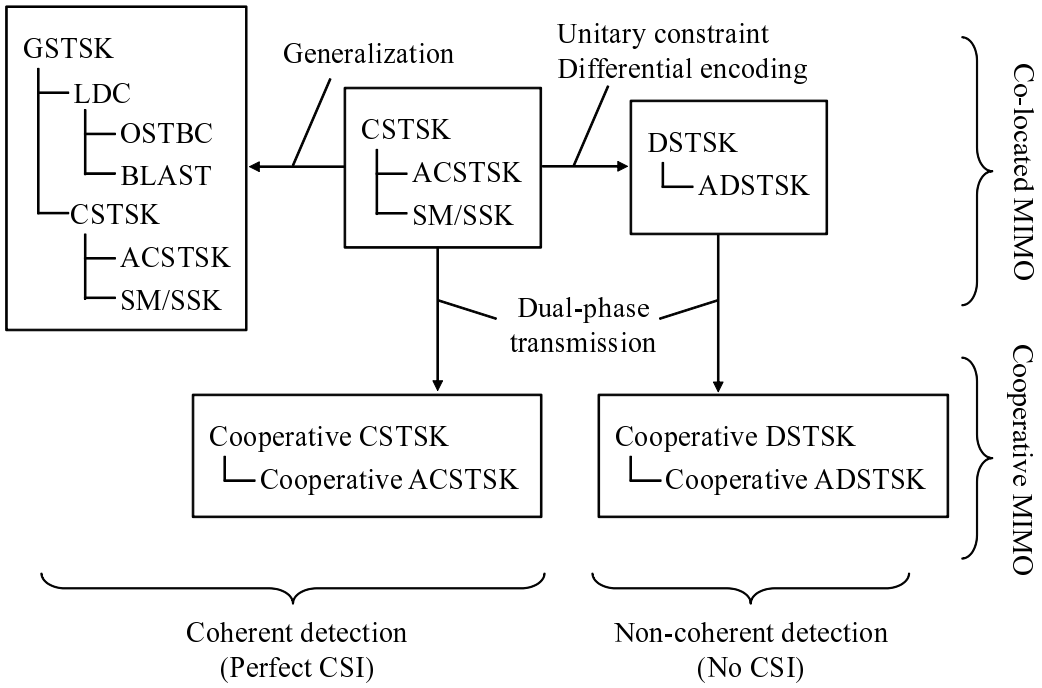

Figure 7.1: Link between the co-located CSTSK, ACSTSK, DSTSK, ADSTSK and GSTSK schemes as well as the cooperative CSTSK, ACSTSK, DSTSK and ADSTSK schemes.

proposed in Section 5.4.1, while IEI-free joint ML detection designed for the cooperative DSTSK scheme was presented in Section 5.4.2.

Section 5.5 characterized the achievable performance of the cooperative CSTSK, ACSTSK, DSTSK and ADSTSK schemes, while the basic system parameters employed were listed in Tables 5.2 and 5.3. More specifically, it can be seen from the BER results of Figs. 5.6–5.8 that our cooperative CSTSK scheme of Fig. 5.2 was capable of outperforming the cooperative OSTBCs. It was also found from Fig. 5.10 that as expected, our cooperative DSTSK scheme attained a 3-dB lower performance in comparison to that of the cooperative CSTSK scheme endowed with perfect CSI. We note however from Fig. 5.10 that upon introducing CSI errors the cooperative CSTSK scheme exhibited an error floor, hence emphasizing the benefits of the cooperative DSTSK scheme of Fig. 5.3. The effective throughput of the cooperative CSTSK, ACSTSK, DSTSK and ADSTSK as well as the co-located CSTSK schemes was compared in Figs. 5.12(a) and 5.12(b). Additionally, the schematics, the parameters, the complexity and the achievable BER of the family of uncoded co-located and cooperative STSK schemes were compared and summarized in Table 5.7, while the relationship of all the STSK schemes proposed in the thesis is shown in Fig. 7.1.

- **Chapter 6 [2–4, 14]:** In Chapter 5, the STSK concept was applied to the family of cooperative MIMO systems, where we proposed the cooperative CSTSK, ACSTSK, DSTSK and ADSTSK schemes, which exploit a useful diversity gain, while combating

the effects of correlated shadow fading. More specifically, the cooperative ACSTSK and ADSTSK schemes enable us to dispense with symbol-level IRS, since only a single RN is activated in each symbol duration during the cooperative-transmission phase. Nevertheless, in these cooperative schemes severe performance degradations may be imposed, when the IRS error exceeds the symbol duration, hence destroying the structure of the STSK codeword. In Chapter 6, we presented LS-code assisted CDSTS schemes for RNs having large IRS errors, in the context of DS-CDMA uplink.

Section 6.2 described the CDSTS system obeying the architecture of Fig. 6.1. More specifically, while the system models of the SN and of the RNs were discussed in Sections 6.2.1 and 6.2.2, the optimal ML detection algorithm employed at the DN was derived in Section 6.2.2 and Eq. (6.24). Section 6.3 highlighted the basic properties of LS codes having an IFW, hence eliminating the effects of MPI, MUI and IRS errors in our asynchronous CDSTS system. In Section 6.4 we characterized the achievable performance of the CDSTS scheme, where the basic system parameters were listed in Table 6.1. The achievable BER characterized in Figs. 6.2–6.5 showed that our CDSTS scheme is capable of attaining a beneficial cooperative diversity gain as well as path-diversity gain, provided that the maximum IRS delay combined with the delay-spread is within the IFW.

In Section 6.5, we incorporated the recent DTC philosophy into our CDSTS scheme, in order to achieve additional turbo processing gains. Section 6.6 provided the architectural overview of our DTC-aided CDSTS scheme seen in Fig. 6.7, while the system model of the SN, the RNs and the DN were outlined in Sections 6.6.1, 6.6.2 and 6.6.3.

The EXIT chart analysis and the BER calculations of our DTC-aided CDSTS system were presented in Sections 6.7 and 6.8, respectively, where the related system parameters were summarized in Table 6.2. The simulation results revealed that the proposed LS code-assisted DTC-aided CDSTS scheme is capable of achieving spatial diversity and turbo processing gains as well as time-diversity, while combating the effects of the relays' synchronization errors and CSI estimation errors.

7.2 Future Work

In this section, we briefly discuss a number of future research ideas.

7.2.1 Efficient Near-Optimal Detection for the High-P GSTSK Scheme

In Chapter 4, we proposed the GSTSK scheme of Fig. 4.2, which simultaneously activates P out of Q dispersion matrices. In this scheme, upon increasing the value of P, the GSTSK receiver has to cope with the equivalent number of ICI contributions. Thus, a higher P leads to a higher computational complexity at the receiver, as seen in Eq. (4.14), although

it enhances the bandwidth efficiency, as formulated in Eq. (4.5). We introduced the optimal ML detector for the uncoded scenario as well as the MAP soft-demapper for an turbo-coded scenario, which may result in a high complexity for a high-P scenario. To this end, it may be useful to develop more efficient near-optimal detectors for the GSTSK scheme, such as a Genetic Algorithm (GA)-aided detector [125], the MCMC detector [156–158], the ACO detector [128] and the PSO detector [159].

7.2.2 Bio-Inspired Algorithm Assisted Dispersion-Matrix Design

In our STSK family proposed in Chapters 2, 3, 4 and 5, we employed only a random search method for dispersion-matrix optimization, for the sake of simplicity. More specifically, the DCMC capacity was used as the cost function of the random search in the CSTSK scheme, while the rank- and determinant-criterion was used for that of the DSTSK and GSTSK schemes. However, there are numerous other approaches, which may potentially simplify the dispersion-matrix optimization, while achieving a comparable performance. For example, it might be useful to optimize the dispersion matrices with the aid of Genetic Algorithms (GAs), as proposed in [160] in the context of the LDCs of Section 2.2.3.

7.2.3 Distributed Turbo Coding Assisted Cooperative STSK Scheme

In Chapter 5, we proposed the family of cooperative STSK schemes operating in uncoded scenarios. In order to achieve a near-capacity performance, we may be able to invoke the concept of Distributed Turbo Coding (DTC) detailed in Section 6.5. Since the STSK scheme outperformed OSTBCs and LDCs as shown in Chapters 2 and 4, the DTC-assisted cooperative STSK arrangement has the potential of outperforming the DTC-assisted cooperative OSTBCs [161].

Furthermore, it may also be useful to incorporate LS spreading codes into the cooperative STSK scheme for the sake of achieving robustness against synchronization errors between RNs, while retaining the STSK's benefits. In this arrangement, by jointly optimizing the LS code's parameters as well as the STSK's dispersion matrices, we may potentially reduce the associated complexity.

7.2.4 Multiple-Symbol Differential Detection for DSTSK Schemes

Although the differential encoding technique advocated in Chapters 3 and 5 assists us in avoiding high-complexity channel estimation, its performance degrades for transmission over rapidly fluctuating channels, namely where the channel envelope changes substantially over the duration of two successive space-time codewords. To overcome this limitation, a sophisticated Multiple-Symbol Differential Detection (MSDD) technique was proposed in the context of both single antenna-aided transmissions [162] as well as for co-located MIMO transmis-

sions [163], where $(N_{\text{window}} - 1)$ data symbols are jointly detected from N_{window} received symbols. Therefore, invoking the concept of MSDD may be useful for improving our DSTSK and CDSTS systems suffering from rapid channel envelope variations, which constitutes our future work.

7.2.5 Irregular Precoded STSK Schemes for Near-Capacity Operation

In [98], the IRregular Precoded LDCs (IR-PLDCs) was proposed, where the irregular inner-code structure associated with a set of LDCs facilitates the proposed systems' near-capacity operation across a wide range of SNRs, while maintaining an infinitesimally low BER. Motivated by this IR-PLDC arrangement, the IRregular Precoded STSK (IP-PSTSK) structure may also have the potential of attaining the same advantage, while facilitating STSK's low-complexity single-stream ML detection due to the absence from any ICI in the equivalent system model. To elaborate a little further, since the GSTSK scheme's architecture subsumes LDCs as described in Section 4.2.2.2, the IR-PGSTSK architecture may have the potential of achieving a near-capacity operation and may outperform IR-PLDCs.

7.2.6 Multi-Carrier Transmissions for the CDSTS System

Our CDSTS system was designed so that the total maximum asynchronous delay becomes less than the IFW width of LS codes for the sake of circumventing the asynchronous nature of the relay nodes. However, the number of LS codes exhibiting a sufficiently wide IFW is limited. Hence LS codes strike a design tradeoff between the code length LLS, the number of codes PLS and the IFW width W_0. To extend the degree of design freedom and hence to accommodate higher synchronous delays, Multi-Carrier (MC) transmission may be incorporated into our CDSTS system, as described in [150]. More specifically, the IFW duration of the LS codes may be extended by a factor corresponding to the number of subcarriers, since the chip duration of each subcarrier is proportionately increased. As a additional benefit, the system becomes tolerant to channel-induced dispersion.

Appendix A

Dispersion Matrices for CSTSK/ACSTSK Schemes

• Dispersion matrices for the BPSK-modulated CSTSK$(2, 2, 2, 1)$ scheme, which can be commonly used for the BPSK-modulated ACSTSK$(2, 2, 2, 1)$ scheme

$$\boldsymbol{A}_1 = \boldsymbol{I}$$

• Dispersion matrices for the BPSK-modulated CSTSK$(2, 2, 2, 2)$ scheme, which can be commonly used for the BPSK-modulated ACSTSK$(2, 2, 2, 2)$ scheme

$$\boldsymbol{A}_1 = \begin{bmatrix} -0.2474 + j0.9537 & 0.0000 + j0.0000 \\ 0.0000 + j0.0000 & 0.2763 + j0.9762 \end{bmatrix},\ \boldsymbol{A}_2 = \begin{bmatrix} 0.0000 + j0.0000 & 0.0247 - j1.0047 \\ 0.0553 + j0.9934 & 0.0000 + j0.0000 \end{bmatrix}$$

• Dispersion matrices for the BPSK-modulated CSTSK$(2, 2, 2, 4)$ scheme, which can be commonly used for the BPSK-modulated ACSTSK$(2, 2, 2, 4)$ scheme

$$\boldsymbol{A}_1 = \begin{bmatrix} 0.0000 + j0.0000 & 0.3683 - j1.1336 \\ 0.3381 + j0.6820 & 0.0000 + j0.0000 \end{bmatrix},\ \boldsymbol{A}_2 = \begin{bmatrix} -0.5585 - j0.7017 & 0.0000 + j0.0000 \\ 0.0000 + j0.0000 & 0.5315 - j0.9556 \end{bmatrix}$$

$$\boldsymbol{A}_3 = \begin{bmatrix} -1.0462 + j0.5061 & 0.0000 + j0.0000 \\ 0.0000 + j0.0000 & 0.7025 + j0.3948 \end{bmatrix},\ \boldsymbol{A}_4 = \begin{bmatrix} 0.0000 + j0.0000 & -0.7149 - j0.3850 \\ -1.1564 + j0.0584 & 0.0000 + j0.0000 \end{bmatrix}$$

• Dispersion matrices for the QPSK-modulated CSTSK$(2, 2, 2, 4)$ scheme

$$\boldsymbol{A}_1 = \begin{bmatrix} 0.0002 + j0.1810 & 0.8053 + j0.0538 \\ -1.0650 - j0.3093 & -0.2929 + j0.0047 \end{bmatrix},\ \boldsymbol{A}_2 = \begin{bmatrix} -0.0945 + j0.9968 & -0.6147 + j0.0826 \\ 0.1045 - j0.1268 & -0.7007 - j0.3077 \end{bmatrix}$$

$$\boldsymbol{A}_3 = \begin{bmatrix} -0.8263 - j0.2239 & 0.2992 + j0.6753 \\ 0.0804 + j0.0062 & -0.8362 + j0.1261 \end{bmatrix},\ \boldsymbol{A}_4 = \begin{bmatrix} -0.4286 - j0.1218 & -0.4714 - j0.2877 \\ -0.5521 - j0.5868 & -0.0195 + j0.9203 \end{bmatrix}$$

• Dispersion matrices for the BPSK-modulated CSTSK$(2, 2, 2, 8)$ scheme

$$\boldsymbol{A}_1 = \begin{bmatrix} 0.3073 + j0.2339 & -0.9920 - j0.0838 \\ -0.3933 + j0.2801 & -0.4238 + j0.6686 \end{bmatrix}, \boldsymbol{A}_2 = \begin{bmatrix} 0.8337 + j0.0712 & -0.3666 - j0.2330 \\ 0.7861 + j0.5588 & -0.2906 + j0.3106 \end{bmatrix}$$

$$\boldsymbol{A}_3 = \begin{bmatrix} 0.0233 + j0.0014 & 0.0361 - j0.8406 \\ 0.8229 - j0.2163 & -0.5989 + j0.4570 \end{bmatrix}, \boldsymbol{A}_4 = \begin{bmatrix} 0.1473 - j0.1843 & 0.3118 + j0.9189 \\ -0.3510 - j0.9070 & -0.1961 - j0.1358 \end{bmatrix}$$

$$\boldsymbol{A}_5 = \begin{bmatrix} -0.5268 - j0.1020 & -0.3205 + j0.5082 \\ -0.2496 + j0.7647 & -0.6920 - j0.4746 \end{bmatrix}, \boldsymbol{A}_6 = \begin{bmatrix} -0.2308 + j0.7628 & 0.1127 - j0.6292 \\ 0.6195 + j0.1333 & 0.7440 - j0.0364 \end{bmatrix}$$

$$\boldsymbol{A}_7 = \begin{bmatrix} 0.7182 - j0.2568 & 0.1348 + j0.0253 \\ -0.4148 + j0.8167 & 0.1342 + j0.7364 \end{bmatrix}, \boldsymbol{A}_8 = \begin{bmatrix} 0.0235 - j0.7745 & -0.4686 - j0.5776 \\ 0.8614 + j0.0145 & 0.0866 - j0.3111 \end{bmatrix}$$

• Dispersion matrices for the BPSK-modulated CSTSK$(2, 2, 2, 16)$ scheme

$$\boldsymbol{A}_1 = \begin{bmatrix} 0.4470 + j0.0899 & 0.7602 - j0.5466 \\ 0.6192 + j0.2354 & -0.2550 + j0.6416 \end{bmatrix}, \boldsymbol{A}_2 = \begin{bmatrix} -0.9336 - j0.4439 & 0.3604 - j0.1097 \\ 0.3624 + j0.2059 & 0.7270 - j0.2953 \end{bmatrix}$$

$$\boldsymbol{A}_3 = \begin{bmatrix} 0.2615 + j0.2240 & 0.3064 - j0.1908 \\ -0.3858 - j0.2955 & -1.1873 + j0.3245 \end{bmatrix}, \boldsymbol{A}_4 = \begin{bmatrix} -0.4832 + j0.0333 & -0.4922 - j1.0080 \\ -0.4118 + j0.0312 & 0.5697 + j0.1099 \end{bmatrix}$$

$$\boldsymbol{A}_5 = \begin{bmatrix} 0.3769 - j0.2619 & -0.7687 - j0.2142 \\ -0.4861 + j0.9484 & 0.1116 - j0.0666 \end{bmatrix}, \boldsymbol{A}_6 = \begin{bmatrix} -0.0298 - j0.6982 & 0.6996 + j0.6212 \\ -0.3270 + j0.4720 & 0.5520 + j0.0447 \end{bmatrix}$$

$$\boldsymbol{A}_7 = \begin{bmatrix} -0.2404 - j0.1444 & 0.2346 + j0.1702 \\ -1.1947 - j0.1399 & 0.3891 + j0.4890 \end{bmatrix}, \boldsymbol{A}_8 = \begin{bmatrix} -0.3085 + j1.1375 & -0.6898 + j0.0435 \\ -0.0930 - j0.0040 & 0.0044 + j0.3528 \end{bmatrix}$$

$$\boldsymbol{A}_9 = \begin{bmatrix} -0.5560 + j0.8612 & 0.5009 - j0.5021 \\ -0.3862 - j0.4367 & -0.1065 + j0.3084 \end{bmatrix}, \boldsymbol{A}_{10} = \begin{bmatrix} 0.6277 + j0.5022 & 0.4876 - j0.1872 \\ -0.2433 + j0.9066 & -0.4054 - j0.1886 \end{bmatrix}$$

$$\boldsymbol{A}_{11} = \begin{bmatrix} -0.6643 + j0.4227 & -0.3402 + j0.0667 \\ 0.3813 - j0.7520 & 0.1145 - j0.7320 \end{bmatrix}, \boldsymbol{A}_{12} = \begin{bmatrix} 0.3452 - j0.0767 & 0.9149 - j0.1669 \\ 0.9160 + j0.0234 & 0.2572 - j0.3231 \end{bmatrix}$$

$$\boldsymbol{A}_{13} = \begin{bmatrix} -0.4346 + j0.0738 & 0.4665 - j0.2154 \\ 0.0384 + j0.9741 & -0.7006 + j0.3169 \end{bmatrix}, \boldsymbol{A}_{14} = \begin{bmatrix} 0.3885 + j0.2160 & 0.5378 + j0.1503 \\ -0.4933 + j0.5490 & 0.8867 - j0.3994 \end{bmatrix}$$

$$\boldsymbol{A}_{15} = \begin{bmatrix} 0.2717 + j0.1355 & 0.2938 - j0.6477 \\ 0.1653 + j0.8992 & 0.7524 + j0.0007 \end{bmatrix}, \boldsymbol{A}_{16} = \begin{bmatrix} 0.2965 - j0.5320 & -0.0758 - j1.1938 \\ 0.3514 + j0.0796 & 0.0040 - j0.2613 \end{bmatrix}$$

• Dispersion matrices for the QPSK-modulated CSTSK$(3, 2, 2, 4)$ scheme

$$\boldsymbol{A}_1 = \begin{bmatrix} 0.1576 + j0.2226 & 0.0834 + j0.3128 \\ 0.5212 - j0.8496 & -0.0013 + j0.0859 \\ -0.0857 - j0.1527 & -0.3833 + j0.8016 \end{bmatrix}, \boldsymbol{A}_2 = \begin{bmatrix} 0.7750 + j0.8504 & 0.1997 + j0.3323 \\ -0.2871 - j0.1739 & 0.5764 - j0.0784 \\ -0.1705 + j0.1574 & 0.1439 + j0.0131 \end{bmatrix}$$

$$\boldsymbol{A}_3 = \begin{bmatrix} 0.5764 - j0.0988 & 0.5809 - j0.1924 \\ 0.0527 - j0.3238 & 0.7604 + j0.4080 \\ 0.1703 - j0.3069 & -0.3340 - j0.4432 \end{bmatrix}, \boldsymbol{A}_4 = \begin{bmatrix} 0.3126 + j0.1824 & -0.3898 - j0.5231 \\ -0.6893 + j0.3081 & 0.2205 + j0.3061 \\ 0.2897 + j0.2663 & -0.6186 + j0.4401 \end{bmatrix}$$

• Dispersion matrices for the 8-PSK modulated CSTSK$(3, 2, 2, 8)$ scheme

$$\boldsymbol{A}_1 = \begin{bmatrix} -0.3004 - j0.0851 & -0.5751 + j0.1096 \\ -0.1276 + j1.0183 & -0.2113 + j0.1873 \\ -0.3897 + j0.1733 & -0.3467 - j0.3532 \end{bmatrix}, \ \boldsymbol{A}_2 = \begin{bmatrix} 0.0417 - j0.1950 & 0.6609 + j0.3697 \\ -0.3282 + j0.6485 & 0.7036 - j0.1895 \\ 0.3958 + j0.3428 & -0.1143 - j0.2006 \end{bmatrix}$$

$$\boldsymbol{A}_3 = \begin{bmatrix} 0.6896 - j0.2101 & 0.2777 + j0.3861 \\ 0.1139 + j0.1366 & 0.3816 - j0.0568 \\ -0.1513 + j0.3383 & 0.5344 + j0.8067 \end{bmatrix}, \ \boldsymbol{A}_4 = \begin{bmatrix} -0.4194 + j0.3000 & -0.1861 + j0.0637 \\ -0.4607 + j0.3887 & 0.2187 + j0.6741 \\ -0.0900 - j0.2984 & 0.1206 + j0.8475 \end{bmatrix}$$

$$\boldsymbol{A}_5 = \begin{bmatrix} -0.3674 - j0.0757 & -0.1060 + j0.4035 \\ 0.0179 - j0.3796 & 0.2175 + j0.3668 \\ -0.8406 + j0.0350 & -0.1652 - j0.7899 \end{bmatrix}, \ \boldsymbol{A}_6 = \begin{bmatrix} -0.3842 - j0.4024 & 0.3809 - j0.2354 \\ -0.3558 - j0.3678 & 0.2873 - j0.6271 \\ -0.2225 + j0.4551 & 0.4703 + j0.5240 \end{bmatrix}$$

$$\boldsymbol{A}_7 = \begin{bmatrix} -0.1888 - j0.5969 & -0.5091 - j0.2274 \\ 0.3276 + j0.0346 & -0.3845 + j0.5597 \\ -0.1933 + j0.2262 & 0.3727 - j0.7072 \end{bmatrix}, \ \boldsymbol{A}_8 = \begin{bmatrix} 0.4781 - j0.5985 & -0.3340 - j0.2010 \\ -0.4031 - j0.1665 & 0.5244 + j0.1485 \\ 0.4878 + j0.4562 & 0.5505 + j0.1582 \end{bmatrix}$$

• Dispersion matrices for the QPSK modulated CSTSK$(4, 3, 2, 4)$ scheme

$$\boldsymbol{A}_1 = \begin{bmatrix} 0.1024 - j0.2341 & 0.4977 + j0.6853 \\ -0.6330 - j0.1320 & -0.4416 - j0.0036 \\ -0.2227 + j0.2795 & -0.0523 - j0.3674 \\ -0.2563 - j0.1965 & -0.0515 - j0.4814 \end{bmatrix}, \ \boldsymbol{A}_2 = \begin{bmatrix} 0.0982 - j0.2913 & 0.0370 - j0.1133 \\ 0.5472 - j0.2291 & -0.6641 + j0.0268 \\ 0.4923 + j0.4695 & -0.2568 + j0.0591 \\ 0.3491 - j0.5222 & -0.1496 - j0.3853 \end{bmatrix}$$

$$\boldsymbol{A}_3 = \begin{bmatrix} -0.1040 - j0.4427 & 0.4768 + j0.4045 \\ 0.0496 - j0.2212 & -0.0010 - j0.3472 \\ 0.6669 + j0.5908 & -0.2399 + j0.1691 \\ -0.2788 + j0.3373 & 0.0288 + j0.3976 \end{bmatrix}, \ \boldsymbol{A}_4 = \begin{bmatrix} -0.5346 - j0.4128 & 0.5053 - j0.0619 \\ 0.3919 - j0.1720 & 0.3737 - j0.7552 \\ -0.0983 - j0.1909 & 0.3079 - j0.1969 \\ -0.0462 - j0.4342 & -0.0994 - j0.1060 \end{bmatrix}$$

• Dispersion matrices for the 8-PSK modulated CSTSK$(4, 3, 2, 8)$ scheme

$$\boldsymbol{A}_1 = \begin{bmatrix} -0.7117 - j0.0698 & -0.3639 + j0.1998 \\ 0.2009 - j0.5487 & 0.0978 - j0.2948 \\ -0.0915 + j0.5737 & -0.3070 - j0.0160 \\ 0.0183 + j0.1508 & 0.5780 - j0.2988 \end{bmatrix}, \ \boldsymbol{A}_2 = \begin{bmatrix} 0.1576 + j0.4350 & -0.5848 + j0.4745 \\ -0.1532 + j0.2530 & -0.5587 - j0.2135 \\ 0.3522 + j0.2994 & -0.1459 - j0.3042 \\ -0.4133 - j0.3104 & -0.3008 + j0.2975 \end{bmatrix}$$

$$\boldsymbol{A}_3 = \begin{bmatrix} -0.1580 - j0.2650 & -0.1024 + j0.0595 \\ -0.3433 + j0.5437 & -0.3483 + j0.0722 \\ 0.7029 - j0.0261 & -0.3818 - j0.2480 \\ -0.1575 + j0.0364 & -0.6039 - j0.5078 \end{bmatrix}, \ \boldsymbol{A}_4 = \begin{bmatrix} 0.1922 + j0.3104 & 0.4439 + j0.1583 \\ 0.6301 + j0.1943 & -0.0583 - j0.1620 \\ -0.1169 + j0.3116 & -0.3875 - j0.6964 \\ 0.2623 + j0.2663 & -0.4499 + j0.3036 \end{bmatrix}$$

$$\boldsymbol{A}_5 = \begin{bmatrix} -0.4885 + j0.2251 & 0.0256 + j0.5944 \\ -0.1713 - j0.0758 & -0.3240 + j0.7098 \\ 0.2118 + j0.2211 & 0.2643 + j0.3988 \\ 0.5766 + j0.0804 & 0.0158 + j0.2260 \end{bmatrix}, \ \boldsymbol{A}_6 = \begin{bmatrix} -0.2906 - j0.0035 & -0.2446 + j0.3452 \\ -0.5113 - j0.0916 & 0.2280 + j0.1229 \\ 0.4448 - j0.0238 & -0.1735 + j0.3008 \\ -0.4017 + j0.8686 & -0.1593 + j0.3735 \end{bmatrix}$$

$$\boldsymbol{A}_7 = \begin{bmatrix} -0.1134 - j0.1876 & 0.5939 + j0.1130 \\ -0.6177 - j0.5900 & -0.2134 + j0.0681 \\ 0.2312 - j0.1388 & 0.1723 - j0.5647 \\ 0.1885 + j0.5015 & -0.2338 + j0.2085 \end{bmatrix}, \ \boldsymbol{A}_8 = \begin{bmatrix} -0.5180 + j0.0641 & 0.3893 - j0.4745 \\ 0.1399 + j0.5044 & -0.0603 + j0.3759 \\ 0.3094 + j0.2691 & -0.5917 + j0.2173 \\ -0.0919 - j0.3751 & -0.4376 + j0.1607 \end{bmatrix}$$

• Dispersion matrices for the 16-QAM modulated CSTSK$(4, 3, 2, 16)$ scheme

$$\boldsymbol{A}_1 = \begin{bmatrix} 0.0496 - j0.0840 & 0.0264 + j0.1153 \\ -0.8877 + j0.1693 & -0.1702 + j0.2401 \\ -0.3640 + j0.5442 & -0.0404 - j0.0858 \\ 0.0990 + j0.0568 & 0.2522 - j0.7476 \end{bmatrix}, \boldsymbol{A}_2 = \begin{bmatrix} 0.2000 + j0.1240 & -0.3475 - j0.3734 \\ 0.2094 - j0.6232 & -0.0301 - j0.5553 \\ -0.3858 + j0.3895 & -0.2166 - j0.4898 \\ -0.4824 + j0.3379 & 0.0788 - j0.0488 \end{bmatrix}$$

$$\boldsymbol{A}_3 = \begin{bmatrix} 0.3462 + j0.0514 & 0.4202 - j0.4998 \\ -0.0545 + j0.3863 & 0.1603 + j0.1520 \\ 0.6354 + j0.0687 & -0.4332 + j0.1611 \\ -0.7317 + j0.1250 & 0.2754 - j0.0358 \end{bmatrix}, \boldsymbol{A}_4 = \begin{bmatrix} -0.2594 - j0.5268 & -0.6838 + j0.0277 \\ 0.0820 + j0.3635 & 0.2810 - j0.0770 \\ 0.6232 + j0.4789 & -0.1126 + j0.0897 \\ -0.1214 - j0.0180 & 0.0902 - j0.5490 \end{bmatrix}$$

$$\boldsymbol{A}_5 = \begin{bmatrix} 0.0755 + j0.7327 & -0.5548 - j0.0384 \\ 0.4295 + j0.4155 & 0.4865 - j0.1847 \\ -0.0628 + j0.1802 & 0.2930 - j0.0790 \\ 0.2003 + j0.0237 & 0.5872 + j0.0791 \end{bmatrix}, \boldsymbol{A}_6 = \begin{bmatrix} 0.1262 - j0.1141 & -0.8941 + j0.0056 \\ 0.4344 + j0.5529 & 0.2070 - j0.0894 \\ 0.0711 - j0.0258 & -0.4801 + j0.0161 \\ 0.3740 - j0.4691 & 0.1637 - j0.0565 \end{bmatrix}$$

$$\boldsymbol{A}_7 = \begin{bmatrix} 0.3982 + j0.0072 & 0.1256 - j0.3902 \\ 0.3699 + j0.2938 & -0.5296 + j0.0435 \\ 0.4108 + j0.6295 & 0.5366 - j0.0564 \\ -0.3595 + j0.2732 & -0.3167 + j0.0863 \end{bmatrix}, \boldsymbol{A}_8 = \begin{bmatrix} -0.1281 - j0.8758 & -0.2516 + j0.0710 \\ -0.1443 - j0.1944 & -0.0621 - j0.6839 \\ -0.2556 - j0.0435 & 0.2595 - j0.4491 \\ 0.1907 + j0.4925 & -0.0435 - j0.0321 \end{bmatrix}$$

$$\boldsymbol{A}_9 = \begin{bmatrix} -0.6681 - j0.3758 & 0.0235 + j0.0446 \\ -0.2728 - j0.0176 & 0.5220 + j0.1908 \\ -0.2194 + j0.1322 & 0.5702 - j0.5275 \\ -0.1095 + j0.3921 & -0.4370 - j0.0231 \end{bmatrix}, \boldsymbol{A}_{10} = \begin{bmatrix} -0.2880 + j0.6192 & 0.1584 + j0.5697 \\ 0.0352 - j0.1955 & -0.1710 + j0.3989 \\ -0.2896 + j0.6461 & 0.1543 + j0.1572 \\ 0.2622 + j0.4922 & 0.0144 - j0.3085 \end{bmatrix}$$

$$\boldsymbol{A}_{11} = \begin{bmatrix} 0.1129 - j0.3340 & -0.0420 - j0.2189 \\ -0.6178 + j0.0680 & 0.2219 - j0.0921 \\ 0.5494 - j0.1176 & 0.6746 - j0.6323 \\ -0.1885 - j0.0467 & -0.1127 - j0.4012 \end{bmatrix}, \boldsymbol{A}_{12} = \begin{bmatrix} -0.0323 + j0.0120 & -0.3115 + j0.2497 \\ 0.0458 - j0.2240 & 0.0874 - j0.1037 \\ -0.2918 + j0.4023 & -0.3918 + j0.0893 \\ 0.5579 - j0.4294 & 0.5052 - j0.7807 \end{bmatrix}$$

$$\boldsymbol{A}_{13} = \begin{bmatrix} -0.5472 - j0.7290 & -0.0407 + j0.0319 \\ -0.3496 + j0.4977 & -0.2271 - j0.2653 \\ 0.0204 + j0.0184 & 0.1195 - j0.1417 \\ 0.0641 + j0.2159 & 0.5555 + j0.5293 \end{bmatrix}, \boldsymbol{A}_{14} = \begin{bmatrix} 0.1552 + j0.7106 & 0.1384 - j0.0467 \\ 0.2066 - j0.3791 & 0.6181 + j0.2478 \\ 0.0372 + j0.3613 & 0.3832 + j0.3012 \\ 0.1153 + j0.1980 & 0.0569 + j0.6281 \end{bmatrix}$$

$$\boldsymbol{A}_{15} = \begin{bmatrix} -0.2533 - j0.3510 & -0.4840 - j0.2008 \\ 0.3273 + j0.5620 & 0.1338 + j0.5708 \\ -0.5595 + j0.3629 & 0.3977 + j0.0826 \\ 0.0069 - j0.0148 & 0.3616 - j0.1748 \end{bmatrix}, \boldsymbol{A}_{16} = \begin{bmatrix} 0.0579 - j0.2382 & -0.4981 - j0.4107 \\ -0.4259 - j0.5461 & 0.0683 + j0.2351 \\ -0.0910 + j0.4439 & -0.1683 + j0.0580 \\ -0.0871 - j0.8007 & 0.10466 - j0.295 \end{bmatrix}$$

• Dispersion matrices for the BPSK-modulated ACSTSK$(2, 2, 2, 8)$ scheme

$$\boldsymbol{A}_1 = \begin{bmatrix} -1.2177 + j0.4542 & 0.0000 + j0.0000 \\ 0.0000 + j0.0000 & 0.0803 + j0.5519 \end{bmatrix}, \boldsymbol{A}_2 = \begin{bmatrix} 0.4784 + j0.5077 & 0.0000 + j0.0000 \\ 0.0000 + j0.0000 & 0.3464 - j1.1804 \end{bmatrix}$$

$$\boldsymbol{A}_3 = \begin{bmatrix} 0.0000 + j0.0000 & -0.4947 + j0.0967 \\ 0.2189 - j1.3031 & 0.0000 + j0.0000 \end{bmatrix}, \boldsymbol{A}_4 = \begin{bmatrix} 0.0000 + j0.0000 & 0.7093 - j0.9319 \\ 0.7293 - j0.3105 & 0.0000 + j0.0000 \end{bmatrix}$$

$$\boldsymbol{A}_5 = \begin{bmatrix} 0.0000 + j0.0000 & 0.5332 + j0.7032 \\ -0.7856 - j0.7771 & 0.0000 + j0.0000 \end{bmatrix}, \boldsymbol{A}_6 = \begin{bmatrix} 0.7041 + j0.3098 & 0.0000 + j0.0000 \\ 0.0000 + j0.0000 & -1.1637 + j0.2326 \end{bmatrix}$$

$$\boldsymbol{A}_7 = \begin{bmatrix} 0.1424 - j0.1197 & 0.0000 + j0.0000 \\ 0.0000 + j0.0000 & -1.2311 - j0.6706 \end{bmatrix}, \boldsymbol{A}_8 = \begin{bmatrix} 0.0000 + j0.0000 & -0.0745 - j0.5435 \\ -1.3013 + j0.0757 & 0.0000 + j0.0000 \end{bmatrix}$$

• Dispersion matrices for the BPSK-modulated ACSTSK$(2, 2, 2, 16)$ scheme

$$\boldsymbol{A}_1 = \begin{bmatrix} 0.0000 + j0.0000 & 0.8031 - j0.4412 \\ -0.2436 + j1.0493 & 0.0000 + j0.0000 \end{bmatrix}, \boldsymbol{A}_2 = \begin{bmatrix} 0.0000 + j0.0000 & -1.1516 + j0.1904 \\ 0.2945 + j0.7421 & 0.0000 + j0.0000 \end{bmatrix}$$

$$\boldsymbol{A}_3 = \begin{bmatrix} -1.2761 - j0.2585 & 0.0000 + j0.0000 \\ 0.0000 + j0.0000 & 0.5301 - j0.1539 \end{bmatrix}, \boldsymbol{A}_4 = \begin{bmatrix} 0.2259 - j0.7915 & 0.0000 + j0.0000 \\ 0.0000 + j0.0000 & -0.6130 - j0.9730 \end{bmatrix}$$

$$\boldsymbol{A}_5 = \begin{bmatrix} 0.0000 + j0.0000 & -1.1303 - j0.3615 \\ -0.6660 - j0.3848 & 0.0000 + j0.0000 \end{bmatrix}, \boldsymbol{A}_6 = \begin{bmatrix} 0.0000 + j0.0000 & 0.0743 - j0.0868 \\ 0.7739 - j1.1781 & 0.0000 + j0.0000 \end{bmatrix}$$

$$\boldsymbol{A}_7 = \begin{bmatrix} -1.1306 - j0.6506 & 0.0000 + j0.0000 \\ 0.0000 + j0.0000 & 0.1665 - j0.5204 \end{bmatrix}, \boldsymbol{A}_8 = \begin{bmatrix} -0.0275 + j0.6862 & 0.0000 + j0.0000 \\ 0.0000 + j0.0000 & -1.1717 + j0.3943 \end{bmatrix}$$

$$\boldsymbol{A}_9 = \begin{bmatrix} 0.7791 + j0.1917 & 0.0000 + j0.0000 \\ 0.0000 + j0.0000 & 0.3834 - j1.0997 \end{bmatrix}, \boldsymbol{A}_{10} = \begin{bmatrix} -0.9554 - j0.0981 & 0.0000 + j0.0000 \\ 0.0000 + j0.0000 & -0.9222 - j0.4764 \end{bmatrix}$$

$$\boldsymbol{A}_{11} = \begin{bmatrix} 0.0000 + j0.0000 & -0.2042 + j0.6732 \\ -1.1201 - j0.5006 & 0.0000 + j0.0000 \end{bmatrix}, \boldsymbol{A}_{12} = \begin{bmatrix} 0.4783 + j0.0061 & 0.0000 + j0.0000 \\ 0.0000 + j0.0000 & 1.0341 + j0.8378 \end{bmatrix}$$

$$\boldsymbol{A}_{13} = \begin{bmatrix} 0.0000 + j0.0000 & 0.0333 + j1.0358 \\ -0.9604 - j0.0602 & 0.0000 + j0.0000 \end{bmatrix}, \boldsymbol{A}_{14} = \begin{bmatrix} -0.6342 - j0.7164 & 0.0000 + j0.0000 \\ 0.0000 + j0.0000 & -0.9722 + j0.3735 \end{bmatrix}$$

$$\boldsymbol{A}_{15} = \begin{bmatrix} 0.0000 + j0.0000 & -0.0638 + j1.2030 \\ 0.6897 - j0.2703 & 0.0000 + j0.0000 \end{bmatrix}, \boldsymbol{A}_{16} = \begin{bmatrix} 0.0000 + j0.0000 & 0.2033 + j1.1485 \\ -0.1287 - j0.7893 & 0.0000 + j0.0000 \end{bmatrix}$$

• Dispersion matrices for the QPSK-modulated ACSTSK$(2, 2, 2, 4)$ scheme

$$\boldsymbol{A}_1 = \begin{bmatrix} -0.2910 + j1.2575 & 0.0000 + j0.0000 \\ 0.0000 + j0.0000 & 0.4427 + j0.3716 \end{bmatrix}, \boldsymbol{A}_2 = \begin{bmatrix} 0.0000 + j0.0000 & -0.1373 + j1.2269 \\ -0.5767 + j0.3787 & 0.0000 + j0.0000 \end{bmatrix}$$

$$\boldsymbol{A}_3 = \begin{bmatrix} 0.0000 + j0.0000 & 0.6037 - j0.0209 \\ -0.8463 - j0.9586 & 0.0000 + j0.0000 \end{bmatrix}, \boldsymbol{A}_4 = \begin{bmatrix} 0.5971 + j0.5889 & 0.0000 + j0.0000 \\ 0.0000 + j0.0000 & -0.3294 + j1.0900 \end{bmatrix}$$

• Dispersion matrices for the 8-PSK modulated ACSTSK$(3, 2, 2, 8)$ scheme

$$\boldsymbol{A}_1 = \begin{bmatrix} 0.0000 + j0.0000 & -0.3861 - j0.8623 \\ -0.5232 + j0.9130 & 0.0000 + j0.0000 \\ 0.0000 + j0.0000 & 0.0000 + j0.0000 \end{bmatrix}, \boldsymbol{A}_2 = \begin{bmatrix} -0.6769 + j0.0050 & 0.0000 + j0.0000 \\ 0.0000 + j0.0000 & -1.1901 + j0.3544 \\ 0.0000 + j0.0000 & 0.0000 + j0.0000 \end{bmatrix}$$

$$\boldsymbol{A}_3 = \begin{bmatrix} 0.0000 + j0.0000 & -0.1193 + j0.6103 \\ 0.0000 + j0.0000 & 0.0000 + j0.0000 \\ 0.2542 - 1.2445 & 0.0000 + j0.0000 \end{bmatrix}, \boldsymbol{A}_4 = \begin{bmatrix} 0.0000 + j0.0000 & 0.0000 + j0.0000 \\ 0.0000 + j0.0000 & 0.8381 + j0.3463 \\ 0.7953 + j0.7384 & 0.0000 + j0.0000 \end{bmatrix}$$

$$\boldsymbol{A}_5 = \begin{bmatrix} 0.0000 + j0.0000 & 0.9194 + j0.6571 \\ 0.1888 + j0.8291 & 0.0000 + j0.0000 \\ 0.0000 + j0.0000 & 0.0000 + j0.0000 \end{bmatrix}, \boldsymbol{A}_6 = \begin{bmatrix} -0.2003 + j1.1839 & 0.0000 + j0.0000 \\ 0.0000 + j0.0000 & -0.5107 + j0.5454 \\ 0.0000 + j0.0000 & 0.0000 + j0.0000 \end{bmatrix}$$

$$\boldsymbol{A}_7 = \begin{bmatrix} 0.0000 + j0.0000 & -1.0870 + j0.6871 \\ 0.0000 + j0.0000 & 0.0000 + j0.0000 \\ -0.5024 - j0.3063 & 0.0000 + j0.0000 \end{bmatrix}, \boldsymbol{A}_8 = \begin{bmatrix} 0.0000 + j0.0000 & 0.0000 + j0.0000 \\ 0.0000 + j0.0000 & -0.8485 - j0.7975 \\ 0.6900 - j0.4099 & 0.0000 + j0.0000 \end{bmatrix}$$

Appendix B

Dispersion Matrices for DSTSK/ADSTSK Schemes

• Dispersion matrices for the DSTSK$(M, 2, T = M, 1)$ scheme, which can be commonly used for the ACSTSK$(M, 2, T = M, 1)$ scheme

$$\boldsymbol{A}_1 = \boldsymbol{I}$$

• Dispersion matrices for the BPSK-modulated DSTSK$(2, 2, 2, 2)$ scheme, which can be commonly used for the BPSK-modulated ADSTSK$(2, 2, 2, 2)$ scheme

$$\boldsymbol{A}_1 = \begin{bmatrix} -2.0355 + j0.0000 & 0.0000 + j0.0000 \\ 0.0000 + j0.0000 & 2.0851 + j0.0000 \end{bmatrix}, \ \boldsymbol{A}_2 = \begin{bmatrix} -0.4778 + j0.0000 & 0.0000 + j0.0000 \\ 0.0000 + j0.0000 & -0.4937 + j0.0000 \end{bmatrix}$$

• Dispersion matrices for the 8-PAM DSTSK$(2, 2, 2, 2)$ scheme

$$\boldsymbol{A}_1 = \begin{bmatrix} -0.0089 + j0.0000 & -0.9058 - j0.4234 \\ -0.9058 + j0.4234 & -0.0040 + j0.0000 \end{bmatrix}, \ \boldsymbol{A}_2 = \begin{bmatrix} 0.6207 + j0.0000 & 0.7803 - j0.0665 \\ 0.7803 + j0.0665 & -0.6234 + j0.0000 \end{bmatrix}$$

• Dispersion matrices for the BPSK-modulated DSTSK$(2, 2, 2, 4)$ scheme

$$\boldsymbol{A}_1 = \begin{bmatrix} -0.7258 + j0.0000 & 0.0830 + j1.1346 \\ 0.0830 - j1.1336 & 0.5019 + j0.0000 \end{bmatrix}, \ \boldsymbol{A}_2 = \begin{bmatrix} 0.5610 + j0.0000 & 1.1171 - j0.1855 \\ 1.1171 + 0j.1855 & -0.2025 + j0.0000 \end{bmatrix},$$

$$\boldsymbol{A}_3 = \begin{bmatrix} -0.0281 + j0.0000 & 0.2061 + j0.3085 \\ 0.2061 - j0.3085 & -0.1648 + j0.0000 \end{bmatrix}, \ \boldsymbol{A}_4 = \begin{bmatrix} 0.6732 + j0.0000 & -0.4042 + j0.3062 \\ -0.4042 - j0.3062 & -0.6678 + j0.0000 \end{bmatrix}$$

• Dispersion matrices for the 4-PAM DSTSK$(2, 2, 2, 4)$ scheme

$$\boldsymbol{A}_1 = \begin{bmatrix} -0.1216 + j0.0000 & -0.6216 - j0.2135 \\ -0.6216 + j0.2135 & 0.6667 + j0.0000 \end{bmatrix}, \ \boldsymbol{A}_2 = \begin{bmatrix} -1.2083 + j0.0000 & -0.1505 + j0.6034 \\ -0.1505 - j0.6034 & 1.1274 + j0.0000 \end{bmatrix},$$

$$\boldsymbol{A}_3 = \begin{bmatrix} 0.0195 + j0.0000 & -0.1032 + j0.9672 \\ -0.1032 - j0.9672 & 0.0264 + j0.0000 \end{bmatrix}, \ \boldsymbol{A}_4 = \begin{bmatrix} 0.5826 + j0.0000 & -0.5251 + j0.1942 \\ -0.5251 - j0.1942 & -0.5591 + j0.0000 \end{bmatrix}$$

• Dispersion matrices for the BPSK-modulated DSTSK$(2, 2, 2, 8)$ scheme

$$\boldsymbol{A}_1 = \begin{bmatrix} 0.1084 + j0.0000 & -0.1964 - j0.1428 \\ -0.1964 + j0.1428 & -0.3022 + j0.0000 \end{bmatrix}, \boldsymbol{A}_2 = \begin{bmatrix} 0.2025 + j0.0000 & -0.8994 - j0.3979 \\ -0.8994 + j0.3979 & -0.1825 + j0.0000 \end{bmatrix},$$

$$\boldsymbol{A}_3 = \begin{bmatrix} -0.8781 + j0.0000 & -0.0879 - j0.3311 \\ -0.0879 + j0.3311 & 0.2252 + j0.0000 \end{bmatrix}, \boldsymbol{A}_4 = \begin{bmatrix} 0.0244 + j0.0000 & -0.4335 + j0.2926 \\ -0.4335 - j0.2926 & -0.1752 + j0.0000 \end{bmatrix},$$

$$\boldsymbol{A}_5 = \begin{bmatrix} -0.7765 + j0.0000 & 0.2346 + j0.4610 \\ 0.2346 - j0.4610 & 0.6440 + j0.0000 \end{bmatrix}, \boldsymbol{A}_6 = \begin{bmatrix} -1.7076 + j0.0000 & -0.8468 + j0.3734 \\ -0.8468 - j0.3734 & 0.8742 + j0.0000 \end{bmatrix},$$

$$\boldsymbol{A}_7 = \begin{bmatrix} 0.1159 + j0.0000 & 0.4315 - j1.2964 \\ 0.4315 + j1.2964 & 0.5029 + j0.0000 \end{bmatrix}, \boldsymbol{A}_8 = \begin{bmatrix} 0.5465 + j0.0000 & 0.6368 - j0.0977 \\ 0.6368 + j0.0977 & -0.2468 + j0.0000 \end{bmatrix}$$

• Dispersion matrices for the 8-PAM DSTSK$(2, 2, 2, 8)$ scheme

$$\boldsymbol{A}_1 = \begin{bmatrix} -1.4721 + j0.0000 & -0.3984 + j0.3992 \\ -0.3984 - j0.3992 & 0.6660 + j0.0000 \end{bmatrix}, \boldsymbol{A}_2 = \begin{bmatrix} -0.6168 + j0.0000 & 0.0762 + j0.9948 \\ 0.0762 - 0.9948 & -0.2529 + j0.0000 \end{bmatrix},$$

$$\boldsymbol{A}_3 = \begin{bmatrix} 0.9270 + j0.0000 & 0.8177 + j0.3899 \\ 0.8177 - j0.3899 & -0.7440 + j0.0000 \end{bmatrix}, \boldsymbol{A}_4 = \begin{bmatrix} 0.1543 + j0.0000 & 0.7122 - j0.0597 \\ 0.7122 + j0.0597 & -0.3334 + j0.0000 \end{bmatrix},$$

$$\boldsymbol{A}_5 = \begin{bmatrix} 0.0126 + j0.0000 & 0.2049 + j0.6086 \\ 0.2049 - j0.6086 & -0.6106 + j0.0000 \end{bmatrix}, \boldsymbol{A}_6 = \begin{bmatrix} -0.6332 + j0.0000 & 0.0462 + j0.3991 \\ 0.0462 - j0.3991 & 0.1955 + j0.0000 \end{bmatrix},$$

$$\boldsymbol{A}_7 = \begin{bmatrix} -0.2510 + j0.0000 & 0.7211 - j0.5317 \\ 0.7211 + j0.5317 & 0.9348 + j0.0000 \end{bmatrix}, \boldsymbol{A}_8 = \begin{bmatrix} -0.7305 + j0.0000 & 0.6227 + j0.3666 \\ 0.6227 - j0.3666 & 0.1653 + j0.0000 \end{bmatrix}$$

• Dispersion matrices for the BPSK-modulated DSTSK$(3, 2, 3, 2)$ scheme, which can be commonly used for the BPSK-modulated ADSTSK$(3, 2, 3, 2)$ scheme

$$\boldsymbol{A}_1 = \begin{bmatrix} 1.8176 + j0.0000 & 0.0000 + j0.0000 & 0.0000 + j0.0000 \\ 0.0000 + j0.0000 & 2.4580 + j0.0000 & 0.0000 + j0.0000 \\ 0.0000 + j0.0000 & 0.0000 + j0.0000 & -1.9670 + j0.0000 \end{bmatrix},$$

$$\boldsymbol{A}_2 = \begin{bmatrix} -0.6621 + j0.0000 & 0.0000 + j0.0000 & 0.0000 + j0.0000 \\ 0.0000 + j0.0000 & 0.4048 + j0.0000 & 0.0000 + j0.0000 \\ 0.0000 + j0.0000 & 0.0000 + j0.0000 & -0.4276 + j0.0000 \end{bmatrix}$$

• Dispersion matrices for the BPSK-modulated DSTSK$(3, 2, 3, 4)$ scheme

$$\boldsymbol{A}_1 = \begin{bmatrix} -0.0066 + j0.0000 & -0.3423 - j0.0666 & -0.2535 + j0.1349 \\ -0.3423 + j0.0666 & 0.3769 + j0.0000 & 0.0209 + j0.0843 \\ -0.2535 - j0.1349 & 0.0209 - j0.0843 & 0.1156 + j0.0000 \end{bmatrix},$$

$$\boldsymbol{A}_2 = \begin{bmatrix} 1.2798 + j0.0000 & 0.0332 - j0.7717 & -0.4195 - j0.0799 \\ 0.0332 + j0.7717 & 0.4323 + j0.0000 & -0.5450 + j1.7825 \\ -0.4195 + j0.0799 & -0.5450 - j1.7825 & 0.6259 + j0.0000 \end{bmatrix},$$

$$\boldsymbol{A}_3 = \begin{bmatrix} -0.0168 + j0.0000 & 0.8700 + j0.0870 & -0.3205 + j0.3351 \\ 0.8700 - j0.0870 & -0.0743 + j0.0000 & 0.7625 - j0.1162 \\ -0.3205 - j0.3351 & 0.7625 + j0.1162 & 0.9158 + j0.0000 \end{bmatrix},$$

$$\boldsymbol{A}_4 = \begin{bmatrix} -0.2635 + j0.0000 & 1.0668 - j0.7052 & 0.7734 - j0.8937 \\ 1.0668 + j0.7052 & 0.8134 + j0.0000 & 0.3043 - j0.2268 \\ 0.7734 + j0.8937 & 0.3043 + j0.2268 & 1.3770 + j0.0000 \end{bmatrix}$$

• Dispersion matrices for the 4-PAM DSTSK$(3, 2, 3, 4)$ scheme

$$\boldsymbol{A}_1 = \begin{bmatrix} 0.3252 + j0.0000 & 0.7609 + j0.0249 & -0.8498 - j0.2038 \\ 0.7609 - j0.0249 & -2.5279 + j0.0000 & -0.1865 + j0.4335 \\ -0.8498 + j0.2038 & -0.1865 - j0.4335 & -0.8376 + j0.0000 \end{bmatrix},$$

$$\boldsymbol{A}_2 = \begin{bmatrix} 0.5490 + j0.0000 & 0.6619 - 0.1083 & 0.0625 - j1.2561 \\ 0.6619 + j0.1083 & 0.6893 + j0.0000 & -0.1971 + j0.7703 \\ 0.0625 + j1.2561 & -0.1971 - j0.7703 & -1.6348 + j0.0000 \end{bmatrix},$$

$$\boldsymbol{A}_3 = \begin{bmatrix} 0.4162 + j0.0000 & -0.2772 + j0.3975 & -1.4471 - j0.6350 \\ -0.2772 - j0.3975 & 0.2148 + j0.0000 & -0.8643 - j0.5671 \\ -1.4471 + j0.6350 & -0.8643 + j0.5671 & 0.6156 + j0.0000 \end{bmatrix},$$

$$\boldsymbol{A}_4 = \begin{bmatrix} -1.4616 + j0.0000 & -0.9542 - j0.3886 & -0.5788 - j0.0811 \\ -0.9542 + j0.3886 & -1.6255 + j0.0000 & 0.7923 + j0.6186 \\ -0.5788 + j0.0811 & 0.7923 - j0.61856 & 0.5539 + j0.0000 \end{bmatrix}$$

• Dispersion matrices for the BPSK-modulated DSTSK$(3, 2, 3, 8)$ scheme

$$\boldsymbol{A}_1 = \begin{bmatrix} -0.8492 + j0.0000 & -0.7337 - j1.663 & 0.1151 + j0.0459 \\ -0.7337 + j1.663 & -1.8201 + j0.0000 & -0.1476 - j0.2671 \\ 0.1151 - j0.0459 & -0.1476 + j0.2671 & 0.2217 + j0.0000 \end{bmatrix},$$

$$\boldsymbol{A}_2 = \begin{bmatrix} 0.1633 + j0.0000 & -0.2416 + j0.4737 & -0.0827 - j0.0279 \\ -0.2416 - j0.4737 & 0.4937 + j0.0000 & -0.3370 + j0.3671 \\ -0.0827 + j0.0279 & -0.3370 - j0.3671 & -2.2917 + j0.0000 \end{bmatrix},$$

$$\boldsymbol{A}_3 = \begin{bmatrix} -0.0746 + j0.0000 & 0.8566 + j0.3176 & -0.7423 + j0.3690 \\ 0.8566 - j0.3175 & -0.7644 + j0.0000 & -0.1491 + j0.0304 \\ -0.7423 - j0.3690 & -0.1491 - j0.0304 & 2.0230 + j0.0000 \end{bmatrix},$$

$$\boldsymbol{A}_4 = \begin{bmatrix} -1.0368 + j0.0000 & 0.5176 + j0.6502 & -0.9425 + j0.8205 \\ 0.5176 - j0.6502 & 0.6641 + j0.0000 & 0.6581 + j1.8123 \\ -0.9425 - j0.8205 & 0.6581 - j1.8123 & -0.0404 + j0.0000 \end{bmatrix},$$

$$\boldsymbol{A}_5 = \begin{bmatrix} 0.8599 + j0.0000 & -0.8652 + j1.0086 & -0.3388 - j0.2124 \\ -0.8652 - j1.0086 & 0.8620 + j0.0000 & 0.0771 - j0.0242 \\ -0.3388 + j0.2124 & 0.0771 + j0.0242 & 0.2979 + j0.0000 \end{bmatrix},$$

$$\boldsymbol{A}_6 = \begin{bmatrix} -0.7234 + j0.0000 & 0.8740 + j0.2934 & -1.5922 - j1.4497 \\ 0.8740 - j0.2934 & -1.1955 + j0.0000 & 1.1998 + j0.0583 \\ -1.5922 + j1.4497 & 1.1998 - j0.0583 & -1.0588 + j0.0000 \end{bmatrix},$$

$$\boldsymbol{A}_7 = \begin{bmatrix} -1.7952 + j0.0000 & -0.2765 + j0.0663 & 0.4684 + j0.0709 \\ -0.2765 - j0.0663 & -0.1886 + j0.0000 & -0.4550 - j0.0939 \\ 0.4684 - j0.0709 & -0.4550 + j0.0939 & -0.8526 + j0.0000 \end{bmatrix},$$

$$\boldsymbol{A}_8 = \begin{bmatrix} -0.6598 + j0.0000 & 0.1745 + j0.3144 & -0.2049 - j1.0815 \\ 0.1745 - j0.3144 & -1.9033 + j0.0000 & -0.0131 + j0.6627 \\ -0.2049 + j1.0815 & -0.0131 - j0.6627 & -0.7969 + j0.0000 \end{bmatrix}$$

• Dispersion matrices for the BPSK-modulated DSTSK$(4, 2, 4, 2)$ scheme

$$\boldsymbol{A}_1 = \begin{bmatrix} 1.3762 + j0.0000 & -0.6866 - j0.8013 & 0.0890 + j1.1130 & -0.6197 + j1.0403 \\ -0.6866 + j0.8013 & -0.1192 + j0.0000 & 0.2024 - j0.3096 & 0.1297 + j0.3339 \\ 0.0890 - j1.1130 & 0.2024 + j0.3096 & -1.4079 + j0.0000 & 0.0148 - j0.3757 \\ -0.6197 - j1.0403 & 0.1297 - j0.3339 & 0.0148 + j0.3757 & 0.4337 + j0.0000 \end{bmatrix},$$

$$\boldsymbol{A}_2 = \begin{bmatrix} 0.4643 + j0.0000 & 0.1096 + j0.0612 & 0.1883 - j0.3164 & -0.0587 - j0.1543 \\ 0.1096 - j0.0612 & -0.6638 + j0.0000 & -0.9853 + j0.6169 & 1.2422 - j0.5069 \\ 0.1883 + j0.3164 & -0.9853 - j0.6169 & -0.4203 + j0.0000 & -0.1236 - j0.8790 \\ -0.0587 + j0.1543 & 1.2422 + j0.5069 & -0.1236 + j0.8790 & 0.4575 + j0.0000 \end{bmatrix}$$

• Dispersion matrices for the BPSK-modulated ADSTSK$(2, 2, 2, 4)$ scheme

$$\boldsymbol{A}_1 = \begin{bmatrix} 2.8290 + j0.0000 & 0.0000 + j0.0000 \\ 0.0000 + j0.0000 & -0.2573 + j0.0000 \end{bmatrix}, \ \boldsymbol{A}_2 = \begin{bmatrix} -0.6756 + j0.0000 & 0.0000 + j0.0000 \\ 0.0000 + j0.0000 & 2.3581 + j0.0000 \end{bmatrix},$$

$$\boldsymbol{A}_3 = \begin{bmatrix} -1.2468 + j0.0000 & 0.0000 + j0.0000 \\ 0.0000 + j0.0000 & -1.1330 + j0.0000 \end{bmatrix}, \ \boldsymbol{A}_4 = \begin{bmatrix} -0.1644 + j0.0000 & 0.0000 + j0.0000 \\ 0.0000 + j0.0000 & 0.5958 + j0.0000 \end{bmatrix}$$

• Dispersion matrices for the 4-PAM ADSTSK$(2, 2, 2, 4)$ scheme

$$\boldsymbol{A}_1 = \begin{bmatrix} -0.1826 + j0.0000 & 0.0000 + j0.0000 \\ 0.0000 + j0.0000 & -1.3128 + j0.0000 \end{bmatrix}, \ \boldsymbol{A}_2 = \begin{bmatrix} -2.5107 + j0.0000 & 0.0000 + j0.0000 \\ 0.0000 + j0.0000 & 0.8974 + j0.0000 \end{bmatrix},$$

$$\boldsymbol{A}_3 = \begin{bmatrix} 1.0886 + j0.0000 & 0.0000 + j0.0000 \\ 0.0000 + j0.0000 & -1.9327 + j0.0000 \end{bmatrix}, \ \boldsymbol{A}_4 = \begin{bmatrix} -1.5037 + j0.0000 & 0.0000 + j0.0000 \\ 0.0000 + j0.0000 & -0.2140 + j0.0000 \end{bmatrix}$$

• Dispersion matrices for the BPSK-modulated ADSTSK$(2, 2, 2, 8)$ scheme

$$\boldsymbol{A}_1 = \begin{bmatrix} -1.4387 + j0.0000 & 0.0000 + j0.0000 \\ 0.0000 + j0.0000 & -0.4907 + j0.0000 \end{bmatrix}, \ \boldsymbol{A}_2 = \begin{bmatrix} -0.5447 + j0.0000 & 0.0000 + j0.0000 \\ 0.0000 + j0.0000 & 1.0144 + j0.0000 \end{bmatrix},$$

$$\boldsymbol{A}_3 = \begin{bmatrix} -0.7483 + j0.0000 & 0.0000 + j0.0000 \\ 0.0000 + j0.0000 & -1.3357 + j0.0000 \end{bmatrix}, \ \boldsymbol{A}_4 = \begin{bmatrix} 2.2070 + j0.0000 & 0.0000 + j0.0000 \\ 0.0000 + j0.0000 & -0.3311 + j0.0000 \end{bmatrix},$$

$$\boldsymbol{A}_5 = \begin{bmatrix} -0.0646 + j0.0000 & 0.0000 + j0.0000 \\ 0.0000 + j0.0000 & -2.0332 + j0.0000 \end{bmatrix}, \ \boldsymbol{A}_6 = \begin{bmatrix} -0.4125 + j0.0000 & 0.0000 + j0.0000 \\ 0.0000 + j0.0000 & -0.2126 + j0.0000 \end{bmatrix},$$

$$\boldsymbol{A}_7 = \begin{bmatrix} 1.0116 + j0.0000 & 0.0000 + j0.0000 \\ 0.0000 + j0.0000 & -0.0711 + j0.0000 \end{bmatrix}, \ \boldsymbol{A}_8 = \begin{bmatrix} 0.1650 + j0.0000 & 0.0000 + j0.0000 \\ 0.0000 + j0.0000 & -0.6066 + j0.0000 \end{bmatrix}$$

• Dispersion matrices for the 8-PAM ADSTSK$(2, 2, 2, 8)$ scheme

$$\boldsymbol{A}_1 = \begin{bmatrix} -0.6704 + j0.0000 & 0.0000 + j0.0000 \\ 0.0000 + j0.0000 & -1.2194 + j0.0000 \end{bmatrix}, \ \boldsymbol{A}_2 = \begin{bmatrix} 2.0942 + j0.0000 & 0.0000 + j0.0000 \\ 0.0000 + j0.0000 & -0.3265 + j0.0000 \end{bmatrix},$$

$$\boldsymbol{A}_3 = \begin{bmatrix} 1.0534 + j0.0000 & 0.0000 + j0.0000 \\ 0.0000 + j0.0000 & 0.6948 + j0.0000 \end{bmatrix}, \ \boldsymbol{A}_4 = \begin{bmatrix} 0.1616 + j0.0000 & 0.0000 + j0.0000 \\ 0.0000 + j0.0000 & 1.5990 + j0.0000 \end{bmatrix},$$

$$\boldsymbol{A}_5 = \begin{bmatrix} 0.2940 + j0.0000 & 0.0000 + j0.0000 \\ 0.0000 + j0.0000 & -1.3817 + j0.0000 \end{bmatrix}, \ \boldsymbol{A}_6 = \begin{bmatrix} 0.8357 + j0.0000 & 0.0000 + j0.0000 \\ 0.0000 + j0.0000 & 0.3733 + j0.0000 \end{bmatrix},$$

$$\boldsymbol{A}_7 = \begin{bmatrix} 1.4136 + j0.0000 & 0.0000 + j0.0000 \\ 0.0000 + j0.0000 & -2.1170 + j0.0000 \end{bmatrix}, \ \boldsymbol{A}_8 = \begin{bmatrix} -0.5276 + j0.0000 & 0.0000 + j0.0000 \\ 0.0000 + j0.0000 & 0.1621 + j0.0000 \end{bmatrix}$$

• Dispersion matrices for the BPSK-modulated ADSTSK$(3, 2, 3, 2)$ scheme

$$\boldsymbol{A}_1 = \begin{bmatrix} 1.8176 + j0.0000 & 0.0000 + j0.0000 & 0.0000 + j0.0000 \\ 0.0000 + j0.0000 & 2.4580 + j0.0000 & 0.0000 + j0.0000 \\ 0.0000 + j0.0000 & 0.0000 + j0.0000 & -1.9670 + j0.0000 \end{bmatrix},$$

$$\boldsymbol{A}_2 = \begin{bmatrix} -0.6621 + j0.0000 & 0.0000 + j0.0000 & 0.0000 + j0.0000 \\ 0.0000 + j0.0000 & 0.4048 + j0.0000 & 0.0000 + j0.0000 \\ 0.0000 + j0.0000 & 0.0000 + j0.0000 & -0.4276 + j0.0000 \end{bmatrix}$$

• Dispersion matrices for the BPSK-modulated ADSTSK$(3, 2, 3, 4)$ scheme

$$\boldsymbol{A}_1 = \begin{bmatrix} -2.8517 + j0.0000 & 0.0000 + j0.0000 & 0.0000 + j0.0000 \\ 0.0000 + j0.0000 & -1.1587 + j0.0000 & 0.0000 + j0.0000 \\ 0.0000 + j0.0000 & 0.0000 + j0.0000 & 0.2902 + j0.0000 \end{bmatrix},$$

$$\boldsymbol{A}_2 = \begin{bmatrix} -0.7541 + j0.0000 & 0.0000 + j0.0000 & 0.0000 + j0.0000 \\ 0.0000 + j0.0000 & 0.7897 + j0.0000 & 0.0000 + j0.0000 \\ 0.0000 + j0.0000 & 0.0000 + j0.0000 & 0.8014 + j0.0000 \end{bmatrix},$$

$$\boldsymbol{A}_3 = \begin{bmatrix} 0.1659 + j0.0000 & 0.0000 + j0.0000 & 0.0000 + j0.0000 \\ 0.0000 + j0.0000 & -2.4877 + j0.0000 & 0.0000 + j0.0000 \\ 0.0000 + j0.0000 & 0.0000 + j0.0000 & 1.2237 + j0.0000 \end{bmatrix},$$

$$\boldsymbol{A}_4 = \begin{bmatrix} 1.2336 + j0.0000 & 0.0000 + j0.0000 & 0.0000 + j0.0000 \\ 0.0000 + j0.0000 & 0.1223 + j0.0000 & 0.0000 + j0.0000 \\ 0.0000 + j0.0000 & 0.0000 + j0.0000 & 2.0063 + j0.0000 \end{bmatrix}$$

• Dispersion matrices for the 4-PAM ADSTSK$(3, 2, 3, 4)$ scheme

$$\boldsymbol{A}_1 = \begin{bmatrix} -1.6672 + j0.0000 & 0.0000 + j0.0000 & 0.0000 + j0.0000 \\ 0.0000 + j0.0000 & -1.3821 + j0.0000 & 0.0000 + j0.0000 \\ 0.0000 + j0.0000 & 0.0000 + j0.0000 & 1.1652 + j0.0000 \end{bmatrix},$$

$$\boldsymbol{A}_2 = \begin{bmatrix} -1.2592 + j0.0000 & 0.0000 + j0.0000 & 0.0000 + j0.0000 \\ 0.0000 + j0.0000 & 0.7414 + j0.0000 & 0.0000 + j0.0000 \\ 0.0000 + j0.0000 & 0.0000 + j0.0000 & 0.2152 + j0.0000 \end{bmatrix},$$

$$\boldsymbol{A}_3 = \begin{bmatrix} -2.4733 + j0.0000 & 0.0000 + j0.0000 & 0.0000 + j0.0000 \\ 0.0000 + j0.0000 & 0.3654 + j0.0000 & 0.0000 + j0.0000 \\ 0.0000 + j0.0000 & 0.0000 + j0.0000 & -2.0782 + j0.0000 \end{bmatrix},$$

$$\boldsymbol{A}_4 = \begin{bmatrix} -0.1646 + j0.0000 & 0.0000 + j0.0000 & 0.0000 + j0.0000 \\ 0.0000 + j0.0000 & 1.7351 + j0.0000 & 0.0000 + j0.0000 \\ 0.0000 + j0.0000 & 0.0000 + j0.0000 & 1.6187 + j0.0000 \end{bmatrix}$$

• Dispersion matrices for the BPSK-modulated ADSTSK$(3, 2, 3, 8)$ scheme

$$\boldsymbol{A}_1 = \begin{bmatrix} -0.1644 + j0.0000 & 0.0000 + j0.0000 & 0.0000 + j0.0000 \\ 0.0000 + j0.0000 & -2.4782 + j0.0000 & 0.0000 + j0.0000 \\ 0.0000 + j0.0000 & 0.0000 + j0.0000 & -0.2850 + j0.0000 \end{bmatrix},$$

$$\boldsymbol{A}_2 = \begin{bmatrix} 2.1956 + j0.0000 & 0.0000 + j0.0000 & 0.0000 + j0.0000 \\ 0.0000 + j0.0000 & -0.1010 + j0.0000 & 0.0000 + j0.0000 \\ 0.0000 + j0.0000 & 0.0000 + j0.0000 & -0.7649 + j0.0000 \end{bmatrix},$$

$$\boldsymbol{A}_3 = \begin{bmatrix} -0.3474 + j0.0000 & 0.0000 + j0.0000 & 0.0000 + j0.0000 \\ 0.0000 + j0.0000 & -0.5936 + j0.0000 & 0.0000 + j0.0000 \\ 0.0000 + j0.0000 & 0.0000 + j0.0000 & 0.4630 + j0.0000 \end{bmatrix},$$

$$\boldsymbol{A}_4 = \begin{bmatrix} 0.3906 + j0.0000 & 0.0000 + j0.0000 & 0.0000 + j0.0000 \\ 0.0000 + j0.0000 & -1.0181 + j0.0000 & 0.0000 + j0.0000 \\ 0.0000 + j0.0000 & 0.0000 + j0.0000 & 0.8321 + j0.0000 \end{bmatrix},$$

$$\boldsymbol{A}_5 = \begin{bmatrix} -0.7029 + j0.0000 & 0.0000 + j0.0000 & 0.0000 + j0.0000 \\ 0.0000 + j0.0000 & 0.4034 + j0.0000 & 0.0000 + j0.0000 \\ 0.0000 + j0.0000 & 0.0000 + j0.0000 & 0.1764 + j0.0000 \end{bmatrix},$$

$$\boldsymbol{A}_6 = \begin{bmatrix} 1.3614 + j0.0000 & 0.0000 + j0.0000 & 0.0000 + j0.0000 \\ 0.0000 + j0.0000 & -1.4555 + j0.0000 & 0.0000 + j0.0000 \\ 0.0000 + j0.0000 & 0.0000 + j0.0000 & 2.0408 + j0.0000 \end{bmatrix},$$

$$\boldsymbol{A}_7 = \begin{bmatrix} -0.8089 + j0.0000 & 0.0000 + j0.0000 & 0.0000 + j0.0000 \\ 0.0000 + j0.0000 & -0.2969 + j0.0000 & 0.0000 + j0.0000 \\ 0.0000 + j0.0000 & 0.0000 + j0.0000 & 1.4588 + j0.0000 \end{bmatrix},$$

$$\boldsymbol{A}_8 = \begin{bmatrix} -0.9904 + j0.0000 & 0.0000 + j0.0000 & 0.0000 + j0.0000 \\ 0.0000 + j0.0000 & -0.8697 + j0.0000 & 0.0000 + j0.0000 \\ 0.0000 + j0.0000 & 0.0000 + j0.0000 & -1.0309 + j0.0000 \end{bmatrix}$$

Appendix C

Dispersion Matrices for GSTSK Schemes

• Dispersion matrices for the QPSK-modulated GSTSK$(2, 2, 2, 3, 2)$ scheme

$$\boldsymbol{A}_1 = \begin{bmatrix} -0.0430 - j0.4169 & 0.3392 + j0.4057 \\ -0.1675 - j0.6891 & 0.1309 - j0.1571 \end{bmatrix},$$

$$\boldsymbol{A}_2 = \begin{bmatrix} 0.5424 + j0.3117 & 0.5050 + j0.1248 \\ -0.0450 - j0.3354 & -0.4010 + j0.2505 \end{bmatrix},$$

$$\boldsymbol{A}_3 = \begin{bmatrix} -0.3533 - j0.1903 & 0.0467 - j0.1050 \\ -0.0310 - j0.1274 & -0.2489 + j0.8641 \end{bmatrix},$$

and the associated bit-to-matrix-selection rule of

$B_1 = 1$	$\boldsymbol{A}_1$	$\boldsymbol{A}_2$	$\boldsymbol{A}_3$
0	off	on	on
1	on	off	on

(C.1)

• Dispersion matrices for the QPSK–modulated GSTSK$(2, 2, 2, 4, 2)$ scheme

$$\boldsymbol{A}_1 = \begin{bmatrix} 0.0484 + j0.4063 & 0.1447 + j0.2695 \\ -0.0708 - j0.7268 & -0.2394 + j0.3853 \end{bmatrix}, \quad \boldsymbol{A}_2 = \begin{bmatrix} -0.1664 - j0.1420 & 0.3071 + j0.0207 \\ 0.7926 - j0.3143 & -0.1209 + j0.3404 \end{bmatrix},$$

$$\boldsymbol{A}_3 = \begin{bmatrix} 0.1746 + j0.1623 & -0.2896 - j0.5806 \\ -0.3414 - j0.0842 & -0.6314 - j0.0036 \end{bmatrix}, \quad \boldsymbol{A}_4 = \begin{bmatrix} 0.4287 - j0.4923 & 0.4863 - j0.3542 \\ 0.1094 + j0.3312 & 0.2674 + j0.1367 \end{bmatrix}$$

and the associated bit-to-matrix-selection rule of

$B_1 = 2$	$\boldsymbol{A}_1$	$\boldsymbol{A}_2$	$\boldsymbol{A}_3$	$\boldsymbol{A}_4$
00	off	off	on	on
01	off	on	off	on
10	on	off	on	off
11	on	on	off	off

(C.2)

• Dispersion matrices for the QPSK-modulated GSTSK$(2, 2, 2, 4, 3)$ scheme

$$\boldsymbol{A}_1 = \begin{bmatrix} -0.2762 + j0.0874 & 0.2201 + j0.4326 \\ 0.5113 + j0.0311 & -0.2610 + j0.1293 \end{bmatrix}, \boldsymbol{A}_2 = \begin{bmatrix} 0.4845 - j0.4192 & 0.2106 - j0.2404 \\ -0.1041 + j0.0795 & -0.1944 - j0.3148 \end{bmatrix},$$
$$\boldsymbol{A}_3 = \begin{bmatrix} 0.0820 + j0.2622 & 0.0687 + j0.4508 \\ 0.1218 - j0.2998 & -0.3878 - j0.3582 \end{bmatrix}, \boldsymbol{A}_4 = \begin{bmatrix} 0.3795 + j0.4517 & -0.3644 - j0.0884 \\ 0.2255 + j0.2737 & -0.1742 + j0.1481 \end{bmatrix},$$

and the associated bit-to-matrix-selection rule of

$B_1 = 2$	$\boldsymbol{A}_1$	$\boldsymbol{A}_2$	$\boldsymbol{A}_3$	$\boldsymbol{A}_4$
00	off	on	on	on
01	on	off	on	on
10	on	on	off	on
11	on	on	on	off

(C.3)

• Dispersion matrices for the 8-PSK modulated GSTSK$(3, 2, 3, 5, 2)$ scheme

$$\boldsymbol{A}_1 = \begin{bmatrix} 0.3313 - j0.0934 & -0.2093 + j0.0059 & 0.3430 - j0.1426 \\ 0.0256 - j0.2123 & 0.4258 - j0.1198 & -0.1492 + j0.3136 \\ -0.2001 - j0.1485 & -0.4746 - j0.7163 & 0.1930 + j0.0034 \end{bmatrix},$$
$$\boldsymbol{A}_2 = \begin{bmatrix} 0.0533 - j0.5840 & -0.2676 + j0.0331 & 0.2379 + j0.2635 \\ -0.3727 + j0.1888 & -0.2517 - j0.3823 & 0.1967 + j0.1229 \\ -0.2409 - j0.0039 & 0.0660 - j0.0738 & -0.6645 + j0.1008 \end{bmatrix},$$
$$\boldsymbol{A}_3 = \begin{bmatrix} -0.4773 + j0.0533 & -0.1435 + j0.2393 & 0.5933 - j0.0776 \\ 0.2637 + j0.0093 & -0.2280 - j0.4797 & 0.1906 + j0.0211 \\ 0.2209 - j0.2538 & -0.0108 - j0.2367 & 0.5170 - j0.0911 \end{bmatrix},$$
$$\boldsymbol{A}_4 = \begin{bmatrix} 0.1434 + j0.2098 & -0.3781 - j0.1050 & -0.5476 + j0.0826 \\ -0.0158 + j0.2100 & 0.1294 - j0.5712 & -0.3051 + j0.0995 \\ -0.1745 + j0.5746 & -0.1668 - j0.1640 & 0.0265 - j0.2613 \end{bmatrix},$$
$$\boldsymbol{A}_5 = \begin{bmatrix} 0.1083 + j0.1886 & -0.3862 + j0.4963 & -0.3009 + j0.0908 \\ 0.3435 - j0.4493 & -0.1621 + j0.0307 & 0.0856 + j0.0560 \\ 0.0548 - j0.4980 & -0.2469 + j0.3589 & -0.3752 - j0.1402 \end{bmatrix},$$

and the associated bit-to-matrix-selection rule of

$B_1 = 3$	$\boldsymbol{A}_1$	$\boldsymbol{A}_2$	$\boldsymbol{A}_3$	$\boldsymbol{A}_4$	$\boldsymbol{A}_5$
000	off	off	off	on	on
001	off	off	on	off	on
010	off	on	off	off	on
011	on	off	off	off	on
100	off	off	on	on	off
101	off	on	off	on	off
110	on	off	on	off	off
111	on	on	off	off	off

(C.4)

• Dispersion matrices for the QPSK modulated GSTSK$(3, 2, 3, 4, 2)$ scheme

$$\boldsymbol{A}_1 = \begin{bmatrix} -0.1822 + j0.1836 & -0.2895 - j0.0459 & -0.3266 + j0.0084 \\ -0.5410 - j0.2791 & 0.1808 + j0.2297 & -0.2651 - j0.0169 \\ 0.3534 + j0.1326 & -0.1305 - j0.4133 & -0.4618 + j0.4126 \end{bmatrix},$$

$$\boldsymbol{A}_2 = \begin{bmatrix} 0.1842 + j0.1422 & -0.5593 + j0.2209 & -0.4014 - j0.1404 \\ 0.4117 - j0.3931 & 0.0114 + j0.3390 & 0.1421 + j0.0166 \\ -0.4571 - j0.0340 & -0.1677 + j0.0778 & -0.1288 - j0.4278 \end{bmatrix},$$

$$\boldsymbol{A}_3 = \begin{bmatrix} -0.4247 - j0.0167 & -0.3032 + j0.5709 & 0.1076 + j0.0303 \\ 0.2298 - j0.3942 & -0.1249 - j0.2413 & -0.0714 - j0.4140 \\ 0.0966 + j0.3641 & -0.3253 + j0.1979 & 0.3606 + j0.1160 \end{bmatrix},$$

$$\boldsymbol{A}_4 = \begin{bmatrix} 0.3281 - j0.1621 & 0.3511 + j0.0513 & -0.1194 + j0.1961 \\ 0.0298 - j0.0971 & -0.1283 - j0.1433 & -0.8044 - j0.0415 \\ -0.0857 - j0.0824 & -0.4824 + j0.1671 & -0.3798 - j0.2691 \end{bmatrix},$$

and the associated bit-to-matrix-selection rule of (C.2)

• Dispersion matrices for the QPSK modulated GSTSK$(4, 3, 2, 4, 2)$ scheme

$$\boldsymbol{A}_1 = \begin{bmatrix} 0.0299 - j0.1020 & 0.4425 - j0.2662 \\ 0.2726 + j0.1483 & -0.0559 - j0.3410 \\ -0.3271 - j0.2669 & 0.1458 - j0.2913 \\ -0.3701 - j0.0422 & -0.2563 + j0.1321 \end{bmatrix}, \quad \boldsymbol{A}_2 = \begin{bmatrix} -0.0711 + j0.3619 & 0.2243 + j0.1159 \\ 0.4538 - j0.3395 & -0.2508 - j0.0462 \\ 0.1265 - j0.1662 & 0.2317 + j0.4949 \\ -0.0151 - j0.2088 & 0.0119 + j0.1671 \end{bmatrix},$$

$$\boldsymbol{A}_3 = \begin{bmatrix} 0.2882 + j0.2000 & 0.3496 - j0.1670 \\ 0.3239 + j0.0699 & -0.0464 + j0.2996 \\ 0.0451 + j0.3059 & 0.1131 + j0.2448 \\ 0.5046 + j0.2367 & -0.1024 - j0.1890 \end{bmatrix}, \quad \boldsymbol{A}_4 = \begin{bmatrix} 0.0345 - j0.2121 & 0.3626 + j0.1942 \\ -0.0728 - j0.1235 & 0.1816 + j0.2065 \\ -0.5099 + j0.4933 & -0.1793 - j0.0472 \\ -0.1182 - j0.2119 & 0.2991 - j0.0493 \end{bmatrix},$$

and the associated bit-to-matrix-selection rule of (C.2)

• Dispersion matrices for the QPSK modulated GSTSK$(4, 3, 2, 4, 3)$ scheme

$$\boldsymbol{A}_1 = \begin{bmatrix} -0.2967 + j0.1024 & 0.1205 + j0.1049 \\ -0.4659 + j0.1510 & 0.1941 + j0.24376 \\ -0.0025 + j0.1061 & -0.1843 + j0.0773 \\ -0.2069 - j0.0876 & 0.3219 - j0.0208 \end{bmatrix}, \quad \boldsymbol{A}_2 = \begin{bmatrix} -0.0154 + j0.0843 & 0.2794 + j0.1523 \\ 0.1793 - j0.0934 & 0.1179 + j0.1503 \\ 0.1606 + j0.6016 & 0.1818 + j0.0636 \\ -0.1510 + j0.1081 & 0.0060 + j0.1464 \end{bmatrix},$$

$$\boldsymbol{A}_3 = \begin{bmatrix} 0.2119 + j0.1779 & 0.0066 + j0.1259 \\ -0.0886 - j0.3110 & 0.3234 - j0.0966 \\ 0.1010 - j0.1726 & -0.3926 - j0.1288 \\ -0.0628 - j0.2474 & -0.2555 - j0.1206 \end{bmatrix}, \quad \boldsymbol{A}_4 = \begin{bmatrix} -0.3699 - j0.1245 & -0.1934 - j0.0692 \\ -0.0622 + j0.0802 & 0.3784 - j0.2848 \\ 0.2015 + j0.0358 & -0.1641 - j0.1847 \\ 0.1811 + j0.2469 & -0.1782 + j0.0952 \end{bmatrix},$$

and the associated bit-to-matrix-selection rule of (C.3)

• Dispersion matrices for the QPSK modulated GSTSK$(4, 3, 2, 4, 4)$ scheme

$$\boldsymbol{A}_1 = \begin{bmatrix} 0.1440 - j0.0192 & -0.3150 + j0.1453 \\ -0.1915 + j0.3373 & -0.1548 + j0.2180 \\ -0.2169 - j0.1536 & 0.1607 - j0.1283 \\ 0.0933 + j0.0095 & -0.0053 - j0.1221 \end{bmatrix}, \boldsymbol{A}_2 = \begin{bmatrix} 0.0456 - j0.3065 & -0.1288 + j0.0332 \\ 0.0959 + j0.0995 & -0.0512 + j0.1182 \\ 0.1450 + j0.1549 & -0.4218 + j0.2045 \\ 0.1104 + j0.1231 & 0.0690 + j0.2318 \end{bmatrix},$$

$$\boldsymbol{A}_3 = \begin{bmatrix} 0.0511 + j0.0125 & -0.1564 - j0.0928 \\ -0.2562 + j0.1759 & 0.2337 - j0.0743 \\ 0.0567 + j0.0084 & -0.0884 - j0.2360 \\ 0.2705 - j0.3274 & 0.2339 - j0.0752 \end{bmatrix}, \boldsymbol{A}_4 = \begin{bmatrix} 0.0291 + j0.0885 & 0.0599 + j0.0500 \\ 0.0169 - j0.1736 & -0.2250 + j0.2613 \\ -0.1158 - j0.1165 & -0.2216 + j0.1107 \\ 0.3318 - j0.2790 & 0.0053 + j0.2441 \end{bmatrix},$$

where all the dispersion matrices are activated in each symbol, similarly to LDCs.

• Dispersion matrices for the 8-PSK modulated GSTSK$(4, 3, 2, 4, 2)$ scheme

$$\boldsymbol{A}_1 = \begin{bmatrix} 0.2557 + j0.1359 & -0.5040 - j0.1736 \\ -0.4014 + j0.2189 & 0.1617 + j0.0290 \\ 0.2470 - j0.3019 & 0.4304 + j0.0966 \\ 0.0138 + j0.2102 & 0.0670 + j0.0193 \end{bmatrix}, \boldsymbol{A}_2 = \begin{bmatrix} 0.5902 + j0.2545 & 0.2331 + j0.0594 \\ -0.3878 + j0.0859 & 0.2656 + j0.1212 \\ -0.1218 + j0.3066 & 0.0713 - j0.3066 \\ -0.1354 + j0.0002 & 0.1147 - j0.2160 \end{bmatrix},$$

$$\boldsymbol{A}_3 = \begin{bmatrix} 0.2853 - j0.0812 & -0.0552 + j0.0706 \\ 0.2349 + j0.1208 & -0.2203 - j0.1515 \\ 0.1193 + j0.1248 & -0.0931 - j0.2385 \\ 0.4846 + j0.2358 & 0.5952 + j0.1509 \end{bmatrix}, \boldsymbol{A}_4 = \begin{bmatrix} -0.1576 - j0.2594 & 0.5511 + j0.1164 \\ -0.3226 - j0.0211 & -0.2234 + j0.3198 \\ -0.1547 - j0.0421 & 0.0817 - j0.1316 \\ -0.0960 + j0.4823 & -0.1644 - j0.1238 \end{bmatrix},$$

and the associated bit-to-matrix-selection rule of (C.2)

• Dispersion matrices for the BPSK-modulated GSTSK$(5, 2, 1, 6, 3)$ scheme

$$\boldsymbol{A}_1 = \begin{bmatrix} 0.2030 - j0.2675 \\ -0.0675 - j0.0932 \\ 0.1328 - j0.3143 \\ -0.1936 - j0.0632 \\ 0.1554 - j0.1592 \end{bmatrix}, \boldsymbol{A}_2 = \begin{bmatrix} 0.0937 - j0.0189 \\ -0.4340 - j0.0247 \\ 0.3034 - j0.0642 \\ -0.0604 + j0.0811 \\ -0.1530 + j0.0738 \end{bmatrix}, \boldsymbol{A}_3 = \begin{bmatrix} -0.0604 - j0.2227 \\ 0.0186 + j0.1037 \\ 0.0636 - j0.0127 \\ 0.1831 + j0.2988 \\ -0.3739 - j0.0465 \end{bmatrix},$$

$$\boldsymbol{A}_4 = \begin{bmatrix} -0.2071 - j0.2723 \\ 0.0314 + j0.0302 \\ -0.0005 + j0.2188 \\ -0.3962 - j0.0537 \\ -0.0687 + j0.0440 \end{bmatrix}, \boldsymbol{A}_5 = \begin{bmatrix} -0.0095 - j0.1689 \\ 0.0795 - j0.1856 \\ 0.1374 + j0.2471 \\ 0.1541 + j0.2324 \\ 0.2486 + j0.2107 \end{bmatrix}, \boldsymbol{A}_6 = \begin{bmatrix} -0.0255 - j0.1517 \\ 0.0960 + j0.1282 \\ 0.2132 - j0.0119 \\ 0.1827 - j0.2297 \\ 0.1141 + j0.3732 \end{bmatrix},$$

and the associated bit-to-matrix-selection rule of

$B_1 = 4$	$\boldsymbol{A}_1$	$\boldsymbol{A}_2$	$\boldsymbol{A}_3$	$\boldsymbol{A}_4$	$\boldsymbol{A}_5$	$\boldsymbol{A}_6$
0000	off	off	off	on	on	on
0001	off	on	on	off	off	on
0010	on	off	off	on	off	on
0011	off	off	on	off	on	on
0100	on	on	off	off	off	on
0101	off	on	off	off	on	on
0110	off	off	on	on	off	on
0111	on	off	on	off	off	on
1000	off	off	on	on	on	off
1001	on	on	off	off	on	off
1010	off	on	off	on	on	off
1011	on	off	off	on	on	off
1100	on	off	on	off	on	off
1101	off	on	on	on	off	off
1110	on	on	on	off	off	off
1111	on	on	off	on	off	off

(C.5)

- Dispersion matrices for the BPSK-modulated GSTSK$(5, 2, 2, 6, 3)$ scheme

$$\boldsymbol{A}_1 = \begin{bmatrix} 0.2242 + j0.2041 & 0.0467 - j0.0428 \\ -0.1560 - j0.0270 & -0.1426 + j0.0574 \\ 0.0098 - j0.0794 & 0.0356 + j0.1554 \\ 0.3770 + j0.1255 & -0.1441 - j0.1655 \\ -0.1006 + j0.4845 & -0.1678 + j0.1058 \end{bmatrix}, \quad \boldsymbol{A}_2 = \begin{bmatrix} -0.1632 + j0.1954 & 0.0026 - j0.1601 \\ -0.1560 + j0.2211 & 0.2109 + j0.2533 \\ -0.0839 - j0.1255 & -0.4563 + j0.1746 \\ -0.0986 - j0.0889 & 0.2449 - j0.0032 \\ 0.0060 + j0.2262 & -0.0565 + j0.0297 \end{bmatrix},$$

$$\boldsymbol{A}_3 = \begin{bmatrix} 0.0118 + j0.3247 & 0.2697 + j0.0814 \\ 0.1361 - j0.0511 & -0.0232 + j0.0666 \\ 0.1830 + j0.0303 & 0.0547 - j0.1870 \\ -0.2130 - j0.4194 & -0.0685 - j0.1976 \\ -0.0182 + j0.1684 & -0.0597 - j0.2932 \end{bmatrix}, \quad \boldsymbol{A}_4 = \begin{bmatrix} 0.0298 + j0.0952 & -0.0475 + j0.0104 \\ 0.34648 + j0.1317 & 0.0242 + j0.4057 \\ 0.0464 - j0.3908 & 0.0486 - j0.2343 \\ -0.2306 - j0.0004 & 0.0618 - j0.0874 \\ 0.2258 - j0.0586 & -0.0894 + j0.1121 \end{bmatrix},$$

$$\boldsymbol{A}_5 = \begin{bmatrix} 0.05123 - j0.1623 & 0.2967 + j0.0952 \\ 0.1455 + j0.0358 & -0.4341 + j0.1543 \\ 0.1817 + j0.0173 & 0.0833 + j0.0881 \\ -0.1042 + j0.1235 & -0.0291 + j0.2290 \\ 0.0956 + j0.2404 & 0.2027 + j0.2655 \end{bmatrix}, \quad \boldsymbol{A}_6 = \begin{bmatrix} 0.4022 + j0.0274 & -0.3001 + j0.0382 \\ 0.0692 - j0.3477 & -0.0828 - j0.1906 \\ -0.0005 + j0.0671 & -0.2233 + j0.0812 \\ -0.1702 - j0.1094 & -0.1872 - j0.1720 \\ 0.0987 + j0.0439 & 0.2417 + j0.0846 \end{bmatrix},$$

and the associated bit-to-matrix-selection rule of (C.5)

• Dispersion matrices for the BPSK-modulated GSTSK$(5, 2, 3, 6, 3)$ scheme

$$\boldsymbol{A}_1 = \begin{bmatrix} 0.4353 - j0.2383 & 0.1144 - j0.0066 & -0.0106 + j0.0683 \\ 0.1108 + j0.0294 & 0.1479 - j0.3635 & 0.1231 + j0.1544 \\ 0.0737 + j0.0049 & 0.2565 + j0.2541 & 0.0768 - j0.2835 \\ -0.0320 - j0.1387 & 0.1161 + j0.0800 & 0.1363 + j0.3508 \\ 0.1268 - j0.2298 & 0.0144 + j0.2135 & 0.0252 - j0.1030 \end{bmatrix},$$

$$\boldsymbol{A}_2 = \begin{bmatrix} 0.0629 - j0.1444 & -0.0493 - j0.0743 & 0.2337 + j0.2099 \\ -0.3162 - j0.0927 & 0.0459 + j0.1413 & -0.2802 - j0.0680 \\ 0.0331 + j0.1481 & -0.3673 + j0.0631 & 0.1428 - j0.1406 \\ -0.0496 + j0.0024 & 0.2226 + j0.1995 & 0.1304 - j0.0054 \\ -0.0772 + j0.2307 & 0.2911 - j0.0761 & -0.4240 - j0.1199 \end{bmatrix},$$

$$\boldsymbol{A}_3 = \begin{bmatrix} 0.0989 + j0.0189 & 0.2155 - j0.3178 & -0.2463 + j0.1742 \\ -0.0214 + j0.2191 & -0.2073 + j0.0741 & 0.0424 - j0.1051 \\ 0.0354 + j0.0841 & -0.0564 + j0.1375 & 0.2081 + j0.1197 \\ 0.3364 + j0.2682 & 0.2226 + j0.0315 & -0.0328 + j0.2086 \\ 0.2122 - j0.0177 & -0.3335 + j0.0375 & -0.3287 - j0.0860 \end{bmatrix},$$

$$\boldsymbol{A}_4 = \begin{bmatrix} 0.2077 - j0.0742 & 0.1932 + j0.0008 & 0.1089 + j0.0359 \\ -0.4415 - j0.0473 & 0.2250 + j0.2363 & -0.2505 + j0.1465 \\ -0.1378 - j0.2304 & 0.0800 - j0.0319 & -0.0039 + j0.0696 \\ -0.0364 + j0.3818 & -0.1967 - j0.1323 & 0.1092 + j0.0030 \\ 0.3904 + j0.0221 & 0.0245 - j0.1611 & 0.0621 - j0.1738 \end{bmatrix},$$

$$\boldsymbol{A}_5 = \begin{bmatrix} -0.1227 + j0.1278 & 0.1678 - j0.2538 & -0.0316 - j0.0720 \\ 0.2404 + j0.0865 & 0.0653 - j0.1210 & -0.3235 - j0.0470 \\ -0.0393 + j0.3375 & -0.0048 + j0.1611 & -0.3199 - j0.0417 \\ -0.2903 - j0.1560 & 0.0186 + j0.3476 & -0.0573 - j0.1000 \\ 0.1268 - j0.1480 & -0.2700 + j0.0495 & 0.1431 - j0.2375 \end{bmatrix},$$

$$\boldsymbol{A}_6 = \begin{bmatrix} 0.1142 + j0.0679 & 0.3103 + j0.1732 & -0.1050 - j0.1123 \\ 0.2361 - j0.2603 & 0.0109 - j0.0701 & -0.1587 - j0.2692 \\ -0.2828 + j0.0974 & -0.1374 - j0.1599 & 0.1639 - j0.2307 \\ -0.0270 + j0.1225 & 0.5040 - j0.2564 & 0.0345 - j0.0680 \\ -0.1182 - j0.0057 & -0.0188 - j0.0789 & 0.1210 + j0.1251 \end{bmatrix},$$

and the associated bit-to-matrix-selection rule of (C.5)

• Dispersion matrices for the BPSK-modulated GSTSK$(5, 2, 4, 6, 3)$ scheme

$$\boldsymbol{A}_1 = \begin{bmatrix} 0.1053 - j0.1905 & 0.0522 - j0.0069 & 0.0802 + j0.2917 & -0.0869 + j0.1677 \\ -0.1945 + j0.1663 & -0.1006 - j0.1592 & -0.0681 + j0.0312 & -0.0440 + j0.1909 \\ 0.2789 + j0.0073 & 0.0287 + j0.3317 & 0.2169 - j0.2212 & -0.1913 - j0.0435 \\ 0.1592 + j0.0637 & 0.3195 - j0.0198 & 0.4267 + j0.0015 & -0.3519 - j0.0061 \\ 0.0267 - j0.0135 & 0.0590 - j0.2349 & 0.0524 + j0.2051 & -0.1009 - j0.3683 \end{bmatrix},$$

$$\boldsymbol{A}_2 = \begin{bmatrix} 0.0396 + j0.1761 & 0.0917 + j0.0525 & 0.2947 + j0.1024 & 0.3438 + j0.2342 \\ -0.2340 + j0.0366 & 0.0732 - j0.0074 & 0.0517 + j0.1824 & -0.0766 - j0.2142 \\ 0.1755 - j0.0419 & 0.2774 + j0.5064 & 0.2385 + j0.2241 & 0.1891 - j0.2283 \\ 0.2129 - j0.1652 & 0.0295 - j0.2910 & 0.1978 - j0.0316 & 0.0807 + j0.1660 \\ -0.1979 + j0.1241 & 0.0610 - j0.0221 & 0.0508 - j0.1197 & 0.0292 + j0.0132 \end{bmatrix},$$

$$\boldsymbol{A}_3 = \begin{bmatrix} 0.2211 + j0.0577 & 0.0199 + j0.1525 & -0.0765 - j0.1902 & 0.0575 + j0.1131 \\ -0.0778 - j0.1356 & 0.1909 + j0.3095 & 0.0236 + j0.0644 & -0.4245 + j0.1366 \\ 0.1090 + j0.0910 & 0.0408 - j0.1472 & 0.0799 + j0.0783 & 0.0286 - j0.0572 \\ -0.1292 - j0.0042 & 0.3548 + j0.3113 & 0.2867 - j0.1579 & -0.1637 + j0.1812 \\ 0.1058 - j0.2537 & -0.2624 - j0.2824 & 0.1997 - j0.1218 & 0.1790 + j0.2486 \end{bmatrix},$$

$$\boldsymbol{A}_4 = \begin{bmatrix} -0.0282 - j0.2393 & 0.3850 - j0.0713 & 0.0913 - j0.1343 & -0.0872 + j0.1492 \\ -0.0260 - j0.1835 & -0.0977 + j0.0466 & -0.5107 - j0.3649 & 0.1013 + j0.0361 \\ -0.0419 - j0.0865 & 0.1136 + j0.0429 & 0.0632 - j0.2360 & -0.0080 - j0.1390 \\ -0.1791 - j0.1530 & 0.0492 + j0.0969 & -0.1680 + j0.1130 & -0.4623 - j0.1180 \\ -0.0010 + j0.1825 & -0.0174 - j0.0360 & 0.1042 - j0.3398 & -0.0214 + j0.1165 \end{bmatrix},$$

$$\boldsymbol{A}_5 = \begin{bmatrix} 0.1382 - j0.0500 & 0.2399 - j0.2041 & 0.2319 + j0.1167 & -0.3954 - j0.1628 \\ 0.1211 + j0.3607 & -0.0369 - j0.2112 & -0.0390 + j0.1760 & -0.1115 - j0.0483 \\ -0.1735 - j0.0626 & -0.0623 - j0.1190 & 0.2789 + j0.1505 & 0.1564 + j0.0542 \\ -0.1046 - j0.1687 & -0.1790 + j0.0256 & 0.0536 + j0.2667 & -0.0656 - j0.0695 \\ -0.3033 - j0.0822 & -0.0975 + j0.0686 & 0.4009 - j0.0772 & -0.3165 + j0.0974 \end{bmatrix},$$

$$\boldsymbol{A}_6 = \begin{bmatrix} 0.1814 + j0.2954 & -0.1230 + j0.0640 & -0.2277 - j0.1544 & -0.1114 - j0.2852 \\ 0.3138 - j0.1608 & -0.3478 + j0.0180 & 0.1845 - j0.0832 & 0.3224 + j0.1364 \\ -0.1385 - j0.2613 & 0.0413 + j0.0388 & 0.0999 + j0.1177 & 0.1467 - j0.1058 \\ 0.12693 - j0.1076 & 0.0389 - j0.1217 & -0.2866 - j0.4412 & -0.1287 + j0.0810 \\ 0.0057 + j0.0903 & 0.00811 - j0.1945 & 0.0294 - j0.0582 & 0.2687 + j0.0411 \end{bmatrix},$$

and the associated bit-to-matrix-selection rule of (C.5)

• Dispersion matrices for the BPSK-modulated GSTSK$(5, 2, 5, 6, 3)$ scheme

$$\boldsymbol{A}_1 = \begin{bmatrix} -0.0488 + j0.1681 & -0.1353 - j0.0483 & -0.2390 - j0.1659 & -0.1349 + j0.0635 & 0.0282 - j0.1922 \\ -0.0524 + j0.0457 & 0.1263 + j0.2016 & 0.0655 - j0.3611 & -0.2483 + j0.0863 & -0.1305 + j0.1512 \\ -0.2006 - j0.3723 & 0.1636 - j0.0280 & -0.2995 + j0.2503 & -0.2525 - j0.2474 & 0.2747 - j0.0132 \\ -0.1433 + j0.2768 & 0.3611 + j0.1365 & 0.0343 + j0.0379 & 0.0832 - j0.0517 & -0.2835 + j0.2252 \\ -0.0352 - j0.3038 & -0.1914 - j0.1246 & 0.0647 + j0.0446 & 0.0188 + j0.2014 & -0.0285 + j0.1521 \end{bmatrix},$$

$$\boldsymbol{A}_2 = \begin{bmatrix} 0.3819 - j0.0446 & 0.0506 + j0.1020 & -0.1416 + j0.2515 & 0.1114 - j0.1571 & -0.2598 - j0.2634 \\ -0.0419 - j0.2306 & -0.0351 + j0.0560 & -0.0246 - j0.0014 & -0.0354 + j0.0976 & -0.1820 - j0.0160 \\ 0.0473 + j0.0912 & -0.2928 - j0.0092 & -0.2890 - j0.0966 & 0.2459 - j0.1285 & -0.0284 - j0.0676 \\ 0.3645 + j0.0277 & 0.0705 - j0.0690 & 0.0952 + j0.0056 & 0.1678 - j0.1590 & 0.1080 + j0.1701 \\ -0.0490 + j0.2706 & -0.0723 - j0.0197 & -0.2819 - j0.0330 & -0.4517 + j0.2582 & -0.1552 - j0.4121 \end{bmatrix},$$

$$\boldsymbol{A}_3 = \begin{bmatrix} -0.1971 - j0.1078 & -0.0350 - j0.3357 & -0.0923 + j0.2260 & -0.1906 + j0.1219 & 0.1293 + j0.0204 \\ 0.0506 - j0.0723 & 0.2109 + j0.3246 & -0.0336 + j0.0628 & 0.3193 + j0.1169 & -0.1697 - j0.1459 \\ 0.3218 + j0.3106 & 0.1009 - j0.0086 & 0.0214 + j0.2083 & 0.0686 - j0.3666 & -0.1607 - j0.2984 \\ -0.0107 - j0.1805 & 0.0466 + j0.012 & -0.1263 + j0.3669 & 0.1606 - j0.0229 & 0.1155 + j0.1165 \\ 0.3187 + j0.1878 & -0.1101 + j0.0324 & -0.1620 + j0.1312 & -0.2173 - j0.2067 & 0.0385 - j0.1193 \end{bmatrix},$$

$$\boldsymbol{A}_4 = \begin{bmatrix} -0.0272 - j0.2562 & 0.0653 - j0.0915 & -0.0042 - j0.0913 & -0.2493 + j0.3238 & 0.0643 - j0.1089 \\ -0.1462 + j0.0059 & -0.0080 + j0.1454 & 0.1597 + j0.0843 & -0.1976 + j0.2288 & -0.0360 - j0.0101 \\ -0.1100 - j0.0510 & 0.1568 + j0.2616 & 0.5232 - j0.0619 & 0.1641 - j0.3815 & -0.1594 + j0.0006 \\ -0.0990 - j0.0210 & -0.1079 - j0.1503 & 0.15404 - j0.0373 & -0.0744 - j0.2765 & 0.0955 + j0.1713 \\ -0.0658 + j0.4534 & 0.3478 - j0.1252 & 0.0516 + j0.0591 & -0.0296 + j0.2239 & -0.1022 + j0.2024 \end{bmatrix},$$

$$\boldsymbol{A}_5 = \begin{bmatrix} -0.0789 + j0.0266 & 0.2389 - j0.2220 & 0.4173 + j0.0652 & -0.138 - j0.2097 & 0.2263 - j0.1195 \\ 0.2271 + j0.2986 & -0.0508 + j0.2381 & -0.0770 + j0.1208 & -0.0272 - j0.1688 & -0.2812 + j0.3714 \\ 0.1406 + j0.1556 & -0.1227 - j0.0836 & -0.0051 - j0.0294 & -0.0172 + j0.1625 & -0.1756 - j0.1372 \\ 0.0620 + j0.4403 & 0.2982 - j0.0238 & -0.0368 - j0.0086 & -0.0451 + j0.1598 & 0.1943 + j0.1487 \\ -0.0825 - j0.2026 & 0.2541 - j0.0030 & 0.0137 + j0.2108 & -0.3113 + j0.0104 & -0.0201 + j0.0764 \end{bmatrix},$$

$$\boldsymbol{A}_6 = \begin{bmatrix} -0.0595 - j0.0853 & -0.2188 + j0.3854 & 0.1346 - j0.0560 & 0.1161 + j0.1596 & 0.0007 - j0.2782 \\ -0.2173 - j0.0491 & 0.1468 + j0.0724 & 0.1661 + j0.2498 & 0.0547 - j0.4447 & 0.3081 - j0.4184 \\ 0.3241 + j0.1814 & 0.0632 - j0.0071 & -0.3282 - j0.0101 & 0.0543 + j0.0679 & 0.1005 + j0.0578 \\ -0.0153 + j0.2054 & -0.0635 + j0.1576 & -0.022 + j0.1905 & -0.1192 + j0.0429 & 0.2222 + j0.0938 \\ 0.2248 + j0.0475 & 0.1474 + j0.0996 & -0.0113 - j0.1362 & -0.0540 + j0.1387 & 0.3106 + j0.0990 \end{bmatrix},$$

and the associated bit-to-matrix-selection rule of (C.5)

Glossary

3G	Third Generation
ACO	Ant-Colony Optimization
ACSTSK	Asynchronous Coherent Space-Time Shift Keying
ADSTSK	Asynchronous Differential Space-Time Shift Keying
AEs	Antenna Elements
AF	Amplify-and-Forward
ASK	Amplitude-Shift Keying
AWGNs	Additive White Gaussian Noises
BER	Bit-Error Rate
BLAST	Bell Labs Layered Space-Time
BLER	BLock Error Ratio
BS	Base Station
CC	Convolutional Channel
CCMC	Continuous-input Continuous-output Memoryless Channel
CDMA	Code-Division Multiple Access
CDSTS	Cooperative Differential Space-Time Spreading
CIRs	Channel Impulse Responses
CRC	Cyclic Redundancy Check
CSI	Channel State Information
CSTSK	Coherent Space-Time Shift Keying

D/A	Digital-to-Analog
DCMC	Discrete-input Continuous-output Memoryless Channel
DF	Decode-and-Forward
DLDC	Differential Linear Dispersion Code
DOAs	Directions-of-Arrival
DODs	Directions-of-Departure
DOSTBC	Differential Orthogonal Space-Time Block Code
DPSK	Differential Phase-Shift Keying
DS-CDMA	Direct-Sequence Code-Division Multiple Access
DSTCs	Differential Space-Time Codes
DSTSK	Differential Space-Time Shift Keying
DTC	Distributed Turbo Coding
EGC	Equal Gain Combining
EXIT	EXtrinsic Information Transfer
FDMA	Frequency-Division Multiple Access
FEC	Forward Error Correction
GA	Genetic Algorithm
GSTSK	Generalized Space-Time Shift Keying
IAI	Inter-Antenna Interference
IAS	Inter-Antenna Synchronization
ICI	Inter-Channel Interference
IEI	Inter-Element Interference
IFW	Interference-Free Window
IIR	Infinite Impulse Response
IRS	Inter-Relay Synchronization
ISI	Inter-Symbol Interference
LBER	Least Bit-Error Rate

LDC	Linear Dispersion Code
LLR	Log-Likelihood Ratio
LMS	Least Mean Square
LS	Loosely Synchronized
LTE	Long-Term Evolution
MAC	Medium Access Control
MAI	Multiple Access Interference
MAP	Maximum A Priori
MBER	Minimum Bit-Error Rate
MC	Multi-Carrier
MC-MBER	Markov Chain assisted Minimum Bit-Error Rate
MCMC	Markov Chain Monte Carlo
MGFs	Moment-Generating Functions
MIMO	Multiple-Input Multiple Output
ML	Maximum Likelihood
MMSE	Minimum Mean-Square Error
MPI	Multi-Path Interference
MRC	Maximum-Ratio Combining
MS	Mobile Station
MSDD	Multiple-Symbol Differential Detection
MU-MIMO	Multi-User Multiple-Input Multiple-Output
MUD	Multi-User Detection
MUT	Multi-User Transmission
OSTBCs	Orthogonal Space-Time Block Codes
PAM	Palse Amplitude Modulation
PDF	Probability Density Function
PSK	Phase-Shift Keying

PSO	Particle Swarm Optimization
QAM	Quadrature Amplitude Modulation
QOSTBCs	Quasi-Orthogonal Space-Time Block Codes
RD	Relay-Destination
RLS	Recursive Least Square
RN	Relay Node
RSC	Recursive Systematic Convolutional
S/P	Serial-to-Parallel
SC	Selection Combining
SCG	Simplified Conjugate Gradient
SD	Sphere Detection
SDM	Space Division Multiplexing
SDMA	Space Division Multiple Access
SIR	Signal-to-Interference Ratio
SISO	Soft-Input Soft-Output
SM	Spatial Modulation
SN	Source Node
SNR	Signal-to-Noise Ratio
SR	Source-Relay
SSK	Space-Shift Keying
ST	Space-Time
STBCs	Space-Time Block Codes
STCs	Space-Time Codes
STE	Space-Time Equalization
STS	Space-Time Spreading
STSK	Space-Time Shift Keying
STTCs	Space-Time Trellis Codes

TASTBCs	Threaded Algebraic Space-Time Block Codes
TD-CDMA	Time-Division and Code-Division Multiple Access
TDMA	Time-Division Multiple Access
TVLT	Time Variant Linear Transformation
UL	UpLink
URC	Unity-Rate Convolutional
USTM	Unitary Space-Time Modulation
VAA	Virtual Antenna Array
WiMAX	Worldwide interoperability for Microwave Access
ZF	Zero-Forcing

Bibliography

[1] S. Sugiura, S. Chen, and L. Hanzo, "Coherent and differential space-time shift keying: a dispersion matrix approach," *IEEE Transactions on Communications*, 2011. in press.

[2] S. Sugiura, S. Chen, and L. Hanzo, "Distributed differential space-time spreading for the asynchronous relay aided interference-free cooperative CDMA uplink," in *IEEE International Conference on Communications*, (Cape Town, South Africa), pp. 1–5, May 2010.

[3] S. Sugiura, S. X. Ng, L. Kong, S. Chen, and L. Hanzo, "Multiple-relay aided distributed turbo coding assisted unitary differential space-time spreading for asynchronous cooperative networks," in *IEEE 71st Vehicular Technology Conference (VTC2010-Spring)*, (Taipei, Taiwan), pp. 1–5, May 2010.

[4] S. Sugiura, S. Chen, and L. Hanzo, "Cooperative differential space-time spreading for the asynchronous relay aided CDMA uplink using interference rejection spreading code," *IEEE Signal Processing Letters*, vol. 17, no. 2, pp. 117–120, 2010.

[5] S. Sugiura, D. Yang, S. Chen, L.-L. Yang, and L. Hanzo, "Effect of array geometry on the capacity of the turbo-coded beamforming uplink," in *IEEE 70th Vehicular Technology Conference (VTC2009-Fall)*, (Anchorage, Alaska), pp. 1–4, September 2009.

[6] S. Sugiura and L. Hanzo, "Iterative detection assisted cooperative vehicular ad hoc networking using differential linear dispersion coding," in *IEEE 70th Vehicular Technology Conference (VTC2009-Fall)*, (Anchorage, Alaska), pp. 1–5, September 2009.

[7] S. Sugiura, S. Chen, and L. Hanzo, "Markov chain minimum bit error rate detection for multi-functional MIMO systems," in *IEEE International Conference on Communications*, (Dresden, Germany), pp. 1–5, June 2009.

[8] S. Sugiura, N. Wu, and L. Hanzo, "Improved Markov chain MBER detection for steered linear dispersion coded MIMO systems," in *IEEE 69th Vehicular Technology Conference (VTC2009-Spring)*, (Barcelona, Spain), pp. 1–5, April 2009.

[9] S. Sugiura, S. Chen, and L. Hanzo, "Reduced-complexity iterative Markov chain MBER detection for MIMO systems," *IEEE Signal Processing Letters*, vol. 16, pp. 160–163, March 2009.

[10] S. Sugiura, S. Chen, and L. Hanzo, "A unified MIMO architecture subsuming space shift keying, OSTBC, BLAST and LDC," in *IEEE 72nd Vehicular Technology Conference (VTC2010-Fall)*, (Ottawa, Canada), pp. 1–5, 6–9 September 2010.

[11] S. Sugiura, S. Chen, and L. Hanzo, "Space-time shift keying: A unified MIMO architecture," in *IEEE Global Telecommunications Conference*, (Miami, Florida, USA), 6–10 December 2010. in press.

[12] S. Sugiura, S. Chen, and L. Hanzo, "Packet-reliability based decode-and-forward relaying aided distributed space-time shift keying," in *IEEE Global Telecommunications Conference*, (Miami, Florida, USA), 6–10 December 2010. in press.

[13] S. Sugiura, S. Chen, and L. Hanzo, "CRC-activated decode-and-forward relaying aided distributed space-time shift keying," *IEEE Transactions on Vehicular Technology*, 2010. submitted.

[14] S. Sugiura, S. X. Ng, L. Kong, S. Chen, and L. Hanzo, "Multiple-relay aided differential distributed turbo coding for asynchronous cooperative networks," *IEEE Transactions on Vehicular Technology*, 2010. submitted.

[15] S. Sugiura, S. Chen, and L. Hanzo, "Generalized space-time shift keying designed for flexible diversity-, multiplexing- and complexity-tradeoffs," *IEEE Transactions on Wireless Communications*, 2010. submitted.

[16] S. Chen, S. Sugiura, and L. Hanzo, "Semi-blind joint channel estimation and data detection for space-time shift keying systems," *IEEE Signal Processing Letters*, 2010. submitted.

[17] G. J. Foschini, "Layered space-time architecture for wireless communication in a fading environment when using multi-element antennas," *Bell Labs Technical Journal*, vol. 1, no. 2, pp. 41–59, 1996.

[18] G. J. Foschini and M. J. Gans, "On limits of wireless communications in a fading environment when using multiple antennas," *Wireless Personal Communications*, vol. 6, no. 3, pp. 311–335, 1998.

[19] I. E. Telatar, "Capacity of multi-antenna Gaussian channels," *European transactions on telecommunications*, vol. 10, no. 6, pp. 585–595, 1999.

[20] S. M. Alamouti, "A simple transmit diversity technique for wireless communications," *IEEE Journal on Selected Areas in Communications*, vol. 16, no. 8, pp. 1451–1458, 1998.

[21] V. Tarokh, H. Jafarkhani, and A. R. Calderbank, "Space-time block codes from orthogonal designs," *IEEE Transactions on Information Theory*, vol. 45, no. 5, pp. 1456–1467, 1999.

[22] V. Tarokh, N. Seshadri, and A. R. Calderbank, "Space-time codes for high data rate wireless communication: performance criterion and code construction," *IEEE Transactions on Information Theory*, vol. 44, no. 2, pp. 744–765, 1998.

[23] L. Hanzo, O. Alamri, M. El-Hajjar, and N. Wu, *Near-capacity Multi-functional MIMO Systems: Sphere-packing, Iterative Detection and Cooperation*. John Wiley and IEEE Press, 2009.

[24] L. Hanzo, J. Blogh, and S. Ni, *3G, HSPA and FDD versus TDD Networking: Smart Antennas and Adaptive Modulation*. John Wiley and IEEE Press, 2008.

[25] A. Ghosh, D. R. Wolter, J. G. Andrews, and R. Chen, "Broadband wireless access with WiMax/802.16: current performance benchmarks and future potential," *IEEE Communications Magazine*, vol. 43, no. 2, pp. 129–136, 2005.

[26] H. Ekstrom, A. Furuskar, J. Karlsson, M. Meyer, S. Parkvall, J. Torsner, M. Wahlqvist, E. Res, and G. Aachen, "Technical solutions for the 3G long-term evolution," *IEEE Communications Magazine*, vol. 44, no. 3, pp. 38–45, 2006.

[27] L. Hanzo, T. H. Liew, and B. L. Yeap, *Turbo Coding, Turbo Equalisation, and Space-Time Coding for Transmission over Fading Channels*. John Wiley and IEEE Press, 2002.

[28] A. Goldsmith, *Wireless communications*. Cambridge University Press, 2005.

[29] D. G. Brennan, "Linear diversity combining techniques," *Proceedings of the IRE*, vol. 47, no. 6, pp. 1075–1102, 1959.

[30] A. Goldsmith, "Capacity of Rayleigh fading channels under different adaptive transmission and diversity-combining techniques," *IEEE Transactions on Vehicular Technology*, vol. 48, no. 4, pp. 1165–1181, 1999.

[31] A. Wittneben, "Basestation modulation diversity for digital SIMULCAST," in *41st IEEE Vehicular Technology Conference*, (St. Louis, MO), pp. 848–853, 1991.

[32] N. Seshadri and J. H. Winters, "Two signaling schemes for improving the error performance of frequency-division-duplex (FDD) transmission systems using transmitter antenna diversity," in *43rd IEEE Vehicular Technology Conference*, (Secaucus, NJ), pp. 508–511, 1993.

[33] V. Tarokh, H. Jafarkhani, and A. R. Calderbank, "Space-time block coding for wireless communications: performance results," *IEEE Journal on selected areas in communications*, vol. 17, no. 3, pp. 451–460, 1999.

[34] H. Jafarkhani, "A quasi-orthogonal space-time block code," *IEEE Transactions on Communications*, vol. 49, no. 1, pp. 1–4, 2001.

[35] Y. Xin, Z. Wang, and G. B. Giannakis, "Space–time diversity systems based on linear constellation precoding," *IEEE Transactions on Wireless Communications*, vol. 2, no. 2, 2003.

[36] H. E. Gamal and M. O. Damen, "Universal space-time coding," *IEEE Transactions on Information Theory*, vol. 49, no. 5, pp. 1097–1119, 2003.

[37] V. Tarokh, N. Seshadri, and A. R. Calderbank, "Space-time codes for high data rate wireless communication: Performance criterion and code construction," *IEEE Transactions on Information Theory*, vol. 44, no. 2, pp. 744–765, 1998.

[38] L. Hanzo, S. X. Ng, T. Keller, and W. Webb, *Quadrature Amplitude Modulation: From Basics to Adaptive Trellis-Coded, Turbo-Equalised and Space-Time Coded OFDM, CDMA and MC-CDMA Systems*. John Wiley and IEEE Press, 2004.

[39] B. Hochwald, T. L. Marzetta, and G. B. Papadias, "A transmitter diversity scheme for wideband CDMA systems based on space-time spreading," *IEEE Journal on Selected Areas in Communications*, vol. 19, no. 1, pp. 48–60, 2001.

[40] V. Tarokh and H. Jafarkhani, "A differential detection scheme for transmit diversity," *IEEE Journal on Selected Areas in Communications*, vol. 18, no. 7, pp. 1169–1174, 2000.

[41] B. M. Hochwald and T. L. Marzetta, "Unitary space-time modulation for multiple-antenna communications in Rayleigh flat fading," *IEEE transactions on Information Theory*, vol. 46, no. 2, pp. 543–564, 2000.

[42] B. L. Hughes, "Differential space-time modulation," *IEEE Transactions on Information Theory*, vol. 46, no. 7, pp. 2567–2578, 2000.

[43] Z. Liu, G. B. Giannakis, and B. L. Hughes, "Double differential space-time block coding for time-selective fading channels," *IEEE Transactions on Communications*, vol. 49, no. 9, pp. 1529–1539, 2001.

[44] R. Schober and L. H. J. Lampe, "Noncoherent receivers for differential space-time modulation," *IEEE Transactions on Communications*, vol. 50, no. 5, pp. 768–777, 2002.

[45] Y. Zhu and H. Jafarkhani, "Differential modulation based on quasi-orthogonal codes," *IEEE Transactions on Wireless Communications*, vol. 4, no. 6, pp. 3005–3017, 2005.

[46] G. J
"ongren and M. Skoglund, "Quantized feedback information in orthogonal space-time block coding," *IEEE Transactions on Information Theory*, vol. 50, no. 10, pp. 2473–2486, 2004.

[47] M. Vu and A. Paulraj, "Optimal linear precoders for MIMO wireless correlated channels with nonzero mean in space-time coded systems," *IEEE Transactions on Signal Processing*, vol. 54, no. 6, pp. 2318–2332, 2006.

[48] W. Zhang, X. G. Xia, and P. C. Ching, "High-rate full-diversity space-time-frequency codes for broadband mimo block-fading channels," *IEEE Transactions on Communications*, vol. 55, no. 1, pp. 25–34, 2007.

[49] H. Shin and M. Z. Win, "MIMO diversity in the presence of double scattering," *IEEE Transactions on Information Theory*, vol. 54, no. 7, pp. 2976–2996, 2008.

[50] T. T. Kim and G. Caire, "Diversity gains of power control with noisy CSIT in MIMO channels," *IEEE Transactions on Information Theory*, vol. 55, no. 4, pp. 1618–1626, 2009.

[51] H. Wang, J. Lee, S. Kim, and D. Hong, "Capacity enhancement of secondary links through spatial diversity in spectrum sharing," *IEEE Transactions on Wireless Communications*, vol. 9, no. 2, pp. 494–499, 2010.

[52] P. W. Wolniansky, G. J. Foschini, G. D. Golden, and R. A. Valenzuela, "V-BLAST: An architecture for realizing very high data rates over the rich-scattering wireless channel," in *Proceedings of the International Symposium on Signals, Systems, and Electronics (ISSSE'98)*, (Pisa, Italy), pp. 295–300, 1998.

[53] P. W. Golden, C. J. Foschini, R. Valenzuela, and P. W. Wolniansky, "Detection algorithm and initial laboratory results using V-BLAST space-time communication architecture," *Electronics Letters*, vol. 35, no. 1, pp. 14–16, 1999.

[54] E. Viterbo and J. Boutros, "A universal lattice code decoder for fading channels," *IEEE Transactions on Information Theory*, vol. 45, no. 5, pp. 1639–1642, 1999.

[55] F. Hasegawa, J. Luo, K. R. Pattipati, P. Willett, and D. Pham, "Speed and accuracy comparison of techniques for multiuser detection in synchronous CDMA," *IEEE Transactions on Communications*, vol. 52, no. 4, pp. 540–545, 2004.

[56] H. Sampath, P. Stoica, and A. Paulraj, "Generalized linear precoder and decoder design for MIMO channels using the weighted MMSE criterion," *IEEE Transactions on Communications*, vol. 49, no. 12, pp. 2198–2206, 2001.

[57] G. J. Foschini and M. J. Gans, "On limits of wireless communications in a fading environment when using multiple antennas," *Wireless personal communications*, vol. 6, no. 3, pp. 311–335, 1998.

[58] C. E. Shannon, "A mathematical theory of communication," *ACM SIGMOBILE Mobile Computing and Communications Review*, vol. 5, no. 1, pp. 3–55, 2001.

[59] S. X. Ng and L. Hanzo, "On the MIMO channel capacity of multidimensional signal sets," *IEEE Transactions on Vehicular Technology*, vol. 55, no. 2, pp. 528–536, 2006.

[60] R. Mesleh, H. Haas, C. W. Ahn, and S. Yun, "Spatial modulation – a new low complexity spectral efficiency enhancing technique," in *First International Conference on Communications and Networking (CHINACOM)*, (Beijing, China), pp. 1–5, Oct. 2006.

[61] R. Mesleh, H. Haas, S. Sinanovic, C. W. Ahn, and S. Yun, "Spatial modulation," *IEEE Transactions on Vehicular Technology*, vol. 57, no. 4, pp. 2228–2242, 2008.

[62] Y. A. Chau and S.-H. Yu, "Space modulation on wireless fading channels," in *IEEE 54th Vehicular Technology Conference (VTC2001-Fall)*, vol. 3, pp. 1668–1671, 2001.

[63] J. Jeganathan, A. Ghrayeb, and L. Szczecinski, "Spatial modulation: optimal detection and performance analysis," *IEEE Communications Letters*, vol. 12, no. 8, pp. 545–547, 2008.

[64] R. Mesleh, S. Engelken, S. Sinanovic, and H. Haas, "Analytical SER calculation of spatial modulation," in *IEEE 10th International Symposium on Spread Spectrum Techniques and Applications*, (Bologna, Italy), pp. 272–276, 25–28, August 2008.

[65] R. Mesleh, S. Ganesan, and H. Haas, "Impact of channel imperfections on spatial modulation OFDM," in *IEEE 18th International Symposium on Personal, Indoor and Mobile Radio Communications*, (Athens, Greece), pp. 1–5, 3-6 September 2007.

[66] J. Jeganathan, A. Ghrayeb, L. Szczecinski, and A. Ceron, "Space shift keying modulation for MIMO channels," *IEEE Transactions on Wireless Communications*, vol. 8, no. 7, pp. 3692–3703, 2009.

[67] R. Mesleh, I. Stefan, H. Haas, and P. M. Grant, "On the performance of trellis coded spatial modulation," in *International ITG Workshop on Smart Antennas*, (Berlin, Germany), pp. 1–8, 16–18 February 2009.

[68] J. Jeganathan, A. Ghrayeb, and L. Szczecinski, "Generalized space shift keying modulation for MIMO channels," in *IEEE 19th International Symposium on Personal, Indoor and Mobile Radio Communications (PIMRC)*, (Cannes, France), pp. 1–5, 2008.

[69] I. E. Telatar, "Capacity of multi-antenna Gaussian channels," *European Transactions on Telecommunications*, vol. 10, no. 6, pp. 585–595, 1999.

[70] S. L. Ariyavisitakul, "Turbo space-time processing to improve wireless channel capacity," *IEEE Transactions on communications*, vol. 48, no. 8, pp. 1347–1359, 2000.

[71] H. Bolckei, D. Gesbert, and A. J. Paulraj, "On the capacity of OFDM-based spatial multiplexing systems," *IEEE Transactions on Communications*, vol. 50, no. 2, pp. 225–234, 2002.

[72] A. Gorokhov, D. A. Gore, and A. J. Paulraj, "Receive antenna selection for MIMO spatial multiplexing: theory and algorithms," *IEEE Transactions on signal processing*, vol. 51, no. 11, 2003.

[73] H. Vikalo, B. Hassibi, and T. Kailath, "Iterative decoding for MIMO channels via modified sphere decoding," *IEEE Transactions on Wireless Communications*, vol. 3, no. 6, pp. 2299–2311, 2004.

[74] M. Sharif and B. Hassibi, "On the capacity of MIMO broadcast channels with partial side information," *IEEE Transactions on Information Theory*, vol. 51, no. 2, pp. 506–522, 2005.

[75] J. G. Andrews, W. Choi, and R. W. H. Jr, "Overcoming interference in spatial multiplexing MIMO cellular networks," *IEEE Wireless Communications*, vol. 14, no. 6, 2007.

[76] C. Studer, A. Burg, and H. Bolcskei, "Soft-output sphere decoding: Algorithms and VLSI implementation," *IEEE Journal on Selected Areas in Communications*, vol. 26, no. 2, pp. 290–300, 2008.

[77] J. Zhang, R. Chen, J. G. Andrews, A. Ghosh, and R. W. H. Jr, "Networked MIMO with clustered linear precoding," *IEEE Transactions on Wireless Communications*, vol. 8, no. 4, pp. 1910–1921, 2009.

[78] J. Xu, R. Hormis, and X. Wang, "MIMO video broadcast via transmit-precoding and SNR-scalable video coding," *IEEE Journal on Selected Areas in Communications*, vol. 28, no. 3, pp. 456–466, 2010.

[79] T. Handte, A. Muller, and J. Speidel, "BER analysis and optimization of generalized spatial modulation in correlated fading channels," in *IEEE 70th Vehicular Technology Conference (VTC 2009-Fall)*, pp. 1 –5, sept. 2009.

[80] M. D. Renzo and H. Haas, "On the performance of SSK modulation over correlated Nakagami-m fading channels," in *IEEE International Conference on Communications*, (Cape Town, South Africa), pp. 1–5, May 2010.

[81] M. Jiang and L. Hanzo, "Multiuser MIMO-OFDM for next-generation wireless systems," *Proceedings of the IEEE*, vol. 95, no. 7, pp. 1430–1469, 2007.

[82] A. Paulraj, R. Nabar, and D. Gore, *Introduction to Space-Time Wireless Communications*. Cambridge University Press, 2003.

[83] L. C. Godara, "Applications of antenna arrays to mobile communications I: Performance improvement, feasibility, and system considerations," *Proceedings of the IEEE*, vol. 85, no. 7, pp. 1031–1060, 1997,.

[84] L. C. Godara, "Application of antenna arrays to mobile communications II: Beam-forming and direction-of-arrival considerations," *Proceedings of the IEEE*, vol. 85, no. 8, pp. 1195–1245, 1997.

[85] J. H. Winters, "Smart antennas for wireless systems," *IEEE Personal Communications*, vol. 5, no. 1, pp. 23–27, 1998.

[86] L. Zheng and D. N. C. Tse, "Diversity and multiplexing: a fundamental tradeoff in multiple-antenna channels," *IEEE Transactions on Information Theory*, vol. 49, no. 5, pp. 1073–1096, 2003.

[87] V. Tarokh, A. Naguib, N. Seshadri, and A. R. Calderbank, "Combined array processing and space-time coding," *IEEE Transactions on Information Theory*, vol. 45, no. 4, pp. 1121–1128, 1999.

[88] B. Hassibi and B. M. Hochwald, "High-rate codes that are linear in space and time," *IEEE Transactions on Information Theory*, vol. 48, no. 7, pp. 1804–1824, 2002.

[89] B. Hassibi and B. M. Hochwald, "Cayley differential unitary space-time codes," *IEEE Transactions on Information Theory*, vol. 48, no. 6, pp. 1485–1503, 2002.

[90] G. Jongren, M. Skoglund, and B. Ottersten, "Combining beamforming and orthogonal space-time block coding," *IEEE Transactions on Information Theory*, vol. 48, no. 3, pp. 611–627, 2002.

[91] M. Tao and R. S. Cheng, "Generalized layered space-time codes for high data rate wireless communications," *IEEE Transactions on Wireless Communications*, vol. 3, no. 4, pp. 1067–1075, 2004.

[92] M. El-Hajjar, B. Hu, L.-L. Yang, and L. Hanzo, "Coherent and differential downlink space-time steering aided generalised multicarrier DS-CDMA," *IEEE Transactions on Wireless Communications*, vol. 6, pp. 3857–3863, November 2007.

[93] R. W. Heath and A. J. Paulraj, "Linear dispersion codes for MIMO systems based on frame theory," *IEEE Transactions on Signal Processing*, vol. 50, no. 10, pp. 2429–2441, 2002.

[94] R. W. Heath and A. J. Paulraj, "Switching between diversity and multiplexing in MIMO systems," *IEEE Transactions on Communications*, vol. 53, no. 6, pp. 962–968, 2005.

[95] H. E. Gamal, G. Caire, and M. O. Damen, "The MIMO ARQ channel: Diversity-multiplexing-delay tradeoff," *IEEE Transactions on Information Theory*, vol. 52, no. 8, pp. 3601–3621, 2006.

[96] M. El-Hajjar and L. Hanzo, "Layered steered space-time codes and their capacity," *Electronics Letters*, vol. 43, no. 12, pp. 680–682, 2007.

[97] A. Sezgin, E. A. Jorswieck, and E. Costa, "LDC in MIMO Ricean channels: Optimal transmit strategy with MMSE detection," *IEEE Transactions on Signal Processing*, vol. 56, no. 1, pp. 313–328, 2008.

[98] N. Wu and L. Hanzo, "Near-capacity irregular-convolutional-coding-aided irregular precoded linear dispersion codes," *IEEE Transactions on Vehicular Technology*, vol. 58, no. 6, pp. 2863–2871, 2009.

[99] T. Cover and A. E. Gamal, "Capacity theorems for the relay channel," *IEEE Transactions on Information Theory*, vol. 25, no. 5, pp. 572–584, 1979.

[100] A. Sendonaris, E. Erkip, and B. Aazhang, "Increasing uplink capacity via user cooperation diversity," in *IEEE International Symposium on Information Theory*, (Cambridge, MA), p. 156, 1998.

[101] J. N. Laneman and G. W. Wornell, "Energy-efficient antenna sharing and relaying for wireless networks," in *IEEE Wireless Communications and Networking Conference (WCNC)*, vol. 1, (Chicago, IL), pp. 7–12, 2000.

[102] M. Dohler, E. Lefranc, and H. Aghvami, "Space-time block codes for virtual antenna arrays," in *13th IEEE International Symposium on Personal, Indoor and Mobile Radio Communications (PIMRC)*, vol. 1, (Lisbon, Portugal), 2002.

[103] A. Sendonaris, E. Erkip, B. Aazhang, Q. Inc, and C. A. Campbell, "User cooperation diversity. Part I. System description," *IEEE Transactions on Communications*, vol. 51, no. 11, pp. 1927–1938, 2003.

[104] A. Sendonaris, E. Erkip, B. Aazhang, Q. Inc, and C. A. Campbell, "User cooperation diversity. Part II. Implementation aspects and performance analysis," *IEEE Transactions on Communications*, vol. 51, no. 11, pp. 1939–1948, 2003.

[105] J. N. Laneman and G. W. Wornell, "Distributed space-time-coded protocols for exploiting cooperative diversity in wireless networks," *IEEE Transactions on Information Theory*, vol. 49, no. 10, pp. 2415–2425, 2003.

[106] B. Zhao and M. C. Valenti, "Distributed turbo coded diversity for relay channel," *Electronics letters*, vol. 39, p. 786, 2003.

[107] J. N. Laneman and D. N. C. Tse and G. W. Wornell, "Cooperative diversity in wireless networks: Efficient protocols and outage behavior," *IEEE Transactions on Information theory*, vol. 50, no. 12, pp. 3062–3080, 2004.

[108] M. Janani, A. Hedayat, T. E. Hunter, and A. Nosratinia, "Coded cooperation in wireless communications: space-time transmission and iterative decoding," *IEEE Transactions on Signal Processing*, vol. 52, no. 2, pp. 362–371, 2004.

[109] R. U. Nabar, H. Bolcskei, and F. W. Kneubuhler, "Fading relay channels: performance limits and space-time signal design," *IEEE Journal on Selected Areas in Communications*, vol. 22, no. 6, pp. 1099–1109, 2004.

[110] P. Tarasak, H. Minn, and V. K. Bhargava, "Differential modulation for two-user cooperative diversity systems," *IEEE Journal on Selected Areas in Communications*, vol. 23, no. 9, pp. 1891–1900, 2005.

[111] A. Bletsas, A. Khisti, D. P. Reed, and A. Lippman, "A simple cooperative diversity method based on network path selection," *IEEE Journal on Selected Areas in Communications*, vol. 24, no. 3, pp. 659–672, 2006.

[112] Y. Jing and B. Hassibi, "Distributed space-time coding in wireless relay networks," *IEEE Transactions on Wireless Communications*, vol. 5, no. 12, p. 3524, 2006.

[113] Y. Li, B. Vucetic, T. F. Wong, and M. Dohler, "Distributed turbo coding with soft information relaying in multihop relay networks," *IEEE Journal on Selected Areas in Communications*, vol. 24, no. 11, pp. 2040–2050, 2006.

[114] L. Xiao, T. E. Fuja, J. Kliewer, and J. Costello, "A network coding approach to cooperative diversity," *IEEE Transactions on information theory*, vol. 53, no. 10, p. 3714, 2007.

[115] A. Bletsas, H. Shin, and M. Z. Win, "Cooperative communications with outage-optimal opportunistic relaying," *IEEE Transactions on Wireless Communications*, vol. 6, no. 9, pp. 3450–3460, 2007.

[116] Y. Jing and H. Jafarkhani, "Distributed differential space-time coding for wireless relay networks," *IEEE Transactions on Communications*, vol. 56, no. 7, pp. 1092–1100, 2008.

[117] B. Sirkeci-Mergen and A. Scaglione, "Randomized space-time coding for distributed cooperative communication," *IEEE Transactions on Signal Processing*, vol. 55, no. 10, pp. 5003–5017, 2007.

[118] V. Tarokh and H. Jafarkhani, "A differential detection scheme for transmit diversity," *IEEE Journal on Selected Areas in Communications*, vol. 18, no. 7, pp. 1169–1174, 2000.

[119] T. Himsoon, W. Su, and K. J. R. Liu, "Differential transmission for amplify-and-forward cooperative communications," *IEEE Signal Processing Letters*, vol. 12, pp. 597–600, Sept. 2005.

[120] G. Wang, Y. Zhang, and M. Amin, "Differential distributed space–time modulation for cooperative networks," *IEEE Transactions on Wireless Communications*, vol. 5, no. 11, p. 3097, 2006.

[121] F. Willems, "The discrete memoryless multiple access channel with partially cooperating encoders," *IEEE Transactions on Information Theory*, vol. 29, no. 3, pp. 441–445, 1983.

[122] S. Wei, D. L. Goeckel, and M. C. Valenti, "Asynchronous cooperative diversity," *IEEE Transactions on Wireless Communications*, vol. 5, no. 6, pp. 1547–1557, 2006.

[123] S. W. KIM, "Randomized parity forwarding in large-scale cooperative broadcast network," *IEEE transactions on communications*, vol. 58, no. 3, pp. 860–868, 2010.

[124] M. D. Renzo and H. Haas, "Performance comparison of different spatial modulation schemes in correlated fading channels," in *IEEE International Conference on Communications*, (Cape Town, South Africa), pp. 1–6, May 2010.

[125] L. Hanzo, L.-L. Yang, E.-L. Kuan, and K. Yen, *Single and Multi-carrier DS-CDMA: Multi-user Detection, Space-time Spreading, Synchronisation, Networking, and Standards*. John Wiley and IEEE Press, 2003.

[126] L. Hanzo, M. Münster, B. J. Choi, and T. Keller, *OFDM and MC-CDMA for Broadband Multi-User Communications, WLANs and Broadcasting*. John Wiley and IEEE Press, 2003.

[127] B. Farhang-Boroujeny, H. Zhu, and Z. Shi, "Markov chain Monte Carlo algorithms for CDMA and MIMO communication systems," *IEEE Transactions on Signal Processing*, vol. 54, no. 5, pp. 1896–1909, 2006.

[128] M. Dorigo and T. Stützle, *Ant Colony Optimization*. MIT Press, 2004.

[129] D. Divsalar, S. Dolinar, and F. Pollara, "Serial concatenated trellis coded modulation with rate-1 inner code," in *IEEE Global Telecommunications Conference*, vol. 2, (San Francisco, CA), pp. 777–782, November–December 2000.

[130] S. ten Brink, "Convergence behavior of iteratively decoded parallel concatenated codes," *IEEE Transactions on Communications*, vol. 49, no. 10, pp. 1727–1737, 2001.

[131] J. G. Proakis, *Digital communications*. McGraw-Hill, New York, 2001.

[132] V. Tarokh, H. Jafarkhani, and A. R. Calderbank, "Space-time block coding for wireless communications: performance results," *IEEE Journal on Selected Areas in Communications*, vol. 17, no. 3, pp. 451–460, 1999.

[133] A. Ashikhmin, G. Kramer, and S. ten Brink, "Extrinsic information transfer functions: model and erasure channel properties," *IEEE Transactions on Information Theory*, vol. 50, no. 11, pp. 2657–2673, 2004.

[134] M. Tüchler, "Design of serially concatenated systems depending on the block length," *IEEE Transactions on Communications*, vol. 52, no. 2, pp. 209–218, 2004.

[135] H. Jafarkhani and V. Tarokh, "Multiple transmit antenna differential detection from generalized orthogonal designs," *IEEE Transactions on Information Theory*, vol. 47, no. 6, pp. 2626–2631, 2001.

[136] B. M. Hochwald and W. Sweldens, "Differential unitary space-time modulation," *IEEE Transactions on Communications*, vol. 48, no. 12, pp. 2041–2052, 2000.

[137] C. S. Hwang, S. H. Nam, J. Chung, and V. Tarokh, "Differential space time block codes using nonconstant modulus constellations," *IEEE Transactions on Signal Processing*, vol. 51, no. 11, pp. 2955–2964, 2003.

[138] M. K. Simon and M. S. Alouini, *Digital communication over fading channels*. Wiley-IEEE Press, 2005.

[139] A. Hedayat, H. Shah, and A. Nosratinia, "Analysis of space-time coding in correlated fading channels," *IEEE Transactions on Wireless Communications*, vol. 4, no. 6, pp. 2882–2891, 2005.

[140] J. Wang, X. Wang, and M. Madihian, "On the optimum design of space-time linear-dispersion codes," *IEEE Transactions on Wireless Communications*, vol. 4, no. 6, pp. 2928–2938, 2005.

[141] W. C. Jakes and D. C. Cox, *Microwave Mobile Communications*. John Wiley and IEEE Press, 1994.

[142] R. C. Palat, A. Annamalai, and J. H. Reed, "Accurate bit-error-rate analysis of bandlimited cooperative OSTBC networks under timing synchronization errors," *IEEE Transactions on Vehicular Technology*, vol. 58, no. 5, pp. 2191–2200, 2009.

[143] X. Li, "Space-time coded multi-transmission among distributed transmitters without perfect synchronization," *IEEE Signal Processing Letters*, vol. 11, no. 12, pp. 948–951, 2004.

[144] Y. Li and X. G. Xia, "A family of distributed space-time trellis codes with asynchronous cooperative diversity," *IEEE Transactions on Communications*, vol. 55, no. 4, pp. 790–800, 2007.

[145] X. Guo and X. G. Xia, "A distributed space-time coding in asynchronous wireless relay networks," *IEEE Transactions on Wireless Communications*, vol. 7, no. 5, pp. 1812–1816, 2008.

[146] Z. Li and X. G. Xia, "An Alamouti coded OFDM transmission for cooperative systems robust to both timing errors and frequency offsets," *IEEE Transactions on Wireless Communications*, vol. 7, no. 5 Part 2, pp. 1839–1844, 2008.

[147] M. Sharp, A. Scaglione, and B. Sirkeci-Mergen, "Randomized cooperation in asynchronous dispersive links," *IEEE Transactions on Communications*, vol. 57, no. 1, pp. 64–68, 2009.

[148] T. Wang, A. Cano, G. B. Giannakis, and J. N. Laneman, "High-performance cooperative demodulation with decode-and-forward relays," *IEEE Transactions on Communications*, vol. 55, no. 7, pp. 1427–1438, 2007.

[149] M. El-Hajjar, O. Alamri, S. X. Ng, and L. Hanzo, "Turbo detection of precoded sphere packing modulation using four transmit antennas for differential space-time spreading," *IEEE Transactions on Wireless Communications*, vol. 7, no. 3, pp. 943–952, 2008.

[150] H. Wei, L.-L. Yang, and L. Hanzo, "Interference-free broadband single-and multicarrier DS-CDMA," *IEEE Communications Magazine*, vol. 43, no. 2, pp. 68–73, 2005.

[151] J. Wu, C. Xiao, and K. B. Letaief, "Multiuser channel estimation for CDMA systems over frequency-selective fading channels," *IEEE Transactions on Wireless Communications*, vol. 4, pp. 1724–1736, July 2005.

[152] S. X. Ng, Y. Li, and L. Hanzo, "Distributed turbo trellis coded modulation for cooperative communications," in *IEEE International Conference on Communications, Dresden, Germany*, June 2009.

[153] S. ten Brink, J. Speidel, and R.-H. Yan, "Iterative demapping and decoding for multilevel modulation," in *IEEE Global Telecommunications Conference*, vol. 1, pp. 579–584, 1998.

[154] M. Tüchler, A. C. Singer, and R. Koetter, "Minimum mean squared error equalization using a priori information," *IEEE Transactions on Signal Processing*, vol. 50, no. 3, pp. 673–683, 2002.

[155] K. Lee and L. Hanzo, "Iterative detection and decoding for hard-decision forwarding aided cooperative spatial multiplexing," in *IEEE International Conference on Communications (ICC09), Dresden, Germany*, June 2009.

[156] Z. Yang, B. Lu, and X. Wang, "Bayesian Monte Carlo multiuser receiver for space-time coded multicarrier CDMA systems," *IEEE Journal on Selected Areas in Communications*, vol. 19, no. 8, pp. 1625–1637, 2001.

[157] R. Chen, J. S. Liu, and X. Wang, "Convergence analyses and comparisons of Markov chain Monte Carlo algorithms in digital communications," *IEEE Transactions on Signal Processing*, vol. 50, no. 2, pp. 255–270, 2002.

[158] A. Doucet and X. Wang, "Monte Carlo methods for signal processing: a review in the statistical signal processing context," *IEEE Signal Processing Magazine*, vol. 22, no. 6, pp. 152–170, 2005.

[159] K. K. Soo, Y. M. Siu, W. S. Chan, L. Yang, and R. S. Chen, "Particle-swarm-optimization-based multiuser detector for CDMA communications," *IEEE Transactions on Vehicular Technology*, vol. 56, no. 5, pp. 3006–3013, 2007.

[160] M. Jiang and L. Hanzo, "Unitary linear dispersion code design and optimisation for MIMO communication systems," *IEEE Signal Processing Letters*, vol. 17, no. 5, pp. 497–500, 2010.

[161] L. Kong, S. X. Ng, R. Maunder, and L. Hanzo, "Successive relaying aided near-capacity irregular distributed space-time coding," in *IEEE Global Telecommunications Conference*, (Honolulu, Hawaii, USA), pp. 1–5, 6–9 September 2009.

[162] P. Ho and D. Fung, "Error performance of multiple-symbol differential detection of PSK signals transmitted over correlated Rayleigh fading channels," *IEEE Transactions on Communications*, vol. 40, no. 10, pp. 1566–1569, 1992.

[163] V. Pauli and L. Lampe, "Tree-search multiple-symbol differential decoding for unitary space-time modulation," *IEEE Transactions on Communications*, vol. 55, no. 8, pp. 1567–1576, 2007.

Index

Author Index

D

E

F

G

H

I

J

K

L

M

X

Y

Z